Chapter 2

MAGNETOTRANSPORT PROPERTIES OF ULTRATHIN METALLIC MULTILAYERS: MICROSTRUCTURAL MODIFICATIONS LEADING TO SENSOR APPLICATIONS

C. Christides

Department of Engineering Sciences, School of Engineering, University of Patras, 26 110 Patras, Greece

Contents

1. SENSORS, MATERIALS, AND DEVICES

1.1. Sensor Characteristics

In man-made devices, where the information is transmitted and processed in electrical form through the transport of electrons, a sensor is defined as a device that receives a *signal* or a *stimulus* and responds with an electrical signal [1]. The *stimulus* is the quantity, physical property, or condition that is sensed as an input signal. Since a sensor does not function by itself, it is always a part of a data acquisition system. Thus, a sensor responds to the *stimulus* and converts it into an electrical signal which is compatible with electronic circuits. The sensor's output signal may be in a form of voltage, current, or charge. An ideal or theoretical output-stimulus relationship exists for every sensor that is characterized by the so-called *transfer function*. This function establishes dependence between the electrical signal S produced by the sensor, and the stimulus s: $S = f(s)$. The transfer function may be a simple linear connection or a nonlinear dependence,

Handbook of Surfaces and Interfaces of Materials, edited by H.S. Nalwa
Volume 4: Solid Thin Films and Layers

that determines the most important characteristics of a sensor:

(i) In the general case of a nonlinear function, the *sensitivity* is defined as the slope $b = dS(s_0)/ds$ at any particular input value s_0, and is not a fixed number as for a linear relationship: $S = \alpha + bs$.

(ii) *Full scale output* is the algebraic difference between the electrical output signals measured with maximum input stimulus and the lowest input stimulus applied.

(iii) *Accuracy errors* arising from hysteresis, that is a deviation of the sensor's output at a specified point of the input signal when it is approached from the opposite direction, and nonlinearity, which is the maximum deviation of a real transfer function from the approximation straight line.

(iv) *Inherent noise*, which arises within the sensor's circuit no matter how well it was designed, produces systematic distortions of the output signal. Such distortions are related to the sensor's transfer function. The noise signals can, generally, be described by an equivalent circuit that contains two additional generators. One is a *voltage noise* generator e_n and the other is a *current noise* generator i_n. One contribution to the sensor noise is thermal resistance noise (also called Johnson noise), which is always present in resistive devices as a *voltage noise*. This noise source contributes a background to the voltage spectral density, which is representative of noise power, considered equal to $S_V = 4k_B T R \Delta f$ (in units of volts squared per Hertz), where k_B is the Boltzmann constant, T is the temperature, R is the total resistance of the sensor, and Δf is the bandwidth, in Hertz, over which the measurement is made.

From the physical point of view, a sensor is a converter of generally nonelectrical effects into electrical signals. Often several transformation steps are required before the electric output signal can be generated. These steps involve changes of types of energy where the final step must produce an electrical signal of desirable format. Since there are several physical effects which cause generation of electrical signals in response to nonelectrical influences, sensor classification schemes range from very simple to the complex. Thus, depending of what it measures (stimulus), what its specifications are, what physical phenomenon it is sensitive to, what conversion mechanism is employed, what material it is fabricated from, and what is its field of application, a broad and representative classification scheme [1] can be constructed. Magnetic memories and sensors are one of the oldest, yet one of the most widely used, solid-state devices. Already at an annual sale of about 40 billion dollars, the market is still growing rapidly thanks to ever-increasing demands in data storage and to new applications of magnetic devices in the field of sensors.

1.2. All-Metal Thin-Film Magnetoresistive Sensors

Today's computers and their precursors are based on an idea known as *stored program electronic computer*, which relies on electronic logic gates and memory. The speed of computers has doubled every three years, a trend known as Moore's law. Thus, the number of circuits that fits on a chip doubles while the price remains the same every year and a half. That trend has been driven by the steady shrinking of the size of microcircuits, as defined by the smallest feature size, or linewidth. However, besides the computing power of the microprocessors, the performance of a computer depends on faster random-access memories (RAM) and denser magnetic storage of information as well. In 1993, the cost of one megabyte of storage capacity was about one dollar, a dramatic decrease from 10^4 dollars per megabyte in 1956 when IBM first introduced the disk-drive technology. In 1998, the cost of one megabyte had decreased further, to less than five cents. The rapid areal density increase and the stunning price–performance improvement have transformed the disk drive into the ubiquitous storage workhorse for computers of all sizes.

IBM innovations in the technology of magnetic hard-disk drives have driven up storage density at a phenomenal rate, now approaching 60% per year [2]. This increase is comparable to the growth in semiconductor industry described by Moore's law. The *areal density*—the number of discrete bits of information that can be squeezed onto a square inch of disk real estate—has been increased at a pattern of magnetic fields that magnetized bits on a circular track directly below on the spinning disk. To read back the data, the head was placed above the track. As the bits spun beneath the head, the sweep of their magnetic fields generated opposing voltages in the head. Since the detectable magnetic flux (stimulus) from a bit decreases as the bit gets smaller, a *scaling* approach to increased density requires reducing the read–write head's dimensions while increasing its sensitivity. To sustain such progress, the technology of recording-head fabrication will need to continue to advance at a rapid pace.

In 1969, the IBM T. J. Watson Research Center, invented a method for making the wire coils by the same photolithographic thin-film techniques used to make semiconductor chips [3]. That method led to very small and sensitive read heads that IBM first used in products [3] in 1979. However, the increased tendency for miniaturization in hard-disk drives required more sensitive sensors than the inductive coils in the reading heads, with an ability to measure smaller magnetic fields. Thus, the reading coils had to be replaced by an alternative material, able to operate as an electromagnetic sensor. The electrical resistivity of a magnetoresistive (MR) thin ferromagnetic film [4] changes according to the strength and the orientation of the magnetic field it experiences. In ferromagnetic materials, the "ordinary" anisotropic transport effects, observed in nonmagnetic films, are present but are accompanied by stronger phenomena having similar geometrical dependences and symmetries. The galvanomagnetic effects unique to ferromagnets are called "extraordinary," "spontaneous," or "anomalous" because of their greater strength relative to the ordinary effects. The extraordinary galvanomagnetic effects derive their strength from the fact that the role of the external field is replaced by an internal field proportional to the magnetization **M**, which is generally much stronger than an applied field. The mechanism by which the microscopic internal field associated with **M** couples to the current density

J in ferromagnets is the spin-orbit interaction between the electron trajectory (orbit) and the magnetization (spin). Thus, while the ordinary effects can be understood as consequences of the classical Lorentz force on the current carriers, *the spontaneous effects are quantum mechanical in origin*.

In a ferromagnet, the magnetoresistance is expected to have a spontaneous contribution that depends on the orientation of magnetization. It is referred to as *anisotropic magnetoresistance* (AMR). Thus, Kohler's rule can be generalized to read for a ferromagnet as: $\Delta\rho/\rho = \alpha(H/\rho)^2 + \beta(\mathbf{M}/\rho)^2$, where the first term describes the ordinary magnetoresistance and the second term describes the spontaneous (anisotropic) magnetoresistance. The AMR effect is observed in many systems [5] to vary as: $\Delta\rho(H)/\rho_{\text{av}} = (\Delta\rho/\rho_{\text{av}})(\cos^2\theta - 1/3)$, where θ is the angle between **J** and **M**, $\rho_{\text{av}} = (\rho_{\parallel} + 2\rho_{\perp})/3$, $\Delta\rho = \rho_{\parallel} - \rho_{\perp}$, $\Delta\rho(H) = \rho(H) - \rho_{\text{av}}$, and $\rho_{\parallel}$ ($\rho_{\perp}$) is the the resistivity in a direction parallel (perpendicular) to **M**. Note that the AMR ratio $\Delta\rho(H)/\rho_{\text{av}}$ is even in the magnetization orientation, $\cos\theta$, as observed and predicted by Kohler's rule.

The incentive to try the AMR effect in recording heads was substantial: MR read elements were expected to be three to five times more sensitive than inductive designs while performing just as well with the smaller diameter disks that were becoming popular. They would also permit the inductive coil to be designed solely for writing data [6]. MR sensors had been used first in the low-density, low-data-rate applications such as magnetic tape players. However, for years, scientists trying to make MR heads for the much more demanding disk-drive environment encountered severe problems with nonlinearity and noise. These problems were solved in the mid-1980s and led to the world's first practical disk-drive head with an MR read element in 1991. Because the MR effect depends on the volume of the sensor, scientists know that an MR head's sensitivity decreases as its dimensions shrink. A density of 5 gigabytes per inch is thought to be close to the limit of MR technology.

Fortunately, a related technology, giant magnetoresistive (GMR) sensing can provide much more sensitivity for a given size head. GMR is the change of resistance when the magnetic alignment of adjacent ferromagnetic (FM) layers separated by nonmagnetic material (NM), called spacer, is changed [7, 8]. GMR sensors consist of multiple layers of materials, some of them only a few atoms thick. The GMR effect depends upon the unusual and extraordinarily sensitive way in which current flows through these layers in the presence of a magnetic field. The MR ratio in these multilayer systems is not a function of the angle between **J** and **M** as it is for AMR, but rather depends on the relative orientation of **M** in adjacent layers. GMR has been observed [9, 10] to obey the equation: $\Delta\rho(\psi)/\rho = (\Delta\rho/\rho)_{\text{gmr}}(1 - \cos\psi)/2$, where ψ is the angle between the magnetizations in the two sets of layers. The angle between either magnetization and the applied field, $\theta = \psi/2$, is important because it indicates the component of magnetization parallel to the field. Since $1 - \cos(2\theta) = 2\sin^2\theta$, then the GMR ratio becomes: $\Delta\rho(\theta)/\rho = (\Delta\rho/\rho)_{\text{gmr}}\sin^2\theta$. For hard-axis magnetization $\mathbf{M}/\mathbf{M}_s = \cos\theta = H/H_a$ (H_a is the anisotropy field). Thus, an approximate form of the field dependence, sometimes observed for GMR in antiferromagnetically coupled multilayers when the field is applied along the hard axis, is: $\Delta\rho(\theta)/\rho = (\Delta\rho/\rho)_{\text{gmr}}(1 - (H/H_a)^2)$. Usually, the field dependence of GMR is much more complicated than implied by this simple expression.

The most useful GMR sensor design for disk drives is known [11, 12] as a *spin valve*. This is a trilayer structure, with an NM layer sandwiched between soft FM layers in which the magnetization of one of the magnetic layers in pinned antiparallel to the applied magnetic field. The pinning is accomplished by an additional magnetic layer strongly antiferromagnetically (AF) coupled to the back of one of the soft FM layers [9, 10, 13]. The involved spin-polarized electron transport from magnetic to nonmagnetic metallic layers gave the idea to create electronic devices that exploit both, the charge and the spin of an electron for their operation [14]. Lucent Technologies introduced the term *spintronics* for such devices.

GMR offers two significant advantages over competing devices. First, the large change in resistance yields a stronger signal, and second, the technology became compatible with integrated circuit (IC) technology [14], so that GMR devices can be included as part of a chip package to make smaller, faster, less expensive sensors and memory chips. The initial GMR devices sold were magnetic field sensors, which were first shipped in 1995. In 1997, IBM marketed hard-disk memory systems using GMR read heads, which had a far greater economic impact than the magnetic field sensors. The processes used to fabricate such recording heads comprise a combination of lithography, deposition (vacuum or plating), and etching steps. Recording heads are eventually formed into sliders that "fly" over magnetic disks to perform "read" and "write" functions. While several hundred silicon very large-scale integration (VLSI) chips can be obtained from one silicon wafer, over 10,000 sliders can be produced from one recording-head wafer. On the other hand, one slider contains only one read element and one write element while each silicon chip contain millions of transistors. This relatively low head-device density on a wafer lessens cleanliness requirements.

Several companies are currently working on nonvolatile memory technologies using GMR materials [14–16], and Honeywell has demonstrated working memory chips. Galvanic isolators are another rapidly emerging area for GMR. New materials and applications, particularly in advanced sensors and memory systems, are under development, and the outlook for widespread applications is promising. In particular, the two-component nature of spintronic devices is expected to allow the production of spin transistors [17] and spin-based memory devices [14, 18]. Currently, emphasis shifts to spin valves patterned into micrometer and submicrometer structures, entering the regime of only a few domains within the FM layers [19]. Micrometer size Co/Cu GMR multilayers have been fabricated [20] by focused ion-beam direct deposition without any lithographic processes. This is a clean process without cross contamination that allows the fabrication of monolithic GMR and semiconductor devices. Furthermore, nanofabrication offers unprecedented capabilities in patterning materials with a

size smaller than the magnetic domain wall, and in manipulating the size, shape, orientation, and composition of nanostructures [21]. Patterned magnetic nanostructures, as small as 100 nm, can lead to innovative MR sensors based on unique properties of single-domain nanostructures [21].

A novel detection scheme has been demonstrated [22] which uses MR materials (AMR or GMR) to measure fields much smaller (<0.01 Oe) than the saturation field of the MR material. This technique consists of applying an ac excitation field to the MR element and then processing the output wave form. Both symmetric and asymmetric MR materials have been used to measure the earth's field with enough precision for compass applications. It has been argued that an MR sensor using these techniques would have some advantages over previous designs, including small size and power needs and implementation of a single excitation stripe for both excitation and feedback biasing.

1.3. Spin Engineering of Metallic Thin-Film Structures

The large magnetic field-dependent changes in resistance possible in thin-film ferromagnet–nonmagnetic (FM–NM) metallic multilayers, was first observed [7] in France in 1988. Changes in resistance with a magnetic field of up to 70% were observed. This phenomenon is due to spin-dependent scattering. Electrons can exist in two quantum states: spin-up if their spin is parallel to the magnetic field of their surroundings and spin-down if the spin is antiparallel to the magnetic field. In nonmagnetic conductors, there are equal numbers of spin-up and spin-down electrons in all energy bands. However, due to the ferromagnetic exchange interaction, there is a difference between the number of spin-up and spin-down electrons in the conduction subbands of ferromagnetic materials. Therefore, the probability of an electron being scattered when it passes into a ferromagnetic conductor depends upon the direction of its spin and the direction of the magnetic moment of the layer. The resistance of two thin ferromagnetic layers separated by a thin nonmagnetic conducting layer can be altered by changing whether the moments of the ferromagnetic layers are parallel or antiparallel. Layers with parallel magnetic moments will have less scattering at the interfaces, longer mean-free paths, and lower resistance. Layers with antiparallel magnetic moments will have more scattering at the interfaces, shorter mean-free paths, and higher resistance. For spin-dependent scattering to be a significant part of the total resistance, the layers must be thinner than the mean-free path of electrons in the bulk material. For many ferromagnets, the mean-free path is tens of nanometers, so the layers themselves must each be typically less than 10 nm.

Antiferromagnetic multilayers (MLs) consist of multiple repetitions of alternating conducting magnetic layers and nonmagnetic layers. The thickness of the nonmagnetic layers is typically 1.5 to 2.0 nm and the thickness is critical. For certain thicknesses, the polarized conduction electrons cause AF coupling between the magnetic layers. Each magnetic layer has its magnetic moment antiparallel to the moments of the magnetic layers on each side, which is exactly the condition needed for maximum spin-dependent scattering. An external field can overcome the coupling which causes this alignment and can align the moments so that all the layers are parallel, giving the low resistance state. If the conducting layer is not the proper thickness, the same coupling mechanism can cause ferromagnetic coupling between the magnetic layers resulting in no GMR effect.

GMR sensors can be created by making four serpentine resistors from this multilayer material. The four resistors are then connected in a Wheatstone bridge configuration. This bridge is the basis behind all standard sensors. The bridge can be configured into a gradiometer, magnetometer, or put on top of integrated electronics. A sensitive bridge can be fabricated from four photolithographically patterned GMR resistors. NVE's GMR Magnetic Field Sensor AAxxx series utilize small magnetic shields that are plated over two of the four equal resistors in a Wheatstone bridge protecting these resistors from the applied field and allowing them to act as reference resistors [23]. Since they are fabricated from the same material, they have the same temperature coefficient as the active resistors. The two remaining GMR resistors are both exposed to the external field. The bridge output is therefore twice the output from a bridge with only one active resistor. The bridge output for a 10% change in these resistors is approximately 5% of the voltage applied to the bridge. Demagnetization factors cause GMR resistors to respond only to the component of magnetic field along their long dimension. However, the narrow resistor traces make GMR resistors immune to transverse fields. Additional permalloy structures are plated onto the substrate to act as flux concentrators. The active resistors are placed in the gap between two flux concentrators.

Unpinned sandwich GMR materials consist of two soft magnetic layers of Fe or Ni or Co alloys separated by a layer of a nonmagnetic conductor such as Cu. With magnetic layers 4- to 6-nm thick separated by a conductor layer, typically 3- to 5-nm thick, there is relatively little magnetic coupling between the layers. For use in sensors, sandwich material is usually patterned into narrow stripes. The magnetic field caused by a current of a few milliamperes per millimeter of stripe width flowing along the stripe is sufficient to rotate the magnetic layers into antiparallel or high resistance alignment. The right-hand rule for magnetic fields from currents provides antiparallel alignment of the moments of the magnetic layers with the moments perpendicular to the current direction. An external magnetic field of 3 to 4 kA/m (35–50 Oe) applied along the length of the stripe is sufficient to rotate the magnetic moments of both layers parallel to the external field. A positive or negative external field parallel to the stripe will produce the same change in resistance. An external field applied perpendicular to the stripe will have little effect due to the demagnetizing fields associated with the extremely narrow dimensions of these magnetic objects. The value usually associated with the GMR effect is the percent change in resistance normalized by the saturated or minimum resistance. Sandwich materials have values of GMR typically 4–9% and saturate with 2.4–5 kA/m (30–60 Oe) applied field.

Spin valves, or antiferromagnetically pinned spin valves, are *low- (saturation) field* GMR structures. For technological applications of GMR such as for MR read heads in computer disk drives, GMR structures must exhibit a change in resistance per unit field (sensitivity) higher than that obtained in AMR heads. Spin valves are similar to the unpinned spin valves or sandwich structures. In their simplest design (Fig. 1), an additional layer of an antiferromagnetic (AF) material is provided on the top or the bottom of a sandwich structure: FM_1–spacer–FM_2–AF, which forms an *exchange-biased sandwich*. This structure takes advantage of a phenomenon that is often referred to as *exchange anisotropy*. Exchange anisotropy arises from an interfacial magnetic exchange coupling between an antiferromagnetic layer and a ferromagnetic layer [24]. The antiferromagnetic material (FeMn or NiO) couples to the adjacent magnetic layer and pins it in a fixed direction. The other magnetic layer is free to rotate. These materials do not require the field from a current to achieve antiparallel alignment or a strong antiferromagnetic exchange coupling to adjacent layers. The direction of the pinning layer is usually fixed by elevating the temperature of the GMR structure above the blocking temperature. Above this temperature, the antiferromagnet is no longer coupled to the adjacent magnetic layer. The structure is then cooled in a strong magnetic field which fixes the direction of the moment of the pinned layer. Since the change in magnetization in the free layer is due to rotation rather than domain-wall motion, hysteresis is reduced. Values for GMR are 4–20% and saturation fields are 0.8–6 kA/m (10–80 Oe).

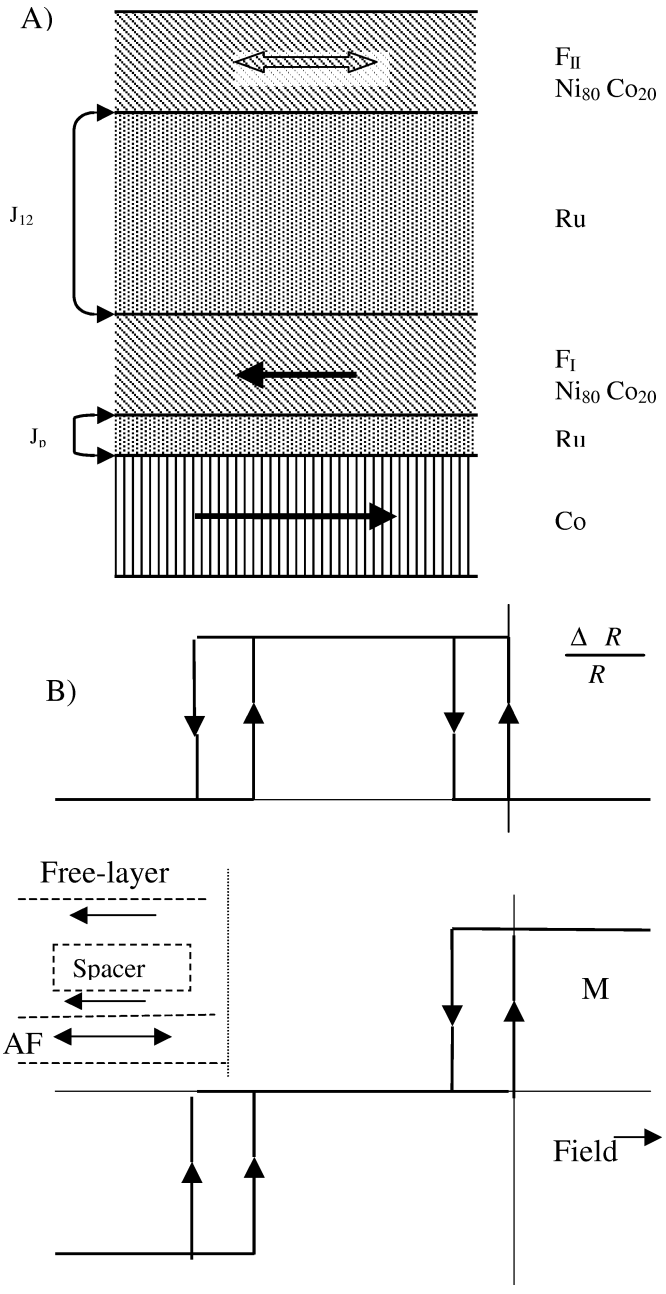

Fig. 1. (A) Schematic of a spin-engineered structure. The exchange-coupling $\mathbf{J}_{12}$ between two $Ni_{80}Co_{20}$ layers is measured by pinning the moment of one of the $Ni_{80}Co_{20}$ layers (F_I) antiparallel to a Co layer. The moment of the Co layer is set equal to the sum of the moments of the two $Ni_{80}Co_{20}$ layers. (B) Schematic of an exchange-biased sandwich structure (spin valve). Magnetoresistance and isothermal magnetization loops are shown.

Linearization of spin-valve sensor response is the major advantage over the parabolic signal response of conventional AMR sensors [28, 27]. In an AMR sensor, resistance depends on the angle between the current flow direction and the magnetization direction of the MR film. Typically, a soft adjacent layer (SAL) provides a transverse biasing to produce the linear read signal. The SAL is usually an NiFeX alloy film, with X representing a third element [25]. To discuss the issue of GMR linearization, a simple spin-valve sensor is considered. It consists of a ferromagnetic free and a ferromagnetic reference layer separated from each other by a thin spacer layer. The magnetization $\mathbf{M}_2$ of the reference layer is pinned along the transverse direction, typically by exchange coupling with an antiferromagnetic layer (e.g., FeMn), while the magnetization $\mathbf{M}_1$ of the free layer is allowed to rotate in response to signal fields. The resultant spin-valve response is: $\Delta R \sim \cos(\theta_1 - \theta_2) \sim \sin\theta$, where θ_1 and θ_2 $(=\pi/2)$ are the directions of the free and the pinned layer magnetizations, respectively. If the magnetic anisotropy hard axis of the free layer is lying along the transverse signal field (H) direction, the magnetic signal response is linear ($\sin\theta_1 \sim H$), yielding in turn a linear spin-valve sensor response ΔR.

The linearity of the spin-valve response depends on both, the precise transverse magnetic orientation of the reference layer and the linearity of the magnetic behavior of the free layer in the transverse direction. If the pinning field of the reference layer is not high enough compared with the transverse demagnetization field or the exchange-bias pinning field is misaligned from the transverse direction, then $\theta_2 \neq \pi/2$, resulting in a nonlinear spin-valve response. In addition, if the AMR response from the free layer is not negligible compared with the spin-valve response, the resultant sensor response is modified from the simple linear spin-valve response by the presence of a parabolic nonlinearity from residual AMR response. Thus, the maintenance of a linear spin-valve response characteristic is an impor-

tant task requiring proper operation of various components of the spin-valve sensor.

Symmetrical spin valves achieve additional spin-dependent scattering by adding a third magnetic layer, a second antiferromagnet layer, and a second conductive layer. The top and bottom magnetic layers are pinned by adjacent antiferromagnetic layers in a fixed direction, and the center layer is free to rotate [26]. Spin valves are receiving a high level of research interest due to their potential for use in magnetic read heads for high density data storage applications.

However, far less attention has been paid to the very large application area of other types of magnetic sensors, such as angle, rotation speed, and position sensors [1]. In these applications, the GMR effect can offer some attractive advantages over anisotropic MR (AMR), like the high MR ratio and the 360° period of the angle dependence. Specifically, in AMR (e.g., single-layer permalloy) films the dependence of the resistance on the angle ϕ between the current direction and the magnetization direction is: $R = R(\phi = 0) - \Delta R \sin^2 \phi$. Thus, two AMR sensing elements can together give 180° output when placed with an angle of 45° relative to each other. On the other hand, the GMR resistance depends on the angle θ between the magnetization directions of adjacent FM layers: $R = R(\theta = 0) + \Delta R(1 - \cos\theta)/2$. Thus, two GMR sensing elements can together give full 360° output when placed at right angles relative to each other. The material requirements for these sensors, that are mainly used in automotive [29, 30] (such as ABS, crankshaft, camshaft sensors in cars) and industrial environments are very different from those for read heads [31, 32]. Robustness at high temperatures (up to ~200 °C) and in large magnetic fields (up to ~100 kA/m) is often a prerequisite. In addition, the output signal should be large and unambiguous. Since in many cases Wheatstone bridge configurations [29, 30] are desired to reduce the effect of temperature variations, it should be possible to realize GMR elements with opposite signs of the resistance change caused by an applied magnetic field. This means that an asymmetric MR curve is preferred.

In a conventional spin valve [33, 34], both the magnetic field and the temperature range for operation is too narrow for sensor applications. The main obstacle is the exchange biasing produced by the conventional pinning layer structure. Philips has demonstrated a robust GMR material system for magnetic sensors [35]. To achieve thermal, magnetic stability and an unambiguous asymmetric MR effect, an *exchange-biased artificial antiferromagnet* (AAF) structure was used. The AAF structure is composed of a $Co_{90}Fe_{10}$/Ru/$Co_{90}Fe_{10}$ sandwich that induces an antiparallel alignment between adjacent magnetic moments (Fig. 2). The pinning is accomplished by an additional $Ir_{18}Mn_{82}$ *bias* layer (~10 nm) below the AAF trilayer. Experiments have shown that this material can withstand magnetic fields >150 kA/m and annealing at temperatures >275 °C without irreversible damage [35], making this GMR system suitable for sensor applications.

Current-perpendicular-to-plane (CPP) GMR is referred [36] to the case in which the current flow is perpendicular to the planes of a multilayer. In the semiclassical approach [37], it is assumed that the interfaces are sufficiently separated and the quantum interference effects due to reflection from the interfaces can be neglected. Thus, if the interfaces are separated by more than a bulk mean-free path then the total resistance can be broken into contributions from the bulk regions and to resistances associated with each interface [38, 39], which can be extracted from experiment. Generally, it is assumed that the interface resistance results from defects at the interfaces (interfacial roughness) of interdiffused atoms. However, the agreement between calculated results [40] and results extracted from experiments on Co/Cu MLs argue that spin-dependent interface resistance may not be dominated by defect scattering as is often assumed. This interface resistance from defect-free interfaces is due to nonzero spin-reflection coefficients at the interface [41, 42].

Some models of the magnetoresistance for *current in-plane* and CPP provide spin asymmetries for interface and bulk scattering in magnetic multilayers. Typically, interface spin asymmetries are four times larger than in the bulk, which leads to the fact that the CPP geometry exhibits three to ten times higher magnetoresistance than the current-in-plane (CIP) configuration. It is worth noting that these asymmetries could be due to diffuse scattering instead of the specular spin reflection discussed here. Schematically, it is easier to imagine the GMR effect as a simple spin-polarizer–analyzer model by considering only specular interface scattering in the CPP geometry. Thus, each interface with a ferromagnet acts as a polarization filter for spins. If the magnetic moments between adjacent magnetic layers are aligned antiparallel then the analog of crossed optical polarization filters leads to little transmission. If they are parallel, they both transmit spins. The smaller magnetoresistance of the CIP geometry can be understood as a shunting effect whereby electrons are able to avoid spin-dependent scattering at the interfaces by traveling inside the layers. To achieve the high magnetoresistance of the CPP geometry, but to avoid its extremely low absolute resistance (~$\mu\Omega$), several attempts have been made to produce one-dimensional wire or thin-film stripe structures in which the current runs perpendicular to the interfaces and is confined to the wire or the thin-film stripes. CPP-GMR MLs are important in nonvolatile computer memory applications that require high device density and submicron device dimensions. In this case, the lateral dimensions of the MLs are constrained, resulting in width dependence of GMR in Cu/Co multilayer nanowires [43] (examined line widths between 750 and 35 nm).

Spin-dependent tunneling (SDT) structures are similar to CPP-GMR MLs except that an extremely thin (~1–2 nm) insulating layer is substituted for the conductive interlayer separating the two magnetic layers. *Magnetic-tunnel junctions* (MTJ) have emerged as another source of large MR effects [44]. Such devices consist of a ferromagnetic (FM) top and a (typically different) FM bottom electrode separated by a thin oxide (insulator) layer, usually Al_2O_3 (sapphire) or $SrTiO_3$, that defines two metal-oxide interfaces. The conduction is due to quantum tunneling through the insulator. The size of the tunneling current between the two magnetic layers is modulated by the di-

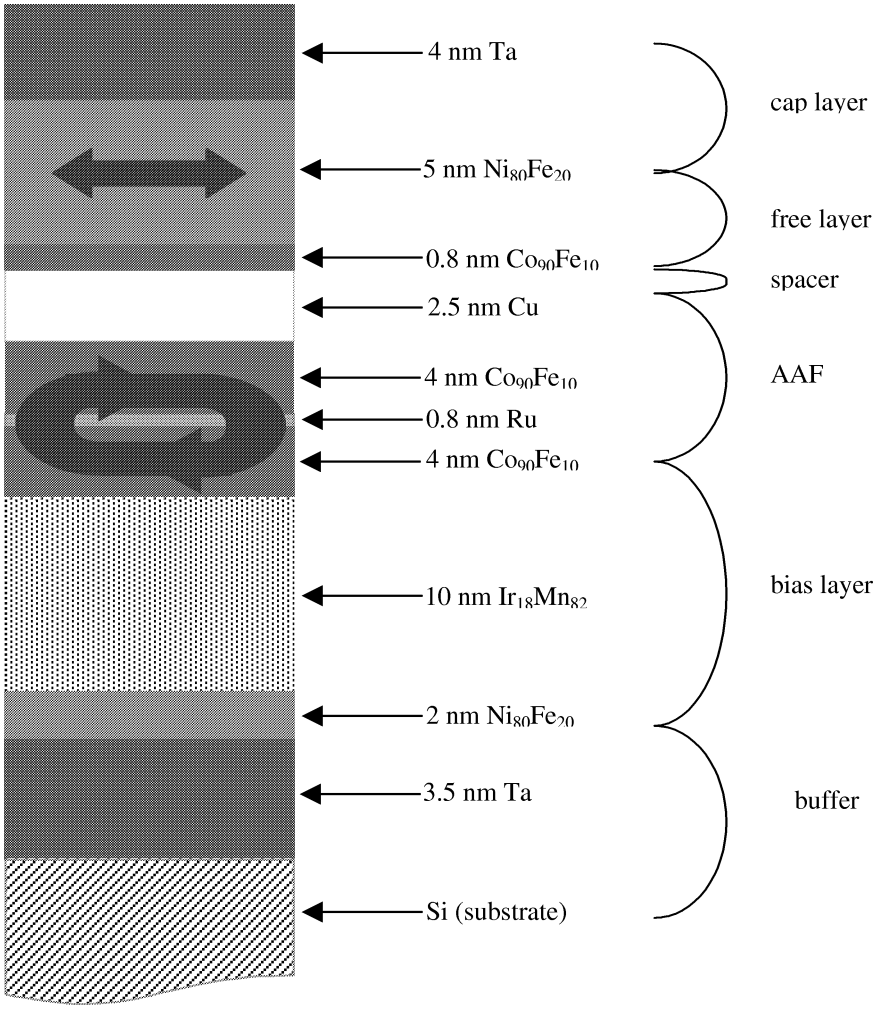

Fig. 2. Schematic of a GMR material system that comprises an exchange-biased artificial antiferromagnet (AAF), suitable for application in magnetic sensors (courtesy of Philips Research Laboratories, Eindhoven).

rection between the magnetization vectors in the two FM layers. The conduction path must be perpendicular to the plane of the GMR material since there is such a large difference between the conductivity of the tunneling path and that of any path in the plane. When the electrodes are FM, the tunneling of electrons across the insulating barrier is spin polarized, and this polarization reflects that of the density of states (DOS) at the Fermi level (E_F) of the electrodes. Spin-polarized tunneling gives rise to *tunneling – MR* (TMR) because the resistance of the junction depends on whether the electrodes have parallel or antiparallel magnetization. This change is found ~10–24%, between 300 and 5 K, in the *tunnel conductance at zero bias with the application of a magnetic field*. However, the physics governing the spin-polarization P of tunneling electrons from a given FM electrode is not clearly understood. This spin polarization was generally thought to reflect a characteristic intrinsic spin polarization of the DOS in the FM:

$$P = \frac{N_\uparrow(E_F) - N_\downarrow(E_F)}{N_\uparrow(E_F) + N_\downarrow(E_F)} \quad (1)$$

Moreover, findings show that the amplitude of the spin polarization and its sign depend on the choice of the barrier material [45], revealing [46] the role of the metal-oxide interface in determining the spin polarization of MTJ. According to Slonczewski's theory [47], the transmission of charge and spin currents occurs through a rectangular barrier separating free-electron-like FM metals. It predicts a strong influence of tunnel barrier height on the orientation of the spins tunneling across the metal-oxide interface, thereby affecting the spin polarization and also affecting the exchange coupling between the FM electrodes. The effective polarization of Co was found to be positive (higher tunneling probability for majority spin electrons) when the barrier is Al_2O_3, and was found to be negative (higher tunneling probability for minority spin electrons) when the barrier is $SrTiO_3$ or $Ce_{0.69}La_{0.31}O_{1.845}$. However, the bias dependence of the TMR is completely different in these two cases, revealing the strong influence of the electronic structure of the barrier and the barrier-electrode interface. The experimental results at low bias are interpreted according to Jul-

liere's [48] expression,

$$\frac{\Delta R}{R} = \frac{R_{AP} - R_P}{R_{AP}} = \frac{2P_1P_2}{1 + P_1P_2} \quad (2)$$

where R_{AP} and R_P are the resistances with magnetizations of the electrodes antiparallel and parallel, respectively, and P_1, P_2 are the electron spin polarizations. In junctions with FM transition-metal electrodes and Al_2O_3 barriers, a normal TMR has been found; that is, the tunnel resistance is smaller when the magnetizations of FM_1 and FM_2 are parallel. This behavior is expected when the sign of the polarization coefficient P is the same for both electrodes and is consistent with the aforementioned uniformly positive spin polarization found for various transition metals in FM–Al_2O_3/Al junctions. However, with types of barriers other than Al_2O_3 the spin polarization of electrons tunneling from Co or NiFe (permalloy) can also be negative [45], resulting in inversion of the TMR ($R_{AP} < R_P$). This indicates opposite polarizations at the FM_1/(barrier) and (barrier)/FM_2 interfaces. Thus, this influence of the barrier on the spin polarization opens new ways [46] to shape and to optimize the TMR.

The angular dependence of TMR was shown [50] to closely follow that of the spin valve: $\Delta\rho(\psi)/\rho = (\Delta\rho/\rho)_{gmr}(1 - \cos\psi)/2$ (ψ is the angle between the magnetizations in the two sets of layers), which is also consistent with Slonczewski's theory [47]. Additionally, the TMR decreases with increasing temperature due [51, 52] primarily to the decrease in *surface* magnetization of the electrodes. This temperature dependence of surface magnetization is probably due to the generation of spin waves: $\mathbf{M}^{surf}(T) = \mathbf{M}_s^{surf}(1-[T/T_c]^{3/2})$. The spin waves break down the independence of the two spin-conduction channels, thus increasing the total conductance and reducing the TMR effect (Eq. (2)) from 77 to 300 K. In Co/Al_2O_3–(soft magnetic layer) tunnel junctions the junction resistance is typically [52] of order 10 kΩ at 300 K and increases with decreasing temperature.

Extremely small SDT devices (several millimeters on a side) with high resistance can be fabricated using photolithography, allowing very dense packing of magnetic sensors in small areas. The quality of tunnel junctions and the reproducibility in fabrication in general depend critically on the properties of the, typically, 1- to 2-nm thin insulating tunnel barrier. Tunneling is moreover extremely surface sensitive in that it displays the band structure of the electrode surface very close to the barrier insulator. Good barrier uniformity without pinholes is the key aspect to obtain current-voltage (I–V) characteristics with low-leakage currents. These conditions are not fulfilled for all barrier materials. It tends to be difficult to form high-quality and highly insulating tunnel barriers in many cases, especially if a transition metal is used as the base electrode. The native oxides and suboxides of transition metals often show poor, undesirable, insulating properties [49]. This inefficiency has been sorted out by the *artificial* tunnel barriers that do not consist of the oxide of the material to be tunneled into.

In SDT devices, the saturation fields depend upon the composition of the magnetic layers and the method of achieving parallel and antiparallel alignment. Values of saturation field range from 0.1 to 10 kA/m (1–100 Oe) offering the possibility of extremely sensitive magnetic sensors with very high resistance suitable for battery operation. The (compared to GMR systems) inherent high absolute resistance due to the tunneling effect and the therefore easily measurable MR give them a high potential for low-power magnetic field sensors [53, 54] and nonvolatile magnetic random-access memory (MRAM) [55, 56]. Table I gives a tentative classification scheme of the aforementioned spin-engineered structures.

Table I. Classification Scheme of Magnetoresistive Sensors*

Properties	AMR	GMR	SDT
Stimulus:	Magnetic field	Magnetic field	Spin-polarized scattering
Specifications:	Proximity, position, rotation detector, magnetic compass, recording read heads	Position, level, displacement sensors, recording read heads, nonvolatile MRAM	Tunnel junctions, nonvolatile MRAM, battery-powered devices
Detection means:	Positive MR	Negative MR, exchange biasing	Negative or positive MR
Conversion phenomenon:	Electromagnetic	Electromagnetic	Spin-dependent tunneling
Material:	Ferromagnetic thin films	Spin-valve heterostructures, multilayers	Compositionally modulated FM_1–oxide–FM_2 junctions
Application:	Magnetometers, navigation, integrated sensors for automobiles, magnetic storage	High-density hard-disk drives, gradiometers, galvanic isolators, spin transistors	Miniaturized computers, cellular telecommunications, space missions

*Specifications and applications of the AMR sensors hold for the GMR sensors as well.

1.4. Magnetoelectronic Memories

At the root of the emerging field of magnetoelectronics are electronic devices with an FM component that lets them not only switch between two stable states in one clock cycle but also retain the state they are in when power is removed (nonvolatile effect). These properties may give huge enhancements of the speed, reliability, and power consumption of solid-state memory. The compact design and the simple operation of magnetoelectronic devices make them ideal storage cells for fast, nonvolatile, random-access memory that can retain information when switched off [14]. Magnetoelectronic devices can be grouped according to the physics of their operation into *hybride ferromagnet-semiconductor structures, magnetic-tunnel junctions*, and *all-metal* spin transistors and spin valves.

At the heart of a random-access memory is an integrated method of addressing the element to write a bit into it or to read a bit out of it. For a two-dimensional array of memory cells, a two-dimensional array of rows and columns of write wires is employed, with each cell inductively coupled to a write wire from one row and another from one column. The process of writing data into a cell is essentially the same for any of the three approaches. In particular, the switching (reversal from positive to negative direction of magnetization) time for transition-metal ferromagnetic film elements is a few nanoseconds, and the write current for an element with dimensions smaller than a micron is a few milliamperes. However, reading a cell's content may utilize any of several physical mechanisms. Thus, a distinguishing characteristic of the three device categories is their readout mechanisms.

If a magnetoelectronic device is to succeed within electronics, it must be capable of being integrated with other systems technologies and it must promise an order of magnitude improvement in one or more valuable performance categories embodied in an established product. Thus, a successful magnetoelectronic memory cell has to fulfil three requirements [57]: (i) should be based on a device with impedance of $\sim$1–10 kΩ, (ii) a readout voltage discrimination of $\sim$20–40 mV (for compatibility with existing sense amplifier circuitry), and (iii) device fabrication must be compatible with standard complementary metal-oxide semiconductor (CMOS) processing steps. Drawbacks for all-metal spin transistors and spin valves are their low impedance and relatively low levels of readout voltage, magnetic-tunnel junctions have strict fabrication requirements, while both approaches incorporate a metal-oxide semiconductor-field-effect transistor (MOSFET) in the memory cell for isolation. However, most important is that *fabrication procedures for multilayer magnetic elements and standard* CMOS *processing are incompatible*. Thus, from the perspective of manufacturability, the most promising choice seems to be the hybrid ferromagnet-semiconductor device [14, 58] because it involves a single ferromagnetic layer that is electrically isolated from the rest of the device structure, which can be protected by insulating layers during processing of the magnetic layer and vice versa. Today, although several prototypes of magnetic RAM have been built [14–16] from the three main device types, the pursuit of integrated magnetic-based RAM is still in its infancy.

2. MORPHOLOGY-INDUCED MAGNETIC AND MAGNETOTRANSPORT CHANGES IN GMR FILMS

2.1. Oscillatory Magnetic Anisotropy and Magnetooptical Response

Oscillatory coupling was shown to be a general property of almost all transition-metal magnetic multilayered structures in which the nonferromagnetic layer comprises one of the 3d, 4d, 5d transition metals or one of the noble metals [59]. The oscillation period was found to be a few atomic planes of the spacer layer, typically $\sim$1 nm, but varying up to $\sim$2 nm of the nonferromagnetic layer. Only those multilayers for which the interlayer coupling is antiferromagnetic display significant GMR effect because the relative orientation of the magnetic moments of neighboring layers is significantly altered by applying a magnetic field. Therefore, the amplitude of the GMR ratio $\Delta R/R$ oscillates with the same period as the interlayer exchange coupling, varying between about zero (parallel alignment of adjacent moments) and local GMR maxima (antiparallel alignment of adjacent moments) that decrease with increasing spacer layer thickness.

The discovery of oscillations in interlayer exchange coupling as a function of nonmagnetic spacer layer thickness has led to a widespread interest in oscillatory magnetic properties in layered structures for both fundamental and technological reasons. Thus, beside the oscillatory GMR, the magnetooptical response [60–63] and magnetic anisotropy [64] also exhibit oscillatory behavior as a function of film thickness. Magnetic anisotropies of ultrathin films, observed [65] in Ni/Cu(100) and [66] Co/Cu(110), are inherently connected to the structure and the morphology of the films. In these systems, strong relaxations of the lattice constants upon growth are found, giving rise to altered magnetic anisotropies. However, changes in film morphology associated with the change from a filled layer to an incompletely filled layer could also cause the magnetic anisotropy to change. Thus, in a layer-by-layer mode of growth, the variations of the film roughness could lead to oscillations of the magnetic anisotropy with a period of one monolayer. This is analogous to the intensity variations observed in a reflection high-energy electron diffraction (RHEED) experiment.

A relatively easy and fast experimental technique, that is used to determine changes in magnetic anisotropy during film growth, is the analysis of the magnetic hysteresis loops determined from the magnetooptical Kerr effect (MOKE). In general, determining anisotropies from hysteresis loops is very inaccurate or is based on assumptions concerning the magnetization reversal mechanism. However, these limitations do not exist in systems that exhibit a superposition of twofold and fourfold anisotropies. A representative system, that is of particular importance in sensor applications, consists of Co films grown on a Cu(100) substrate [67, 68] with a well-defined preferential step edge direction along [1$\bar{1}$0]. Thus, when the easy

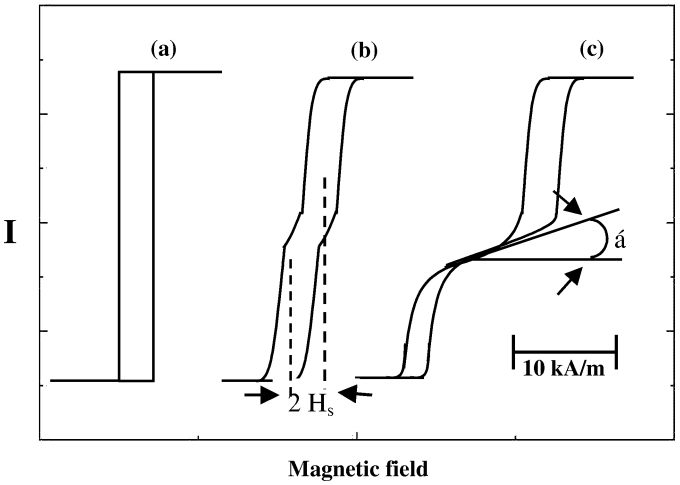

Fig. 3. Schematic MOKE hysteresis loops that can be obtained from a 2.5 monolayer of a Co film grown on a stepped Cu substrate miscut by 0.1° with respect to the (100) orientation: (a) H along the [1$\bar{1}$0] direction, (b) H along the [110] direction, (c) same as (b) but having a bias field of $H_{\text{bias}} = 5$ kA/m along the [1$\bar{1}$0] direction. The definition of the shift field H_{shift} and of the linear initial slope as tan α, is indicated in (b) and (c).

magnetization axis runs parallel to [1$\bar{1}$0] *in situ* MOKE hysteresis loops with the magnetic field applied either parallel (along [1$\bar{1}$0]) or perpendicular (along [110]) to the step edges exhibit a rectangular loop shape or two single loops shifted against each other (Fig. 3), respectively. This difference of the magnetic loops along the [1$\bar{1}$0] and [110] directions, which are magnetically equivalent on a perfect fourfold Co(100) film, can be attributed to the steps and can be described by a uniaxial anisotropy energy [69] constant K_u. With the [1$\bar{1}$0] direction being the easy magnetization axis, the [110] direction is the intermediate axis because it combines the easy character of the fourfold cubic anisotropy with the hard character of the uniaxial anisotropy. Thus, the uniaxial magnetic anisotropy constant K_u of the [1$\bar{1}$0] edges is proportional to the field difference between the zero field and the center of one of the shifted loops, observed in MOKE loops along the intermediate [110] direction. This field difference defines a shift field $H_{\text{shift}} = K_u/\mu_o \mathbf{M}_s$, $\mathbf{M}_s$ the saturation magnetization, that can be determined with high accuracy.

Analysis of transverse Kerr hysteresis loops in terms of anisotropy fields have shown [70] an oscillatory variation of the H_{shift} with a period of one monolayer, with minima at each completed layer, up to 15 monolayers of Co. These loops were taken during the growth of a Co film on a stepped Cu(100) substrate with a bias field $H_{\text{bias}} = 5$ kA/m applied along the [1$\bar{1}$0] easy direction while sweeping the loop along the [110] intermediate axis. This H_{bias} introduces an additional unidirectional anisotropy, resulting in a shift field of the two loops that increases by the bias field while it forces the magnetization into the easy [1$\bar{1}$0] direction as soon as the sweeping field along the [110] axis is reduced to zero. Starting from a single-domain configuration the increasing field along the [110] intermediate axis rotates the magnetization reversibly away from the [1$\bar{1}$0] easy-axis direction. This tilt angle is measured directly by determining the magnetization component along the intermediate axis or by determining the initial slope of the extended linear shift between the two shifted loops (Fig. 3). The slope is related to the anisotropy barrier against which the magnetization has to be rotated. Therefore, the origin of the observed oscillations in H_{shift} can be correlated with oscillations in the uniaxial anisotropy constant K_u as the film surface changes periodically from "flat-to-rough" in a layer-by-layer mode of growth, corresponding to a complete and an incomplete top layer with period one monolayer of Co, respectively.

It has been shown that uniaxial magnetic anisotropies could be generated by lattice symmetry breaking, either by the presence of a surface–interface [71] or by a uniaxial strain due to lattice mismatch [72]. The step-induced magnetic anisotropy originates from two different effects: the missing bonds at the step edges, called Néel pair-bonding model, and the strain within the film. The contribution of these two effects to the step-induced magnetic anisotropies can be separated by studying fcc films as a function of step density because the pair-bonding effect and the biaxial strain effect produce a different step-density dependence of the anisotropy. The step-induced uniaxial magnetic anisotropy of face-centered cubic (fcc) Co films grown on a curved Cu(001) substrate was investigated [68] in the vicinal angle range of 0–6°. The anisotropy strength was found to depend linearly on the step density, indicating that biaxial strain due to in-plane lattice misfit is not the origin of the step-induced anisotropy. By performing [68] Cu absorption experiments, it was observed that the magnetization easy axis switches by 90° when the Co steps are decorated with ∼1 atomic row of Cu per step, independent of the step density. These Cu absorption experiments indicate that the magnetization easy-axis switching is caused only by the Cu absorbates located near the step edges of Co. Thus, it was concluded that, according to the Néel pair-bonding model, modifications to the horizontal bonds rather than to the diagonal bonds are responsible for these observations in fcc thin films.

As in H_{shift}, oscillations in the coercive field H_c were observed with increasing Co layer thickness up to 15 monolayers [64]. Remarkably, both H_{shift} and H_c exhibit a pronounced change in the overall course above ∼16 monolayers. In particular, the observed drop of H_{shift} below the bias field of 5 kA/m indicates that K_u changes sign. Consequently, the easy magnetization axis flips from the [1$\bar{1}$0] to the [110] direction at a critical thickness of ∼16 Co monolayers. This has been correlated with the onset of relaxation of the misfit induced strain in the Co lattice upon growth [73]. Furthermore, the H_c increases strongly above the critical thickness of 16 monolayers [73].

Both, the change of the easy magnetization axis by 90° within the plane and the strengthening of H_c above a critical Co layer thickness, might open the possibility of fabricating GMR read heads without the need for an additional biasing scheme. This idea belongs to Allenspach and Weber [74] and is discussed briefly later. A useful spin-valve-based sensor requires two magnetic layers in a single-domain state separated by a nonmagnetic spacer. The magnetization of the pinned layer

must be fixed along a certain direction, whereas the magnetization of the free layer follows the magnetic field to be sensed, thus changing from more parallel to more antiparallel alignment with respect to the pinned layer when sensing two oppositely oriented bits. For *linear operation* of the device in an applied field, the magnetization of the two layers has to be at an angle of 90° as long as no magnetic field is applied. In currently used spin-valve devices, this biasing is achieved by fixing the magnetization of the pinned layer along its hard magnetization direction either by permanent magnets or by exchange coupling to an antiferromagnetic layer as FeMn or NiO. An alternative way to achieve the required 90° orientation might become possible without the need for external biasing, exploiting the fact that the intrinsic easy magnetization direction as well as the coercive field depends strongly on film thickness [74]. As the H_c increases strongly above the critical thickness of Co (it reaches values of 6 kA/m for the largest thickness investigated [73]), a thick Co layer keeps its magnetization aligned perpendicular to the $[1\bar{1}0]$ step direction, of the Cu(100) substrate, even in the external fields to be sensed and hence remains pinned. A separate film with a thinner Co film, that exhibits a small coercive field, can be used in the place of the free-sensing layer. In this way, the magnetizations of the two Co films remain orthogonal to each other without extrinsic biasing.

Magnetization image of a prototype Co/Cu/Co/Cu(100)-layered structure has shown [70] that the magnetic properties of the single Co layers, with five monolayers for the free layer and 30 monolayers for the pinned layer, are also preserved when a Cu spacer layer of 100 monolayers is used. Thus, the magnetization directions correspond to the easy axes of the single films and subtend an angle of 90°. As described previously, both Co layers remain in a single-domain state when a larger external magnetic field than the coercive field of the free layer rotates its magnetization without to influence the magnetization direction on the pinned layer. To obtain a working GMR device, the Cu(100) substrate must be replaced by an insulating or semiconducting material such as Si(100) or MgO(100) that can serve as a substrate for epitaxially grown or sputtered films [75, 76].

2.2. Comparison between Epitaxial and Polycrystalline GMR Structures

GMR is displayed by a wide variety of inhomogeneous magnetic nanostructures consisting of magnetic entities of thin ferromagnetic layers or particles, separated by thin nonferromagnetic metallic spacer layers [38, 39]. Although the observation initially appeared in single-crystalline (100)Fe/Cr sandwich and superlattice structures grown by molecular beam epitaxy (MBE) [7, 8, 77], it was found soon afterward [78] that similar results could be obtained in polycrystalline multilayers grown by magnetron sputtering. These experiments also revealed that GMR could be obtained in a wide variety of transition-metal magnetic multilayers [38, 59]. Magnetron sputtering allowed the study of many different magnetic multilayered systems. One of these systems, consisting of ferromagnetic cobalt layers separated by thin copper layers, was found to exhibit very large GMR effects that exceed 70% at room temperature [79, 80] for (111) texturing. Qualitatively, the reason for this is that, near the Fermi energy, the band structures of Co and Cu for majority spin carriers are similar, while the band structures for minority spin carriers are different. This leads to a large contrast in spin-dependent scattering of majority and minority carriers as they cross the Co/Cu interfaces. For sputter-grown Co/Cu MLs, it was found [80] that for the most complete antiferromagnetic coupling between Co layers (corresponding to the largest GMR values), it was necessary to use an Fe buffer layer to achieve flat, conformal Co and Cu layers. While the largest GMR values require magnetic fields exceeding ∼20 kOe, GMR values of 50–60% were obtained in fields of several hundred oersteds and values of 20% or more in fields of a few tens of oersteds. These lower values were obtained by using thicker Cu layers [38], for which the interlayer exchange coupling is weaker.

On the other hand, much work was applied to understanding why single-crystalline (111)-oriented Co/Cu MLs grown by MBE show no GMR [81], whereas polycrystalline (111)-textured Co/Cu MLs grown by sputter deposition show very large GMR values, indicating that the GMR effect is not of esoteric (intrinsic) nature. For many years, this was a puzzle which was addressed by many groups [81]. In fact, lack of complete antiferromagnetic coupling at the appropriate spacer thickness was reported by many MBE groups, which was attributed to structural defects such as local ferromagnetic bridges. It is now generally believed that imperfections in the MBE-prepared MLs account for this behavior [82]. The growth of Co/Cu/Co trilayers onto bulk single crystals of Cu(111) was examined by scanning tunneling microscopy (STM), and it was found that at 0 °C, Co nucleated on Cu(111) in triangular islands which were two atoms thick [82]. STM showed that the Co islands nucleated at each of the two threefold sites of the fcc Cu(111) face. One set of the islands follows the correct fcc stacking sequence (ABCabc), while the other set has a stacking error at the interface (ABCbcb). The islands do not coalesce, but have a vertical channel at the interface, which after deposition of five monolayers of Co at room temperature, varied widely, reaching ∼3 nm in places. When Cu is nucleated on top of the twinned Co islands, it also develops twins with vertical channels at the island interfaces. These channels can persist up to many monolayers of Cu overlayer thicknesses. Thus, subsequent deposition can partially fill these channels, forming ferromagnetic bridges between Co layers. These bridges cause a fraction of the sample to be ferromagnetically coupled, obscuring observation of indirect exchange coupling regardless of whether oscillatory indirect coupling is present. The presence of such pinhole defects in Co/Cu multilayers is confirmed by transmission electron microscopy [83].

Eventually, the use of advanced materials growth techniques, such as the use of surfactants to promote smoother films, has finally led to the observation [84] of oscillatory interlayer coupling in MBE-grown (111) Co/Cu. In this way, the twinning of Co/Cu(111) could be inhibited through the use of Pb as a surfactant. Specifically, deposition of Co onto a Pb monolayer on Cu(111) showed [82] that the Co islands grew in a single

orientation with suppression of stacking faults at the Cu/Co interface. Thus, Cu/Co/Cu trilayers grew untwined with the Pb monolayer floating to the top of the structure. The fact that absorbate layers that float out or segregate to the surface during growth can modify or can control epitaxy in a favorable manner, has been used [85, 86] to improve the performance (large GMR ratios at low switching fields) of Co/Cu/Co spin-valve multilayers grown by sputtering. The use of Pb, Au, and O as surfactants during spin-valve sputtering growth led to preparation of smoother and sharper interfaces that decrease the interlayer coupling (lower switching field) and scatter electrons more specularly (larger GMR ratios). Specifically, deposition of about one monolayer of Pb in the early stages of spin-valve growth has a strong tendency to float out or segregate during growth, leaving the GMR unaltered. Au is almost as effective as Pb, however the Au tends to be left behind in the spin valve, and the GMR ratio is reduced slightly [85]. Perhaps the most important result of surfactant layers has been the discovery [86] that the best spin valves are produced by deposition in a continuous background of 5×10^{-9} Torr (7×10^{-7} Pa) O_2. Using this technique, bottom spin valves and symmetric spin valves with record GMR ratios for such structures at room temperature, of 19 and 25%, respectively, have been produced. However, the way that oxygen acts as a surfactant remains unclear.

A key goal of research in the field of GMR sensors is to retain large GMR values while decreasing the size of the magnetic switching or saturation field required to produce the effect. The use of surfactant layers to modify film growth of Co/Cu/Co spin valves in a way that helped to achieve the goal of large GMR ratios at a low field has shown how important is the development of improved techniques for the control of atomic structure during thin-film deposition. Epitaxial Co/Cu(111) multilayers exhibit a polarization of the Cu conduction due to a good band matching between the Co and the Cu, which is an essential feature for a high GMR ratio. A reduced antiferromagnetic coupling between the Co layers is thought to originate from the fact that there are no extremal spanning vectors of the Fermi surface of Cu along the normal direction [87]. This feature is essential for a low coercivity free layer in spin-valve elements. It was reported [88] that reduced antiferromagnetic coupling of Co layers through Cu(111) spacers can be attributed to stacking faults in the films and reduction of these faults resulted in complete antiferromagnetic coupling. Since these films were grown on Cu(111) substrates, it is not possible to determine their transport properties. The development of methods to produce and to characterize such films on low conductivity substrates is essential for GMR measurements.

The magnetic anisotropy of strained epitaxial Co films deposited on a strained Cu(111) on Si(110) substrate and a miscut Cu(111) single crystal were studied [89]. An unusual uniaxial anisotropy was observed in both cases. This uniaxial anisotropy was related to uniaxial strain in the former case and a slight miscut of the Cu(111) in the later case. Specifically, longitudinal MOKE hysteresis loop measurements of the in-plane component of magnetization reveal an unusual loop shape for the field applied along the Si[$1\bar{1}0$] or the Cu[$\bar{1}10$] direction, which is a loop characteristic of a magnetic hard axis of a film with a combination of uniaxial and triaxial in-plane anisotropy. It has been argued that the uniaxial anisotropy term originates from the uniaxial stress present in the epitaxial relationship of Cu(111) on Si(110) and the step anisitropy for a miscut Cu(111) substrate. However, the observed loops did not comprise two single loops shifted against each other as in fcc Co/Cu(100) films (see Section 2.1), where a superposition of twofold and fourfold anisotropies at step edges induce uniaxial anisotropy that makes the [110] and [$1\bar{1}0$] directions hard- and easy-axis, respectively, depending on the Co layer thickness [68].

Usually, the morphology of epitaxially grown thin films on solid surfaces is controlled by kinetics rather than by equilibrium thermodynamics. A delicate interplay between nucleation, diffusion, and the mass exchange between terraces of different height can cause surprisingly complex morphological features. The mass exchange between terraces is often hindered by an additional activation barrier for the diffusion of adatoms across step edges, called the Schwoebel–Ehrlich barrier [90], which gives rise to a growth in the form of three-dimensional pyramidal structures ("mounds"). These mounds display a characteristic slope, which either becomes steeper with continuing deposition or remains constant [91]. On vicinal surfaces, the Schwoebel–Ehrlich barrier stabilizes step flow growth with equally spaced steps, but may cause meandering instability of the steps and the appearance of new facets [92]. A significant Schwoebel–Ehrlich barrier and three-dimensional growth at lower temperatures has been reported [93] for the (111) surfaces of Pt, Rh, Ag, and Cu, indicating that this barrier depends on the type and the roughness of the step. For steps on a (111) surface, exchange diffusion is favored over hopping. The highest activation is obtained for straight (100) steps and the lowest activation is attained for kinks in a (111) step [94]. Giesen, Icking-Konert, and Ibach have observed [93] a new mechanism of interlayer mass transport which bypasses the Schwoebel–Ehrlich barrier for the diffusion of atoms over step edges. The channel for a rapid mass transport opens when a two-dimensional island engaged in a random walk on a Cu(111) surface touches the boundary of a descending step. The decay rate of the island then increases by $\sim$2 orders of magnitude. Even entire mounds can disappear in a very short time due to ledge contact events caused by equilibrium fluctuations of step edges.

However, the striking GMR differences do not appear only between epitaxial and polycrystalline Co/Cu layers that exhibit (111) texture. *In situ* scanning tunneling microscopy observation [95] of surface evolution in magnetically coupled Cu(100)/[Co(2.1 nm)/Cu(2.1 nm)]$_n$ multilayers, grown by both ion-beam (IBS) and dc-magnetron sputtering (DCM) techniques, shows that the developing layers demonstrate a marked difference in the way in which roughness evolves through the films. For each deposition, a Cu(100) substrate has been used to facilitate epitaxial growth on the (100) terraces. The major difference between the two growth techniques is the incident energy distribution of deposited atoms that is produced. The higher energy IBS system creates a nonconformal roughness that is characterized by comparatively large lateral length

scales. The less energetic DCM system creates an island-upon-island growth that is conformal from layer to layer. In the DCM samples, the island-upon-island tendency is enhanced and leads to pyramidal structures up to five bilayers. Easy-axis MOKE hysteresis loops show that the IBS grown multilayers are ferromagnetically coupled whereas the DCM layers are antiferromagnetically coupled. These differences in roughness evolution have been attributed to adatom mobility over the potential barriers at step edges. The IBS Cu atoms are sufficiently energetic and create uncorrelated roughness, randomizing (canceling) the interactions that favor AF interlayer coupling, whereas the DCM Cu atoms are reflected at the step edges of the pyramidal structures, leading to conformal growth that preserves the sign of the exchange coupling along the growth direction for the studied Co/Cu(100) layer thicknesses.

Interdiffusion and electromigration phenomena are usual sources that influence thin-film formation, properties, and performance in microelectronic applications, where very small lateral as well as depth dimensions of device features and film structures are involved. When these characteristic dimensions become comparable in magnitude to atomic diffusion lengths, then compositional changes can be expected, altering the initial film integrity. This, in turn, frequently leads to instabilities in the functioning of components and devices that are manifested by such effects as decrease in conductivity as well as short- or even open circuiting of conductors, lack of adhesion, and generation of stress. The time it takes for such effects to evolve can be roughly gauged by noting that the diffusion length is given by $\sim 2(Dt)^{1/2}$, where D and t are the appropriate diffusivity and time, respectively. Therefore, $t \approx d^2/4D$, where d is the film or layer thickness. Diffusion mechanisms attempt to describe the details of atomic migration associated with mass transport through materials. The resulting atom movements reflect the marginal properties of materials in that only a very small fraction of the total number of lattice sites, namely, those that are unoccupied, interstitial, or on surfaces, is involved. In epitaxial fcc metallic films, atomic diffusion evolves through lattice and dislocation diffusivity [96], which for Au(001) takes place above $\sim$300 °C with penetration depths of $\sim$100 nm at times of $\sim 10^4$–10^5 s. In polycrystalline films, depending on grain-size distribution, extensive low-temperature ($\sim$120–170 °C) grain boundary penetration occurs at 100 nm of Au thin films within minutes (1–10 min), without much lattice diffusion. The large differences in diffusional penetration times between epitaxial and polycrystalline films is in favor of epitaxial growth when a heat treatment process below $\sim$300 °C is required during fabrication of GMR sensor devices.

While interdiffusion phenomena are driven by chemical concentration gradients, other mass-transport effects rely on electric fields (large current flow), thermal gradients, and stress fields, which give rise to respective electromigration, thermomigration, and creep effects than can similarly affect film integrity. Electromigration, a phenomenon not unlike electrolysis, involves the migration of metal atoms along the length of metallic conductors carrying large direct current densities. Bulk metals approach the melting point when powered with current densities of about 10^4 A/cm^2. On the other hand, thin films can tolerate densities of 10^6 A/cm^2 without immediate melting or open circuiting because the Joule heat is effectively conducted away by the substrate, which behaves as a massive heat sink. In spin-valve-based devices, electromigration effects seriously threaten the integrity of the GMR layers as the physical dimensions scale down to nanometer size ($\sim$0.01 μm). This is related to their intrinsically low impedance and hence their low output voltage. The sense currents needed to achieve a 10-mV readout level correspond to huge current densities on the order of 10^7–10^8 A/cm^2, resulting in electromigration. Ongoing research is focused on developing materials systems with larger coefficients of magnetoresistance in nanometer size sensing cells. Doubling or tripling the relative resistance difference would significantly reduce bias currents and would resolve the associated problems. Today, integrated circuit (IC) technology is limited down to 0.1-μm feature sizes and GMR sensing elements perform above this limit without interdiffusion and electromigration phenomena.

The high GMR ratios achieved in Co/Cu multilayers at room temperature, make them the material of choice in GMR sensing elements. All the previous studies reveal the importance of Cu layering on the morphology on GMR Co/Cu multilayers. The effect of grain size on the GMR of Co/Cu multilayers fabricated by dc-magnetron sputtering has been studied [97] using Co/Cu multilayers grown with identical Co and Cu thicknesses but different grain sizes. Different grain sizes in Co/Cu superlattices were tailored by growing with or without a Cu underlayer (buffer). Grain-to-grain epitaxy caused the large grain underlayer structure to propagate into the multilayer when a Cu buffer is used, whereas without a buffer the multilayer exhibits a fine grain morphology. The enhancement of GMR with increasing grain size can be related to an increase in the mean-free path for electron scattering which leads to a sampling of a larger number of antiferromagnetically coupled layers. These findings emphasize that *subtle structural modifications of magnetic multilayers can lead to dramatically altered properties*. Moreover, the fact that the Co/Cu multilayers with the largest GMR ratio are readily formed using magnetron sputtering, which is a deposition technique compatible with large-scale manufacturing, makes them more attractive candidates for a variety of technological applications.

3. PERFORMANCE PARAMETERS OF MICROFABRICATED GMR MULTILAYERS IN SENSORS

To access the applicability of microfabricated GMR elements in sensors the following measures of performance should be taken into account:

(i) The field-dependent MR(H),

$$\mathrm{MR}(H) = \frac{R(H) - R_{\mathrm{sat}}}{R_{\mathrm{sat}}} \tag{3}$$

where R_{sat} is the limiting value of the resistance that is attained at large applied magnetic fields and MR(H) has a maximum value, called the GMR ratio.

(ii) The field-dependent sensitivity $s(H)$,

$$s(H) = \frac{1}{R}\frac{dR}{dH} \tag{4}$$

with a maximum value,

$$s_{max} \sim \frac{\text{GMR}}{H_s} \tag{5}$$

where H_s is the field for saturation of magnetic moments (parallel alignment) in adjacent layers. This definition assumes that the magnetoresistance per field curve has a peak that can be approximated by a triangle. In practice, the presence of tails on the GMR peak makes the definition of H_s somewhat arbitrary.

(iii) The signal to noise ratio. One contribution to the sensor noise is thermal resistance noise (Johnson noise), which is always present in resistive devices and is caused by thermal smearing of the distribution function of electrons near the Fermi level. This noise source contributes a constant background to the voltage spectral density in the frequency range considered equal to

$$S_V = 4k_B T R \tag{6}$$

A second noise source is Barkhausen noise, which arises from sudden and irreversible domain-wall motion. This noise source can be suppressed by stabilizing a single magnetic domain state and by promoting a coherent process of the magnetization during switching. This can be achieved by providing an easy axis of magnetization perpendicular to the applied magnetic field by using a specific sensor design.

"Flicker" or $1/f$ is a third noise source. This contribution to the sensor noise is a potential limiting factor for applications of magnetoresistive elements in low-frequency magnetic field sensors, or when sensors are miniaturized to allow for higher spatial resolution. The $1/f$ contribution is apparent in the low-frequency range (up to a few kilohertz) while at higher frequencies the contribution of thermal noise becomes dominant in the voltage spectral density spectrum for a GMR-based element [98]. The voltage spectral density for $1/f$ noise can be described phenomenologically by the the relation [98],

$$S_f(f, H) = \frac{\alpha(H)}{N_e f^\gamma} V_{dc}^2 \tag{7}$$

where the exponent γ is of order one and the total number of conduction electrons N_e in the sample is taken equal to the number of atoms in the active area of the GMR element. The dimensionless normalizing constant α is called the Hooge constant [99] which for magnetic materials depends on the magnetic state which in turn depends on the applied magnetic field.

The new GMR technology, to win adoption as a market product over the established AMR products embodied in magnetoresistive sensors [1] (KMZ10 sensors from Philips Semiconductors BV, Eindhoven) and RAMs (sold by Honeywell), must promise an order of magnitude improvment in one or more of these three valuable performance categories. To compete with the high field sensitivity of AMR elements, based on permalloy ($Ni_{20}Fe_{80}$) films, the GMR elements have the advantage of the large coefficients of magnetoresistance that is observed in Co/Cu multilayers. Although the AMR elements are more robust to the conditions of manufacturing processes than spin-valve multilayers their lower MR ratio (about 2 to 3% for magnetization orientations parallel or perpendicular to the sense current) means low readout voltages.

However, spin valves scale poorly for miniaturization. The thickness of the sandwich structure is determined by magnetic coupling constraints, and the aspect ratio of length to width is set to optimize the magnetic anisotropies that give the films the desired magnetic orientations. Thus, the ratio of the length to the width of a planar GMR element (cell) stays the same. As a result, device resistance is constant, independent of minimum feature size. Since a given value of sense current is required to achieve a target output level, the current density increases as the inverse of the minimum feature size so that problems with heating (noise level) become worse as that dimension decreases below 0.1 μm. Fortunately, current IC technology uses MR sensing elements with sizes greater than or equal to 0.1 μm. Since the maximum GMR ratios at room temperature are observed in Co/Cu multilayers, it can be argued that the performance of such GMR sensing cells [100] would be optimized if a Co/Cu/Co sandwich or multilayer can be included with the highest aspect ratio.

In Co/Cu multilayers, the MR(H) is an oscillating function of Cu thickness with maxima at values that correspond to antiferromagnetic exchange coupling between neighboring Co layers. The first two of these antiferromagnetic maxima, which occur at $\sim$1 and 2 nm, respectively, are of particular practical interest because they both give large values of GMR. Of these, the second maximum gives a somewhat reduced value of GMR, but this is offset by an even larger reduction of the saturation field H_s. Consequently, from Eq. (5), s_{max} is significantly larger at the second GMR maximum than at the first GMR maximum. However, the second GMR maximum has the substantial practical drawback that the magnetoresistive hysteresis is a much larger fraction of H_s than for multilayers at the first maximum.

In the next section, plausible ways to achieve significantly reduced MR hysteresis in the response function of Co/NM (NM = noble metals) multilayers while maintaining adequate sensitivity for sensor applications are discussed. In addition, the problem of the magnetization distribution within the multilayers and the ways it changes under the application of a magnetic field is addressed in terms of their magnetoresistive properties. These studies involve complementary information from high-resolution transmission electron microscopy (TEM), X-ray reflectivity, spectroscopic ellipsometry, magnetooptical Kerr effect (MOKE), spin-echo ^{59}Co nuclear magnetic resonance (NMR), and typical magnetotransport measurements.

4. MAGNETOTRANSPORT PROPERTIES IN POLYCRYSTALLINE Co/NM MULTILAYERS

4.1. Planar Hall Effect in Co/Cu Multilayers

The observation of the GMR effect [38, 39], in multilayers (MLs) or in granular thin films of magnetic–nonmagnetic (FM–NM) elements, and the reported [101] extraordinary anisotropic magnetoresistance (AMR) change in Ni/Co MLs, open the way for use of high performance materials in applications of active sensors [29]. The different physical origin of GMR and ordinary-AMR effects leads to different behavior with a magnetic field. The AMR is defined as $\Delta\rho = \rho_{\parallel} - \rho_{\perp}$, where $\rho_{\parallel}$ and $\rho_{\perp}$ are the saturation resistivities with the $I_{\text{ext}} \parallel H_{\text{ext}}$ and $I_{\text{ext}} \perp H_{\text{ext}}$, respectively, while the GMR is defined as $(R_{\max} - R_s)/R_s$ with $R_{\max}$ and R_s the resistance when the film magnetization is zero and maximum, respectively.

All the FM films [4], including those exhibiting GMR, present an AMR effect with $\Delta\rho/\rho$ values from slightly different to zero up to 3–5% in permalloy or Ni films. This AMR effect is small compared to the GMR effect that is of the order of 10–60% at RT. However, the main difference between the magnetotransport properties of most FM systems, like Ni/Co MLs, to those exhibiting the GMR effect is that for the first the MR with $I_{\text{ext}} \parallel H_{\text{ext}}$ is positive and the MR with $I_{\text{ext}} \perp H_{\text{ext}}$ is negative while for the second both MR quantities are negative. In addition, GMR MLs present well-defined maxima and minima of the GMR effect as a function of layer thickness of the nonmagnetic element that correspond to antiferromagnetic (AF) and FM arrangements of magnetic moments in adjacent magnetic layers, respectively. Oscillations were observed as well in resistivity and AMR of epitaxial Ni/Co(111) MLs [102], that do not exhibit the GMR effect, as a function of Ni and Co thicknesses which were attributed to superlattice effects. However, since the GMR and AMR effects have been studied extensively in ultrathin FM–NM MLs, by now there is very little published work concerning the Hall effect of these new structures. Measurements of Hall resistivity ρ_{H} in Fe/Cr [103] and Co(Fe)/Cu [104] MLs exhibit an oscillatory dependence of the spontaneous Hall coefficient R_{H} from the Cr and Cu layer thicknesses, similar to the observed oscillations in their GMR effect, which remain unexplained by now. Some more controversial results of Hall effect measurements [101, 105] were published in Ni/Co MLs. These MLs exhibit large AMR values for low saturation fields that made them possible candidates for use as MR recording sensors [106]. Hall effect measurements of Ni/Co sputtered MLs with a four probe cross-diagonal V_{H}–I configuration, for films with a circular shape, led to observation of a so-called extraordinary AMR effect [101, 105] of 140% at RT. The Ni/Co interfaces were considered responsible for the enhancement of this effect [107] relative to single-layer films, but the mechanism for the high aspect ratio achievement is unclear. Since Hall effect measurements in van der Pauw structures are sensitive to sample geometry, contact size and alignment effects [108], first of all one has to clarify whether this extraordinary AMR effect is a new physical phenomenon or a geometrical effect due to the used specific measurement configuration. To answer these questions, it will be instructive to consider what is known in single-layer FM films.

In FM films with thickness d, when a current I passes through a sample in the presence of a magnetic field, a potential is developed in the direction perpendicular to the current flow. This Hall voltage is given by [109],

$$V_{\text{H}} = \frac{R_s I}{d}\mathbf{M}_s \cos\theta + \frac{\kappa I}{d}(\mathbf{M}_s \sin\theta)^2 \sin 2\phi \qquad (8)$$

assuming that the Hall voltage due to the Lorentz force is negligibly small in magnetic metals [110]. The first term is the spontaneous (or extraordinary) transverse V_{H}^s voltage which arises from asymmetric scattering of the conduction electrons from the magnetic moments in the sample and is proportional to the $\mathbf{M}_s \cos\theta$ component in the film normal z-direction. The second term is the planar (or pseudo-Hall) V_{H}^p voltage [112], which arises because the electric field E and the current density $\mathbf{J}$ are not always parallel in the plane of the film. Thus, if there is a component of magnetization, $\mathbf{M}_s \sin\theta$, in the plane of the film, then because of AMR ($\Delta\rho/\rho \approx \kappa \mathbf{M}_s^2 \sin^2\theta$), the equipotentials may not be perpendicular to the current, and a Hall voltage is detected that exhibits a maximum when the angle ϕ between I and $\mathbf{M}_s$ is 45°. Since both terms in Eq. (8) are inverse proportional to d, the Hall effect is a very sensitive method of detecting the magnetization of thin films. It is well known that the direction of $\mathbf{M}_s$ in thin films is strongly affected by the shape anisotropy. However, for circular or square shaped films with sizes greater than a few millimeters-squared the direction of $\mathbf{M}_s$, away from the edges, is determined from the intrinsic anisotropy and the texture of the deposited film. Therefore, in galvanomagnetic measurements the film (and not the geometrically induced) properties can be seen in relatively large substrates. A geometrical form with a cross shape of four equal arms is frequently used in galvanomagnetic devices, based on permalloy, for pseudo-Hall effect (PHE) measurements [110]. This cross configuration can be well approximated with a square shaped film when the I flows along the one diagonal while the V_{H} is measured along the other diagonal.

MR and V_{H} versus H (V_{H}–H) hysteresis loops measurements have been carried out [111] along the edges and the square diagonals of a [Co(1.2 nm)/Cu(0.7 nm)]$_{30}$ film to investigate whether the published results by Prados *et al.* [101] are due to the used specific diagonal configuration or are intrinsic to Co/Ni MLs only. Figure 4 shows the MR curves of Si(100)/[Co(1.2 nm)/Cu(0.7 nm)]$_{30}$ MLs, observed with an $I_{\text{ext}} = 1$ mA for $I_{\text{ext}} \parallel H_{\text{ext}}$ and $I_{\text{ext}} \perp H_{\text{ext}}$, and the $\mathbf{M}/\mathbf{M}_s$ versus H hysteresis loops with the field direction parallel or vertical to the film plane. The hysteresis loops are evident for the FM arrangement of the Co layer magnetic moments, even at a zero applied field, with the average magnetization lying mainly in the film plane. The observed $\mathbf{M}_r/\mathbf{M}_s(\parallel) = 0.6$ value at remanence point ($H = 0$) is more than the estimated average residual magnetization of $0.5\mathbf{M}_s$ for a stressed material with an isotropic distribution of easy axes and closer to $(2/3) \times 0.832\mathbf{M}_s$ for cubic anisotropy with ⟨100⟩ easy axes

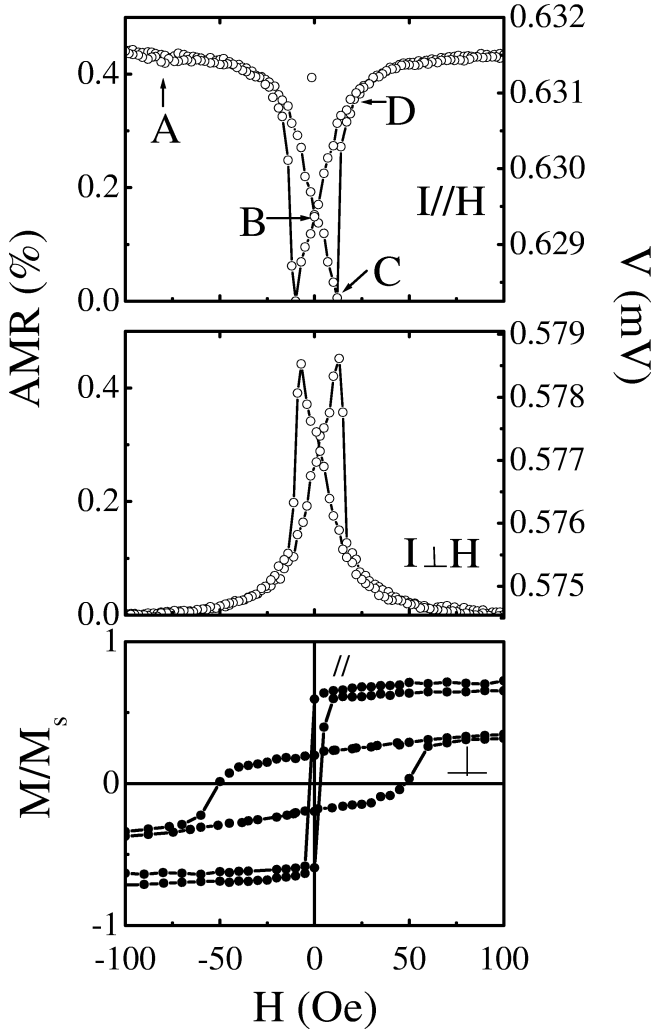

Fig. 4. Anisotropic magnetoresistance and magnetic hysteresis loops for the Si(100)/[Co(1.2 nm)/Cu(0.7 nm)]$_{30}$ multilayers observed at RT with a current of 1 mA. Reproduced with permission from [111].

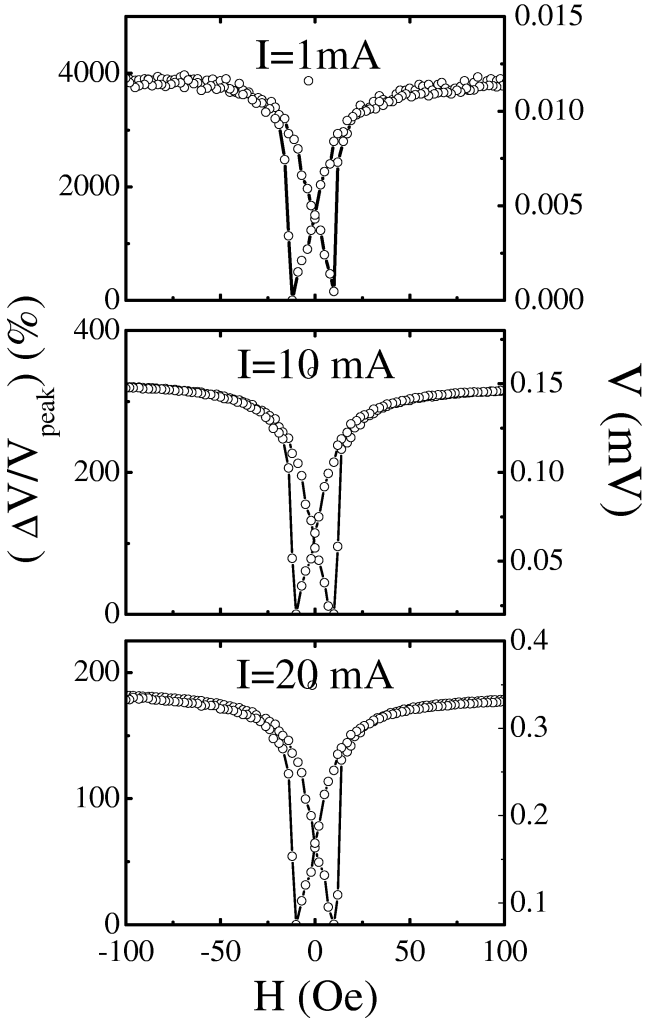

Fig. 5. The pseudo-Hall effect of Si(100)/[Co(1.2 nm)/Cu(0.7 nm)]$_{30}$ multilayers observed for three different currents. Reproduced with permission from [111].

or to $(3/4) \times 0.866\mathbf{M}_s$ for cubic anisotropy with $\langle 111 \rangle$ easy axes [113]. It is evident that the coercive field $H_c = 6$ and 50 Oe, for the parallel and vertical field configurations, respectively, is different from the $H_{\text{peak}} = 12$ Oe in the MR measurements. These AMR measurements are independent from the magnitude of I_{ext}. In Figure 5, the V_{H}–H loops are plotted as a function of I_{ext} that are measured with the current flow applied along one diagonal and the voltage drop detected in the other diagonal in a field forming an angle ϕ of 45° relative to square diagonals. It is shown that the measured voltage along the diagonal is an order of magnitude less than that measured in AMR loops for $I = 1$ mA, while at H_{peak} the voltage approaches zero. This low V_{peak} value gives the $\Delta V / V_{\text{peak}} \approx 4000\%$ effect, which represents the order of magnitude voltage change between the saturating and switching field magnetic moment configurations. The observed V_{H} effect is found to (i) decrease on increasing I_{ext} and (ii) decrease from a maximum at $\phi = 45°$ to $\phi = 0$. The 0.7-nm Cu layer thickness in the MLs corresponds to the first GMR minimum (FM configuration) located prior to the observed [38] first AF GMR maximum at 0.9 nm.

Remarkably, the measured AMR and the V_{H} values fall into the noise level signal for Cu layer thicknesses more than about 1.1 nm that coincide with the limit where pinhole concentration is decreasing. Since a clear AMR signal has been measured either in single-layer FM films or FM–FM′ MLs, such as Ni/Co, or FM–NM$_p$ MLs, with NM$_p$ = Pd and Pt elements [114] that exhibit a large induced magnetic moment, then the observed AMR in Co/Cu MLs for $t_{\text{Cu}} < 1.1$ nm might be associated with the reported d-shell spin polarization of Cu atoms observed from X-ray magnetic circular dichroism measurements [115]. The induced Cu spin moment is found to be primarily situated at the Co/Cu interfaces, which consist of two or three atomic layers of Cu, that correspond to 0.4- to 0.6-nm thickness, and its average moment is shown to fall off inversely with t_{Cu}. At the second AF GMR maximum, for 2.1-nm Cu thickness, a GMR effect of 15% was observed. It is worth noting that for Cu thicknesses less than 1 nm the diagonal ΔV_{H} effect has been found to

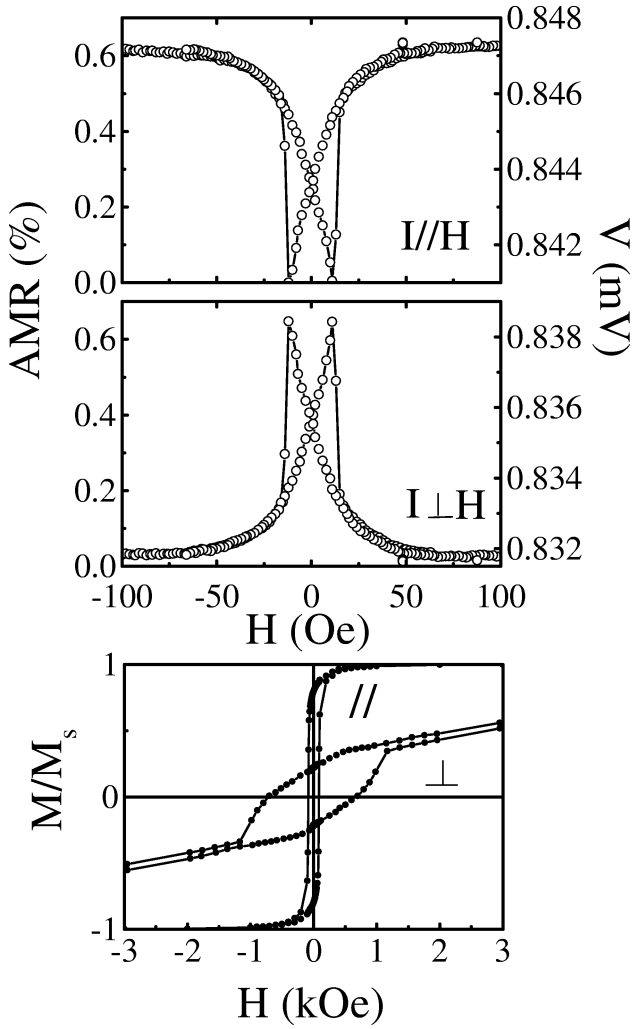

Fig. 6. Anisotropic magnetoresistance and magnetic hysteresis loops for the MgO(100)/[Co(100 nm)] single layer observed at RT with a current of 1 mA. Reproduced with permission from [111].

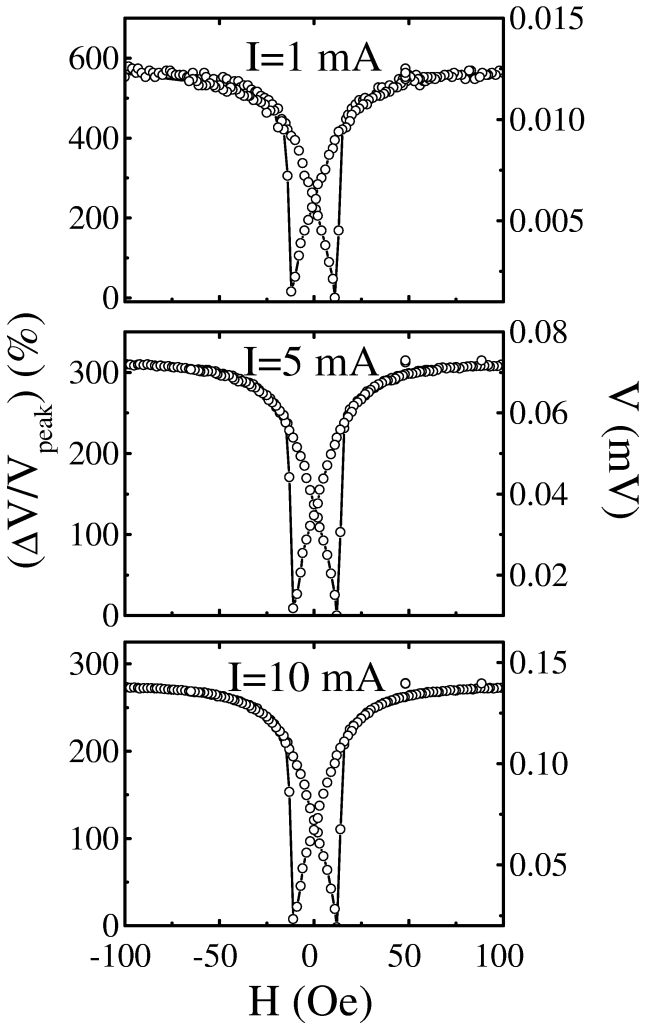

Fig. 7. The pseudo-Hall effect of an MgO(100)/[Co(100 nm)] single layer observed for three different currents. Reproduced with permission from [111].

vary from 400 up to 4000% for $I_{\text{ext}} = 1$ mA, and this variation was strongly dependent from the alignment, along the square diagonal, of the In contacts used to connect the four Cu leads at the corners of the films.

To examine the dependence of the observed extraordinary MR effect upon the electronic scattering at Co/Cu interfaces, a single layer of MgO(100)/[Co(100 nm)] film, grown under exactly the same conditions, has been measured in the three configurations as well. Figure 6 shows the MR curves observed with an $I_{\text{ext}} = 1$ mA for $I_{\text{ext}} \parallel H_{\text{ext}}$ and $I_{\text{ext}} \perp H_{\text{ext}}$ and the $\mathbf{M}/\mathbf{M}_s$ versus H hysteresis loops with the field direction parallel or vertical to the film plane. It is clear from the hysteresis loops that the magnetization vector is in the film plane and a strong anisotropy is opposed to the rotation of magnetization out of the film plane. The observed $H_c = 80$ and 900 Oe, for the parallel and vertical field configuration, respectively, is much larger than the $H_{\text{peak}} = 8$ Oe in the MR measurements. In Figure 7, are plotted the V_{H}–H loops as a function of three different I_{ext}, that were measured with the current flow applied along one diagonal and the voltage drop detected in the other diagonal in a field forming an angle ϕ of 45° relative to square diagonals. For comparison, similar measurements were performed in an $Ni_{81}Fe_{19}$ single layer with a thickness of 100 nm. MR curves with similar shapes as in a Co single layer were observed, but with an AMR effect of 2.5% and $H_{\text{peak}} = 4$ Oe, for the $I_{\text{ext}} \parallel H_{\text{ext}}$ and the $I_{\text{ext}} \perp H_{\text{ext}}$ configurations. In the diagonal configuration, an effect of 170% was measured for an $I_{\text{ext}} = 1$ mA. Although the Co single layer shows an AMR of 0.6%, the corresponding diagonal effect is much larger than that of an $Ni_{81}Fe_{19}$ single layer. Thus, the observed diagonal voltage drop implies that in single layers this effect is enhanced for systems which exhibit larger $\mathbf{M}_s$. Since the $\mathbf{M}$–H loops indicate that the $\mathbf{M}_s$ is lying in the film plane, then the first term in Eq. (8) will vanish and the V_{H}–H loop may arise from a PHE. The shapes of these loops present similarities with loops first observed in $Ni_{90}Fe_{10}$ films that exhibit pure PHE [116].

The observed V_{H}–H loops, for both Co/Cu MLs and Co or NiFe single layers, indicate that a PHE may determine their properties. Strong evidence for that is the observed angular de-

pendence of the V_H–H loop from $\sin 2\phi$, exhibiting a maximum for $\phi = 45°$, the angle between the I and the H directions, and minima (about zero) for $\phi = 0$ and 90°. In these loops, the magnetic moments are aligned along the H direction because the V_H–H scans start from saturation. Two important features in these experimental results need an explanation.

(i) The observed H_c from magnetic hysteresis loops are different from H_{peak} values in AMR and V_H–H loop measurements. However, the obtained H_{peak} values in AMR and V_H–H loops are identical. Since the demagnetizing field away from the edges of a film with thickness d and width w is [110]: $H_D \sim \mathbf{M}_s d/w$, in the examined [111] samples H_D is negligible for planar film measurements. Thus, because the electronic mean-free path in FM films is of the order of ~10 nm, it is expected the switching field, where the magnetization starts to flip over the *local* easy-axis direction in every domain, to be sensed by the MR and PHE signals. On the other hand, the H_c field, detected with dc magnetic loops, corresponds to an emerging magnetic domain distribution after a rotation and/or a domain-wall displacement process that lead to a zero macroscopic magnetization. It has already been pointed out [109] that even for coherent rotation of magnetization the coercivity measured by the Hall effect is not the same as that measured with a magnetometer. Therefore, the specific distribution of easy-axis directions in these films may cause the observed difference between the H_c and the H_{peak} values. According to this explanation, in the top panel of Figure 3 the branch ABC corresponds to reversible magnetization rotation within a domain and at C (the reverse magnetic field) a jump of the magnetization occurs, which results in a sharp change of the AMR and V_H curves. Point D indicates where the reversible **M** rotation starts again in the opposite direction of the magnetic vector. The fact that the flip over of vector **M** does not occur in a unique value of H applied, but in some range ΔH, may be explained by nonuniform rotation processes in addition to uniform magnetization rotation [116]. However, in Figures 5 and 6 it is shown that for the Co film the flip over jump gives a steeper galvanomagnetic effect.

(ii) The most significant issue now is the voltage drop variation in the V_H–H loops for the diagonal configuration. The observed sensitivity to current flow density and alignment of electric contacts at first glance gives the impression that there is an artifact due to high sensitivity of Hall measurements from these effects. Since the contact sizes are negligibly small compared to the film surface, the observed changes of the $\Delta V_H/V_{peak}$ percentage from their alignment along the square diagonals can be attributed only to deviations from the $\phi = 45°$ condition, for the angle between I and H, that gives the maximum effect. On the other hand, the observed decrease of the $\Delta V_H/V_{peak}$ percentage with increasing current intensity can be related to an increase in density of the electric field E dynamic lines along the current direction due to a change of equipotential lines. This usually causes a larger electric field gradient in the current flow direction along the square diagonal. Therefore, because the PHE is basically an AMR effect for $\phi = 45°$, in an FM film with larger average domain sizes relative to an electronic mean path no decrease of $\Delta V_H/V_{peak}$ on increasing I is expected, unless electronic scattering at grain boundaries and interfaces is significant. In this case, on increasing I the net resistance from boundary scattering is increasing as well. Today, there are a few available experimental data describing the effect on resistivity of electronic scattering at magnetic grain boundaries in the presence of an external field H. Specifically, measurements of the resistivity for currents parallel and perpendicular to domain walls [117] of epitaxial hexagonal close-packed (hcp) Co indicate that the large negative room-temperature MR is due to the film micromagnetic structure and ferromagnetic resistivity anisotropy whereas the intrinsic effect of domain-wall interface scattering is minor. Thus, it can be speculated that a combination of the AMR effect with grain boundary scattering can cause the observed decrease of the $\Delta V_H/V_{peak}$ ratio. In support of this argument is that in the cross-diagonal measurements used [111] it could not achieve a significant decrease of the $\Delta V_H/V_{peak}$ ratio, relative to those shown in the bottom panels of Figures 5 and 7, for currents as high as 60 mA. A second indication is coming from the cross section and the planar TEM images that indicate a grain-size distribution centered about 10 nm. These observations suggest that their magnetotransport behavior requires micromagnetics study. In accordance, the PHE curves observed [118] in micron-scale Ni thin-film squares were found, from magnetic force microscopy (MFM), to be strongly affected by their magnetic domain structures, implying that each domain flipping causes a sudden change in the local resistivity of the domain regions. A third indication relies on the significant increase of the $\Delta V_H/V_{peak}$ ratio observed in Co/Cu MLs relative to magnetic single-layer films. This is in agreement with that reported [107] in Ni/Co MLs, where interface effects were considered responsible for enhancement of $\Delta V_H/V_{peak}$. Thus, such effects cannot be induced by nonlinear resistivity contact effects because a similar behavior has not been observed [111] in GMR films of Co/Cu or NiFe/Ag MLs.

Thus, in the cross-diagonal Hall configuration the observation of large $\Delta V_H/V_{peak}$ values should not be associated: (a) with the Ni/Co MLs only but is related to the specific measurement method, (b) with the intrinsic observed AMR effect in FM films, (c) with the so-called extraordinary or spontaneous Hall effect and, (d) with artifacts due to resistivity effects from the contacts. The dependence of $\Delta V_H/V_{peak}$ loops on the angle ϕ between I and H suggests a connection with a PHE mechanism that is associated with electronic scattering in magnetic grain boundaries and interfaces, possibly caused by local truncations of equipotential lines that are not perpendicular to the current and result in a Hall-like voltage. Certainly, at present this PHE mechanism is only a suggestion that needs careful investigation. Additionally, the study of this effect in Ni thin-film squares [118] suggests that the PHE response cannot be explained by lump circuit models. Consequently, the Wheatstone bridge model [101] is a rather poor explanation for the observed behavior of the PHE measurements. Thus far, the experiments reveal the important role of micromagnetic effects

in FM-coupled thin films, that is associated with the observed dependence of PHE response on the applied magnetic field magnitude and direction.

4.2. GMR in Co/Cu MLs

Since the first reports [79] for enhanced GMR amplitudes in Co/Cu MLs, the related research has been focused on the interlayer exchange-coupling mechanism [119–123] and the possible applications of Co/Cu GMR devices. The maximum GMR amplitude (≈60%) at ambient conditions was observed in sputtered (polycrystalline) Co/Cu MLs [79] with (111) texture whereas its GMR ratio and bilinear exchange-coupling strength $\mathbf{J}_{\text{osc}}$ oscillate with decaying amplitude as the Cu layer thickness (t_{Cu}) varies, giving maxima that correspond to an antiferromagnetic (AF) coupling between adjacent Co layers. Thus, when these MLs are of such thickness as to be AF coupled then a reduction of the magnetoresistance occurs if they are subjected to a magnetic field parallel to the interfaces, whereas a minimum value is observed at a saturation (or switching) field H_s where the spins between adjacent magnetic layers come into alignment.

The large GMR ratios and the relatively large sensitivity to changes in magnetic fields, observed at the first two AF maxima with $t_{\text{Cu}} \approx 0.9$ and 2 nm, make these MLs potential candidates for use in sensor devices [124, 125]. However, the undesirable hysteresis that appears in the GMR response function of the first and second AF maximum requires modification of the Co/Cu composition [126, 127] and of the film morphology [131] to achieve negligibly small hysteresis while maintaining adequate sensitivity for sensors. The possible technological applications [14], that can emerge from the large GMR ratios observed in polycrystalline MLs with (111) texture, attract a great deal of scientific interest to investigate the elusive mechanism between the microscopic origin of the GMR phenomenon and the film morphology.

For GMR sensor applications, besides the GMR ratio and the switching field range, equally important is the signal to noise ratio as well. The excessive flicker or $1/f$ noise has been found [98] to be of magnetic origin in GMR sensors. The source of this excess noise level with the applied dc-field H has been attributed [98] to thermal excitations of the magnetization direction. Therefore, the physical origin that creates low hysteresis in the GMR response function should also affect the $1/f$ contribution that depends on [98] the applied dc-magnetic field.

Earlier studies [126, 127] in GMR Co/Cu MLs at the second AF maximum, that exhibit low hysteresis at about 290 K, have shown a dramatic increase of hysteresis below 100 K. These results imply that, while the activation energy for magnetization reversal is reduced by a decrease of [126] t_{Co} or by Co–Cu alloying [127], it remains large relative to thermal energy at low temperatures.

The properties of the micromagnetic state that result in low-field GMR at room temperature were investigated [128] by measuring the temperature dependence of isothermal magnetic and GMR loops in three classes of $[\text{Co}(1\text{ nm})/\text{Cu}(2.1\text{ nm})]_{30}$ MLs between 5 and 300 K. Such macroscopic measurements include combined magnetostructural information. However, micromagnetic parameters such as lateral magnetic correlation length and roughness vary with temperature and are totally different [129, 130] from the corresponding microstructural parameters which remain unaltered in the examined temperature range. It has been shown [131] that these three classes exhibit different GMR ratios, hysteresis, and saturation fields at room temperature as the Co–Cu layering is modified by the deposition conditions. Since Co/Cu interface roughness primarily affects the interlayer exchange coupling whereas the grain-size distribution and the density of grain boundaries alter the magnetostatic energy then the temperature dependence of GMR and magnetic hysteresis loops can separate the major contribution from each one of the two structural characteristics.

For this study, the t_{Cu} was selected at the second AF maximum to avoid such micromagnetic effects on hysteresis loops as those observed [83] at the first AF maximum, due to growth of pinhole defects and FM bridges in the multilayer structure. Specifically, three different microstructures of $\{[\text{Co}(1\text{ nm})/\text{Cu}(2.1\text{ nm})]_{30}/\text{Co}(1\text{ nm})\}$ MLs were deposited by magnetron sputtering on Si(100) substrates [131]. Their microstructure is different in respect to grain size and interface roughness, depending on the deposition conditions [131]. Two parameters were varied to produce the three classes (named A, B, C) of Co/Cu multilayers: (i) the surface roughness of the Si(100) substrate, affecting the mode of growth; (ii) the thermal contact of the substrate with the, water cooled, supporting table that influences internal film stress. The base pressure (3×10^{-7} Torr), deposition rates, and the Ar-gas purity (99.999%) were the same. Thus, class A multilayers were grown on a 100-nm SiO_2 buffer layer with less than 2 nm root mean square surface roughness and direct contact of the substrate with the supporting table. Class B has the difference that the substrate was thermally isolated from the water cooled supporting table (extra internal stress), whereas class C has in addition a rougher (root mean square more than 3 nm) surface of the substrate. These three classes exhibit [131] different GMR ratios, hysteresis, and saturation fields at room temperature as the Co–Cu layering is modified by the deposition conditions. Transmission electron microscopy (TEM) measurements [131] have revealed column-like structures with bimodal distribution of grain sizes. A 90% fraction of columnar grains with sizes more than 15 nm is observed in the sample called A, for sample B it is 70%, and in sample C it is less than 50%. Thus, a larger fraction of grains with sizes less than 10 nm appears progressively from sample A to C.

The X-ray diffraction patterns of class A–C MLs exhibit an intense fcc (111) Co–Cu peak and a weak (200) fcc peak, indicating that the MLs have (111) texture. Selected-area electron diffraction (SAED) planar TEM patterns have shown [131] that at right angles relative to the Si surface there is not any preferred orientation of the (111) Co–Cu planes for all the examined MLs. However, for samples A and B the SAED cross-section patterns show [131] that there is some degree of preferred orientation in the (111) Co–Cu planes relative to

the Si [200] direction only, whereas in class *C* MLs they are randomly arranged. Since bulk Co and Cu layers have similar densities (≈8.9 g/cm^3), the small X-ray contrast results in weak satellite intensities around the fundamental (111) Bragg peak which does not allow a superlattice refinement (SUPREX program) analysis as [133] in Co/Au MLs. It should be emphasized that in previous studies the microstructure of class *A*–*C* MLs has been identified by TEM measurements [131] whereas class *B* MLs have been characterized with nondestructive methods such as spin-echo ^{59}Co nuclear magnetic resonance [133] (NMR) (microscopic technique) and X-ray-reflectivity (XRR) measurements [134] (macroscopic technique) as well. To extract some conclusions about the quality of Co/Cu interface roughness high-resolution XRR measurements on class *A* MLs are compared with XRR spectra taken in class *B* MLs [134].

Figure 8 shows the specular XRR spectrum from class *A* MLs. An attempt to fit the experimental spectrum either with an optical or with a kinematical model [134] gave poor fittings.

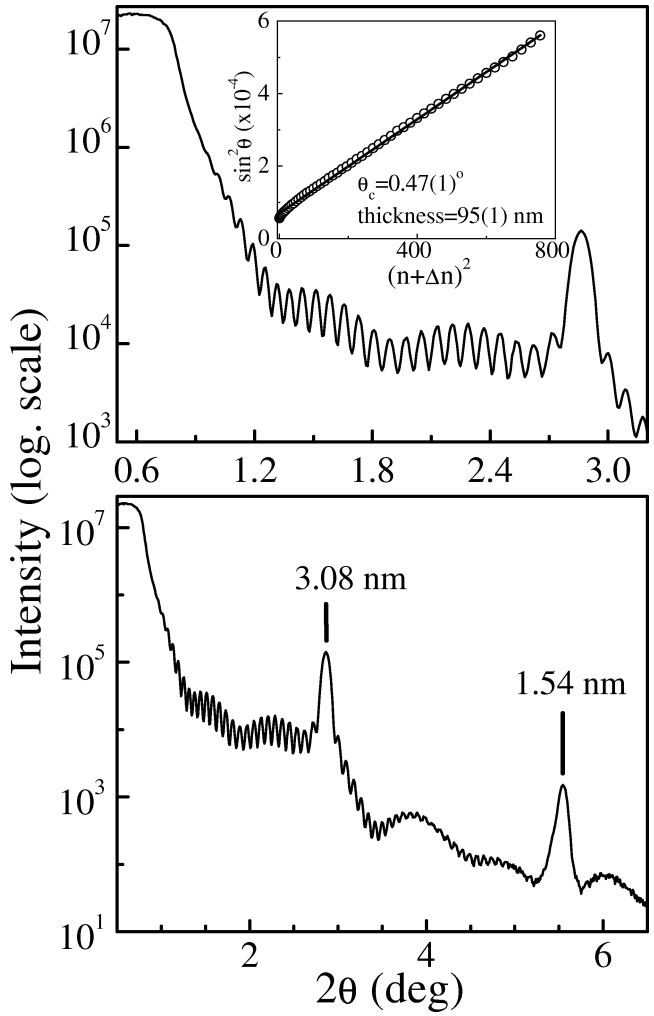

Fig. 8. The bottom plot shows the X-ray reflectivity spectrum from class *A* MLs whereas the plot on top shows an enlargement of the spectrum, with a clear view of the interference fringes used in the calculations. The inset shows the θ_i positions (circles) used in Eq. (11) and the best fit line.

This indicates that, due to incoherent absorption (anomalous dispersion effects) in the layer materials when Cu $K\alpha$ radiation is used, a sophisticated dynamical model [135] is required for a reliable fitting of the observed spectrum. However, the quality of the recorded spectrum allows a straightforward interpretation of the main structural features because there were not detectable geometrical aberration effects [132] introduced by the sample curvature. The first two ($m = 1, 2$) superlattice Bragg peaks appear very intense with small full-width-at-half-maximum, indicating sharp Co/Cu interfaces. In comparison, the XRR spectra observed [134] in class *B* MLs did not show superlattice Bragg-peak intensities of the $m = 2$ or higher order and the amplitude of the interference fringes was suppressed, indicating that interface Co–Cu roughness is larger. It is worth mentioning that the zero peak intensity of the third order ($m = 3$) satellite in Figure 8 shows unambiguously that both, the achieved t_{Cu} and the bilayer thickness Λ, correspond exactly at the position where the maximum GMR ratio is expected at the second antiferromagnetic maximum of Co/Cu MLs because

$$\Lambda = t_{\mathrm{Cu}} + t_{\mathrm{Co}} \quad \text{and} \quad t_{\mathrm{Cu}} \approx 2t_{\mathrm{Co}} \quad \Longrightarrow \quad \Lambda \approx (3/2)t_{\mathrm{Cu}} \tag{9}$$

and the angle-dependent structure factor $F(\theta_m)$ at the Bragg-angle θ_m becomes [136],

$$\begin{aligned} F(\theta_m) &= \frac{\Lambda}{\pi m} \sin\left\{\frac{m\pi t_{\mathrm{Cu}}}{\Lambda}\right\}(\phi_{\mathrm{Cu}} - \phi_{\mathrm{Co}}) \overset{(9)}{\Longrightarrow} \\ F(\theta_m) &= \frac{3t_{\mathrm{Cu}}}{2\pi m} \sin\left\{\frac{2m\pi}{3}\right\}(\phi_{\mathrm{Cu}} - \phi_{\mathrm{Co}}) \\ &= 0 \quad \text{if} \quad m = 3, 6, \ldots \end{aligned} \tag{10}$$

where ϕ_{Cu} and ϕ_{Co} are the scattering amplitude densities for X-rays of a particular wavelength λ. The fact that t_{Cu} and Λ are exactly at the second GMR maximum position makes meaningful the analysis of the observed temperature dependence in the following paragraphs.

Other important differences in film morphology can be traced from XRR spectra by measuring the critical reflection angle θ_c. Beyond the region for total reflection (plateau), the maxima and the minima of its interference fringes can be related to the total film thickness t_f by the modified Bragg equation [137],

$$\sin^2\theta_i = \theta_c^2 + (n_i + \Delta n)^2\lambda^2/4t_f^2 \tag{11}$$

where θ_i is the position of the maximum or minimum intensity of the ith interference fringe, n_i is an integer, Δn is 1/2 and 0 for maximum and minimum, respectively. The inset in the upper part of Figure 8 shows data for the refinement of 40 minima and maxima of well-defined interference fringes between 1.20 and 2.72° in θ. A $t_f = 95(1)$ nm and a $\theta_c = 0.47(1)°$, with numbers in parentheses being the standard deviations, are obtained by least-squares refinement (solid line) of the θ_i positions using Eq. (11). The difference between the nominal (=94 nm) and the estimated t_f is within the accuracy of the standard deviation limits (∼1%) while the Bragg-peak positions (Fig. 8) give a $\Lambda = 3.08$ nm. However, the estimated electron density $\rho_e = 12.4$ g/cm^3 from the obtained $\theta_c(\sim\sqrt{\rho_e})$ is much larger

than the bulk Cu or Co density of about 8.9 g/cm^3, which correspond to a $\theta_c \approx 0.4°$. Since the observed interference fringes indicate a small root mean square interface roughness, then the overestimation of θ_c (ρ_e) by the modified Bragg equation may arise from the different reflectivities reported [138] between interfaces with small and large values of the lateral correlation length ξ. The difference between surfaces with small and large values of ξ can be a factor of 2 in specular reflectivity, whereas for $\xi > 100$ nm an ill-defined θ_c region appears [138]. In accordance, atomic force microscopy measurements [131] on the substrate surface prior deposition and on the film surface revealed that class *A* MLs have atomically smooth substrate-film interfaces whereas both surfaces exhibit a long-range waviness with average periodicity of about 100 nm. Thus, the overestimated θ_c can be attributed to large ξ.

In contrast, a detailed XRR study of class *B* MLs has shown [134] that both, Co/Cu interface and lateral correlation function $C(\xi)$ roughness are governing their layer morphology, while TEM measurements [131] show that class *C* MLs exhibit a large geometrical and chemical (Co–Cu mixing) roughness. Thus, increase of film roughness from class *A* to *C* MLs is an unavoidable result of the larger fraction of small grain sizes that changes the overall film morphology. However, increase of Co/Cu interface roughness weakens the magnitude of interlayer exchange coupling within each columnar structure whereas a larger fraction of small grains makes the magnetostatic contribution an important dipolar energy term in the total magnetic free energy that determines the micromagnetic state of the film. In the following, it is shown that the two different magnetic contributions in the GMR and magnetization hysteresis loops can distinguish the effect of interface roughness from grain-size effects in the temperature dependence of the two data sets.

Isothermal magnetization loops were measured between 5 and 280 K. Figure 9 shows normalized magnetization ($\mathbf{M}/\mathbf{M}_s - \mathbf{H}$) loops, with $\mathbf{M}_s$ being the total saturation magnetization, of sample *A* at 240, 40, and 5 K. The temperature dependence of the $\mathbf{M}/\mathbf{M}_s - H$ loops reveals a large increase of coercivity (H_c) and saturation (H_s) fields below 80 K. Above 200 K there is a negligibly small remanent magnetization ($\mathbf{M}_r$) and the loop shapes indicate an antiparallel alignment of magnetic moments among adjacent Co layers at the demagnetized state ($\mathbf{M} = 0$). Since the temperature dependence of these loops is more prominent in class *B* and *C* MLs, the normalized magnetization curves were plotted (Figs. 10 and 11) as a function of the applied field over temperature ratio H/T. In nanostructured systems, that exhibit an increase of hysteresis by decreasing temperature while their intrinsic magnetic anisotropy is negligibly small, the $\mathbf{M}/\mathbf{M}_s$ versus H/T plots reveal the thermal energy lacked from the magnetic configuration to complete equilibrium with the applied field during the measurement. A comparison of the observed loops in Figures 9–11 reveals that:

(i) Class *A* MLs (about 90% fraction [131] of AF-aligned layers) exhibit an $\mathbf{M}_r < 0.2\mathbf{M}_s$ for all temperatures and the $\mathbf{M}_r$ increases at lower temperatures. This increase of $\mathbf{M}_r$ can

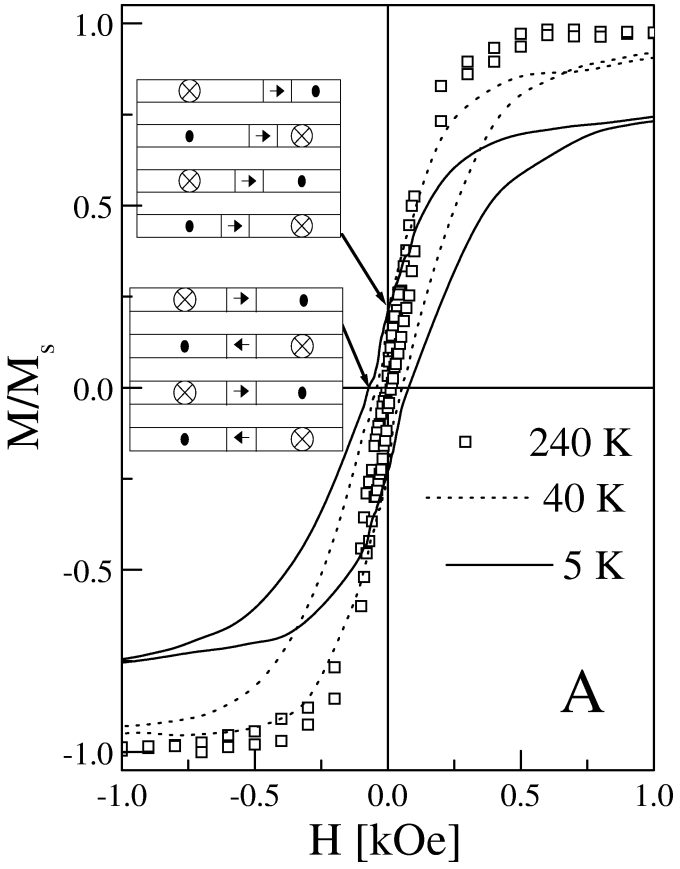

Fig. 9. The isothermal $\mathbf{M}/\mathbf{M}_s$–H loops of class *A* MLs are shown for clarity at three different temperatures only. Schematics of the proposed domain structures are shown at the remnant (upper plot) and demagnetized (down plot) states.

be attributed either to creation of FM-coupled areas or to self-stabilization of magnetic domain walls in Co layers after the multidomain splitting from the saturated state [139, 140]. In AF-coupled, sputter-grown, Co/Cu/Co sandwiches [140], a high domain density state is realized at remanence when coming from saturation. In addition, Co/Cu MLs grown by e-beam evaporation exhibit [141] minor GMR loops with higher GMR ratios than the major loops, indicating that domain-wall effects are predominant around the remnant state. Thus, a configuration with parallel Néel walls [142] (Fig. 9 inset) can account for the observed remanence in the case of the AF-coupled sample *A*. At the center of such Néel walls, the average magnetic components point either parallel or antiparallel to each other between adjacent Co layers. Thus, a larger fraction of Néel walls [142] with parallel moments can be stabilized in the remnant state of class *A* MLs with decreasing temperature. This effect is due to magnetization reversal by wall motion when a high field is applied and then is removed.

(ii) In sample *C*, the $\mathbf{M}_r$ values are lying in the range of $0.4\mathbf{M}_s(280\text{ K}) \leq \mathbf{M}_r(T) \leq 0.8\mathbf{M}_s(5\text{ K})$ while for sample, *B* the $\mathbf{M}_r$ values are between $0.1\mathbf{M}_s(280\text{ K}) \leq \mathbf{M}_r(T) \leq 0.4\mathbf{M}_s(5\text{ K})$. In these MLs, the large $\mathbf{M}_r$ values cannot be explained by the magnetization reversal process that involves self-stabilization of Néel-type walls only. Since class *B* and *C*

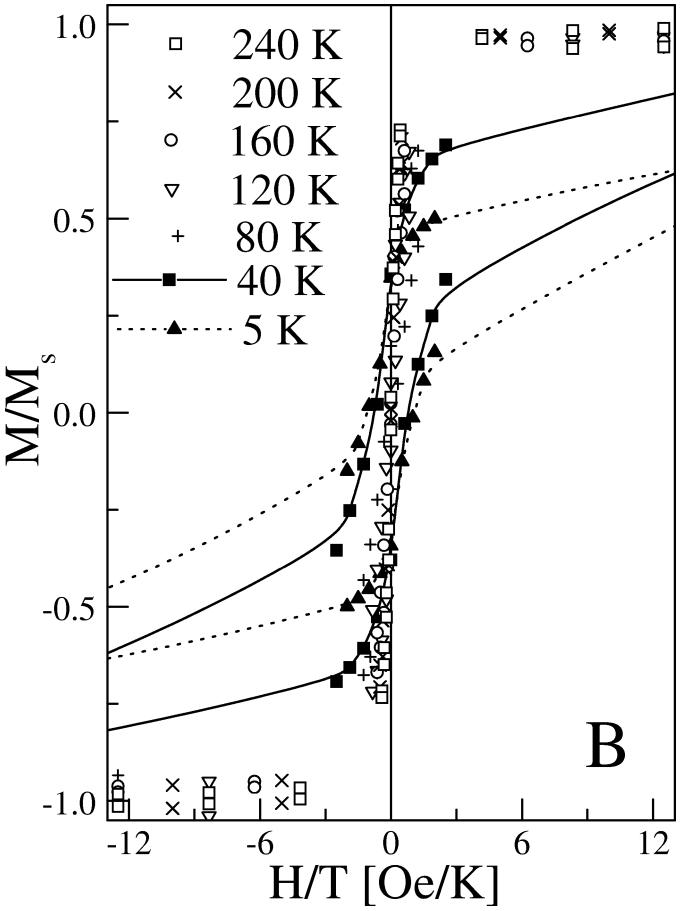

Fig. 10. The isothermal $\mathbf{M}/\mathbf{M}_s$–H loops of class B MLs are shown as a function of temperature. The lines are guides to the eye.

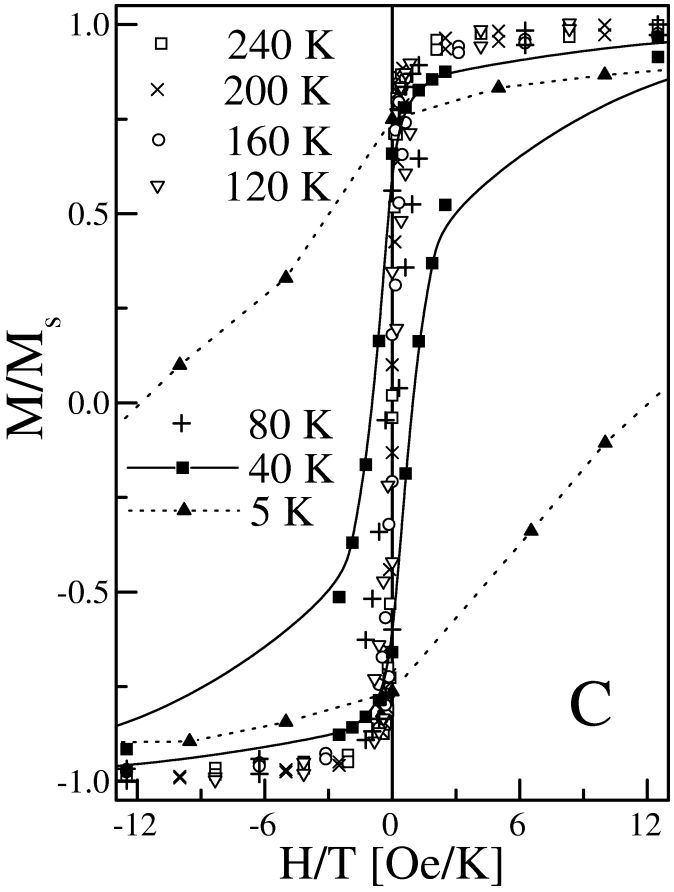

Fig. 11. The isothermal $\mathbf{M}/\mathbf{M}_s$–H loops of class C MLs are shown as a function of temperature. The lines are guides to the eye.

MLs contain different fractions [131] with small size columnar structures then minimization of the magnetostatic energy (long-range dipolar interactions) at grain boundaries results in FM-coupled areas near the small grains. Energy minimization of a Hamiltonian that involves short-range exchange and long-range dipolar interactions has produced [143] thermomagnetic curves for the uniform magnetization and the domain order parameter of ultrathin magnetic films that resemble those in Figure 12 for certain grain sizes. Thus, it can be argued that a short-range-order state [143] appears at elevated temperatures, where the domain walls fluctuate infinitely. This can explain the observed decrease of $\mathbf{M}_r$ above 100 K in the three classes of MLs.

(iii) In sample C, the number of required field units per Kelvin (H/T) for the magnetization reversal process is much higher than that of sample B (Figs. 10 and 11). This indicates that the larger fraction of small grains [131] in class C MLs is responsible for the magnetic hardening at lower temperatures.

The normalized $\mathbf{M}_s(T)/\mathbf{M}_s(5\text{ K})$, $(\mathbf{M}_r(T)/\mathbf{M}_s)^2$ and H_c values are plotted in Figure 12 as a function of temperature for the three classes of MLs. Remarkably, the H_c is highest for the AF loop of sample A whereas the FM-like loops of sample C exhibit higher H_c values than sample B. Such effects can be explained by trapping of magnetic moments in local energy minima of individual grains that form an assembly with random orientations of magnetic easy axes [144]. Since the observed [131] variation in the bimodal distribution of grain sizes affects the short-range exchange, the long-range dipolar interactions and the anisotropy energy as we move from class A to C MLs, it may account for the different increase of H_c and $\mathbf{M}_r$ at lower temperatures as well.

The most interesting result is revealed in the temperature dependence of magnetization which for the three classes of MLs does not follow the linear T, or $T^{3/2}$, or T^2 power laws. These laws were derived [122] for the cases of noncoupling, of FM and AF interlayer coupling, respectively, and observed [145, 146] in fcc Co/Cu MLs at the first AF maximum, where the interlayer coupling term is dominant. The observed disagreement with these power laws in Figure 12 is caused by the significant increase of $\mathbf{M}_s$ below 120 K. An enhancement of $\mathbf{M}_s$ induces a significant increase of the magnetostatic contributions in the long-range dipolar energy term which has not been taken into account in the minimization of the intrinsic magnetic free energy that leads to the specific power laws. Therefore, the intrinsic enhancement of $\mathbf{M}_s$ by decreasing temperature creates an extrinsic increase of magnetostatic dipolar interactions due to geometrical grain factors introduced by the specific microstructure. This extrinsic magnetostatic energy gives rise to a

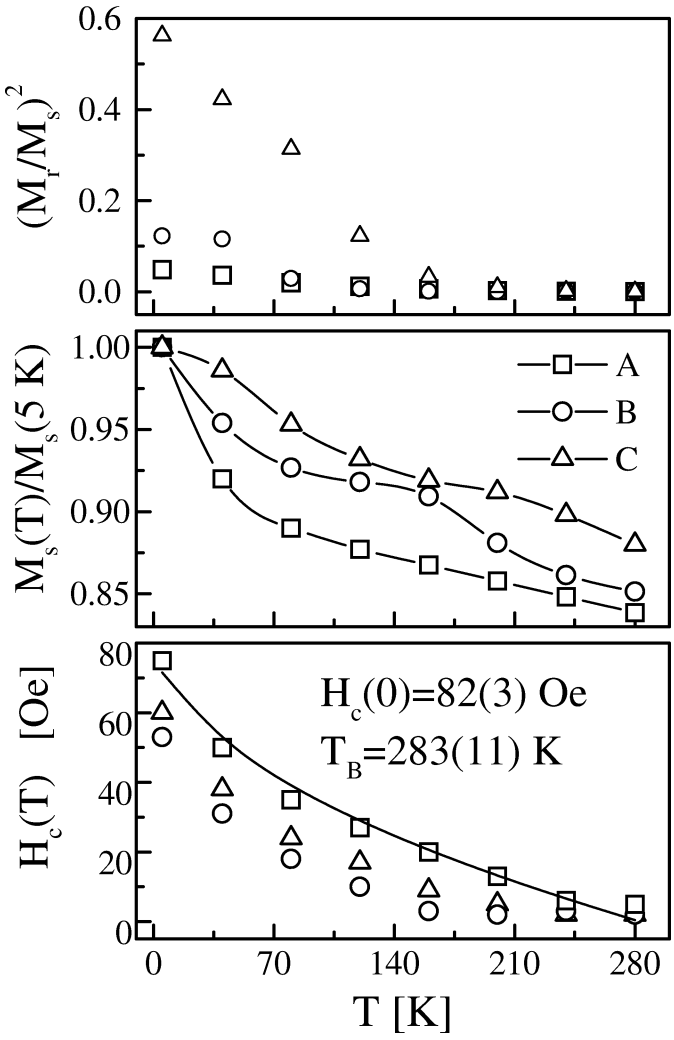

Fig. 12. The bottom plot shows the temperature dependence of the coercive H_c fields obtained from isothermal $\mathbf{M}/\mathbf{M}_s$–H loops of class A (open square), B (open circle), and C (triangle) MLs. The solid line is the best fit using Eq. (12). The middle plot shows the temperature dependence of the normalized magnetization observed in class A–C MLs. The lines are guides to the eye. The plot on top shows the temperature dependence of the square of the normalized residual magnetization $\mathbf{M}_r/\mathbf{M}_s$, observed in class A–C MLs.

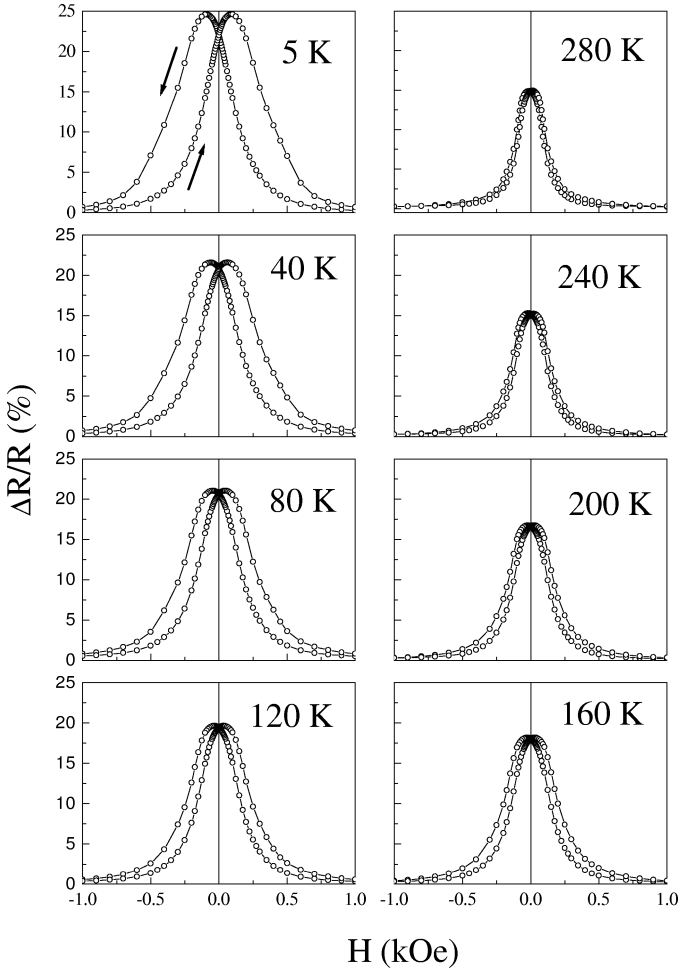

Fig. 13. The temperature dependence of the isothermal GMR loops is shown for class A MLs.

blocking temperature accompanied by a significant increase of hysteresis below 120 K.

Figures 13–15 show the temperature dependence of the GMR loops in the $H \parallel I$ configuration for class A, B, and C MLs, respectively. The large reduction of GMR effect—observed among class A–C MLs—indicates that modification of the magnetic disorder at the Co–Cu interfaces, due to changes of roughness, alters the amount of spin-dependent scattering events. Usually, such effects result [147] in strong temperature dependence of the interlayer exchange-coupling strength and the corresponding H_s in the GMR loops.

Accordingly, Figure 16 shows that the GMR ratios $\Delta R/R_s = (R_{\max} - R_s)/R_s$, with $R_{\max}$ the maximum and R_s the minimum resistance at H_{peak} and H_s magnetic fields respectively, follow a quasi-linear decrease with increasing temperature for the three classes of MLs. Additionally, Figure 16 shows that the H_s exhibits a drop of more than 50% between 5 and 280 K, that evidences the strong sensitivity of the indirect coupling strength to temperature. These H_s values were estimated from the first derivative of the GMR curves, choosing the highest absolute values of field where the derivative line becomes horizontal. However, the most dramatic change occurs in H_{peak} values, where the three classes of MLs exhibit a steep increase below 100 K. This effect is similar to that observed in low-hysteresis GMR MLs with compositions [126, 127]: $[\text{Co}(0.25\ \text{nm})/\text{Cu}(2\ \text{nm})]_{20}$ and $[\text{Co}_{0.5}\text{Cu}_{0.5}(1.1\ \text{nm})/\text{Cu}(2\ \text{nm})]_{20}$.

In AF-coupled Co/Cu MLs, the demagnetized state at H_c can be achieved by domain-phase transformations during the application of a reverse field, that make more and more domains and domain walls vanish [140]. Since the strength of H_c is associated with an intrinsic energy barrier that resists magnetization reversal during demagnetization, it is more feasible to formulate its temperature dependence instead of calculating the normalized loops. The size of the columnar grains [131] indicates that parallel Néel walls can be stabilized nearby planar defects, such

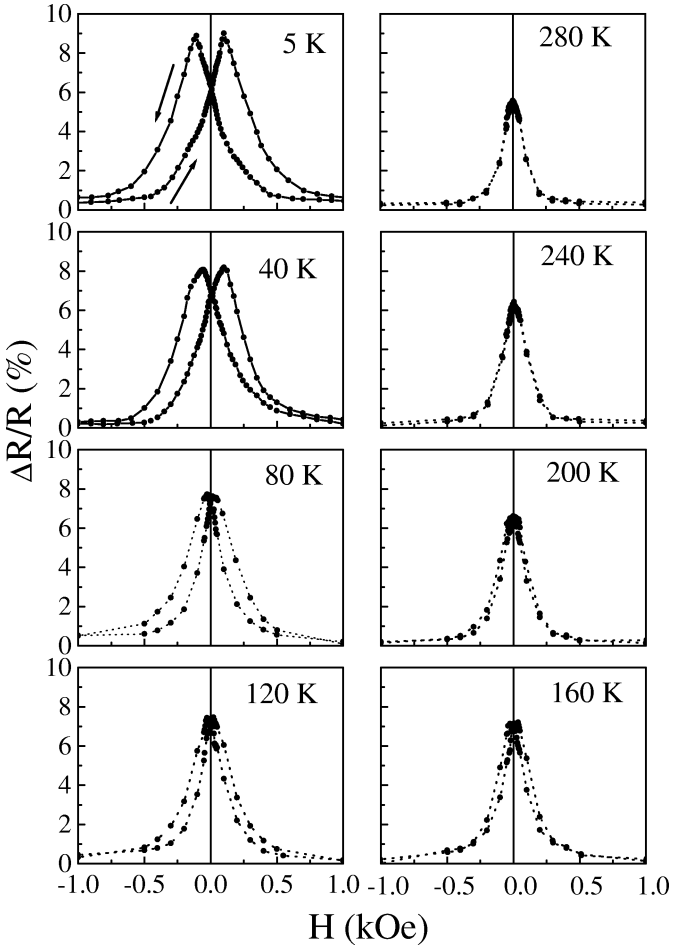

Fig. 14. The temperature dependence of the isothermal GMR loops is shown for class *B* MLs.

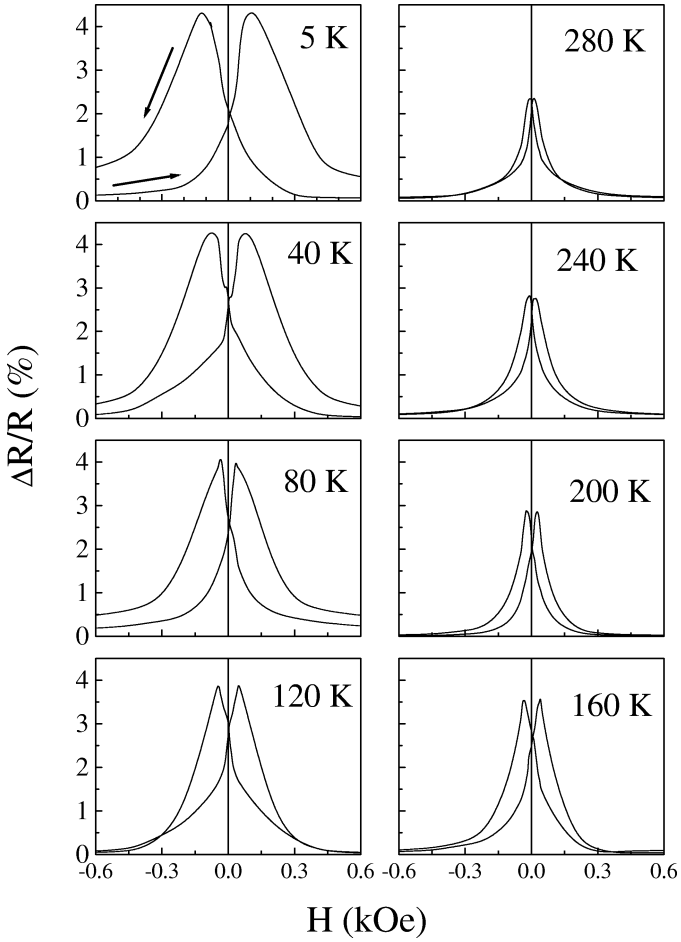

Fig. 15. The temperature dependence of the isothermal GMR loops is shown for class *C* MLs.

as columnar-grain boundaries, forming an assembly of noninteracting domains at the remnant state. Application of the same model as for magnetic nanoparticles can approximate [149] the temperature dependence of $H_c(T)$ by

$$H_c(T) = H_c(0)\left[1 - (T/T_B)^{1/2}\right] \qquad (12)$$

where T_B defines a blocking temperature above which domain walls cannot be stabilized within the Co layers and the $H_c(T \geq T_B) = 0$. Since the involved phenomena concern the stability of micromagnetic states in polycrystalline MLs then, in principle, the magnetic *ripple blocking* or *locking* [150] mechanisms might be related to the physical origin of magnetization dispersion and the concept of T_B in Eq. (12). Equation (12) is used to fit the observed $H_c(T)$ values of sample *A* and the solid line in Figure 12 (bottom plot) gives an $H_c(0) = 82(3)$ Oe and a $T_B = 283(11)$ K. As expected, Eq. (12) cannot fit the observed $H_c(T)$ values in class *B* and *C* MLs because a fraction of relatively small, FM-coupled, Co/Cu grains (not domain walls) coexists [131] with the larger, AF-coupled, columnar structures and the preceding approximations are no longer valid.

The observed variation of H_s and H_{peak} in Figure 16 is comparable to the strong temperature dependence observed on a scale of about 100 K in [123] Co/Ru and [147] Co(hcp)/Cu MLs. Since the H_{peak} values (Fig. 16) depend primarily on the magnetization reversal process, then they may follow the observed temperature variation of H_c (Fig. 12), that is derived from the isothermal M–H loops. Thus, Eq. (12) was used to fit the H_{peak} values observed in class *A* MLs. The solid line in Figure 16 is the best fit to square symbols, showing that Eq. (12) is a good approximation to H_{peak} variation as well. It is worth noting that an exponential function does not fit the observed temperature variation. The 20% difference of T_B values, obtained between the H_{peak} (Fig. 12) and H_c (Fig. 12) fits, indicates that a different thermal coefficient is involved in the second term of Eq. (12).

The most important result is related to the temperature dependence of H_s (Fig. 16) as the Co–Cu layering is modified in the three classes of Co/Cu MLs. So far, two different approximations were used to successfully describe the temperature dependence of H_s in AF-coupled MLs. The first assumes [121] that the temperature dependence originates from fluctuations in the spin-angular momentum of the FM layers rather than from electronic effects in the spacer layers, resulting in an analytical expression for the fractional decrease of $H_s \sim T \ln T$, within

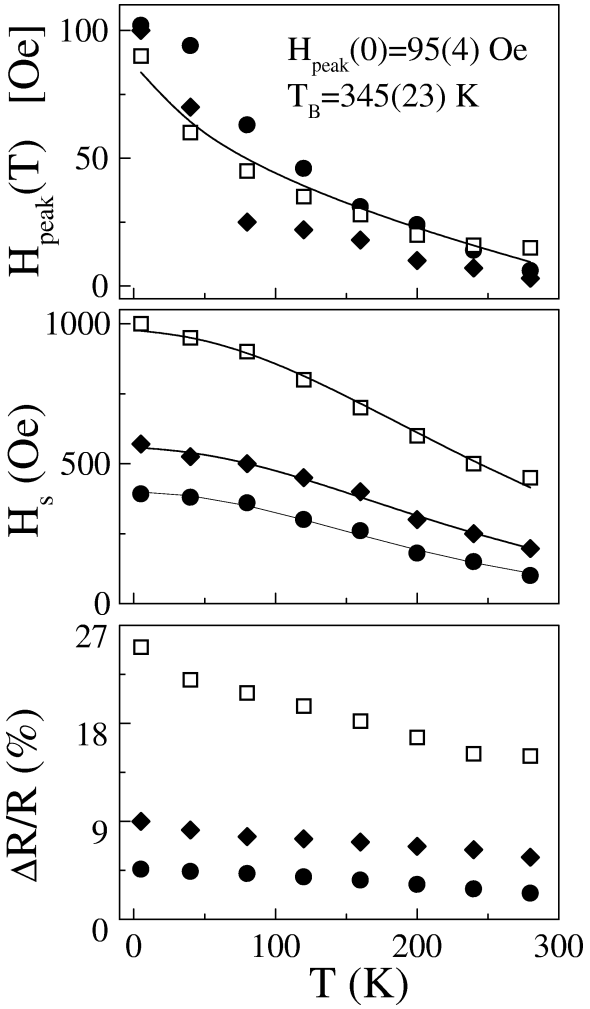

Fig. 16. The temperature dependence of H_{peak} (top), H_s (middle), and the GMR ratios (bottom)—obtained from the isothermal GMR loops of class A (squares), B (diamond symbols), and C (solid circles) MLs—are shown. The solid line is the best fit of H_{peak} for class A MLs, using Eq. (13).

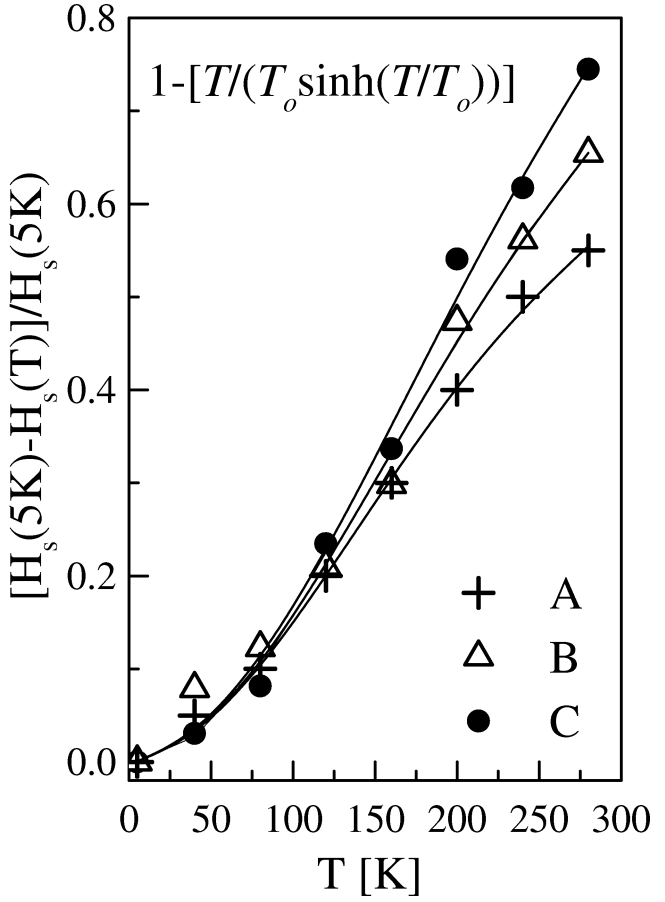

Fig. 17. The temperature dependence of the reduced saturation fields H_s, that were obtained from the isothermal GMR loops, are shown for class A (crosses), B (triangles), and C (solid circles) MLs. The solid lines are the best fits using Eq. (13).

the limits of spin-wave theory. The second approach assumes that the velocity of electrons υ_{F} at the extremal points of the spacer Fermi surface governs the temperature dependence of $\mathbf{J}_{\text{osc}}$ and the one-electron model [119] predicts for the fractional decrease of H_s that

$$[H_s(0) - H_s(T)]/H_s(0) \sim 1 - [(T/T_0)/\sinh(T/T_0)] \quad (13)$$

where the characteristic temperature T_0 is given by

$$T_0 = (\hbar \upsilon_{\text{F}})/(2\pi k_s t_{\text{Cu}}) \quad (14)$$

Figure 17 shows that Eq. (13) fits the fractional decrease of H_s better than the $T \ln T$ function. This shows clearly that the Co/Cu interface roughness governs the temperature dependence of interlayer exchange coupling in the three classes of Co/Cu MLs. Earlier studies [119, 123, 147] indicate that T_0 is of the order of 100 K. In agreement, Figure 17 shows that Eq. (13) fits the fractional decrease of H_s for class A (crosses), class B (triangles), and class C (solid circles) MLs, using a T_0 of 84(4), 96(11), and 105(10) K, respectively.

According to Eq. (14), the ratio υ_{F}/k_s should increase as the T_0 values vary from 84 to 105 K and the Co/Cu interfaces become more disordered in class B and C MLs. However, it was observed [147] that the use of υ_{F} of Cu in Eq. (14) gives theoretical T_0 values which are an order of magnitude larger than the experimentally observed. In Co(hcp)/Cu MLs, the existence of either magnetically dead interfacial Co regions, that could modify the thermal evolution of the potential barrier, or fully confined magnetic carriers in the spacer potential well were proposed [147] as possible explanations for the strong temperature dependence of exchange coupling. It has been argued that [147] chemical roughness changes the spin-dependent potential barrier at the interfaces and alters the character of the electronic states near the Fermi surface. In agreement, the obtained variation of T_0 can be associated with a larger Co–Cu intermixing (chemical roughness) at the interfaces as we move from class A to C MLs.

These results show that the obtained differences among class A–C MLs are due to different degrees of Co–Cu intermixing at the interfaces and are due to different geomet-

ric factors of the grains. Both are crucial for the obtained $(T/T_0)/\sinh(T/T_0)$ dependence of interlayer coupling because an increase of the fraction of small grain sizes increases the film roughness. However, the obtained increase of T_0 as we move from class *A* to *C* MLs can be understood only if we consider it as a thermal blocking or spin-freezing energy that depends on the concentration of Co *loose* spins near the interfaces, rather than as velocity of the carriers [119] at the stationery points of the spacer Fermi surface (Eq. (14)). Thus, it is the thermal activation energy, which magnetically decouples the residual Co spins at the interfaces due to Co–Cu intermixing, that causes the desired lowering of H_s at room temperature.

On the other hand, it is the decrease of $\mathbf{M}_s$ from the magnetic decoupling of interfacial Co spins, which lowers the magnetostatic energy at grain boundaries above the T_B (Eq. (12)), that causes the desired softening of H_c and H_{peak} values observed in Figs. 12 (bottom) and 16, respectively. Thus, the degree of H_c and H_{peak} softening scales with the density of grain boundaries (or the fraction of smaller grain sizes) present in the developed microstructure. The experimental results indicate that the spin structure of the examined Co/Cu MLs is not stable above the obtained T_0 or T_B values because the lowering of dipolar (magnetostatic) interactions [143] at grain boundaries can create a secondary short-range order state where domain walls fluctuate infinitely.

4.3. Low-Field GMR in Co/Au MLs

Another category of FM–NM(111) layered structures where the Ruderman–Kittel–Kasuya–Yosida (RKKY) theory was applied, are [164] Co(0001)/Au(111) epitaxially grown MLs that exhibit perpendicular magnetic anisotropy. For this system, oscillatory magnetic coupling has been reported [173] in Co/Au(111)/Co trilayers with identical Co layer thicknesses and hcp stacking, where three GMR maxima, corresponding to antiferromagnetic coupling between adjacent Co layers, were observed with increasing Au layer thickness (t_{Au}). In this system, the magnetocrystalline anisotropy of hcp Co induces a large coercive field in the GMR curves [173] and the GMR amplitude (≈2%) is an order of magnitude less than in Co/Cu(111) MLs, precluding GMR applications with epitaxial Co/Au MLs. Following the characteristic example of sputter-grown Co/Cu MLs it was shown [156] that sputtered [Co(1 nm)/Au(2.4 nm)]$_{30}$ MLs with (111) texture exhibit a low-field GMR effect that make these films potential candidates for sensor applications [125]. As in sputtered Co/Cu MLs with (111) texture, the intrinsic nature of antiferromagnetic coupling can be supported by: (i) the position of the GMR maximum at $t_{\text{Au}} \approx 2.4$ nm, that is similar in epitaxial hcp Co/Au(111) layers [173] and sputtered (111) Co/Au MLs [156] with varying t_{Au}, (ii) longitudinal Kerr-effect hysteresis loops [174] in [Co(1 nm)/Au(2.4 nm)]$_{30}$ MLs exhibit a manifold loop that is indicative for the coexistence of bilinear and biquadratic interlayer coupling, and (iii) no detectable fraction of (100)-oriented crystallites was observed [156] in both systems.

The Co/Au MLs with $t_{\text{Co}} < 1$ nm exhibit only anisotropic magnetoresistance. In Figure 18 are shown the GMR ratios $\Delta R/R_s = (R_{\max} - R_s)/R_s$, with $R_{\max}$ the maximum and R_s the minimum resistance in different magnetic fields H, as a function of t_{Co} in the $H \parallel I$ configuration. The obtained GMR ratios decrease quasi-linearly with t_{Co}, as in GMR Co/Cu multilayers [134]. In addition, Figure 18 shows that the saturation (H_s) and coercive (H_c) fields, obtained from the GMR curves with $H \parallel I$, approach a saturation value for thicker Co layers. The observed enhancement of H_c and H_s provides evidence for changes in the micromagnetic structure due to modifications in Co layering as t_{Co} increases.

The observed [158] GMR loops with $H \parallel I$ indicate that the film magnetization is lying in-plane [156], contrary to all past studies where this material combination was a typical system exhibiting a large perpendicular anisotropy [164, 173] when 4 to 12 Co monolayers were stacked with relatively thick Au lay-

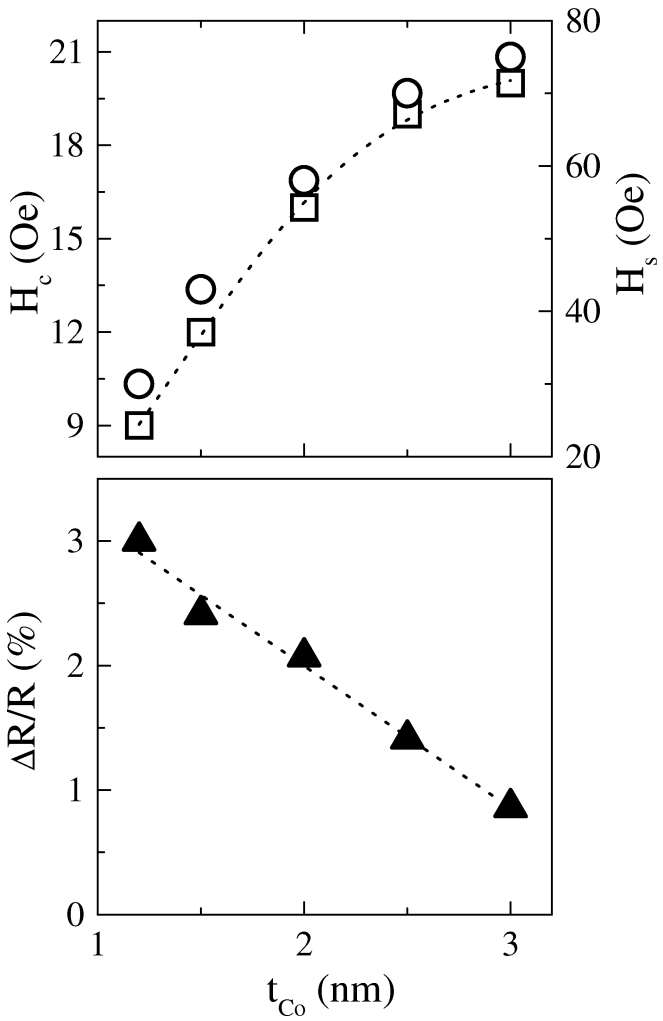

Fig. 18. The top part shows the variation of the H_c (squares) and H_s (circles) parameters from the GMR curves with $H \parallel I$. The corresponding GMR ratios are plotted as a function of t_{Co}. The lines are guides to the eye and the experimental error is within the size of the symbols. Reproduced with permission from [158], copyright 1999, The American Physical Society.

ers. Additionally, isothermal magnetic loops have shown [156] that the film magnetization is in-plane for the examined layer thicknesses. The optimum low-field GMR is observed for $t_{Co} \approx$ 1 nm and its in-plane anisotropy can be attributed [156] to Au-surface-like modifications induced in the Co layer structure. For $t_{Co} \approx 1$ nm the coercive field H_c and the switching field H_s are 0.01 kOe and less than 0.03 kOe, respectively. Comparatively, the observed [173] values in epitaxial trilayers are $H_c \approx 0.5$ kOe and H_s less than 0.05 kOe. This order of magnitude improvement of H_c and the maximum obtained GMR ratio of [156] 3%, that is about 1% higher than that observed in epitaxial trilayers [173], indicate that such differences between the hcp Co(0001)/Au(111) trilayers [173] and in low-field GMR Co/Au MLs [157] arise from the different (fcc) Co layer stacking [133, 157] that alters the magnetocrystalline anisotropy of Co.

Thus far, the variation of the GMR amplitude versus t_{Co} has been reconciled with phenomenological models, considering either the ratio [148] between the probability for a spin-minority electron to be scattered in the FM layer and the increasing current shunting through it or the changes in the micromagnetic state [178] (misalignment of adjacent moments), that give a reduction of the GMR for thicker FM layers. The quasi-linear decrease of GMR observed in Co/Au (Fig. 18) and Co/Cu MLs [134] indicates that the GMR dependence on t_{Co} can be described by a generalized Camley and Barnas [179] model. In the quasi-classical limit [180], this model shows that the current-in-plane GMR varies linearly with $\sin^2(\theta/2)$, when θ is the angle between the magnetizations of adjacent FM layers. The linearity of GMR indicates that t_{Co} changes the degree of magnetic misalignment among the Co layers, imposing an angular dependence of GMR with t_{Co}.

4.3.1. Magnetooptical Kerr Spectra in Co/Au Multilayers

In Figure 19, the longitudinal Kerr-effect hysteresis loops are shown for $t_{Au} = 2.2$, 2.4, 3.6, and 3.9 nm. At the GMR minima ($t_{Au} = 2.2$ and 3.6 nm), they reveal a significant magnetic anisotropy, that may be induced in the Co layers from a high concentration of step edges [165] located at the Co/Au interfaces due to surface reconstruction of the Au(111) planes. For $t_{Au} = 2.4$ nm there is a manifold loop with insignificant residual magnetization, inferring coexistence of the so-called [38, 39, 166] bilinear and biquadratic interlayer coupling terms at the first GMR maximum. However, at the second GMR maximum there is a ferromagnetic loop, characteristic for a random distribution of Co magnetic moments (uncoupled layers) that contributes to bulklike spin scattering [38, 165]. It is worth noting that the observed H_c values from the Kerr loops are different from those in the GMR loops [158]. This indicates that the magnetic properties of the films depend significantly on the structural and topographical quality of the template. Thus, formation of atomic steps near small or large terraces at the Co/Au interfaces creates anisotropy axes along the step edges that induce an azimuthal angle dependence of the hysteresis loops with SMOKE [167].

The polar loops (Fig. 20) confirmed the presence of the interface induced anisotropy which reduces the saturation field below 3 kOe, while the coercive field varies between 10 and 65 Oe. The Kerr spectra show a distinct Au plasma edge peak centered near 2.5 eV. A narrowing and a reduction in the am-

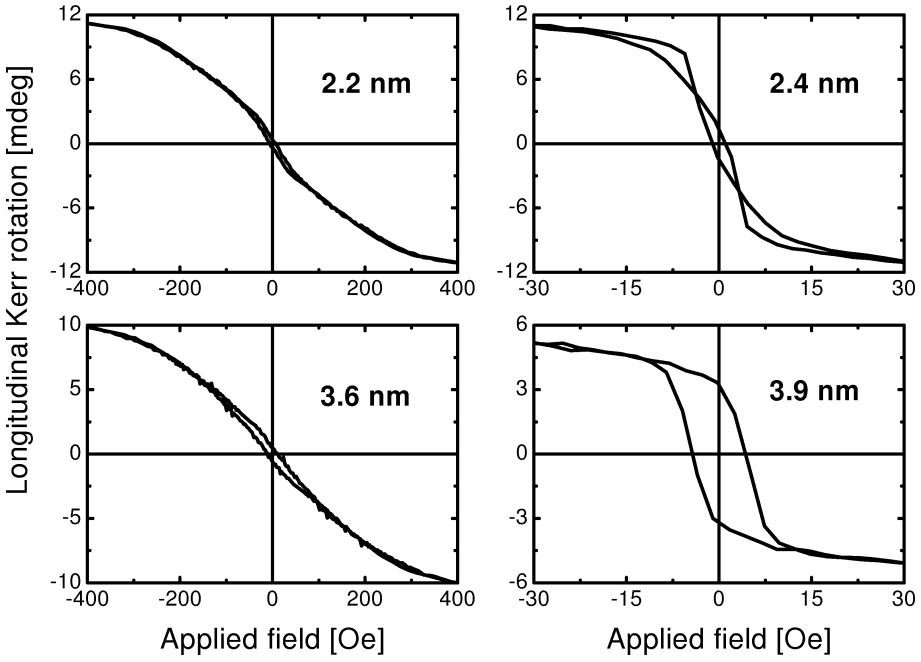

Fig. 19. Longitudinal Kerr-effect hysteresis loops for selected thicknesses t_{Au} at the photon energy of $E =$ 2.76 eV for an *s* polarized wave incident at 45°. Reproduced with permission from [174], copyright 1999.

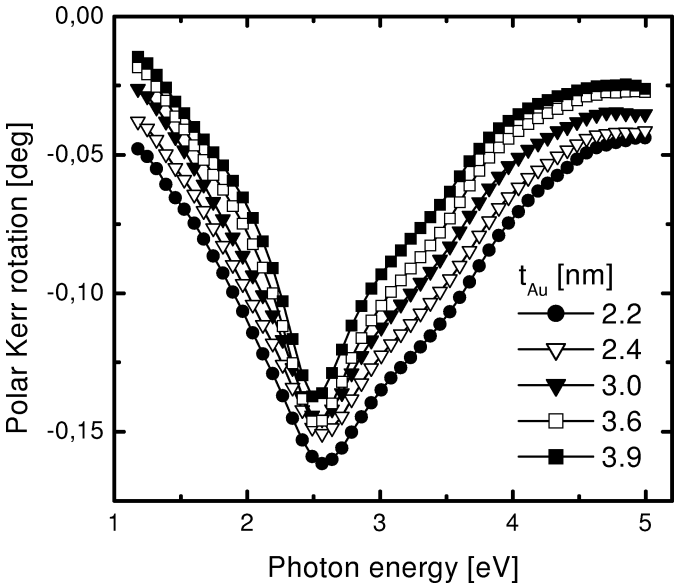

Fig. 20. Saturated polar Kerr rotation spectra of [Co(1 nm)/Au(t_{Au})]$_{30}$ multilayers with a fixed Co thickness and t_{Au} between 2.2 and 4 nm. Reproduced with permission from [174], copyright 1999.

plitude of the peak is observed by increasing t_{Au}. These trends were reproduced by computer simulations [168] with the experimental amplitudes about 50% smaller. This difference can be attributed to extended intralayer and/or interface disorder, located mainly at the ferromagnetic Co layers, and to changes in Au electronic states induced by adjacent Co layers.

Such Kerr spectra indicate that static deposition of the constituents with low rates, on an SiN_x buffer layer, seems to enable the development of a considerable fraction of faults in the atomic packing of Co layers along the growth direction of Co/Au MLs with (111) texture. Thus, the observed differences in magnetotransport properties, between the low-field GMR Co/Au MLs and those grown by MBE [173], can be attributed to the development of a specific microstructure in the magnetic layers.

4.3.2. Dielectric Function Variation Determined from Spectroscopic Ellipsometry

Spectroscopic ellipsometry (SE), which is a nondestructive method that directly measures the complex dielectric function $\varepsilon(\omega) = \varepsilon_1(\omega) + i\varepsilon_2(\omega)$, is applied for the study of the optical properties and the investigation of the elusive mechanism between the microscopic origin of the GMR phenomenon and the film morphology. SE can measure both, the relative changes in the joint density of electronic states near the Fermi surface and the changes in film morphology by varying t_{Co} in the promising GMR [Co(t_{Co})/Au(2.4 nm)]$_{30}$ MLs. In addition, the measurement of $\varepsilon(\omega)$ provides information about the intraband transitions, that depend on grain-size effects, and the interband transitions which are related to the joint density of states at high symmetry points of the Fermi surface [175, 176].

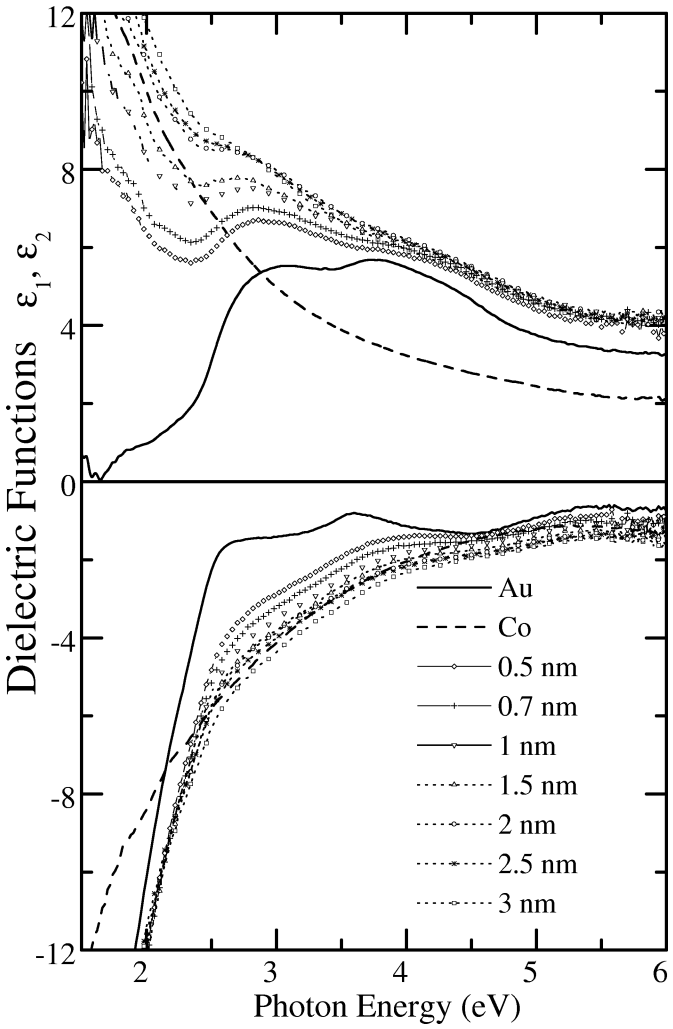

Fig. 21. The obtained real ε_1 (bottom) and imaginary ε_2 (top) parts of the dielectric function are plotted as a function of the photon energy for seven Co/Au multilayers with different t_{Co}. For clarity, the ε_1 and ε_2 values are shown on a shorter scale than the full span range between -25 and 19. Reproduced with permission from [158], copyright 1999, The American Physical Society.

A systematic variation of the real and imaginary parts $\varepsilon_1(\omega)$ and $\varepsilon_2(\omega)$ of the dielectric function has been observed as a function of t_{Co} (Fig. 21). In general, the $\varepsilon(\omega)$ is correlated to the electronic properties of a material. If the solid is a good conductor, like noble metals, the optical wave mainly interacts with conduction electrons and according to the Drude model [175, 176] the plasma frequency ω_p of the electron gas plays the most important role. The experimental data from the Co/Au MLs (Fig. 21) contain the low-frequency intraband or Drude contribution which is evident from the low-energy behavior before the threshold energy of the interband transitions. Because the optical constants are not available in the literature for ultrathin layers of Co and Au, it is preferable to compare the observed dielectric function of Co/Au MLs with that of pure Au or Co thin films.

The film of 100-nm thick Au does not show the part of ε_2 that relates with intraband transitions (solid line in Fig. 21) in

the low photon energy. That part of ε_2 was found [181, 182] to deviate from the Drude model, depending upon the microscopic quality of Au (purity, voids concentration, strain, grain sizes, etc.) and the film thickness. The measured absorption (ε_2) in the Au film exhibits a steep rise at about 2 eV and its yellow color is a manifestation of the rather low threshold for the excitation of 5d band electrons in the conduction band [176, 183]. The supplementary absorption that is located below the absorption edge ($\approx$1.75 eV) of Au is often observed [182] and was attributed to the presence of point defects, like vacancies, or impurities, like gas atoms, in the samples. However, a careful study [182] in Au films with different crystallographic structures has shown that neither the nature nor the location of the contributing interband transitions can be modified by important structural changes of the films. As in some most earlier work [181, 182], an interband onset has been resolved around 2.5 eV from the ε_1 spectrum and is followed by two peaks in ε_2 at about 3.2 and 4 eV. Empirical band calculations of the optical properties [183] qualitatively reproduce the experimental peaks. In contrast to Cu, no evidence of transitions at the X high symmetry point is found in Au, whereas the second peak ($\approx$3.2 and 4 eV) is a sum of contributions [183] from optical transitions near the L critical point for [184] Cu or Au films.

The observed dielectric function of 100-nm thick Co film (dashed line in Fig. 21) is similar to that observed in polycrystalline Co films deposited on Si(100) substrates [185], where the ε_1 and ε_2 exhibit a slow, almost structureless evolution. The physical origin of this phenomenon is related to the minority 3d bands of Co that cut by the Fermi level with complicated Fermi-surface crossings, creating numerous interband transitions [186]. Additionally, it was observed [187] that formation of a surface CoO layer on Co films shifts only the reflectance curves without changing their shapes.

Generally, the observed interband peaks in SE spectra result from the varying k-space contribution. In particular, the L high symmetry point belongs to the faces [188] where the $\langle 111 \rangle$ cubic directions intersect the fcc Brillouin zone of Au. Since the Co/Au MLs exhibit [156, 133] such preferred orientation across the growth direction, then further broadening is expected (Fig. 21) in the interband transitions of the second peak because the Fermi surface of Au intersects the Co/Au interfaces along the [111] direction. The obtained $\varepsilon_1(\omega)$ and $\varepsilon_2(\omega)$ spectra (Fig. 21) exhibit the characteristic features that generally appear [189–192] in FM–NM MLs, with NM = Cu or Pd:

(i) Both the real and imaginary parts of $\varepsilon(\omega)$ show a monotonic, systematic shift with increasing t_{Co}, moving from Au-like optical constants to Co-like constants.

(ii) The $\varepsilon_1(\omega)$ and $\varepsilon_2(\omega)$ spectra exhibit an interband peak at about 2.5 eV and a second broad feature at about 4 eV, in qualitative agreement with polar Kerr rotation spectra [174] and spectra of epitaxially grown Co(0001)/Au(111) MLs [189] or sandwiched [190] structures.

(iii) The large interband broadening that is observed in Au-based MLs, compared to the sharp threshold absorption edge of pure Au films, arise from symmetry breaking at the interfaces of the multilayer and the extra broadening of the intraband contributions due to confinement of the electronic mean-free path from grain boundaries.

A phenomenological expression, that takes into account the free-carrier and photon absorption from intra- and interband electron transitions, was used to fit the observed dielectric function of the Co/Au MLs. The $\varepsilon(\omega)$ fitting function is written [134, 193] as the sum of a Drude term plus a damped Lorentzian oscillator term, centered at the low-energy interband peak position ($h\omega_0/2\pi$) with a strength A and a damping (broadening) factor γ. A second Lorentzian term was used for the feature near 4 eV, to take into account the vast peak broadening in this range. The analytical expression contains a constant background term ε_∞ as well:

$$\varepsilon(\omega) = \varepsilon_\infty - \omega_p^2/(\omega^2 + i\omega\Gamma) + A/(\omega_0^2 - \omega^2 - i\gamma\omega) \quad (15)$$

In the second (Drude) term, $\omega_p = (4\pi N_c e^2/m^*)^{1/2}$ is the unscreened plasma energy related to the density N_c of the free carriers with m^* being the effective optical mass and $\Gamma(\approx 1/\tau_{\mathrm{eff}})$ being the broadening parameter, which is inversely proportional to the free carriers effective [182] scattering time τ_{eff}. A quantitative estimation of ω_p, Γ, the energy peak position, the amplitude—that depends upon the strength factor A—and the broadening γ parameters is achieved by simultaneous least-square fitting of the real and imaginary parts of the $\varepsilon(\omega)$ spectra. The obtained plasma energy ω_p (top) and broadening Γ (bottom) parameters are plotted in Figure 22 against t_{Co}. For comparison, the ω_p and Γ parameters obtained [134] from similar Co/Cu MLs are shown in Figure 22. It is obvious that: (i) there is a distinct difference between the Co/Cu and Co/Au MLs on the variation of ω_p with t_{Co}, and (ii) the broadening parameter Γ for the Co/Au MLs is almost twice the value of the corresponding Co/Cu MLs.

The second derivative $d^2\varepsilon/d\omega^2$, of the complex dielectric function has been calculated numerically from the ellipsometric data [194] to enhance the existing structure in the spectra. From this process, only one interband feature in $d^2\varepsilon/d\omega^2$ was well resolved to allow a quantitative analysis with standard spectral line shapes [175], considering a mixture of a two-dimensional minimum with a saddle critical point [194]:

$$\varepsilon(\omega) = C - A_{\mathrm{CP}} e^{i\phi} \ln(E_{\mathrm{CP}} - \omega - i\Gamma_{\mathrm{CP}}) \quad (16)$$

The derivative spectra were fitted to one-electron critical point line shapes. A least-squares procedure was used, where both the real and imaginary parts of $d^2\varepsilon/d\omega^2$ were fitted simultaneously. Fits of the experimental second derivative $\varepsilon_1''(\omega)$, $\varepsilon_2''(\omega)$ spectra were performed with functions of the second derivative,

$$\begin{aligned} \varepsilon_1''(\omega) &= -A_{\mathrm{CP}} e^{i\phi} (E_{\mathrm{CP}} - \omega - i\Gamma_{\mathrm{CP}})^{-1} \\ \varepsilon_2''(\omega) &= -A_{\mathrm{CP}} e^{i\phi} (E_{\mathrm{CP}} - \omega - i\Gamma_{\mathrm{CP}})^{-2} \end{aligned} \quad (17)$$

where the angle ϕ represents the amount of mixing ($0 < \phi < \pi/2$). Thus, $\phi = 0$ corresponds to a minimum ($\mathbf{M}_o$), $\phi = \pi/2$ corresponds to a saddle point, and $\phi = \pi$ corresponds to a maximum ($\mathbf{M}_3$) critical point [175]. A_{CP} is the amplitude parameter

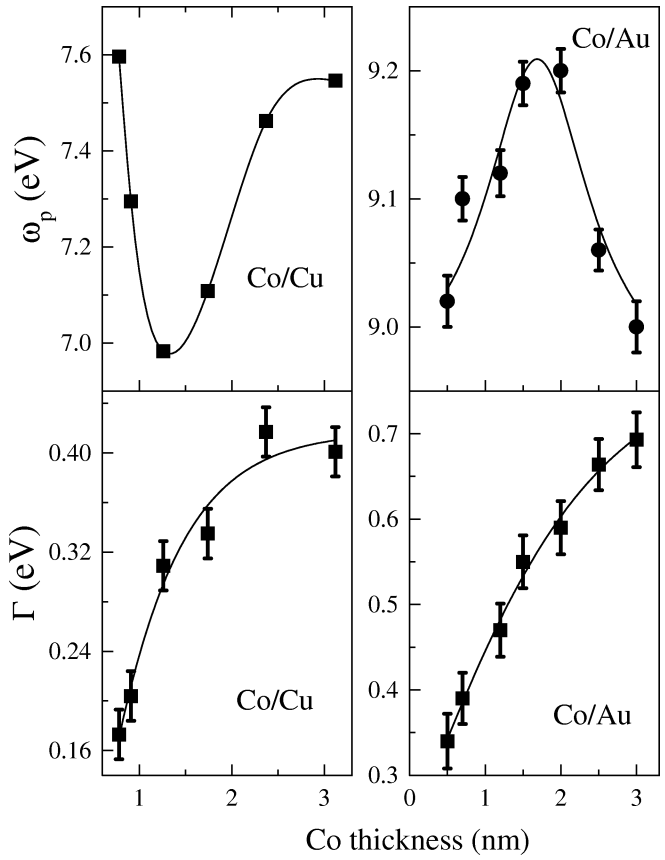

Fig. 22. The estimated values of the plasma energy ω_p and the Drude broadening parameter Γ, are plotted as a function of the nominal t_{Co} values for the Co/Cu and Co/Au MLs. Reproduced with permission from [158], copyright 1999, The American Physical Society.

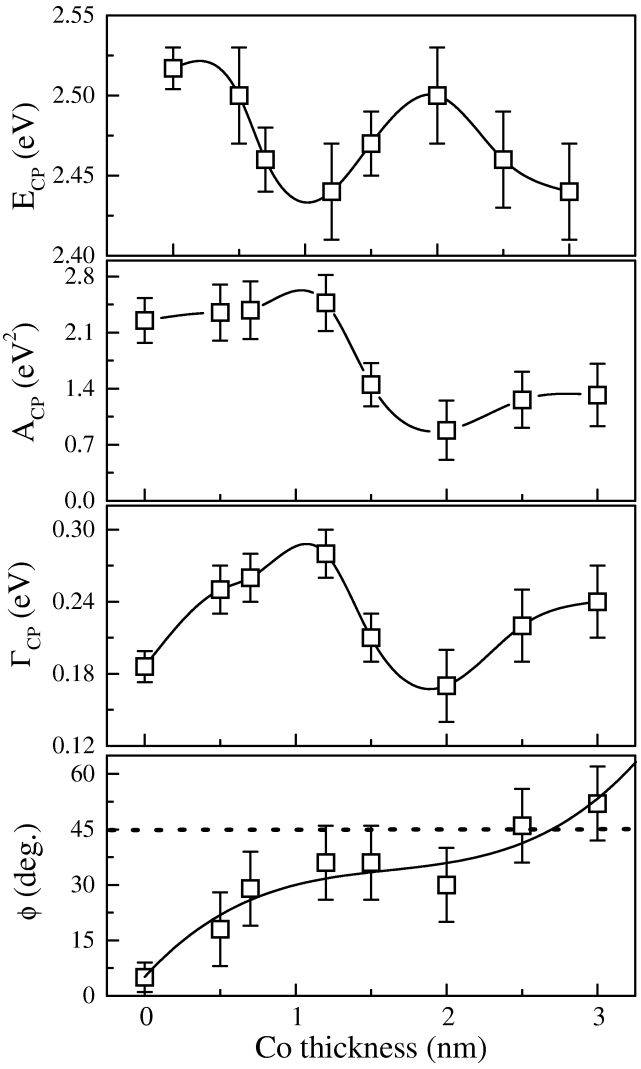

Fig. 23. The variation of the estimated parameters (Eq. (17)) E_{CP}, A_{CP}, Γ_{CP}, and ϕ with t_{Co}, including the corresponding parameters from the pure Au film as well ($t_{\mathrm{Co}} = 0$), is shown. The solid lines are guides to the eye. Reproduced with permission from [158], copyright 1999, The American Physical Society.

that is proportional to the strength of the oscillator, E_{CP} is the critical point energy, Γ_{CP} is its broadening parameter, and C is a constant. In Figure 23, the variation of E_{CP}, A_{CP}, Γ_{CP}, and ϕ with t_{Co} is shown, including the corresponding parameters from the pure Au film as well (t_{Co}=0).

The physical origin of the observed trend in Figures 21 and 22 is discussed later. It was shown [182] that Γ depends upon the optical relaxation time τ_o ($\tau_{\mathrm{eff}} \propto [\tau_o + O\omega^n]$). The τ_o is very sensitive to the presence of volume defects (grain boundaries, imperfections, and impurities inside the grains), degree of specular reflection of the electrons on interfaces, and anomalous skin effect corrections from surface defects. Thus, a comparison among the absolute values of Γ may lead to ambiguous conclusions. Moreover, if we consider a change of the relaxation time that takes into account a correction for the film thickness [189] and if we write the $\Gamma = (\xi/\lambda\tau)$, where ξ is the mean-free path in the bulk and λ is the restricted mean-free path in the MLs, then from Figure 22 the ratio $(\Gamma_{\mathrm{Au}}/\Gamma_{\mathrm{Cu}}) \propto (\lambda_{\mathrm{Cu}}/\lambda_{\mathrm{Au}}) > 1$ emerges for every t_{Co}.

Since the Co/Cu and Co/Au layer thicknesses are the same as a function of t_{Co}, the involved approximation concerns only the ratio ξ/τ, considering that there is no difference between Cu and Au layers. This is a reasonable assumption because Cu and Au exhibit Fermi surfaces with comparable ratios of "belly" to "neck" orbits, according to de Haas-van-Alphen data [195], and have the same Drude relaxation times ($\approx 2.8 \times 10^{-14}$ s) at room temperature. The $(\lambda_{\mathrm{Cu}}/\lambda_{\mathrm{Au}}) > 1$ condition indicates that a larger *spin-independent* scattering occurs in Co/Au MLs. Thus, the larger GMR amplitude observed [134] in Co/Cu MLs (grown under the same deposition conditions) than in Co/Au MLs is in agreement with this finding.

In the examined photon energy range, the major contribution to ω_p arises from the Au or Cu layers despite the fact that only the t_{Co} is varied (Fig. 22). However, only in Co/Au MLs are the ω_p values very close to $\omega_p(\mathrm{Au}) \approx 9.22$ eV for pure Au films [190] whereas in Co/Cu MLs they are well below the $\omega_p(\mathrm{Cu}) \approx 8.4$ eV of pure Cu for all the examined t_{Co} region. Since $\omega_p^2 \propto (N_c/m^*)$, with the optical mass [176, 182] lying between $0.94 \leq m^*_{\mathrm{Au}} \leq 1.05$ for pure Au and lying between $1.32 \leq m^*_{\mathrm{Cu}} \leq 1.45$ for pure Cu, it is reasonable to assume that the observed variation of ω_p in Figure 22 is related

mainly to changes of N_c. Variations of N_c can be explained either with changes in the distribution of grain sizes [184] and/or with structural modifications (internal stress effects) in layering for thicker MLs. This conclusion can be drawn from the reversal of the nonmonotonic variation of ω_p with t_{Co} (Fig. 22) when the Cu layers are replaced by Au. Specifically, both systems exhibit a nonmonotonic variation, where the ω_p decreases for $t_{\mathrm{Co}} < 1.5$ nm and increases for $t_{\mathrm{Co}} > 1.5$ nm in Co/Cu while the opposite behavior is observed below and above the $t_{\mathrm{Co}} = 2$ nm in Co/Au MLs. The nonmonotonic variation can be related to changes in grain-size distribution as a function of t_{Co}. Indeed, cross-section TEM images [157] show that the morphology of the columns in these Co/Au MLs is more spiked for $t_{\mathrm{Co}} > 2$ nm. In addition, planar view micrographs show a bimodal distribution of grain sizes with a larger fraction of small grains relative to multilayers with $t_{\mathrm{Co}} \leq 2$ nm.

The obtained variation of intraband parameters in Figure 22 coincides with the t_{Co} region where the obtained H_s and H_c fields from the GMR curves increase for the [134] Co/Cu and Co/Au MLs (Fig. 18). These results together with the observed TEM differences between [131] Co/Cu and Co/Au MLs [157] indicate that the reverse variation of ω_p is due to layer modifications in the two systems. Such differences between Co/Cu and Co/Au MLs with (111) texture can be initiated by the lattice mismatch at the interfaces, that is about 2 and 15%, respectively, and the unique ability of Au layers to minimize the stress at the interface during growth [196] of Co on Au(111) with a mechanism that is known as surface reconstruction [197].

The steep rise of $\varepsilon_2(\omega)$ in Au (Fig. 21) is due to the optical plasma resonance absorption edge that is sensitive [184] to grain-size effects as well. The observed (Fig. 21) smearing of the Au resonance edge and the broadening of the Au interband transitions with increasing t_{Co} is comparable with the reported size-dependent change in interband transitions [184] of Cu or Au nanoparticles. The reported changes in transmittance optical spectra were associated with an increase in the curvature of the d levels due to reduced $N(E_{\mathrm{F}})$ at the surface with decreasing size of Cu particles [184]. The analysis of the interband transitions indicates that there is a modification of the joint density of electronic states inside the NM layers of Co/Au and Co/Cu MLs as a function of t_{Co}. Since the Co layers expand significantly along the growth direction for thinner Co layers [133, 157], then a change of $N(E_{\mathrm{F}})$ can be associated with changes in Co layer density at the Co/Au interfaces as their lattice relaxes from an Au-surface-like to a Co-bulklike structure [157] with increasing t_{Co}. TEM measurements [157] in these Co/Au MLs show clearly that for $t_{\mathrm{Co}} \leq 2$ nm the Co lattice is expanded by 4.4% relative to bulk value while the Au lattice is compressed along the growth direction. As a result, an average fcc lattice between Co and Au layers was observed. For thicker Co layers, the fcc Co lattice is expanded by 2.9% along the growth direction whereas no average lattice is formed in this case and both elements exhibit interplanar spacings close to their bulk values.

The obtained variation of ϕ together with the nonmonotonic behavior of the interband parameters (Fig. 23) indicate that the band pairs of Au exhibit a change in the singular behavior from a minimum critical point in pure Au ($\phi \approx 5°$) to a mixture of a minimum with a saddle point in the range between $1 < t_{\mathrm{Co}} < 2$ nm ($20° < \phi < 40°$) that transforms to a pure saddle critical point for $t_{\mathrm{Co}} > 2$ nm ($\phi \approx 45°$). Such changes near the high symmetry lines of the band structure are directly related to changes in the curvature of the upper 5d conduction band of Au, that can be reconciled with effective-mass theory. It is worth mentioning here that the m^* in ω_p is the free-electron mass from states near the bottom of the s, p conduction band, whereas the curvature changes near interband transitions correspond to effective masses from the top of conduction band. Previous studies of the quantum-well states in Cu films deposited [198] on fcc Co(001) and Ag films on Fe(001) have shown an enhancement of the effective masses relative to free-electron mass as a function of the NM layer thickness. Such changes were attributed to strong modification in the Fermi surface crossings of the quantum well states by strong hybridization with the d bands of the FM layer [198].

However, the maximum GMR amplitude ($\approx 60\%$) at ambient conditions was observed in sputtered (polycrystalline) Co/Cu MLs [79] with (111) texture, rather than in Co/Cu(111) superlattices [172] grown by molecular beam epitaxy (MBE), which exhibit atomically smooth interfaces favoring the creation of discrete thin-film resonance states [169]. Photoemission experiments revealed [171] the spatial variation of the quantum-well wave function within a Cu(100) film and confirmed that the amplitude of these spin-polarized electron waves is modulated by an *envelope* function of longer wavelength. So far, a generalized [120] RKKY model uses such an *envelope* function with wave vector ($\mathbf{k}_{\mathrm{edge}} - \mathbf{k}_{\mathrm{F}}$) to reproduce the oscillatory GMR period observed in (100), (110), and (111) textured NM spacers. However, fcc NMs with (111) texture along the growth direction of the MLs present a more complicated case than NM(100). The problem with NM(111) is that for wave vectors $\mathbf{k}_{\mathrm{edge}}$, of s, p band edges close to the Fermi wave vectors $\mathbf{k}_{\mathrm{F}}$, there are no quantum-well states at the Fermi level when the parallel wave vector to [111] direction is $2\mathbf{k}^{\parallel} = 2(\mathbf{k}_{\mathrm{edge}} - \mathbf{k}_{\mathrm{F}}) = 0$ (at L critical point), while averaging over all finite $\mathbf{k}^{\parallel}$ the different periods compensate each other [169]. Thus, the disagreement between the observed and calculated (with RKKY theory) oscillatory period in fcc modulated Co/Cu MLs with (111) texture [120] is due to limited understanding of the properties of the spin-dependent electron confinement in these structures. The theory explains how [170, 199] spin-dependent electron confinement helps the formation of spin-polarized quantum-well states in NM(100) spacers. The spin polarization of NM(100) levels was explained in terms of the spin-dependent reflectivities at the FM–NM interface. For the high symmetry direction $\mathbf{k}^{\parallel} = 0$ (along the ΓX-direction) of fcc Co, the spin minority Δ_1 d band hybridizes with the s, p bands [169, 170] and creates a gap in the vicinity of E_{F}. This gap defines the degree of confinement of the quantum-well state in NM, where propagating waves will be reflected back into the spacer layer. Since for the majority band structure the hybridization gap is displaced to higher binding energies and the majority NM spin states in the vicinity of E_{F} become less

strongly confined, then the quantum-well states that survive in NM(100) carry minority spin.

In GMR MLs with NM(111) spacers, there are no spin-polarized quantum-well states [169] for $\mathbf{k}^{\parallel} = 0$ near the E_F at the L critical point. However, most important, there is no sd hybridization along the [111] direction as in Δ_1 d band of fcc Co(100). Thus, contrary to Cu/Co(100) layers, in the case of (111) texture there should not be quantum-well interference due to multiple electron reflections within the FM layer. Consequently, an increase of t_{Co} should affect in a different way the magnetotransport properties of the examined Co/Au and [134] Co/Cu MLs because the specular reflections of the electron waves on interface potential steps is reduced. The SE spectra as a function of t_{Co} provide experimental evidence for changes in N(E_F) (Fig. 23) and ω_p (Fig. 22) due to changes in Co layering [133, 157]. Such changes in Co layering can cause larger interface roughness, giving a significant contribution to interface resistance [200], that implies a smaller contribution from the interface potential steps and therefore smaller step heights for thicker Co layers. A semiclassical model, that solves the Boltzmann equation [180] taking into account spin-dependent electron scattering on impurities as well as on interfacial roughness, predicts a linear variation of the current-in-plane GMR with $\sin^2(\theta/2)$. Within the semiclassical approach [180], the angular variation of GMR always leads to linear dependence on $\sin^2(\theta/2)$ when either bulk or interface scattering is considered as the origin of the GMR effect. Thus, the observed quasi-linear decrease of GMR (Fig. 18) can be understood as a progressive increase of misalignment between the magnetic components of adjacent Co layers with increasing t_{Co}. The proposed angular dependence of GMR on t_{Co} is equivalent to contributions from biquadratic interlayer coupling, observed [131] in low-field GMR Co/Cu MLs due to a progressive increase of magnetic misalignment by changes in film morphology.

In conclusion, the use of SE has made it possible to measure the concerted action of the developed film morphology and the spin-dependent electronic structure at the Fermi level in fcc modulated Co/Au and Co/Cu MLs with (111) texture. In this way, common microstructural and electronic aspects that affect the dependence of the magnetotransport properties on t_{Co} were studied. Both, [158] Co/Au and [134] Co/Cu MLs exhibit a quasi-linear decrease of the GMR amplitude with increasing t_{Co}. In addition, an enhancement of the H_c and H_s values coincides with the t_{Co} range where the intra- and interband parameters in Figures 22 and 23 exhibit extrema. These results indicate that both, low-field GMR, Co/Cu and Co/Au MLs exhibit drastic changes in Co layering at $t_{Co} \approx 1.5$ nm. Since for larger t_{Co} values very small GMR amplitudes were observed, then the SE measurements determine the t_{Co} values where changes in Co layer roughness increase the interface resistance considerably. As a consequence, the smaller contribution from the interface potential steps reduces the spin-dependent scattering at interfaces and, within the limits of the semiclassical approximation [179, 180], drives an interchange of GMR contributions from interface to bulk scattering with increasing t_{Co}.

4.3.3. TEM in Co/Au MLs

Ultrathin magnetic layers or multilayered (MLs) structures composed of alternating Co and noble metals have attracted a great deal of interest because they exhibit perpendicular magnetic anisotropy [214, 215] and quantum size effects leading [79, 173] to GMR. Generally, the dependence of the film morphology on atomic-size mismatch effects at interfaces is of major importance for fundamental and technological reasons [79, 173, 214, 215]. In particular, the influence of a large deposit atom on small underlayer atoms, and vice versa, for two elements which are completely immiscible in the bulk has been largely investigated [196, 206, 214–217]. Especially, ultrathin Co/Au(111) layers and superlattices have shown a large diversity in magnetic domain sizes [214, 215] and related film morphology [196, 206, 216] that depend strongly on the deposition conditions used. It was observed [206, 196] that surface reconstruction of Au(111) influences the nucleation and the subsequent growth of Co layers. Thus, during growth on an Au(111) surface, depending on the stacking period of the close-packed planes, the Co structure can be either a hexagonal close-packed (hcp), a fcc, or a twinned fcc one. TEM and HREM studies of Co/Au MLs, grown by other techniques as for instance ultrahigh vacuum (UHV) physical vapor deposition or molecular beam epitaxy (MBE), have shown an hcp stacking of the close-packed Co planes [196, 206, 216, 218–222].

Traditionally, sputtering is a simple and rapid method for growth of polycrystalline thin films having a morphology that can easily be adjusted by the deposition conditions. However, it has been shown [156] that sputter-grown Co/Au MLs, with (111) texture, exhibit low-field GMR due to low magnetocrystalline anisotropy in Co layers. Analyses of their X-ray diffraction and ^{59}Co NMR spectra [133] provide indirect evidence that Co layers are severely expanded along the growth direction and exhibit an unusual Co stacking. A detailed study of the magnetotransport and optical properties [158] as a function of Co layer thickness has also revealed a significant change in the distribution of grain sizes with profound influences on the variation of the GMR effect.

A study of the film morphology and the Co crystal structure of the low-field GMR Co/Au MLs as a function of Co layer thickness, using TEM and high-resolution-electron-microscopy (HREM) has shown [157]:

(i) $[Co(1\ nm)/Au(2.5\ nm)]_{30}$ multilayers.

The $[Co(1\ nm)/Au(2.5\ nm)]_{30}$ MLs exhibit the maximum GMR ratio [156]. The growth of $[Co(1\ nm)/Au(2.5\ nm)]_{30}$ MLs on (001) Si, with an intervening 100-nm thick SiN_x buffer layer, is strongly textured with the (111) planes of Au oriented normal to the direction of growth, as in low-field GMR Co/Cu MLs [131]. The MLs exhibit a characteristic columnar mode of growth (Fig. 24a), with a highly twinned structure, where the twin planes are the (111) planes of growth [156]. The corresponding electron diffraction pattern of the MLs, in Figure 24b, shows reflections of the [011] and the [112] zone axes of Au and the [011] axis of the Si substrate, with the $11\bar{1}$ reflection of Au oriented exactly parallel to the 004 reflection of Si for

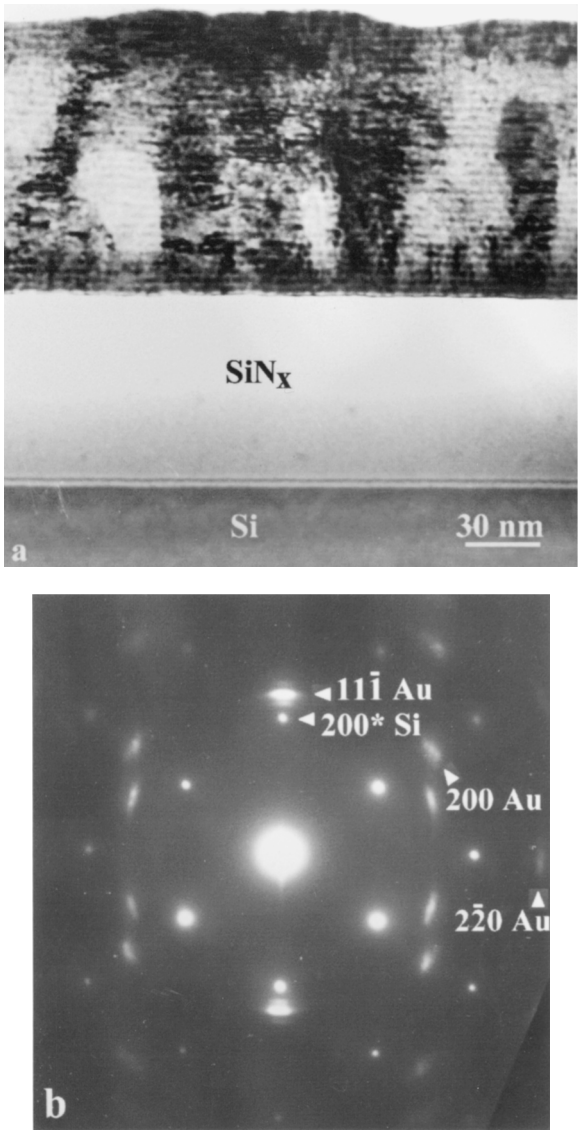

Fig. 24. (a) Bright-field (BF) TEM image illustrating the columnar mode of growth of the low-field GMR [Co(1 nm)/Au(2.5 nm)]$_{30}$ multilayers on an Si(001)/SiN_x substrate. The Co/Au layers appear as successive bright and dark bands, respectively. (b) Corresponding diffraction pattern where the twinning reflections reveal the existence of multiple twin planes, having as twin planes the (111) planes of growth. Reproduced with permission from [157], copyright 2000, Elsevier Science.

both zone axes of Au. These zone axes were observed in all diffraction patterns, which can easily be explained by considering the statistical distribution of the various orientations. Thus, within the large field of view of the selected-area aperture of the microscope, one always expects to find columns having these zone axes orientations. The arc-shaped intensity of the reflections arising from the MLs, as shown in Figure 24b, indicates that they consist of small misoriented grains within a range of 10°, whereas the satellite reflections around the fundamental 11$\bar{1}$ reflection of Au verify the overall modulated structure. The crystal structure of the MLs is rather homogeneous, since the columns grow unperturbed over many successive Co/Au layers or even from the bottom to the top surface of the MLs. From the diffraction patterns, the d spacing of the (111) planes of Au was found to be $d_{11\bar{1}}(\mathrm{Au}) = 0.229$ nm, which is smaller in respect to the bulk Au value of 0.2355 nm. In addition, the d spacing of the 200 reflection of Au was found to be $d_{200}(\mathrm{Au}) = 0.198$ nm, which is reduced by 2.5% relative to bulk Au value of 0.2039 nm. In addition, the interplanar spacing of the 2$\bar{2}$0 reflection of the [112] zone axis is $d_{2\bar{2}0}(\mathrm{Au}) = 0.141$ nm, contracted by 2.2% relative to its bulk value of 0.1442 nm. Since the $d_{11\bar{1}}$ spacing of Au is reduced by 2.8%, it is concluded that there is an almost isotropic volume contraction in the unit cell of Au, that is slightly higher along the normal to the close-packed planes of growth.

Dark field (DF) images, taken from a plan view specimen, reveal [157] that the typical columnar diameters are of the order of a few tens of nanometers while the corresponding diffraction pattern depicts the characteristic 2$\bar{2}$0 ring of polycrystalline Au, as was expected from the preferred orientation of growth. Another faint ring, closer to the central spot, with a measured d spacing of 0.249 nm has been indexed as the (1/3)4$\bar{2}$2 reflections of Au (theoretical value of $d = 0.2496$ nm). These reflections, although forbidden, often appear in gold crystals and their presence is due to twins and microtwins between the columnar grains, that are misoriented relative to the ⟨111⟩ direction of growth [220, 222] by 10 to 15°. It is worth noting, that the $d_{220}(\mathrm{Au}) = 0.144$ nm measured from the plan view diffraction pattern is very close to bulk value. This is due to strain relaxation inside the MLs, since the plan view specimens were perforated by ion milling and the substrate was completely removed in the transparent to the electron beam area of the specimen. However, no characteristic polycrystalline rings of hcp or fcc Co were identified in the diffraction patterns of the plan view specimens.

All of the foregoing, in conjunction with the absence of separate reflections from hcp or fcc Co in the diffraction patterns of the cross-section-TEM (XTEM) specimens, show that an average fcc lattice is formed throughout the columnar structure of the MLs and thus Co exhibits a cubic structure. Therefore, we concluded that Co layers were grown epitaxially over Au and that the d spacing of the (111) planes of Co, along the direction of growth, should be severely expanded to conform with the d spacing of the (111) planes of the average lattice, which is $\langle d_{111}\rangle = 0.229$ nm. In a first approximation, assuming that there are distinct nanocrystalline Co layers, the d_{111} of Co can be calculated from the expression $\langle d_{111}\rangle = \Lambda/(N_{\mathrm{Au}} + N_{\mathrm{Co}})$, where Λ is the bilayer thickness and N_{Au} and N_{Co} are the numbers of atomic planes of Au and Co per bilayer, respectively. Using $\Lambda = 3.5$ nm and $N_{\mathrm{Au}} = (2.5\ \mathrm{nm}/0.2355\ \mathrm{nm}) = 10.62$ atomic planes of Au in one bilayer, the expression gives an N_{Co} of 4.67 Co atomic planes and thus $d_{111}(\mathrm{Co}) = (1\ \mathrm{nm}/4.67) = 0.214$ nm, that is larger than the 0.205 nm of bulk fcc Co. The expansion of d_{111}(Co) spacing along the growth direction is 4.4% and induces severe strain in the Co layers, reducing the atomic density of Co. Since the data provide evidence for an epitaxial growth of Co on Au, then a volume expansion of the Co unit cell is expected, being more prominent along the growth direction.

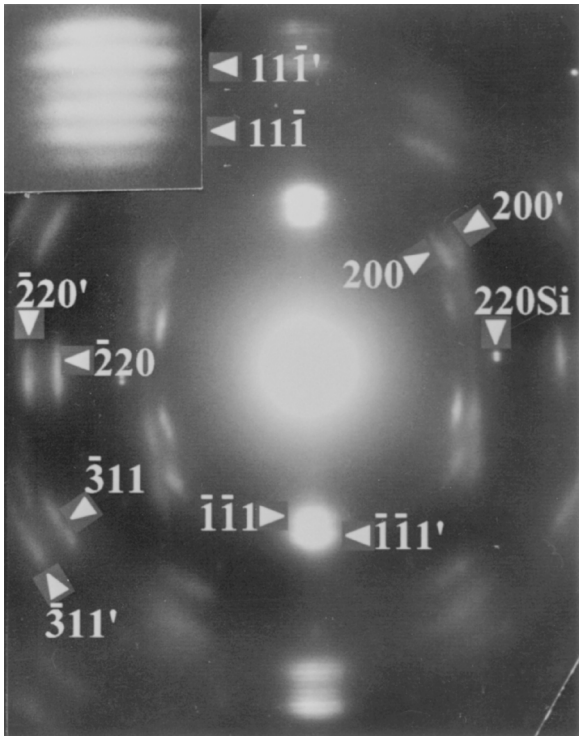

Fig. 25. Diffraction pattern from an XTEM specimen of [Co(3 nm)/Au(2.5 nm)]$_{30}$ multilayers sputter grown on an Si(001)/SiN_x substrate. Separate Co reflections (primed indices) are visible, aligned in parallel to Au reflections, that belong to the [011] and [112] zone axes. Twinning reflections of both elements are also aligned in parallel. Reproduced with permission from [157], copyright 2000, Elsevier Science.

(ii) [Co(3 nm)/Au(2.5 nm)]$_{30}$ multilayers.

The bright-field (BF) image has shown [157] that for [Co(3 nm)/Au(2.5 nm)]$_{30}$ MLs, with a Co layer thickness larger than an Au layer thickness, the samples exhibit a similar texture as in the previous case. A columnar and twinned, overall, structure is also observed here, with the same (111) twin planes. However, plan view micrographs have shown a bimodal distribution of grain sizes with a larger fraction of small grains relative to the previous case. In cross-section specimens, the electron diffraction pattern of the MLs (Fig. 25) contains reflections from the [011] and the [112] zone axes of Au and well-resolved reflections from Co, oriented exactly parallel to all the Au reflections. It was found that the value of $d_{11\bar{1}}$(Au) = 0.233 nm is much closer to the bulk value in contrast to the results of the previous case. The d spacing of the $\bar{2}20$ reflection was found to be $d_{\bar{2}20}$(Au) = 0.143 nm which is contracted by 1% from its bulk value. Thus, an isotropic volume contraction of an Au unit cell is still present.

To determine whether Co adopts an fcc or an hcp structure, the ratios of the relative distances from the central spot and the angles between the Co reflections were estimated. In this way, it is possible to distinguish whether the expanded d(Co) = 0.211 nm value of the first-order reflection, relates to the d_{111} of fcc Co (0.205 nm) or relates to the d_{0002} (0.2035 nm) of hcp Co. Since the Co and Au reflections are oriented in parallel, then the reflections of Co in Figure 25 can be assigned to the [011] and the [112] zone axes of cubic Co. In the first zone axis, the measurements give a relative ratio of 1.15 and an angle of 55° between the 200/11$\bar{1}$ reflections, which are very close to the theoretical 1.155 and 54.74° values. In the [112] zone axis, the relative ratios between the $\bar{2}20/\bar{1}\bar{1}1$ and the $\bar{3}11/\bar{1}\bar{1}1$ reflections are determined to be 1.64 and 1.93, respectively, in agreement with the theoretical values of 1.633 and 1.915. The measured angles are 90 and 59°, respectively, which are also in excellent agreement with the theoretical values of 90 and 58.52°. If the Co structure is hexagonal, the reflections of Co in Figure 25 should belong to the [01$\bar{1}$0] and the [2$\bar{1}\bar{1}$0] zone axes, taking into consideration an epitaxial growth. For the first zone axis, the theoretical distance ratio between the 2$\bar{1}\bar{1}$0/0002 reflections is 1.587. This ratio is far from the 1.64 measured value, although the angle between these reflections is 90° which matches the theoretical one. However, the measured distance ratio between the $2\bar{1}\bar{1}\bar{2}/000\bar{2}$ reflections is 1.93, instead of the theoretical 1.876 value, and the corresponding angle is 59°, instead of the theoretical 57.79° value. For the [2$\bar{1}\bar{1}$0] zone axis, a relative ratio of 1.15 and an angle of 55° are measured between the 01$\bar{1}$1/0002 reflections, whereas the theoretical values are 1.045 and 61.38°, respectively. The 01$\bar{1}$0-type reflections that belong to this zone axis could not be identified in the diffraction patterns.

A diffraction pattern from a plan view specimen has shown [157] that the $2\bar{2}0$ ring of polycrystalline Au with a $d_{2\bar{2}0}$(Au) = 0.143 nm is in agreement with that measured from cross-section specimens. This experimental value is still smaller than the theoretical value of 0.1442 nm. Thus, despite the perforation of the specimen, a partially relaxed state of Au layers is expected due to larger thicknesses of the MLs. Next to a $2\bar{2}0$ ring of Au, a fainter ring with d = 0.129 nm appeared, that was identified as the $2\bar{2}0$ ring of cubic Co (theoretical value $d_{2\bar{2}0}$(Co) = 0.1256 nm) by taking into account a moderate expansion of Co lattice parameters. If the Co structure is hexagonal, this ring should correspond to the $11\bar{2}0$ reflection of polycrystalline Co, having a theoretical $d_{11\bar{1}0}$(Co) = 0.1253 nm, close to the measured value as well. In that case, the viewing direction should lie parallel to the [0001] zone axis of Co, that includes the strong 10$\bar{1}$0-type reflections with a $d_{10\bar{1}0}$(Co) = 0.217 nm. However, no such ring is detected in plan view diffraction patterns. The appearance of the faint (1/3)$\bar{4}22$, 111, and 311 rings of Au can be explained again as in the previous case.

It is obvious from the electron diffraction analysis, that the experimental data are in agreement with the theoretical values only if the Co layers exhibit a cubic symmetry. Since the reflections of cubic Co are oriented exactly parallel to the corresponding reflections of Au, it is verified that Co layers grow epitaxially on Au. However, an average lattice cannot be considered when the Co layer thickness is close or is larger than the Au layer thickness, because the diffraction patterns show distinct Co reflections with d_{111}(Co) and d_{111}(Au) spacings close to their bulk values. The inset in Figure 25 shows an enlarged area of the diffraction pattern, where the satellite reflections arising from the bilayer modulation can be resolved next to the

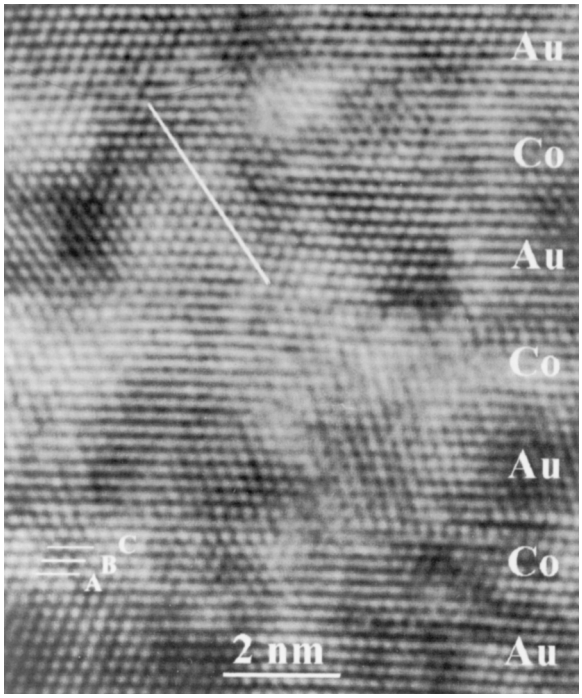

Fig. 26. High-resolution TEM image of the low-field GMR $[Co(1\ nm)/Au(2.5\ nm)]_{30}$ multilayers, illustrating the ABCabc stacking sequence of the closed-packed planes in Co layers. The white inclined solid line depicts the trace of a $(\bar{1}11)$ plane that transverses successive Au and Co layers without any change in orientation. Reproduced with permission from [157], copyright 2000, Elsevier Science.

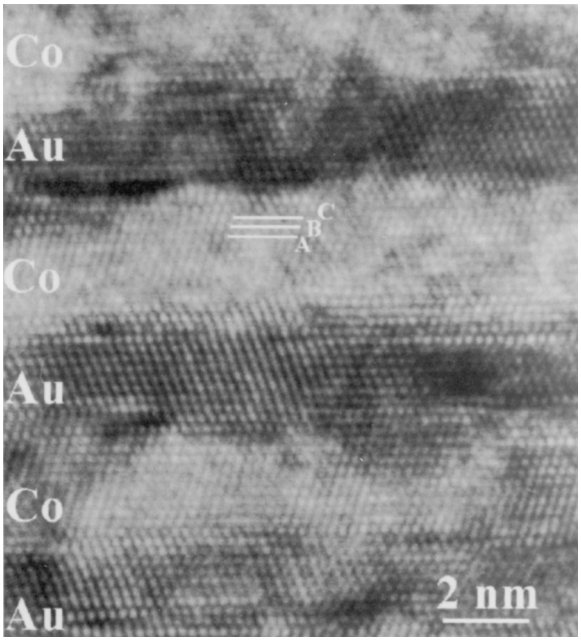

Fig. 27. High-resolution TEM image of the $[Co(3\ nm)/Au(2.5\ nm)]_{30}$ multilayers, where the ABCabc stacking sequence of the closed-packed planes in Co layers indicates the formation of fcc Co during growth. Reproduced with permission from [157], copyright 2000, Elsevier Science.

first-order $11\bar{1}$ reflections of Au and Co. As mentioned earlier, the d spacing of (111) Co planes along the growth direction was found to be 0.211 nm, that is expanded by 2.9% relative to the corresponding bulk value. In addition the d_{220} of Co is 0.129 nm, expanded by 2.7% relative to its bulk value. Thus, a volume expansion of the Co unit cell is detected, that is slightly higher along the normal to the close-packed planes of growth, but overall can be considered as isotropic expansion. The Co lattice expansion is reduced as the Co layer thickness increases and the strain is gradually relaxed.

(iii) The growth process.

To understand the growth process of the MLs deposition, HREM observations were performed on both types of specimens. These observations were performed at the same orientation as the conventional TEM observations. Two typical cases are presented in Figures 26 and 27. As seen from both HREM images, the growth of Co progresses with a stacking sequence of close-packed planes which are oriented parallel to the surface of the substrate successively with the (111) planes of Au. The MLs structures contain planar defects, as stacking faults and twin boundaries, that are mostly lying parallel to the planes of growth. The existence of these planar defects within the Co layers can modify the stacking sequence of the close-packed planes and are expected to alter the stacking along the direction of growth from fcc to hcp and vice versa. However, this phenomenon will be localized in the defected area only and, generally, is not expected to influence the observed long-range fcc symmetry inside the Co layers.

As illustrated in Figure 26, the observed stacking sequence in the undefected areas of both Co and Au layers of the $[Co(1\ nm)/Au(2.5\ nm)]_{30}$ MLs is ABCABC and the d spacings of the (111) planes of Co and Au are more or less the same, indicating a large expansion of the d_{111}(Co) relative to its bulk value. The white inclined solid line depicts the trace of a $(\bar{1}11)$ plane that transverses successive Au and Co layers without any change in orientation. This observation supports the results of the electron diffraction analysis, concerning the existence of an average fcc lattice in these types of MLs. As shown in Figure 27, the stacking sequence of close-packed planes in Co layers of the $[Co(3\ nm)/Au(2.5\ nm)]_{30}$ MLs is also ABCabc, indicating the formation of fcc Co during growth. However, the d_{111}(Co) here is less expanded relative to its bulk value, whereas d_{111}(Au) is rather close to its corresponding bulk value. This observation also supports the electron diffraction results and excludes the existence of an average lattice in these types of MLs.

As in Co/Cu MLs, magnetron sputtering has been successfully used to produce high-quality thin Co/Au MLs. These MLs present a well-defined layered morphology, exhibiting textured columnar growth with a twinned crystal structure. For Co layer thicknesses of 1–3 nm and constant Au layer thickness of 2.5 nm, the Co layering corresponds to fcc stacking epitaxially grown on the (111) planes of Au. However, depending on the Co layer thickness, an important difference in the structure was verified. In thinner (1 nm) Co layers, an expanded fcc lattice is obtained, while the Au lattice is compressed. In this case, both

materials tend to form an average fcc lattice with an interplanar spacing along the growth direction closer to Au d spacing. For thicker (3 nm) Co layers an expanded fcc lattice occurs as well, but in this case the expansion is significantly reduced and the Au lattice is only slightly contracted. No average lattice is formed in this case and along the growth direction both elements exhibit interplanar spacings closer to their bulk values.

4.4. Spin-Echo ^{59}Co NMR Used for Nondestructive Evaluation of Co Layering

4.4.1. Changes in NMR Spectra Due to Structural Modifications in Sputter-grown Co/Au and Co/Cu Multilayers

Spin-echo ^{59}Co nuclear magnetic resonance (NMR) has proved [38] to be a powerful method that distinguishes the components from the interfaces and the bulk Co layer [202] and provides information about the local Co atomic packing in multilayered structures. Since the NMR spectra of sputtered GMR Co/Cu MLs have been studied extensively [38, 202], resulting in a unique assignment between the spectral lines and the corresponding Co stacking, we decided to investigate the ^{59}Co NMR spectra of these, low-field GMR, Co/Au MLs in comparison with spectra obtained from Co/Cu MLs as well. The developed Co layering deserves further investigation because it is relating a kinetically grown Co layer structure with possible GMR applications of Co/Au MLs. To indirectly probe the local structure differences in the Co layers of low-field GMR Co/Cu and Co/Au MLs as a function of t_{Co}, complementary information from ^{59}Co NMR and X-ray diffraction (XRD) measurements has been employed [133].

A thorough examination of the structural, magnetotransport and optical properties of the Co/Cu specimens is given in Ref. [134]. For the Co/Cu MLs, the estimated t_{Co} values, obtained from X-ray reflectivity spectra [134], are: 0.78, 1.26, 1.74, 2.37, and 3.12 nm while a $t_{Cu} \approx 2.1$ nm is found for all the samples. In Co/Au MLs, the layer thicknesses were estimated by fitting the measured XRD intensities with the superlattice refinement (SUPREX) program [228]. The resultant t_{Co} values are: 1.24, 1.56, 2.05, 2.46, and 3.11 nm while a $t_{Au} \approx 2.4$ nm is found in all the Co/Au samples. Typical Co/Au XRD profiles are shown in Figure 28. Asymmetric peak intensities are observed below and above the zero-order reflections, that are indexed to (111) fcc Bragg peaks. A superlattice refinement (SUPREX) fitting has shown that [133]:

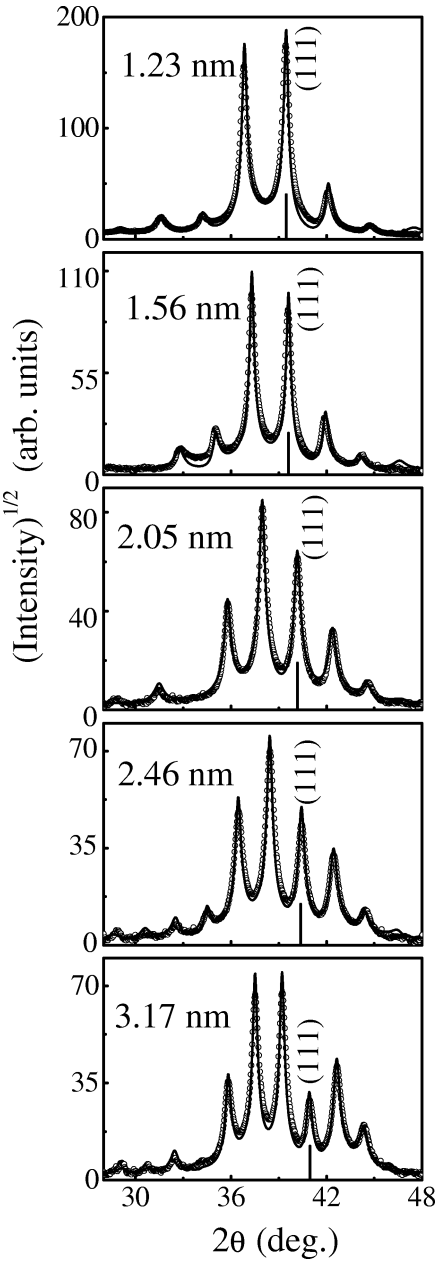

Fig. 28. Plots of medium angle XRD patterns (points) and the corresponding fitting curves (solid line) obtained from the SUPREX analysis of low-field GMR [Co(t_{Co})/Au(2.5 nm)]$_{30}$ multilayers. The obtained Co layer thicknesses t_{Co} are displayed. The position of the zeroth-order reflection, indexed to the (111) fcc Bragg peak, is marked with a bar. Reproduced with permission from [133], copyright 1999, The American Physical Society.

(i) The average, out of film plane, d_{111}-spacing distances of Co and Au layers are expanded relative to bulk (Fig. 29 top). Thus, the obtained d_{Au} parameter is about 0.237 nm while the d_{Co} values scale linearly between 0.208 and 0.214 nm. Comparatively, the corresponding bulk value for fcc Au is $d_{111}^{Au} = 0.2355$ nm, the bulk value for hcp Co along the [0001] direction is $d_{0002}^{Co} = 0.2023$ nm, and the bulk value for fcc Co is $d_{111}^{Co} = 0.2047$ nm. The results in Figure 29 indicate that the strains mostly affect the Co layer structure while the Au layering is unaffected from changes of t_{Co}. The remarkable Co lattice-spacing expansion, that is about 0.04–0.1 nm greater than the bulk fcc or hcp Co values, shows that their layer structure is severely truncated along the growth direction.

(ii) The obtained interface roughness (Fig. 29 middle) remains unchanged in the Au layer and is equal to the d_{Au} (about 0.237 nm).

Comparatively, Figure 30 shows a high magnification TEM image of the low-field GMR [Co(1 nm)/Au(2.5 nm)]$_{30}$ mul-

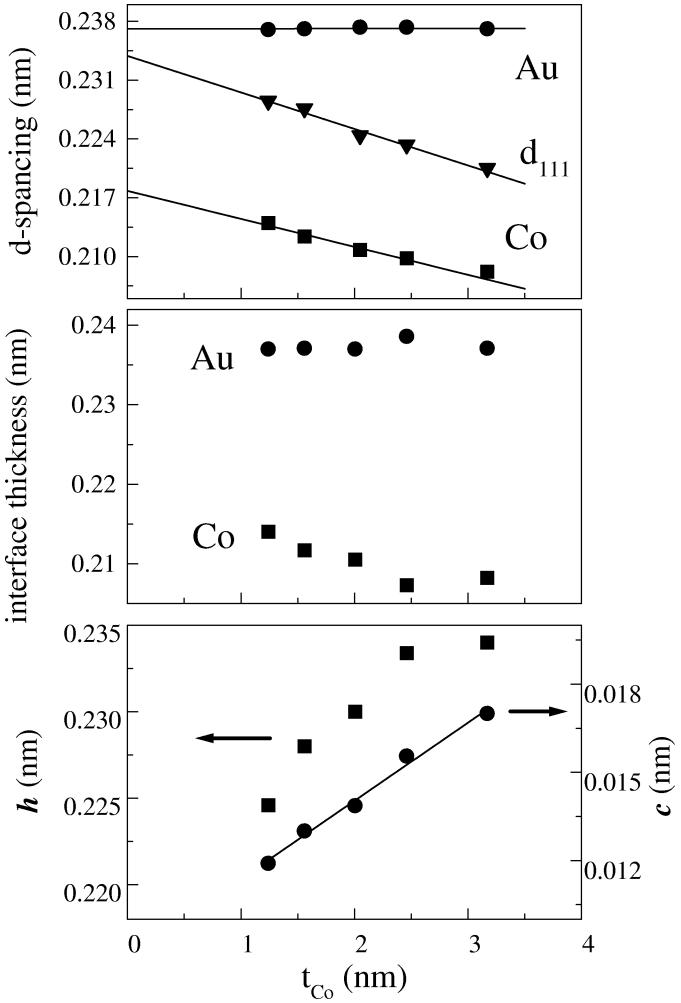

Fig. 29. In low-field GMR [Co(t_{Co})/Au(2.5 nm)]$_{30}$ multilayers the variation of d_{111} spacings and the obtained d_{Au}, d_{Co} as a function of Co layer thickness t_{Co} is shown on top. The variation of the estimated interface roughness t_i for every Co and Au layer is plotted in the middle. The obtained changes for the interface distance h (left axis) and the interface fluctuation width c (right axis) with t_{Co} are shown in the bottom plot. Reproduced with permission from [133], copyright 1999, The American Physical Society.

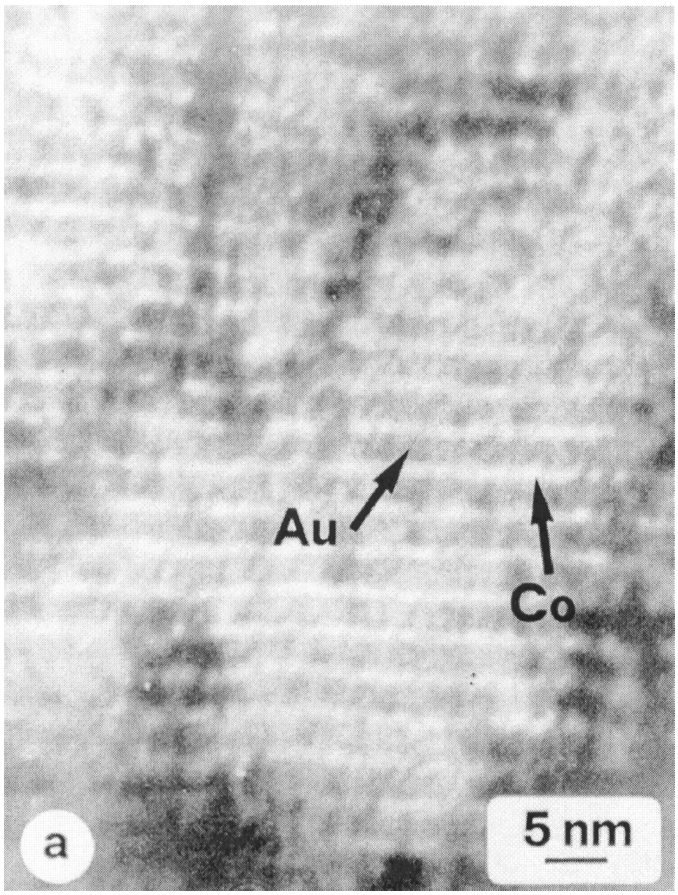

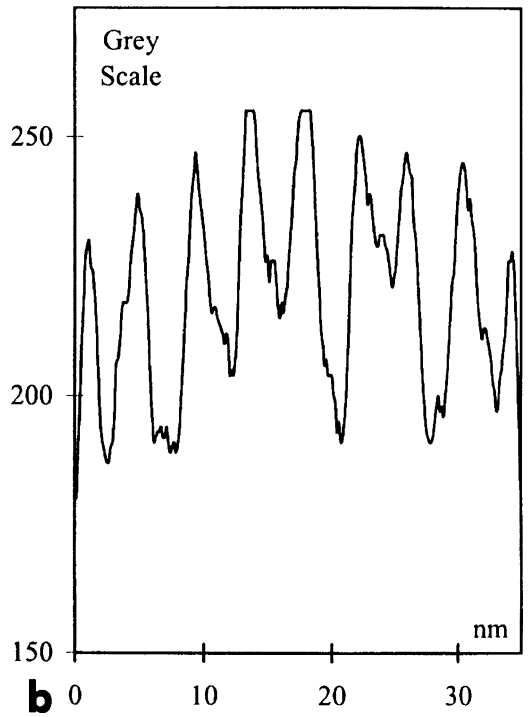

Fig. 30. (a) A high magnification TEM image of a multilayer area showing the morphology of the Co/Au interlayer. (b) A line profile showing the contrast variation across a series of nine successive bilayers. Reproduced with permission from [156], copyright 1998.

tilayers, depicting the morphology of the Co/Au multilayers. A line contrast profile shows the sharpness of Co/Au interfaces across a series of nine successive bilayers.

In contrast to experimental techniques that measure macroscopic properties, zero-field NMR probes the local magnetic environment of the resonating nuclei through the hyperfine field, $B_{hf} = (2\pi/\gamma h)A\langle S\rangle$, A and $\langle S\rangle$ being the hyperfine coupling constant and the average electronic spin, respectively. Thus, NMR is very sensitive to atoms in the first neighbor shell and probes the local environment—the kind and the number of atoms—in the nearest neighbor (nn) shell as well as interatomic distances. It is well established that Co in a regular closed-packed environment [160] has the NMR frequency of 217 MHz for the fcc stacking and 220–226 MHz for the hcp. This frequency can be slightly shifted if a strain is present in a sample [161] but a fingerprint of a purely Co environment remains a well-resolved, relatively narrow line. Such a line, cor-

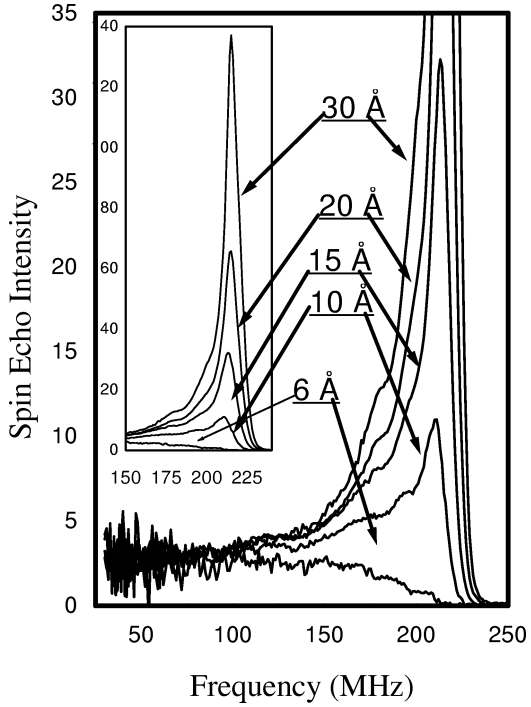

Fig. 31. Spin-echo ^{59}Co NMR spectra in low-field GMR $[Co(t_{Co})/Cu(2.1\ nm)]_{30}$ multilayers at 4.2 K. The integral spectra intensity is normalized to the sample area and reflects the intensity variation with Co layer thickness. The hyperfine frequency range is chosen to present the details of the interface part. The inset shows the details of the bulk part. Reproduced with permission from [133], copyright 1999, The American Physical Society.

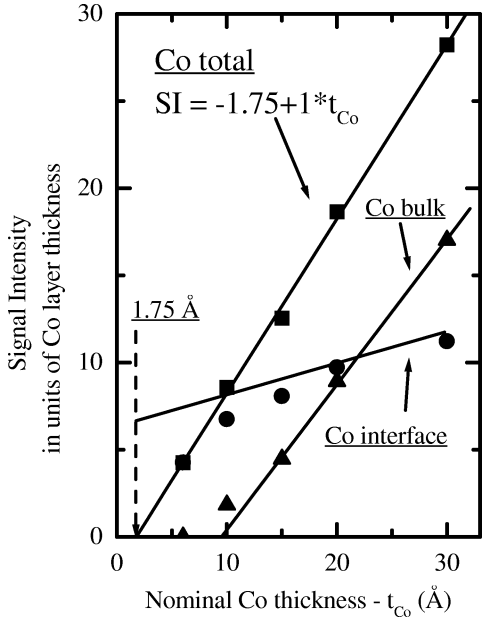

Fig. 32. The variation of signal intensity, obtained from the interface (circles) and bulk (triangles) components of the Co/Cu NMR spectra (Fig. 31), is plotted as a function of nominal t_{Co}. The intercept of the extrapolated bulk line indicates that about 1 nm of deposited Co atoms per layer is involved in the interface signal. The plot representing a sum of the bulk and interface signal intensity (squares) extrapolates to zero at about 0.175 nm. Reproduced with permission from [133], copyright 1999, The American Physical Society.

responding to the "bulk" of the Co layer, is clearly visible in all the recorded spectra from the Co/Cu MLs with $t_{Co} \approx 1$ nm. The bulk line is fully demonstrated in the inset of Figure 31, where its frequency position is slightly below the regular non-strained fcc Co line (212–216 MHz). The lack of structure on the high-frequency side of this peak indicates that there is no significant presence of hcp admixture. According to previous studies [160], it is assumed that each Cu atom introduces a downshift of the NMR frequency by 16 MHz as an nn in a Co host. Thus, the extended tail on the low-frequency side of the main Co line intensity can be assigned to Co atoms located at the Co/Cu interfaces. Figure 31 shows details of the spectrum that exhibit the characteristic features [202] emanating from a Co–Cu interface mixed over several atomic layers.

A coarse estimate of the Co content in the interface region can be made by plotting the variation of signal intensity in the two respective parts of a spectrum with the nominal t_{Co} (Fig. 32). The lower frequency limit for the bulk part has been taken at 205 MHz. The intercept of the extrapolated bulk line indicates that about 1 nm of deposited Co atoms per layer are involved in the interface signal. However, the interface line has a cutoff at a lower value, suggesting that some intensity from the interface is missing due to a nonmagnetic or a very weakly magnetic, fraction of Co atoms. In Figure 32, the sum of bulk and interface signal intensity extrapolates to zero at about 0.175 nm. This indicates that about one atomic plane of deposited Co per Co layer becomes nonmagnetic. A detailed analysis of the spectra, discussed as follows, shows that the local Co concentration that is involved in the nonmagnetic interface layers is less than 20%. Since cross-section TEM images [131] clearly show the Co/Cu multilayer stacking in the columnar grains, a detailed analysis of the interface structure has been performed by assuming symmetric interfaces, using the spectrum modeling procedure described in previous studies [202, 203]. In Figure 33, an example of spectrum decomposition into the hypothetical subspectra computed for each atomic layer in the interface is shown. A bulk Co line can be fitted at 214 MHz (strained fcc Co) as well as a broad line at 205 MHz corresponding to the grain boundaries. The obtained average concentration profile for one bilayer is plotted in Figure 34 for the sample with $t_{Co} = 1.5$ nm, indicating CoCu intermixing due to interdiffusion at their boundaries. However, the absence of a bulk Co signal for $t_{Co} < 1$ nm (Fig. 31) shows that Co does not grow in three-dimensional islands (discontinuous layers) but grows in the layer-by-layer mode, because the Co atoms inside the clusters will give rise to bulk Co NMR intensity in the case of island formation.

A closer examination of the spectra in Figure 31 reveals that with increasing t_{Co} a modification of the interface structure takes place in the frequency range above 150 MHz. This is reflected in the hyperfine field distribution that has been averaged over the entire film volume, implying that internal stresses enhance the interface roughness for thicker MLs. To examine this effect, NMR measurements were performed in three Co/Cu

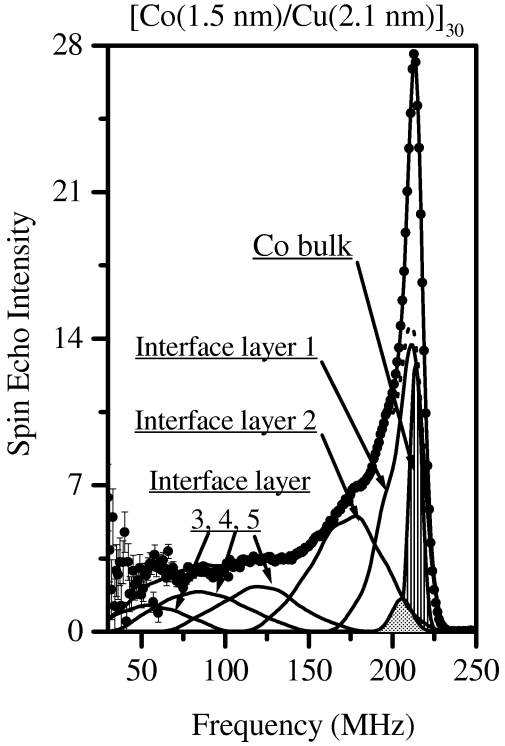

Fig. 33. Experimental and fitted NMR spectrum showing the interface layer contributions and the bulk component (shaded area) from the contribution of the fcc-Co phase. One component corresponding to the grain boundaries is added with a broad line at 205 MHz. Reproduced with permission from [133], copyright 1999, The American Physical Society.

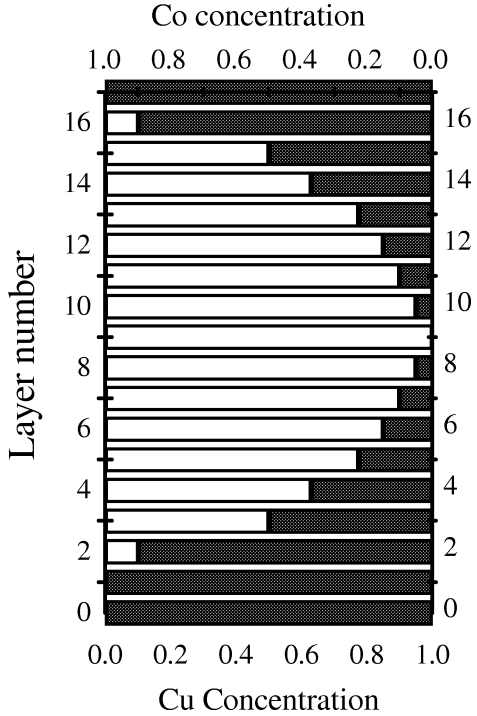

Fig. 34. Average concentration profile for the Co/Cu bilayer obtained from the analysis of the NMR spectrum (Fig. 33) in $[Co(1.5\ nm)/Cu(2.1\ nm)]_{30}$ multilayers. The dark levels show the Co percentage per atomic plane. Reproduced with permission from [133], copyright 1999, The American Physical Society.

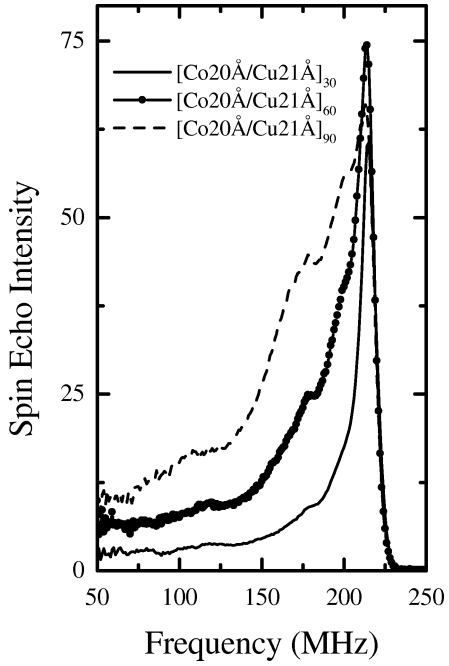

Fig. 35. Experimental NMR spectra from three Co/Cu samples with the same Co and Cu layer thickness but a different number of bilayers. As shown, the relative signal intensity from the interface part of the spectrum grows significantly as the number of bilayers increases. Reproduced with permission from [133], copyright 1999, The American Physical Society.

samples with a different number of bilayers and the same layer thicknesses. As shown in Figure 35, the relative signal intensity from the interface part of the spectrum is growing larger with the number of bilayers rather than with increasing t_{Co} for a constant number of bilayers. Consequently, it may be inferred that an additive Co layer roughness evolves from the bottom to the top of the Co/Cu MLs due to development of internal stress gradients with increasing film thickness.

In Figure 36, the Co/Au MLs exhibit totally different NMR spectra from those observed in GMR Co/Cu MLs [202–204], showing one striking feature that is distinct from all the known NMR spectra in Co-based MLs. Practically there is no resolved bulk Co line even for t_{Co} as thick as 3 nm. This feature is best displayed in Figure 37, where the NMR spectra of Co/Au MLs are compared with the corresponding spectra of Co/Cu MLs for $t_{Co} = 1$ and 3 nm. Thus, it is evident that in these, low-field GMR, Co/Au MLs there is no regular Co environment [156, 158] with 12-Co neighbors located at distances characteristic to the close-packed structures (hcp or fcc). A strong modification of the intralayer Co structure has to be introduced to explain the large distribution of hyperfine fields in the NMR spectra.

As a first source, it is reasonable to assume that an amorphous-like (topological) disorder can be induced in the Co layers due to a large (15%) lattice mismatch between Co and Au. However, the observed [205] NMR spectra of amorphous CoM alloys (M-metalloids like B, P, C) exhibit a well-resolved Co line, corresponding to Co atoms surrounded only with Co nn. The frequency of this line is about 220 MHz, close to that of crystalline Co, and is relatively narrow in contrast to the

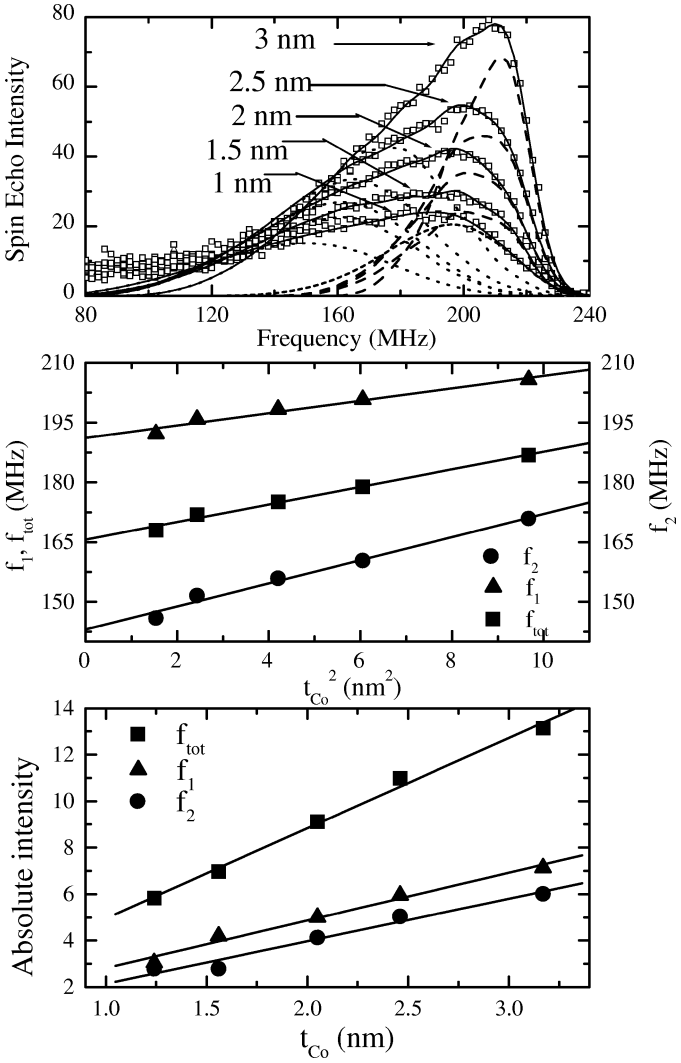

Fig. 36. The experimental (points) and calculated ^{59}Co NMR spectra from low-field GMR [Co(t_{Co})/Au(2.5 nm)]$_{30}$ multilayers at 4.2 K are shown on the top plot. The spin-echo intensity is normalized to the sample area. The obtained frequency positions for the high- (f_1), low- (f_2) frequency zones, and their average frequency (f_{tot}) are plotted in the middle as a function of t_{Co}^2. The integrated intensities for the high- (f_1), low- (f_2) average frequency (f_{tot}) zones are plotted as function of the nominal t_{Co} (bottom). Reproduced with permission from [133], copyright 1999, The American Physical Society.

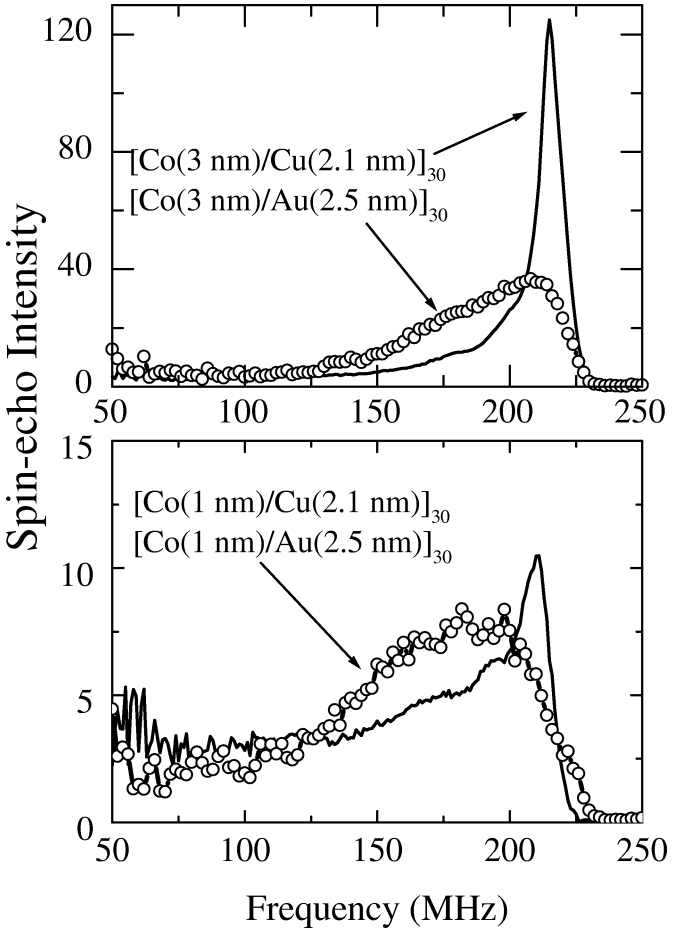

Fig. 37. Comparison of ^{59}Co NMR spectra between Co/Au and Co/Cu multilayers $t_{Co} = 1$ and 3 nm, respectively. Reproduced with permission from [133], copyright 1999, The American Physical Society.

broad and asymmetric line observed (Fig. 36) in the low-field GMR Co/Au MLs. Thus, a glassy disordering, corresponding to isotropic and homogeneous atomic density of amorphous materials, cannot explain the observed NMR spectra.

A second source of structural disorder may arise from a significant doping (intermixing) of Co layers with: (i) Au atoms due to interdiffusion and (ii) other impurities (like Co oxides) from a dirty sputtering chamber. This possibility has been investigated with two Co-rich films, grown under the same deposition conditions: one with a pure Co(60 nm) layer and a second Co(60 nm)/Au(20 nm) film, where the Co layer is protected from oxidation by depositing a Au layer on top. XRD patterns from the as-deposited Co(60 nm) film revealed a broad diffraction feature located (Fig. 38 top) near the fcc and hcp Co Bragg peaks with Miller indices (111) and (200). However, in Co(60 nm)/Au(20 nm) the XRD spectra exhibit an intense fcc (111) Au peak and the subsequent (222) fcc peak, indicating that the top layer of Au is (111) textured. Postannealing of the as-deposited Co(60 nm)/Au(20 nm) film at 650 °C for 4 h and postannealing of the Co(60 nm) film at 450 °C for 24 h, led to recrystallization of the Co layer in the fcc phase (Fig. 37 top). The NMR spectra from the as-deposited and postannealed Co(60 nm)/Au(20 nm) and Co(60 nm) films are shown in Figure 37. In addition, the XRD (Fig. 28) and cross-section Figure 30 TEM measurements [156, 157] provide evidence for a well-defined multilayer structure, indicating that an extended doping or Co–Au intermixing is very unlikely.

To fit the NMR spectra, a model with two spectral components, called "zones," was considered. The component at lower frequencies takes into account the observed intensity from the interfaces, with at least 3 Au nn, whereas the bulk Co layer, with 12 Co nn, corresponds to a high-frequency range. The line broadening in every component was approximated by introducing the concept of magnetic vacancies. As in Co/Cu MLs, a magnetic vacancy at the nn shell of Co is assumed to cause

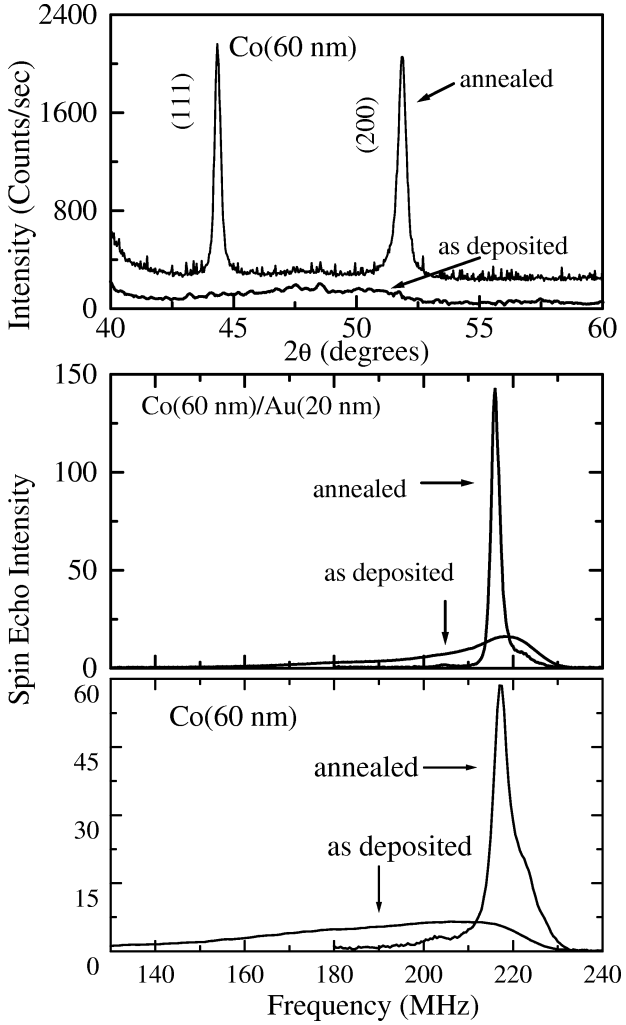

Fig. 38. Typical XRD spectra from the as-deposited and postannealed Co(60 nm) film are shown on the top. The bottom and middle figures show the NMR spectra from the as-deposited and postannealed single layer Co(60 nm) and Co(60 nm)/Au(20 nm) films, respectively. Reproduced with permission from [133], copyright 1999, The American Physical Society.

a frequency downshift of 16 MHz. The observed line broadening was calculated for every component by considering a random distribution of magnetic vacancies in the nn shell of Co that produces a binomial distribution of intensities. In this model, the fitting parameters were the magnetic vacancy concentration and the relative intensities of the respective spectral components. The agreement between experimental and calculated NMR spectra is shown in Figure 36 (top).

The possibility to study the strain of Co with NMR arises from the dependence of the hyperfine field on the atomic distances. In magnetic solids, the influence of the local structure and the symmetry on B_{hf}, the effective hyperfine field sensed by the nuclear spin, arises from two effects: the sensitivity of the transferred hyperfine interaction to the local environment and the dependence of the orbital and the atomic dipolar part of B_{hf} on the local symmetry. These features enable one to discriminate between fcc, bcc, and hcp phases, or stacking faults in the pure phase, through the magnitude of B_{hf}, and between fcc, hcp, and trigonal or tetragonal deformed fcc through its anisotropy [159, 160]. Furthermore, since the B_{hf} is mainly the result of a delicate balance between the spatial distribution of the spin-up and spin-down electrons, it is also sensitive to distortions of these spatial distributions [161] (strain effects). Since in Co/Au MLs the linewidth of the bulk Co component broadens significantly by decreasing t_{Co} (Fig. 36 (top)), then a strain gradient would exist within the Co layer, because the strain induced shift is of the same order as the linewidth. Incoherent Co/Ag and Co/Cu MLs exhibit a [161] shift of B_{hf} with t_{Co} that is proportional to the strain (ε) in the interface plane ($B_{\mathrm{hf}} \sim \varepsilon$) and that is inversely proportional to t_{Co} ($B_{\mathrm{hf}} \sim 1/t_{\mathrm{Co}}$). A meaningful relation between these parameters shows that the average frequencies, f_1 (high frequency) and f_2 (low frequency), scale linearly with t_{Co}^2 (Fig. 36 middle) in Co/Au MLs. Thus, the variation of f_1 and f_2 frequencies does not follow the observed [161] $1/t_{\mathrm{Co}}$ dependence for completely incoherent MLs.

Usually, strain gradient in a film is initiated from internal stress variations as we move from the interfaces toward the middle of a layer. Such a case can be realized in a layer-by-layer mode of growth where the film is subjected to a change of interfacial stress from the bottom to the top. In Figure 36, the variation of NMR intensity as a function of t_{Co} resembles the dependence of the interface distance h parameter (Fig. 29). This may imply that either the assumed concentration of magnetic vacancies originates from misfit dislocations at the Co/Au interfaces or the excessive internal strain exists along the growth direction of Co. Thus, the first one is expected to increase while the second one is expected to relieve strain energy in some way for thicker t_{Co}. Comparatively, previous studies [206] indicate that in semicoherent Co/Au(111) interfaces a large concentration of misfit dislocations appear inside the entire Co layer volume, whereas Co layers on Ag(111) exhibit misfits only near the Co/Ag interface. Additionally, it was shown [206] that magnetic anisotropy is very sensitive in such types of changes at the Co/Au interfaces and the Co layer structure. Furthermore, an NMR study performed [207] in thin Co films grown by molecular beam epitaxy reveals a dependence of the structural phase composition on the substrate and the growth temperature used, which alter significantly the macroscopic magnetic properties.

The observed NMR spectra indicate that Co grows pseudomorphically [208] in the fcc phase between the Cu layers, while in as-made Co/Au MLs a metastable nanostructure of Co is generated. Generally, the major difference between the Co/Cu and Co/Au MLs is the lattice mismatch of the constituent elements along the $\langle 111 \rangle$ direction of growth. This is about 2% for Co on fcc Cu and about 15% for Co on top of fcc Au. In sputtered Co/Ag MLs—that exhibit a 14% lattice mismatch as well—it is observed [159] that Ag forms bridges and discontinuous Co layers for $t_{\mathrm{Co}} < 1.5$ nm. In addition, sputter-grown $Ni_{81}Fe_{19}$/Ag MLs [209, 227] deposited above 300 K and Co layers doped with small amounts of Ag form discontinuous layers and immiscible solid solutions with the Co host, respectively. Conversely, formation of Co–Cu solid solutions [210, 211] and metastable phases [212] were reported in thin films

and nanocrystalline particles. Since the Co/Cu and Co/Au MLs were grown under exactly the same deposition conditions, the deformed Co layer structure in Co/Au MLs can be attributed to: (i) The frequently observed stacking faults in Co films [213], arising from the negligibly small difference in free energy between the fcc and hcp packing in two dimensions. (ii) The large lattice mismatch between Co and Au. (iii) The unique ability [196] of the Au(111) surface to reconstruct during growth of Co layers on Au.

Thus, structural information obtained from XRD data analysis can be used complementary with NMR spectroscopy to indirectly probe the local structure differences in multilayers with magnetic Co layers. Specifically, while the NMR spectra in Co/Cu MLs reveal an fcc Co layer stacking, the low-field GMR Co/Au MLs exhibit a broad distribution of magnetic hyperfine fields that cannot be assigned to any of the known Co structures. Analysis of the Co/Au superlattice reflections from the XRD patterns indicates that the Co layers expand significantly along the growth direction relative to the close-packed lattice values, with the larger expansion confined to thinner Co layers. This Co layer lattice expansion induces a reduced density and the resultant distribution of internal stresses is reflected in the NMR spectra.

4.4.2. The Effect of Annealing on the NMR Spectra of Co/Au MLs

Rapidly quenched $Co_{1-x}Au_x$ films [96] form a typical phase separation system, which can be a reference for the study of amorphous-crystalline transformations after annealing. According to the so-called Ostwald rule [96], heat treatment of quenched $Co_{1-x}Au_x$ films produces transformations from the less stable state, with increased Au–Co atomic solubility in amorphous or single-phase metastable matrices, to a two-phase equilibrium fcc state through a succession of intermediate metastable phases of increasing stability. Thus, heating of amorphous Co–30Au films [96] above 150 °C resulted in an irreversible change from the amorphous structure to a single metastable fcc crystalline structure, which subsequently decomposed into equilibrium Au and Co fcc structures above 300 °C. Practically, it is important that annealing of Co–Au thin films or MLs required [96, 151, 152] only 10 to 60 min to complete structural transformations between 200 and 300 °C, whereas in bulk $Co_{1-x}Au_x$ alloys the microstructural changes continue as a function of aging time [154, 155] up to few days.

This phase separation process is applied to cosputtered [151] $Co_{1-x}Au_x$ thin films or rapidly quenched ribbons to engineer their magnetotransport properties after annealing. Heat treatment of Co/Au multilayers (MLs) at 300 °C revealed [152] a controllable way, with a profound technological impact in magnetic-storage applications, to change the magnetic anisotropy of Co by sharpening the Co/Au interfaces. However, the observed structural transformations in the Co–Au phase diagram of $Co_{1-x}Au_x$ thin films [96, 151], multilayers [152] and rapidly quenched ribbons [154, 155] have been identified by standard X-ray scattering and electron microscopy techniques, but not with spin-echo ^{59}Co NMR measurements.

The observation [156, 158] of low-field GMR in sputter-grown Co/Au MLs has initiated the study [133, 157] of Co layering in these MLs. Investigation of the as-made [Co(1 nm)/Au(2.5 nm)]$_{30}$ MLs, which exhibit the maximum [158] GMR effect, with conventional and high-resolution TEM has shown [157] that the Co layer structure mainly adopts an expanded fcc lattice *without misfit dislocations and* Co–Au *alloying* (without excluding dilution-partial intermixing at the interfaces). These measurements show that the Co lattice is expanded by 4.4% relative to the known closed-packed Co. Remarkably, ^{59}Co NMR spectra of the as-made MLs have revealed [133] a unique profile that could not be assigned to any of the known bulk crystalline or glassy Co structures. In addition, NMR measurements have been used as the microscopic technique to investigate [153] the effect of postannealing on the microstructure of the as-made [Co(1 nm)/Au(2.5 nm)]$_{30}$ MLs.

Six separate MLs of [Co(1 nm)/Au(2.5 nm)]$_{30}$ were grown on Si(100)/SiN_x(70 nm) substrates that were thermally isolated from the water cooled supporting table during deposition. The amorphous SiN_x buffer layer provides an atomically smooth surface where the (111) texture adopted (Fig. 39) by the Co/Au MLs is not induced by the substrate [157]. Five samples were postannealed separately inside the deposition chamber at 200, 300, 350, 400, and 600 °C for 1 h.

Figure 39 shows the low-angle superlattice Bragg peaks and the grouping of the satellite peaks around the zeroth-order (111) peak, from the average (overall) out-of-plane lattice spacing. The low-angle XRD spectra reveal that the multilayered structure persists up to 400 °C. It is worth mentioning that the XRD spectra (Fig. 39) remain the same for longer postannealing times (up to 24 h) at 200 and 300 °C. The observed strong intensity of the superlattice peaks after annealing at 200, 300, and 350 °C can be attributed [152] to interface sharpening. The medium angle spectra show that at 350 °C an extra phase of pure Au coexists with the MLs whereas at 400 °C the layered Co/Au structure is significantly suppressed, exhibiting an almost complete decomposition into Au and Co crystallites. Although the (200) Bragg peak of Au ($d_{200} = 0.2038$ nm) cannot be resolved from the (111) peak of fcc Co ($d_{111} = 0.2047$ nm) or the (0002) peak of hcp Co ($d_{0002} = 0.2023$ nm), the observed peak intensity above 350 °C (centered at $2\theta = 44.404°$ or d spacing $= 0.20385$ nm) indicates that the diffracted intensity from Co crystallites exhibits a vast peak broadening. Since at 400 °C (Fig. 39) there still exists one low-angle superlattice Bragg peak, it can be argued that the Co layers become discontinuous by forming pancake-like clusters, as in [159] Co/Ag MLs.

^{59}Co NMR spectra from the as made sample and from samples annealed at 200, 300, and 350 °C are shown in Figure 40. As seen in Figure 40, annealing up to 300 °C induces only very small changes in the spectral line shapes with respect to the spectrum of the as-made sample. These changes concern the narrowing of the NMR intensity distribution and the shift of the gravity center of the spectrum, from 167 MHz in the

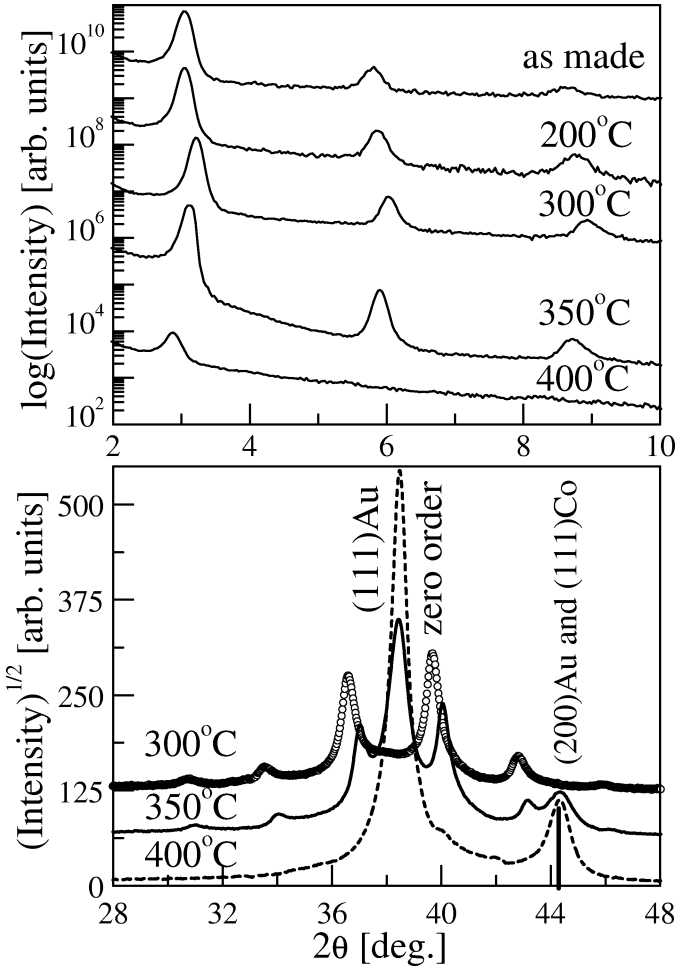

Fig. 39. The temperature evolution of the satellite peaks around the zeroth-order (111) peak from the average Co/Au lattice is shown at the bottom plot for the low-field GMR [Co(1 nm)/Au(2.5 nm)]$_{30}$ multilayers. The corresponding low-angle XRD spectra are shown on top.

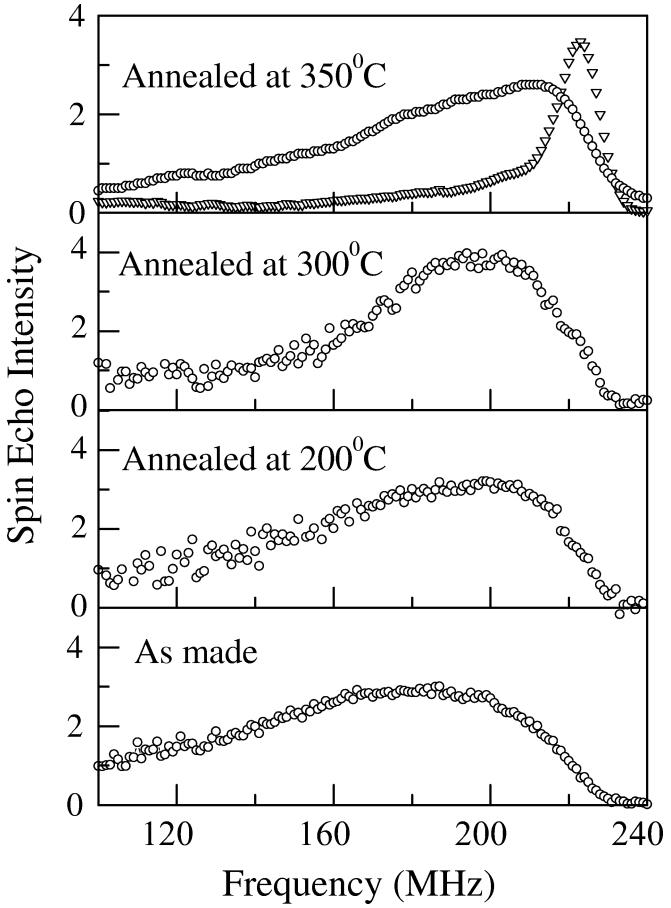

Fig. 40. The spin-echo ^{59}Co NMR spectra, recorded from the as-made Co/Au sample and from samples annealed at 200, 300, and 350 °C are shown. The 350 °C spectrum is decomposed into a low T and a high T (open triangles) subspectrum.

as-made film to 179 MHz for the sample annealed at 300 °C. However, the general profile of these spectra is maintained and, as reported earlier [133], it is characterized by a broad intensity distribution in a frequency range that is well below the characteristic frequency range of the known crystallographic phases [159, 160] of Co.

A dramatic change in the NMR spectrum is observed (Fig. 40) after annealing at 350 °C. Both, the spectral line shape and its radio frequency (rf) power dependence indicate that the multilayer becomes magnetically inhomogeneous. In the NMR experiment, such inhomogeneities are detected by the presence of multiple maxima in the signal intensity as a function of the rf field strength. Thus, samples annealed at 200 and 300 °C exhibit only one maximum of the signal intensity at each frequency, whereas the sample that is annealed at 350 °C exhibits two such maxima in the NMR signal intensity, each observed at a different power of the rf excitation pulses. This behavior indicates that there are two ferromagnetic components in the sample, differing considerably in their magnetic stiffness. The deconvolution of this spectrum is shown in Figure 40. Remarkably, the spectrum of the magnetically stiffer component is almost identical with the spectra observed from the samples annealed up to 300 °C. Thus, Co atoms contributing to the intensity of this spectrum must be located in these parts of the Co layer that retain the nanostructure of the as-made multilayer, which is named the low T structure.

Further insight into magnetic inhomogeneity and magnetic stiffness of the studied system has been obtained by introducing the concept of the restoring field [163] (H_{rest}), which describes the response of local Co magnetization to external rf field excitations. Thus, each value of H_{rest} is determined by the rf field strength that corresponds to a maximum NMR signal and is proportional [163] to magnetic stiffness of the MLs. Now, depending on the source of magnetic stiffness the H_{rest} can be related to the anisotropy field of a single-domain sample, the coercive field resulting from domain-wall effects, the exchange-biasing or dipolar fields at interfaces, and any combination of these fields. Figure 41 shows that the H_{rest} increases considerably at the initial stages of annealing whereas the low-angle XRD spectra (Fig. 39) show an increase of Co/Au interface sharpness, which is accompanied by the appearance [152] of surface anisotropy due to symmetry breaking. Thus, the ob-

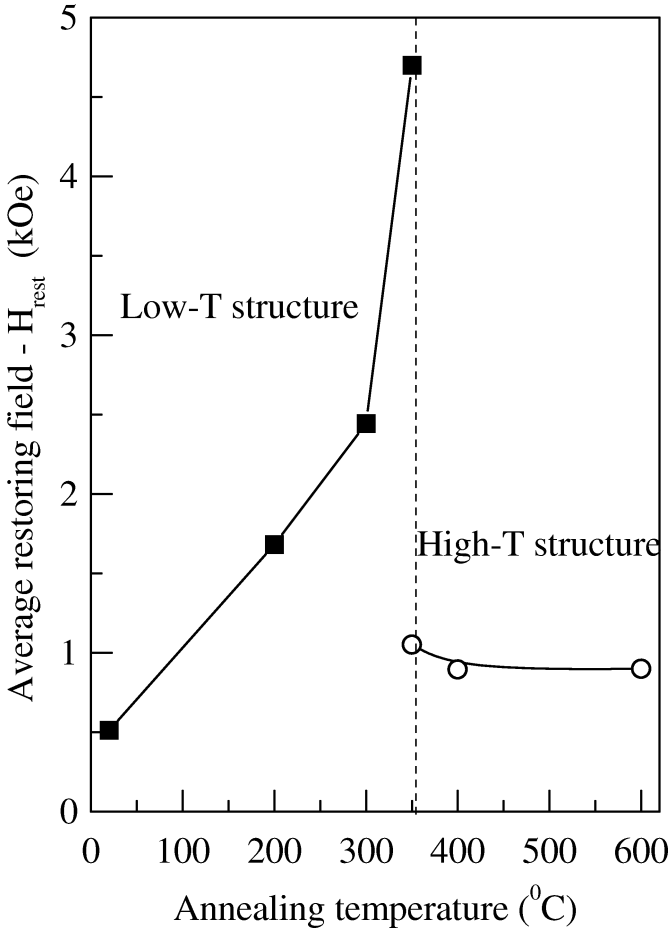

Fig. 41. The average restoring fields, estimated from the low T and high T NMR subspectra (Fig. 40) of Co/Au multilayers, are plotted as a function of the annealing temperature. At 350 °C, the low T and high T components coexist, defining a stiff and a soft magnetic phase, respectively. The lines are guides to the eye.

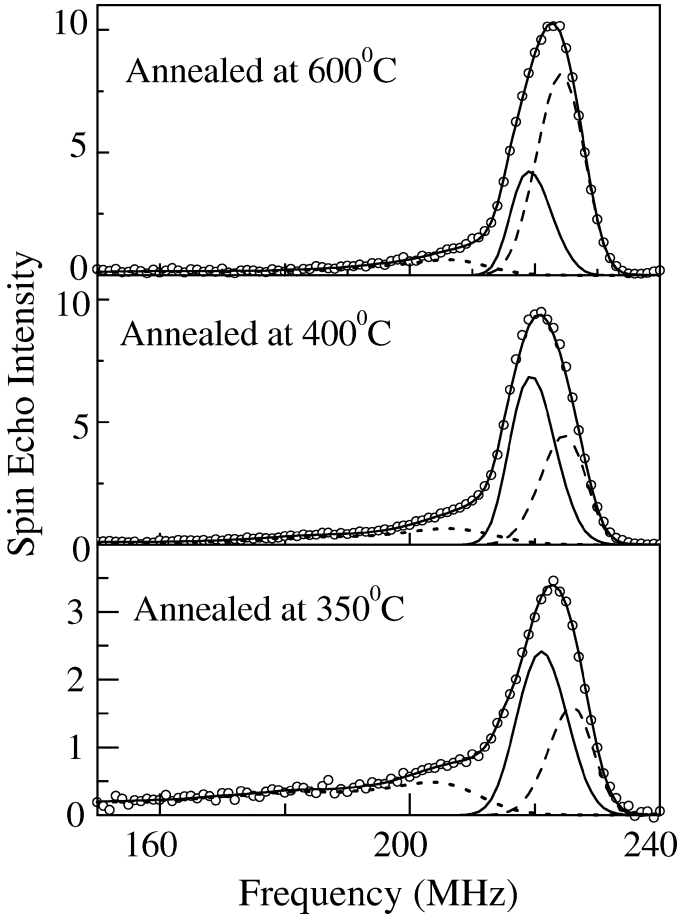

Fig. 42. The NMR spectra of the high T phase are shown for the three annealing temperatures of 350, 400, and 600 °C in Co/Au multilayers. The observed spin-echo intensity can be fitted with three components, corresponding to Co/Au interface (dot line), fcc (solid line), and hcp (dashed line) Co structures.

served increase of the average H_{rest} should be interpreted as an enhancement of interface anisotropy due to improvement of Co/Au interface sharpness. Consequently, the steep decrease of H_{rest}, that remains constant with the annealing temperature at 350 °C and above (open circles in Fig. 41), can be explained by the bridging of Au layers through Co.

Figure 42 shows the subspectrum of the high T structure at 350 °C together with NMR spectra from samples annealed at 400 and 600 °C, where the subspectrum of the low T structure disappears. The observed (Fig. 42) spin-echo intensity can be fitted with three components, centered at the characteristic B_{hf} of Co/Au interface coordination, of fcc- and hcp-Co structures [160]. The integrated intensities of the fitting lines show that the fraction of hcp-Co stacking increases from 38% in the sample annealed at 350 °C to 69% in the sample annealed at 600 °C. This implies that the shift of B_{hf} upon annealing proceeds by a transition to a structure where hexagonal Co stacking dominates. A plot of the gravity center of each NMR spectrum against the annealing temperature (Fig. 43) clearly shows the separation of the low T structure from the thermodynamically stable, close-packed structures of Co at 350 °C.

In conclusion, the complementary use of two nondestructive, one macroscopic (XRD) and one microscopic (NMR), techniques has revealed that polycrystalline [Co(1 nm)/Au(2.5 nm)]$_{30}$ MLs with (111) texture exhibit two regimes with respect to the microstructural characteristics of Co. In the low T structure, the kinetically grown Co layering is characterized by: (i) continuous layers after postannealing up to 300 °C, and (ii) NMR spectra that cannot be assigned to any of the identified structures of Co, indicating the formation of a distorted structure. Postannealing above 350 °C transforms the low T Co structure and modifies the Co layering into a high T configuration, that is characterized by: (i) a microstructure that forms a layered granular film due to penetration of Au across the thinner Co layers, and (ii) NMR spectra, indicating that inside the pancake-like clusters of Co the lattice adopts the known fcc and hcp structures.

A characteristic of the low T Co structure is that the annealing temperature of ~350 °C, above which our Co/Au MLs (Fig. 42) exhibit the usual NMR spectrum of bulk Co, is com-

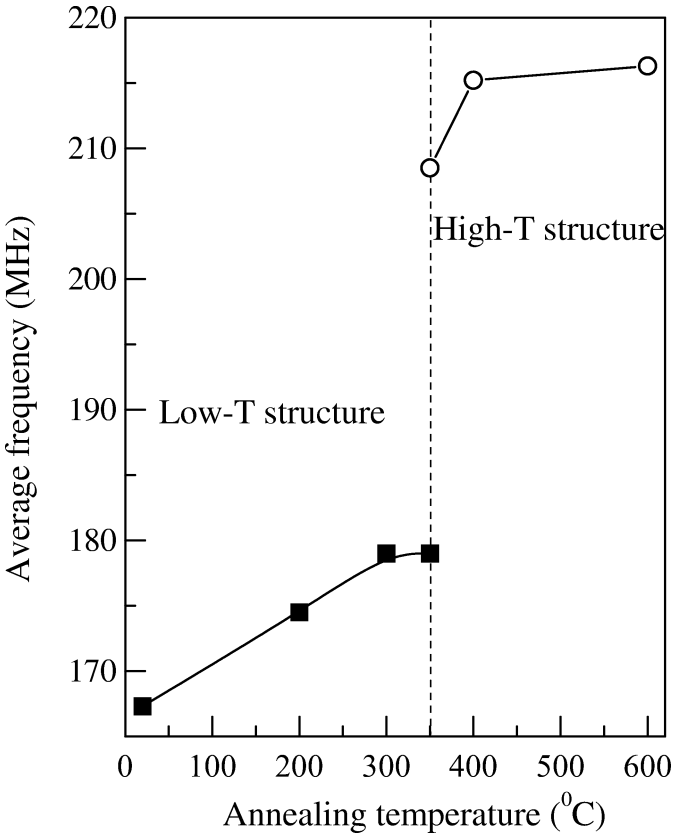

Fig. 43. The gravity center of each NMR Co/Au spectrum is plotted against the annealing temperature. At 350 °C, the low T and high T components coexist, defining two separate gravity centers.

parable with the temperatures where the transformation of bulk hcp Co to fcc stacking occurs (∼420 °C) and the amorphous $Co_{1-x}Au_x$ thin films decompose [96] into equilibrium Co and Au structures (>300 °C). Thus, besides that the featureless NMR spectrum of the low T nanostructure cannot be assigned to a specific Co coordination [133, 153], its thermal stability up to 300 °C and the TEM measurements [157] indicate that an unusual Co nanostructure can be formed when Co layers grow on top of amorphous buffer layers while the substrate temperature is close to room-temperature (RT) during deposition. In general, the importance of these results relies on the fact that makes possible the separation of magnetic inhomogeneites and secondary magnetic phases from complex NMR spectra.

4.5. Structural, Magnetic, and Magnetotransport Properties of NiFe/Ag Multilayers

In NiFe/Ag discontinuous multilayers (DML), consistent annealing is required to produce consistent grain-size distributions [223, 209] for optimization of the GMR effect (≈5% at RT). A systematic change in the saturation magnetostriction (λ_s) and GMR have been observed [224] as a function of annealing temperature (T_{an}). The increase of λ_s from negative to positive values as a function of T_{an} suggests that the films are under tensile stress in the as-deposited state. This stress is gradually reversed with annealing and for $\lambda_s \approx 0$ the GMR is maximum. It is believed that the relieved intralayer strain effects accompanied by grain boundary separation in NiFe layers, after annealing at 340 °C, give rise to micromagnetic changes that favor an increased interlayer antiferromagnetic (AF) exchange coupling $\mathbf{J}_{AF}$.

The observed oscillations in GMR of [232] $Ni_{81}Fe_{19}$/Cu and [79] Co/Cu multilayers as a function of Cu spacer thickness, measured at 4.2 and 300 K, provide evidence for the dependence of J_{AF} from the saturation magnetization $\mathbf{M}_s$ in magnetic layers. In both cases, well-defined oscillations in GMR are found at 4.2 K for increasing Cu thickness. For the Co/Cu system, similar oscillations are found at all temperatures from below 4.2 K to above 400 K whereas in NiFe/Cu only a single oscillation is observed at RT for magnetron sputtered multilayers. This might be a consequence of the AF coupling since in the former system $\mathbf{J}_{AF}$ at the first oscillation peak weakens by only 25% between 4.2 and 300 K, whereas in the latter system $\mathbf{J}_{AF}$ changes by a factor of 2.5. Since the $\mathbf{J}_{AF}$ is related to $\mathbf{M}_s$, to the saturation field H_s and the thickness t_F of the magnetic layers as [226]: $\mathbf{J}_{AF} \approx -H_s\mathbf{M}_s t_F/4$, it is reasonable to argue that in NiFe/Cu multilayers at low temperatures, where the AF coupling is considerably stronger, it is likely that more oscillations in coupling will be observed than at higher temperatures where the coupling may be weak compared to direct FM coupling via defects. As-deposited NiFe/Au multilayers [201] exhibit oscillatory variations in saturation MR as a function of t_{Au} at RT and present the largest magnetic field sensitivities yet reported. However, the estimated $\mathbf{J}_{AF}$ is much weaker than in similarly prepared NiFe/Cu and NiFe/Ag multilayers. Consequently, for this category of NiFe/NM (NM = Cu, Ag, Au) multilayers the contribution of $\mathbf{J}_{AF}$ in the GMR effect is not always the same. Of particular interest are sputter-grown NiFe/Ag multilayers, deposited at RT. Although they exhibit a significant change of the MR effect from RT down to 5 K, an AF layer coupling was not observed at any temperature [227].

The variation of the higher angle diffraction patterns in the vicinity of ⟨111⟩ and ⟨222⟩ Ag superlattice peaks is displayed in Figures 44 and 45 for $t_F \approx 2$ nm as a function of t_{Ag} and for $t_{Ag} \approx 4$ nm versus t_F, respectively. The continuous line is the calculated profile from SUPREX refinement [228]. The observed spectra display two important features:

First, the intensity (I_n) of the $n = 0$ Bragg-peak (I_0) is insensitive for the samples with $t_F \approx 2$ nm as a function of Ag thickness while for those with fixed $t_{Ag} \approx 4$ nm I_0 tends to zero as t_F increases from 1.6 to 2.5 nm and I_{-2} becomes stronger at the same time. For $t_{Ag} = 4$ nm and $t_F = 3$ nm, I_0 almost disappears while the I_{-1} and I_{-2} components become very intensive. It is known that interface roughness effects such as layer thickness fluctuations and interfacial diffusion can cause damping, broadening, and shifting of the $n = 0$ satellite peaks but they cannot reduce the $n = 0$ peak to be less intensive than the satellites. Therefore, stress effects are responsible for the damping of the I_0 peak.

Second, in Ag ⟨222⟩ peak position there is a double Bragg reflection for $t_F = 1.6$ nm which merges to a single peak as

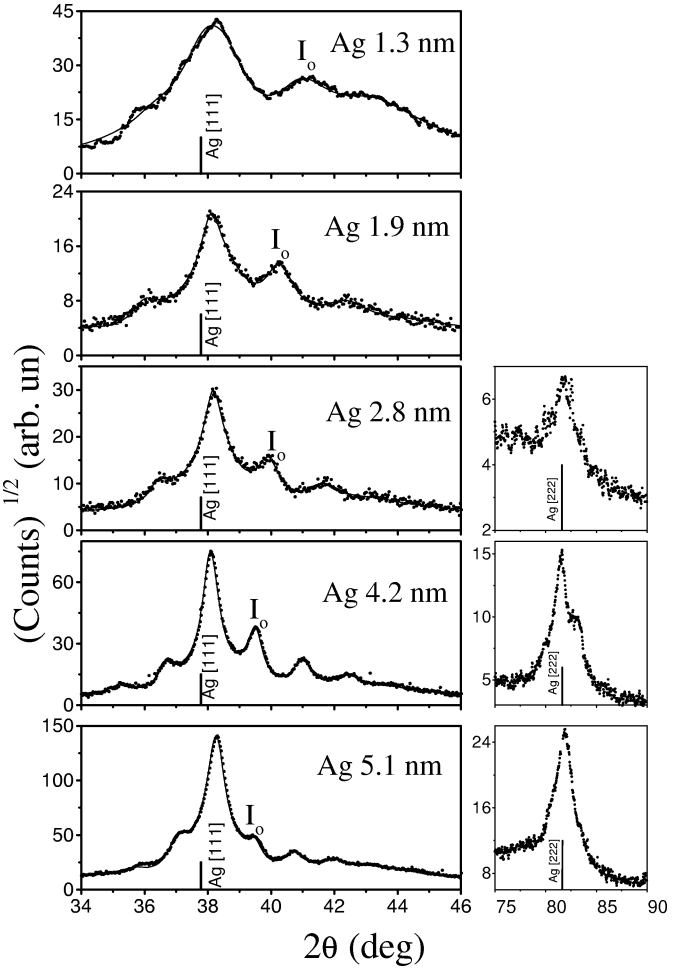

Fig. 44. XRD profiles of NiFe/Ag multilayers with different Ag layer thickness. The solid line is a fit from SUPREX. The position of the zero-order satellite peak is marked as I_0.

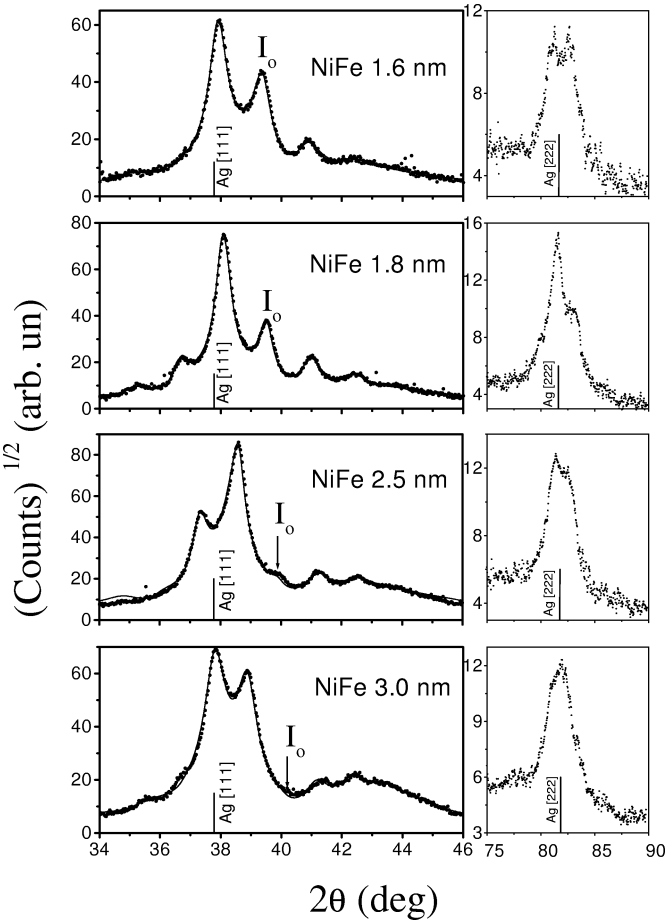

Fig. 45. XRD profiles of NiFe/Ag multilayers with different NiFe layer thicknesses. The position of the zero-order satellite peak is marked as I_0. The solid line is a fit from superlattice refinement (SUPREX) analysis.

the NiFe layer becomes thicker for constant $t_{\mathrm{Ag}} \approx 4$ nm. For $t_F \approx 2$ nm as a function of t_{Ag}, the Ag ⟨222⟩ peak is lost in the background for $t_{\mathrm{Ag}} = 1.3$ and 1.9 nm while only for $t_{\mathrm{Ag}} = 4.2$ nm an additional reflection is clearly seen. Consequently, residual stresses and nucleation of Ag grains through NiFe grain boundary diffusion [225, 201] might be related to the observed variations of the spectra. The estimated values from SUPREX for the lattice expansion of the atomic planes of NiFe and Ag near the interface are plotted in Figure 46. The zero layer in Figure 46 corresponds to the bilateral plane that separates the first atomic layer of each component at the interface.

In Figure 46, there are two major results: (i) The expansion of NiFe layer is always considerably large (about 0.04 nm) compared to the moderate relaxation of Ag (about 0.01 nm) except for $t_F = 2.1$ nm and $t_{\mathrm{Ag}} = 1.3$ nm. The large NiFe interface expansion may arise from both strain effects and varied alloy composition. For (Ni, Fe) phases [JCPDS, No. 23-297] the lattice constant varies from 0.35956 nm ($d_{111} = 0.2076$ nm for 39 atom % of Ni) to 0.35238 nm ($d_{111} = 0.2034$ nm for Ni 100%). These values are considerably smaller to those obtained and therefore strain effects are eminent at interfaces. (ii) For thinner NiFe (<2.5 nm) and Ag (<4.5 nm) layers, the expansion on the top of every layer (dark symbol) is more pronounced relative to the bottom layer which implies that the multilayer film has a concave bending relative to the Si substrate. Since a lattice expansion is apparent in both the top and the bottom of NiFe and Ag layers, their presence can be explained by misfit dislocations and/or atomic intermixing of NiFe with Ag atoms. The fact that the refined roughness parameter is always less than the average $(d_f + d_{\mathrm{Ag}})/2$ value is an indication that chemical interdiffusion occurs. However, NiFe and Ag are immiscible and hence the interdiffussion can be considered as a penetration of atoms into grain boundaries at the interface. For thicker layers, the strain effects, in [NiFe(3 nm)/Ag(4.8 nm)]$_{20}$, are likely to equilibrate since the expansion of the bottom Ag layer exceeds that on top and vice versa for the NiFe layer. This results in a better matching of NiFe/Ag layers (see left bottom in Fig. 46) by creating tensile and compressive interlayer strain in NiFe and Ag layers, respectively. The change in intensities of the superstructure pattern (Fig. 44 bottom) clearly shows the difference. A possible interpretation of changes in elastic strain with

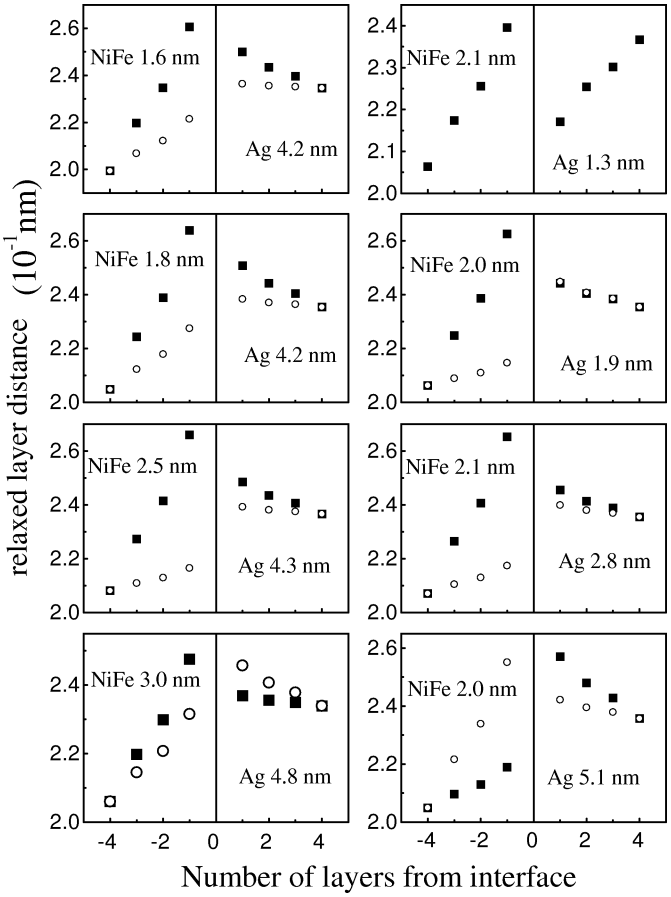

Fig. 46. Estimated values from superlattice refinement (SUPREX) analysis for the lattice expansion of the atomic planes of NiFe and Ag near the interface.

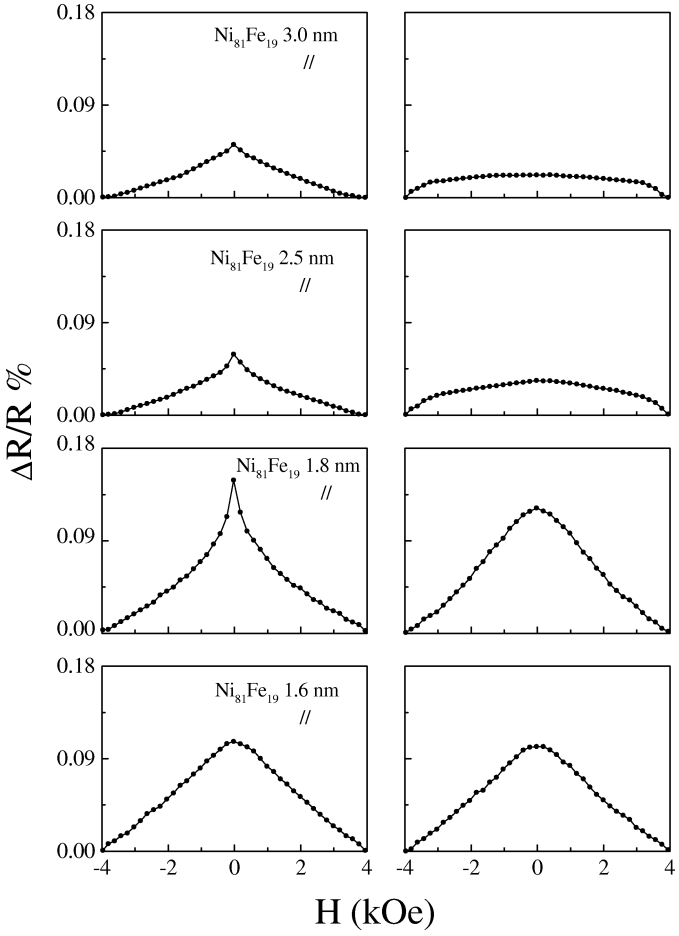

Fig. 47. MR measurements at RT for [NiFe(t_F)/Ag(4 nm)]$_{20}$ as-deposited films, with the external magnetic field direction parallel (left) and perpendicular (right) to film plane.

increasing thickness is the approach [229] to critical thickness t_c, where the d_f and the d_{Ag} relax to its bulk crystal spacing.

An alternative explanation fits better with the study of microstructure and magnetoelastic (ME) coupling coefficients in ultrathin $Ni_{80}Fe_{20}$/Ag films [230]. It is observed that the effective ME coefficients B_{eff} of polycrystalline films have a surface-dependent component which varies inversely with film thickness t_F. This component can change the sign of B_{eff} and can dramatically increase its magnitude for $t_F < 2.6$ nm, whereas it is close to zero for $t_F \approx 3$ nm. In [NiFe(2 nm)/Ag(5.1 nm)]$_{20}$, while there is a more pronounced expansion of the bottom NiFe layer that matches the expansion of the top Ag, a mismatch of the top NiFe and the bottom Ag appears. Since interfacial roughness is yet experimentally difficult to distinguish from interfacial diffuseness, the present data are not sufficient to provide a complete explanation of interface structural modulation.

In Figures 47 and 48, MR measurements are shown at RT for [NiFe(t_F)/Ag(4 nm)]$_{20}$ and [NiFe(2 nm)/Ag(t_{Ag})]$_{20}$ as-deposited films, respectively, with the external magnetic field direction parallel (right) and perpendicular (left) to film plane. It is observed (Fig. 47) that the MR effect is isotropic for $t_F = 1.5$ nm while the maximum MR is achieved for [NiFe(2 nm)/Ag(4 nm)]$_{20}$, which exhibits a characteristic sharpening of the curve around zero field in the parallel direction. There is only one maximum of $\Delta R/R$ at zero field and the rounding of the curve for the perpendicular field direction is caused from film shape anisotropy. MR measurements were performed at 5 K and the observed curves are shown in Figure 49 for some selected samples. A considerable change in the response of transport properties to magnetic field variation occurs relative to RT measurements. In [NiFe(2 nm)/Ag(4 nm)]$_{20}$, the effect is almost isotropic. Two common features appear in these measurements: (i) Saturation of the MR effect is not achieved and there is a linear decrease with an increasing field above 0.5 T. The linear variation might be attributed to superparamagnetic NiFe particles. (ii) Two maximum values of $\Delta R/R$ exist for nonzero negative and positive fields. Note that at RT an optimum MR effect of 1.5%, with $H_s = 100$ Oe, has been observed in [NiFe(2 nm)/Ag(4 nm)]$_{20}$ multilayers after 3 h annealing at 400 °C. In all annealed samples, a coercive field H_c was apparent at the maxima of $\Delta R/R$ loops.

Isothermal magnetic measurements were performed with the field applied parallel ($H_\parallel$) and perpendicular ($H_\perp$) to a film plane at 300, 100, and 5 K. The loop shape was characteristic of ferromagnetically (FM) coupled material without any detectable coercive field (H_c) above 100 K. Figures 50 and 51

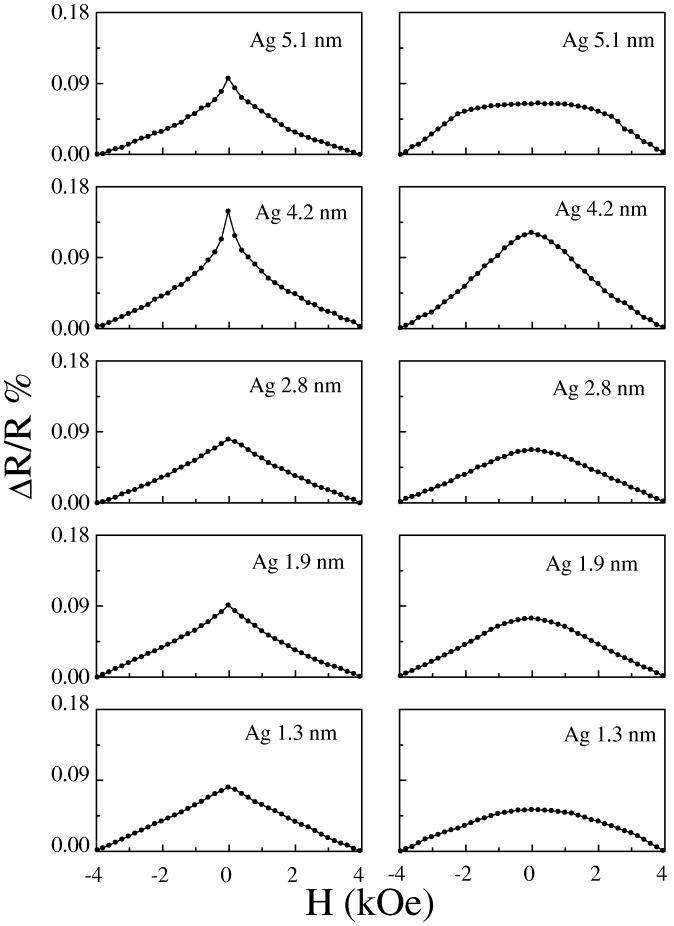

Fig. 48. MR measurements at RT for [NiFe(2 nm)/Ag(t_{Ag})]$_{20}$ as-deposited films, with the external magnetic field direction parallel (left) and perpendicular (right) to film plane.

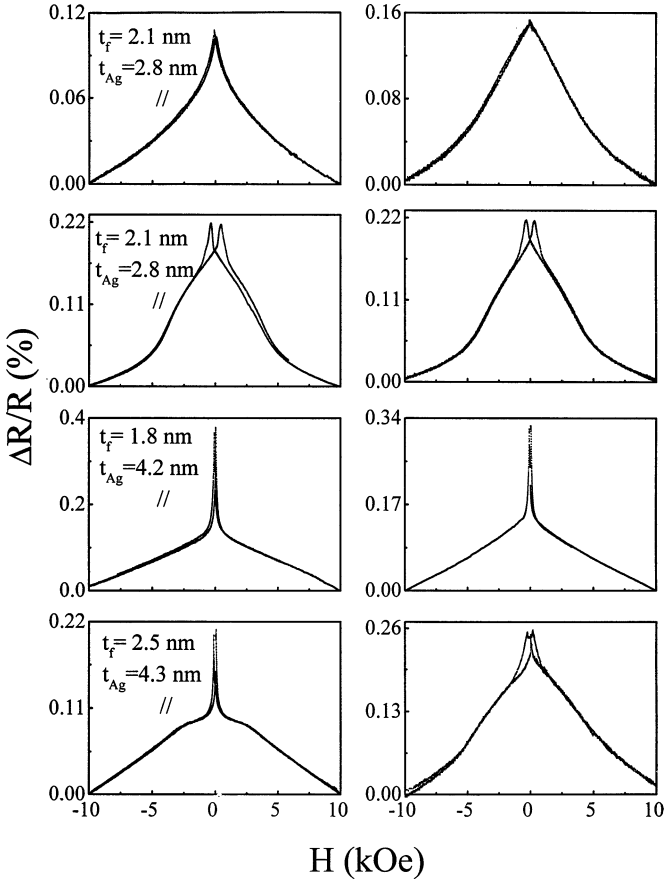

Fig. 49. MR measurements at 5 K for selected NiFe/Ag as-deposited films, with the external magnetic field direction parallel (left) and perpendicular (right) to film plane.

display the observed loops at 5 K where a significant H_c has been observed. It is worth noting that for a pure $Ni_{81}Fe_{19}$ (100-nm thick) film on Si(100), coercivity of more than 1 Oe was not observed at any temperature. A comparison of loops, with $H_{\|}$, for samples with variable t_{Ag} (Fig. 50 left) to those with variable t_F (Fig. 51 left) shows that H_c remains higher than 10 Oe and oscillates as a function of t_{Ag} (Fig. 52) whereas a decrease from 24.4 Oe to a bottom value of about 4 Oe is observed with increasing t_F. For $H_{\perp}$, the loop shape is similar to that expected for uniaxial particles with their easy axes (EA) randomly oriented with an exception for [NiFe(2 nm)/Ag(4 nm)]$_{20}$ and [NiFe(2.5 nm)/Ag(4 nm)]$_{20}$, where rotation of magnetic moments out of the film plane is "easier" and the shape anisotropy does not modify the loop like in the other samples. For both samples, with $H_{\perp}$ geometry, an $H_c \approx 16$ Oe is obtained with a reduced remanence $\mathbf{M}_r/\mathbf{M}_s = 0.18$ and 0.03 for $t_F = 2$ and 2.5 nm, respectively. The variation of d_f, H_c, and $\mathbf{M}_r/\mathbf{M}_s$ as a function of t_{Ag} and t_F at 5 K is presented in Figure 52. The resemblance of d_f and H_c oscillations is seen as a function of t_{Ag} but not for variable t_F. The dependence of d_f and H_c with t_F in Figure 52 indicates that there is no direct relationship between them caused from variable strain. In addition, for d_f larger than the relaxed 0.2048-nm value the H_c approaches a low limit as a function of t_F probably due to proportionality of H_c with the anisotropy field $H_A = \alpha K/\mathbf{M}_s$ (α = grain shape and domain dependent constant) in a first approximation. The reported [150] variation of $\mathbf{M}_s$ with t_F (for $t_F < 5$ nm) may explain the observed H_c versus t_F dependence. Since the XRD analysis excludes the possibility of "bridging" among NiFe layers through Ag, that might vary H_c as well, variations in H_c and d_f with t_{Ag} can be understood in terms of stress-induced anisotropy in thin magnetic films.

In thin films, it is realized, with qualitative reasoning, how stress-induced reorientation of magnetization on the hysteresis loops parameters [231] causes a reduction or an increase of $\mathbf{M}_r$ and H_c. In this case, it is assumed that the initial films are roughly isotropic. This means that the local anisotropy, which determines the domain structure (crystalline and local stresses anisotropy), has an isotropic distribution of the local intrinsic easy axes (EA) for an assembly of noninteracting domains. Accordingly, it is shown [232] that in Ni films the effect of stress on the coercive force can be understood by considering two different micromagnetic reversal processes: irreversible rotation and domain-wall motion. Using these two mechanisms for magnetization reversal and the influence of the

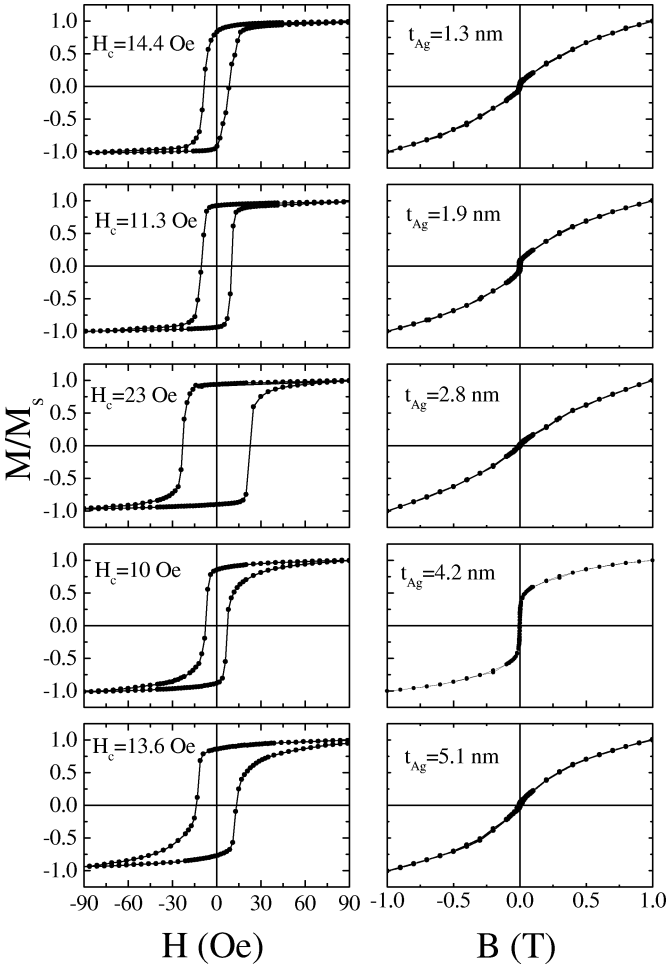

Fig. 50. Hysteresis loops measured at 5 K for [NiFe(2 nm)/Ag(t_{Λ_g})]$_{20}$ as-deposited films, with the external magnetic field direction parallel (left) and perpendicular (right) to film plane.

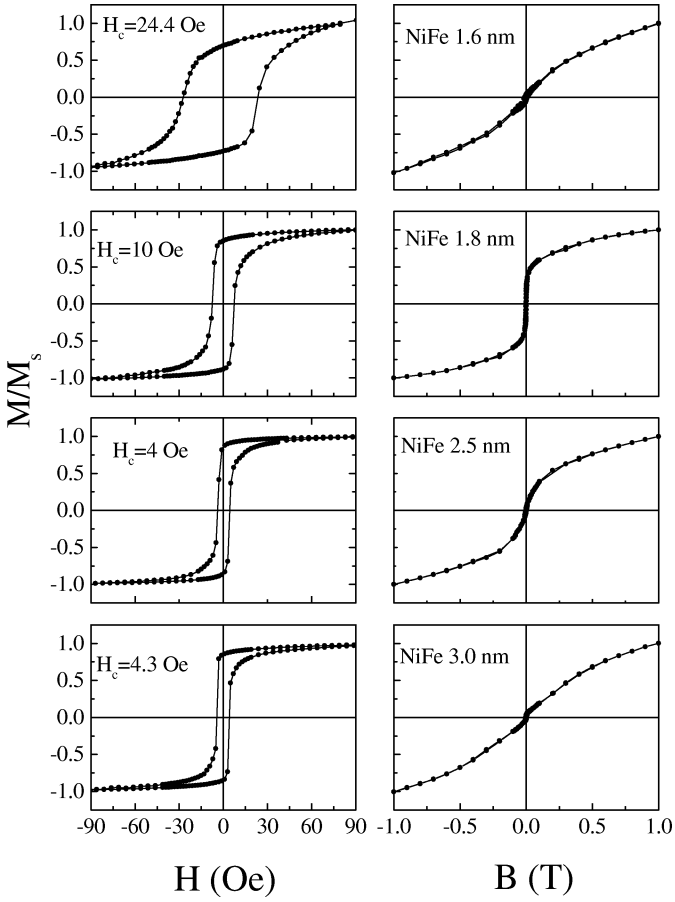

Fig. 51. Hysteresis loops measured at 5 K for [NiFe(t_F)/Ag(4 nm)]$_{20}$ as-deposited films, with the external magnetic field direction parallel (left) and perpendicular (right) to film plane.

magnitude of the antiferromagnetic coupling, the shapes of MR curves in both cases have been calculated for Fe/Cr films as well [226].

In NiFe/Ag samples deposited at RT, it has been shown that the variation of t_{Ag} creates different residual stresses. Therefore, the reorientation of magnetization can be modified in a similar manner with the externally applied stress case. The key point is that stress gives rise to the appearance of an EA in a nearly otherwise isotropic film. In Ni films [232], it is shown that an EA induced by stress is consistent with the relative value of the anisotropy energies involved. If the order of magnitude of the crystalline anisotropy energy K_u is comparable to the stress-induced anisotropy K_s, then it is expected that the second will produce noticeable effects. The residual stress may cause additional negative or positive magnetostriction λ_s even [150] in $Ni_{81}Fe_{19}$, that induces a preferable EA in every layer. By this action, for a material having a homogeneously positive magnetostriction, as in γ-(Ni, Fe), the originally isotropic distribution of domain orientations will be squeezed into a narrower distribution along an EA parallel or vertical to film plane if the induced strain is tensile or compressive, respectively. The observed loops in Figure 51 indicate that the EA lies in the film plane but for [NiFe(2 nm)/Ag(4 nm)] and [NiFe(2.5 nm)/Ag(4 nm)], where magnetization reversal is easier for $H_\perp$, may imply that K_s is minimal and the isotropic distribution of domain orientations is maintained. Figure 51 shows that only these two samples exhibit an abrupt low-field GMR effect, obviously related to easy magnetization reversal.

In this class of GMR MLs, the spin-dependent scattering is obviously derived from the magnetic layers, but of particular importance is whether this spin-dependent scattering (SDS) occurs within the interior of the magnetic layers (bulk scattering) or predominantly at the interfaces between the magnetic and spacer layers (interfacial scattering). The interfacial scattering was examined by inserting a third material (Co) at the interfaces of NiFe/Cu films [240] and the MR effect has been dramatically enhanced at RT and 5 K. This has been attributed primarily to reestablishment [232] of AF coupling at RT but it was granted to interfacial scattering at 5 K. Further analysis of these results [234] in terms of mean-free paths for bulk SDS and interface SDS transmission coefficients is inclined that SDS in FM–Cu is mainly bulk in NiFe, a mixture of bulk and interfacial in Co/Cu and mainly interfacial in Fe/Cu.

XRD data analysis of NiFe/Ag as-deposited MLs provides evidence that there is significant interface strain which is modified as a function of layer thickness. The observed splitting of the ⟨222⟩ Ag superlattice peak for $t_F < 2.5$ nm is assigned to Ag interdiffusion between NiFe grain boundaries. The MR and hysteresis loop data show that for t_F about 1.8 to 2.5 nm and t_{Ag} about 3.8 to 4.3 nm the film is magnetically isotropic and exhibits easy magnetization reversal for low applied fields. The oscillatory variation of H_c and $\mathbf{M}_r/\mathbf{M}_s$ as a function of t_{Ag} can be explained in terms of preferable EA directions in every NiFe layer induced from residual magnetostriction. The hysteresis loop shapes are typical of FM-coupled layers and exhibit a nonzero coercive field below 100 K. The increase of the GMR effect and the $\Delta R/R$ field sensitivity at 5 K shows that an enhancement of the average magnetic moment and hardening of magnetization reversal in individual NiFe layers (bulk scattering model) have a major contribution. Thus, an isotropic EA distribution of magnetic domains—due to small residual intralayer strain effects—is in favour of low-field GMR in sputtered NiFe/Ag multilayers.

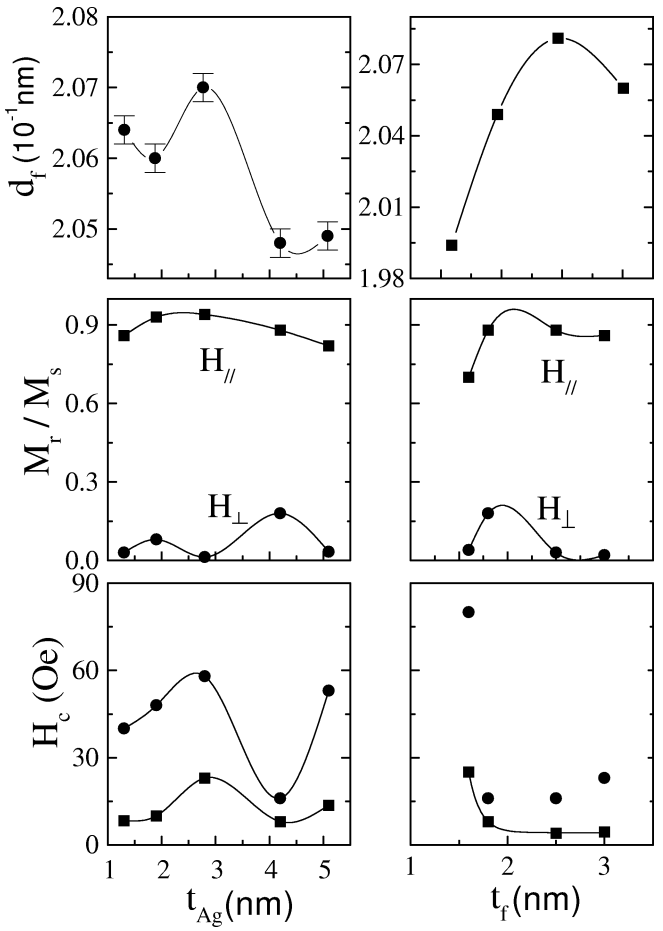

Fig. 52. Variation of the estimated d_f (top), observed $\mathbf{M}_r/\mathbf{M}_s$ (middle), and H_c (bottom) values as a function of t_{Ag} (left) and t_F (right) at 5 K. Solid lines are guides to the eye. Squares are for $H_{\parallel}$ and circles are for $H_{\perp}$ directions.

5. COLOSSAL MAGNETORESISTANCE IN MANGANESE PEROVSKITE FILMS

5.1. Materials Properties

Perovskite is the name of a mineral with the composition $CaTiO_3$. Replacing Ti by Mn^{+3} we also have other perovskite–manganate oxides $MMnO_3$, where M represents a large ion such as La^{+3}, Ca^{+2}, Ba^{+2}, or Sr^{+2}. The basis of the crystal structure is an NaCl-type lattice composed of O^{-2} and M^{+n}, and a small Mn^{+3} ion goes into an octahedral site surrounded by six O^{-2} ions (Fig. 53). Many years ago, the magnetic studies of $MMnO_3$ perovskites reported that, usually, these oxides were antiferromagnetic, but in solid solutions of $La^{+3}Mn^{+3}O_3$ and $Ca^{+2}Mn^{+4}O_3$; $La^{+3}Mn^{+3}O_3$ and $Sr^{+2}Mn^{+4}O_3$; $La^{+3}Mn^{+3}O_3$ and $Ba^{+2}Mn^{+4}O_3$, ferromagnetism appeared [235]. At that time, the magnetic phase diagram of the saturation magnetization against the Mn^{+4} content has shown that in the composition range of 20 to 40% Mn^{+4} of the solid solution the magnetic moments of Mn^{+3} ($\sim 4\mu_B$) and Mn^{+4} ($\sim 3\mu_B$) are aligned ferromagnetically. In this range, the electrical conductivity becomes very large. Zener [236]

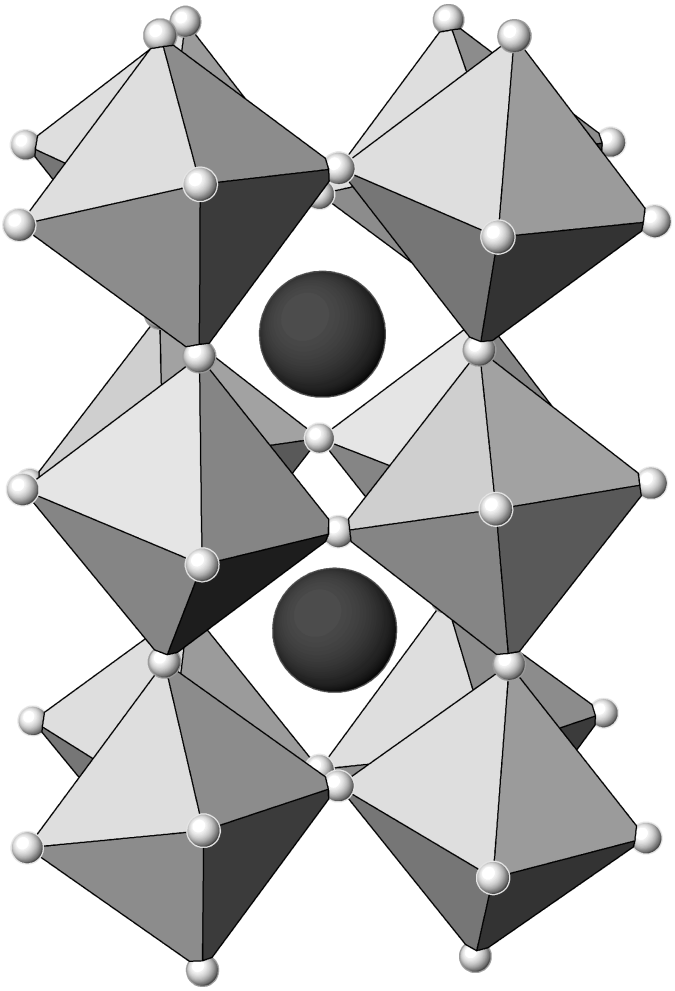

Fig. 53. Schematic of the $LaMnO_3$ perovskite.

explained this phenomenon in terms of *double-exchange interactions*: in this composition range Mn^{+3} and Mn^{+4} coexist, so that conduction electrons carry electric charges in the common d band, thus resulting in high conductivity. Since conduction electrons keep their spins during itinerant motion, Mn ions align their localized spins parallel to those of conduction electrons through the s–d interaction, thus resulting in ferromagnetic alignment. This idea was formulated by Anderson and Hasegawa [236]. Different from the usual exchange or superexchange interaction, this double-exchange theory indicates that electron or hole transfer from site to site depends on the relative angle of the spins at the two Mn sites, θ_{ij}-hopping goes as $\cos(\Delta\theta_{ij})$ and is most likely for parallel spins. Therefore, if antiferromagnetic superexchange interaction acts in addition to double-exchange interaction, spin canting is expected to result [237]. *The colossal MR effect then comes from the applied field reducing the spin misalignment, thus decreasing the resistivity*. The parallels of this field dependence of conductivity with that of ferromagnet–insulator–ferromagnet tunneling, spin valves, and spin switches is noteworthy.

The antiferromagnetic superexchange interaction has first been verified in MnO. The crystal structure of MnO is such that Mn ions form an fcc lattice and oxygen ions are located between each Mn–Mn pair. The direct exchange interaction between Mn ions is very weak because it is interrupted by the interstitial O^{-2} ions and the superexchange interaction acts between Mn ions through the O^{-2} ion as follows: The O^{-2} ion has electronic structure expressed by $(1s)^2(2s)^2(2p)^6$. The p orbit stretches toward the two neighboring Mn ions (named Mn1 and Mn2). One of the p electrons can transfer to the 3d orbit of one of the neighboring Mn ions (say the Mn1). In this case, the electron must retain its spin, so that its sense will be antiparallel to the total spin of Mn^{+2}, because Mn^{+2} has already had five electrons and the vacant orbit must accept an electron with spin antiparallel to that of the five electrons (Hund's rule). On the other hand, the remaining electron in the oxygen p orbit must have spin antiparallel to that of the transferred electron because of the Pauli exclusion principle. Thus, the exchange interaction with the other Mn ion (Mn2) is negative. As a result, the total spin of Mn1 becomes antiparallel to that of Mn2. The superexchange interaction is strongest when the angle Mn1–O–Mn2 is 180°, and becomes weaker as the angle becomes smaller. When the angle is 90°, the interaction tends to become positive.

The interest in magnetoresistance in doped perovskite manganites was initiated by the discovery of a large ($\Delta R/R > 60\%$) negative room-temperature magnetoresistance in a 7-tesla field, in epitaxial $La_{0.67}Ba_{0.33}MnO_x$ thin films [238]. This was followed by a report [239] that thin-film $La_{0.67}Ca_{0.33}MnO_3$ exhibits a $\Delta R/R \approx 127{,}000\%$ at 77 K in a 6-tesla field. This large magnetoresistance effect has been called colossal magnetoresistance (CMR). Thin films with large magnetoresistance at room temperature (Fig. 54) open up new possibilities for applications in diverse areas of technology such as magnetic RAMs and read heads for hard-disk drives. Thin-film deposition technology for complex oxide materials has rapidly progressed due to the effort spent on commercialization of the high-temperature superconductors, which are a class of doped cuprate perovskites with materials characteristics similar to those of the doped manganate perovskites.

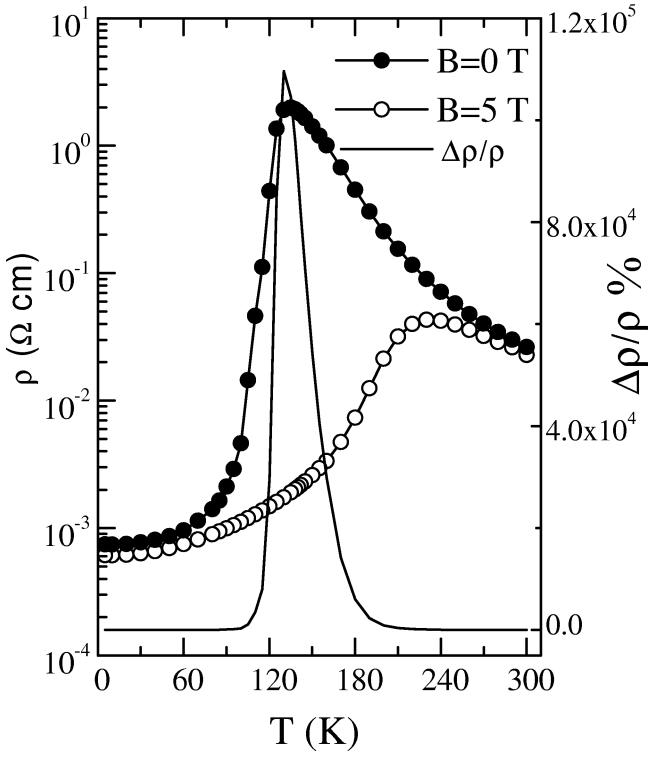

Fig. 54. Resistivity as a function of temperature, measured in 5 tesla and in zero applied field, from a $La_{0.67}Ca_{0.33}MnO_3$ thin film, 100-nm thick, grown on $LaAlO_3(100)$ substrate. The CMR ratio $\Delta\rho/\rho_H = [\rho_0 - \rho_H]/\rho_H$ is plotted as a solid line.

In both bulk and thin-film CMR materials, the basic phenomena of the CMR effect are similar. The resistivity peaks near the Curie temperature, around which the largest magnetoresistance is obtained. Note that the system goes through a metal-insulator (semiconductor) transition at a temperature where a weak magnetic moment still exists. The low-temperature metallic phase shows a resistivity that increases with increasing temperature whereas the opposite is true when the Fermi energy lies in a gap as in a semiconductor or an insulator. The resistivity peaks at this metal-insulator transition but the field induced resistance change, $\Delta R(H)/R$, peaks below this transition. Application of a field expands the ferromagnetic phase, displacing to higher temperatures the metal-insulator transition and hence displacing the sharp increase in metallic resistivity. Thus, the CMR ratio is proportional to the temperature derivative of the $R(T)$ curve times the field derivative of the metal-insulator transition by a derivative chain rule: $\Delta R(H)/R \approx (1/R)(dR/dT)(dT_c/dH)\,dH$. Consequently, *the sharper the resistivity transition and the stronger the field dependence of that transition, the greater will be the CMR ratio*. In addition, there is a correlation among resistivity, magnetization, and the pseudoperovskite cell size. Usually, a larger cell size seems to correlate with a lower Curie temperature, and a lower Curie temperature leads to a higher resistivity peak, which is accom-

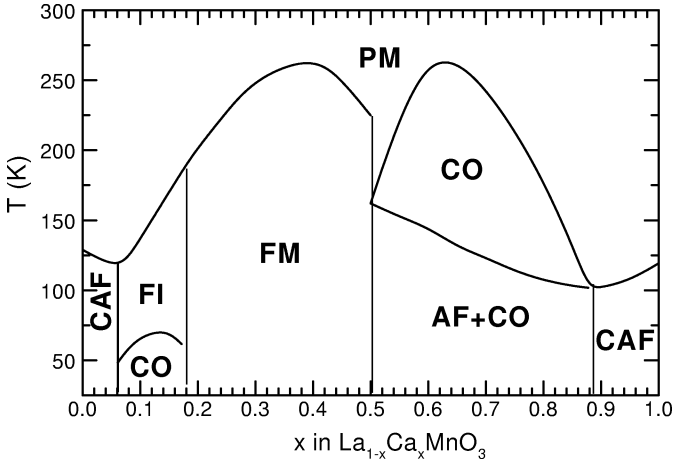

Fig. 55. Magnetic phase diagram of $La_{1-x}Ca_xMnO_3$. CAF is the canted antiferromagnet, AF is the antiferromagnet, FM is the ferromagnet, PM is the paramagnet, FI is the ferromagnetic insulator, CO is the charge ordering.

panied by a larger CMR effect. Thus, a larger CMR effect involves the preparation of the materials in such a way as to suppress its resistance-peak temperature (Fig. 54) to below 150 K.

The perovskite manganites $L_{1-x}A_xMnO_3$ (L = lanthanides and A = alkaline earths) present a remarkably complicated phase diagram as the relative concentration of Mn^{3+} and Mn^{4+} changes [240, 241]. For example, the ground state of the undoped compound $LaMnO_3$ is an antiferromagnetic (AF) insulator. Doping the system with holes, that is substituting Ca^{2+} for La^{3+}, the AF state is suppressed for a ferromagnetic (FM) metallic state ($0.2 < x < 0.5$) that shows colossal negative magnetoresistance (Fig. 55). The spin of the e_g ($S = 1/2$) extra electron in Mn^{3+} ($3d^4$) is ferromagnetically coupled to the t_{2g} ($S = 3/2$) local spin according to Hund's rule, thus making it energetically favorable for the e_g charge carriers to hop from one ion to the next without changing their spin direction. For $x > 0.5$, the AF superexchange interaction in the $Mn^{3+(4+)}-O^{-2}-Mn^{3+(4+)}$ bonds dominates over the FM double exchange in the $Mn^{3+}-O^{-2}-Mn^{4+}$. At half-doping ($x = 1/2$), the system undergoes a paramagnetic (insulating) to FM (metallic) transition at $T_c = 225$ K and then to an AF (insulating) state (Fig. 55) at $T_N = 155$ K. The low temperature AF state presents an unusual charge- and spin-ordered structure, called the CE type [240], where real space ordering of Mn^{3+} and Mn^{4+} takes place.

The application of a magnetic field can melt the charge-ordered AF insulating lattice, through a first-order melting transition, into an FM metal. For $La_{0.5}Ca_{0.5}MnO_3$, Xiao *et al.* [242] experimentally determined the magnetic phase diagram in the H–T plane. It is practically the same with those previously reported for [243] $Nd_{0.5}Sr_{0.5}MnO_3$ and $Pr_{0.5}Sr_{0.5}MnO_3$, except that in the La compound, at low temperatures, the field induced FM state is stable even after removing the applied field. Tokunaga *et al.* [244] determined the phase diagram of $L_{1-x}Ca_xMnO_3$ (L = Pr, Nd) for fields up to 400 kOe, utilizing a non-destructive long pulse magnet. The existing consensus is that the thermodynamically ferromagnetic ("liquid") and antiferromagnetic charge-ordered ("crystal") states correspond to two local minima in the free energy with large and small magnetization values, respectively, which are separated by a potential barrier U. So, an external magnetic field tends to stabilize the high $\mathbf{M}$ state due to the gain $(-\mathbf{M} \cdot H)$ in the free energy rather than the AF charge-ordered state ($\mathbf{M} \simeq 0$), and hence the potential barrier is expected to vary with the field. For the AF–FM transition to occur, the sum of the Zeeman and thermal energies should cover the energy difference between the AF and FM states. This explains why the value of the field needed to melt the charge-ordered AF state decreases with increasing temperature.

5.2. Low-Field Magnetoresistance in Manganites

CMR is a different physical effect than GMR but has a similar formal dependence on magnetization orientation; aligning the moments on adjacent cation sites (AF to FM) causes the resistance to decrease. This is due to the increase in hopping conductivity of the cation e_g electrons for parallel spins. *The field dependence of the CMR effect is not a function of the M–H curve*; many of these compounds show appreciable magnetization in fields of order 100 Oe, but the CMR effect still requires tens of kilogauss. The saturation magnetization field necessary to achieve a full CMR effect in the generic material is large, usually of the order of several tesla. This limitation has been overcome at lower temperatures, where large magnetoresistances in low fields were demonstrated in trilayer manganite/$SrTiO_3$/manganite using a current-perpendicular CPP geometry [245]. A resistance change of a factor of 2 was obtained with a switching field of less than 200 Oe at 4.2 K. The structure was lithographically fabricated with trilayers of $La_{0.67}Sr_{0.33}MnO_3/SrTiO_3/La_{0.67}Sr_{0.33}MnO_3$. The mechanism of the spin-dependent transport process across $SrTiO_3$ is yet to be fully understood [46].

The likelihood of a strongly spin-dependent transport at an interface with misaligned magnetic moment prompts the search for isolation of a single interface by experimental means. Magnetic domain boundaries are considered natural candidates, and the observation of pinning of magnetic domain walls at grain boundaries has led to the investigation of magnetotransport studies in polycrystalline materials, as well as in thin films grown on polycrystalline substrates. An investigation [246] of the possible consequences of magnetic domain boundary pinning by polycrystalline grain boundaries has shown an enhanced magnetoresistance at low temperatures compared to that observed for epitaxial thin films grown on single-crystal substrates. Large low-field magnetoresistance has also been reported [247] in a layered manganite $La_{1.4}Sr_{1.6}Mn_2O_7$ single crystal. Transport measurements with current perpendicular to the Mn–O planes revealed a magnetoresistance as high as 240% in fields below 1 kOe and at temperatures below 100 K. It has been argued that interplane spin-dependent tunneling might cause the observed low-field magnetoresistance.

Another approach is to fabricate [248] a pair of ferromagnetic flux concentrators attached to a ceramic piece of

$La_{0.67}Sr_{0.33}MnO_3$ to locally focus the magnetic field seen by the manganites. This device has achieved an enhancement of magnetoresistance response by a factor of 5900 in fields below 10 Oe. Alternatively, two-dimensional MBE growth was used [249] to fabricate lateral superlattices of manganites with different composition, targeting on interface related magnetic scattering of carriers. An in-plane anisotropic magnetoresistance was observed with a low-field magnetoresistance slope (sensitivity) of $(1/R)(dR/dH) = 36$ per tesla.

5.3. Exchange Bias in La–Ca–Mn–O Multilayers

The existence of unidirectional anisotropy due to exchange coupling between a ferromagnetic and an antiferromagnetic phase was first reported in oxide-coated fine particles [250] of Co. Characteristically, exchange anisotropy results in a displaced magnetic hysteresis loop when the sample is field cooled through the Néel temperature of the antiferromagnetic phase. In early studies, this loop displacement has been explained by assuming an ideal ferromagnetic–antiferromagnetic interface with uncompensated moments in the atomic-plane of the antiferromagnetic layer at the ferromagnetic–antiferromagnetic boundary [250]. Up to date exchange anisotropy effects have been studied mainly in AF–FM systems consisting of transition-metal alloys and metallic oxides (e.g., ferromagnetic = Co, NiFe, Fe_3O_4, and antiferromagnetic = CoO, FeMn) [250–257], where the ferromagnetic or antiferromagnetic interactions are due to *direct-exchange* coupling.

In addition to the scientific interest for investigating the mechanism of ferromagnetic–antiferromagnetic coupling, a great deal of attention has been focused on the technological applications of the resultant exchange bias in spin-valve magnetic field sensors and nonvolatile memories for magnetic-storage devices [38, 24]. Additionaly, a large amount of work has been generated to evaluate the applicability of La manganites, presenting the colossal magnetoresistance (CMR) effect, in spin-polarized tunnel junctions [258] as well as in spin-polarized current injection devices [259]. Fabrication of these heterostructures involves contact of the conducting $La_{2/3}Sr_{1/3}MnO_3$ oxides with another perovskite material. Since the $La_{2/3}A_{1/3}MnO_3$ (A = Sr, Ca) layers are FM, their contact with AF perovskite layers may give rise to exchange coupling and, subsequently, in exchange-biasing effects at the ferromagnetic–antiferromagnetic interfaces that may alter the magnetotransport properties of the junctions.

Several studies have focused on mixed valence manganite-based artificial superstructures [260–268]. The magnetic and transport properties of these structures are not a simple superposition of the response of the individual layers as interface scattering [260, 261], interlayer interactions [262, 263], and strain-driven effects due to lattice mismatch at interfaces [260, 264] considerably modify their magnetotransport properties.

The existence of exchange biasing has been observed [268] on La–Ca–Mn–O multilayers with alternating layers of ferromagnetic (FM) $La_{2/3}Ca_{1/3}MnO_3(\Lambda/2)$ and antiferromagnetic (AF) $La_{1/3}Ca_{2/3}MnO_3(\Lambda/2)$ compositions [269, 270] (Λ is the bilayer thickness) grown either on (001)$LaAlO_3$ or on (001)$SrTiO_3$ single crystals. These multilayers were prepared by pulsed-laser deposition (PLD) of bulk stoichiometric $La_{2/3}Ca_{1/3}MnO_3$ (FM) and $La_{1/3}Ca_{2/3}MnO_3$ (AF) targets on (100)$LaAlO_3$ single-crystal substrates. Both, structural and chemical compatibility between the employed AF and FM layers were important for the coherent growth of atomically perfect interfaces that allowed the development of exchange biasing at low temperatures. The maximum exchange-biasing field (H_{EB}) was observed for multilayers grown on top of (001)$LaAlO_3$. In comparison, high-quality $[La_{0.6}Sr_{0.4}MnO_3(FM)/La_{0.6}Sr_{0.4}FeO_3(AF)]_{20}$ superlattices, grown on (001)$SrTiO_3$, have shown [262] that the AF spin arrangement in the AF layers can modify the FM spin arrangement in adjacent FM layers but exchange biasing is not reported.

The preceding results indicate that significant changes occur in the magnetoelectronic properties at the interfaces, arising from the competition between the magnetic ordering structures. Specifically, the novel physics involved in exchange-biased [24, 271] FM–AF perovskite contacts focus on the mechanism that leads to a *unidirectional* anisotropy as the double-exchange coupling switches to superexchange coupling [272, 273] between juxtaposed FM and AF atomic layers. Thus, the strength of spin coupling at the AF–FM interfaces, relative to their exchange coupling with spins inside the FM or AF layers, seems to be essential for the exchange-biasing mechanism in these heterostructures. Investigation [274] of the interface related mechanism of spin coupling in $[La_{1/3}Ca_{2/3}MnO_3(t_{AF})/La_{2/3}Ca_{1/3}MnO_3(t_{FM})]_{15}$ multilayers reveals that the exchange-biasing strength and the CMR effect can be engineered by independently varying the AF (t_{AF}) and FM (t_{FM}) layer thicknesses.

Magnetic hysteresis loops, measured at 10 K after cooling down from 300 K in zero-field cooling (ZFC) and in 10 kOe (FC), are shown in Figure 56 for an $LaAlO_3$/[FM(4 nm)/AF(4 nm)]$_{15}$ film and an $SrTiO_3$/AF(40 nm)[FM(4 nm)/AF(4 nm)]$_{15}$ film. It is evident that the ZFC loop is symmetric around the zero field, while the FC loop is shifted toward negative fields. This effect can be attributed to exchange biasing at the AF–FM interface, since single-layered FM films do not exhibit any loop displacement after the FC process. If H_1 is the lower and if H_2 is the higher field value where the average film magnetization becomes zero, then the exchange-biasing field is defined as the loop shift $H_{EB} = -(H_1 + H_2)/2$ and the coercivity is defined as the half-width of the loop $H_c = (H_1 - H_2)/2$. Thus, for the FC loop on $LaAlO_3$ (LAO) we find an $H_{EB} = 780$ Oe with $H_c = 680$ Oe, and on $SrTiO_3$ (STO) an $H_{EB} = 690$ Oe with $H_c = 1000$ Oe.

In Figure 57, the variation of the normalized resistivity as a function of temperature, measured in 50 kOe (ρ_H) and in zero applied field (ρ_0) is shown. The resistivity increases drastically as we cool down from 300 K, spanning almost 4 orders of magnitude for the $LaAlO_3$/[FM(4 nm)/AF(4 nm)]$_{15}$ film whereas for the $SrTiO_3$/AF(40 nm)[FM(4 nm)/AF(4 nm)]$_{15}$ sample is less than an order of magnitude. The $\Delta\rho/\rho_H = [\rho_0 - \rho_H]/\rho_H$ ratio gives an estimate of the CMR effect. This ratio becomes

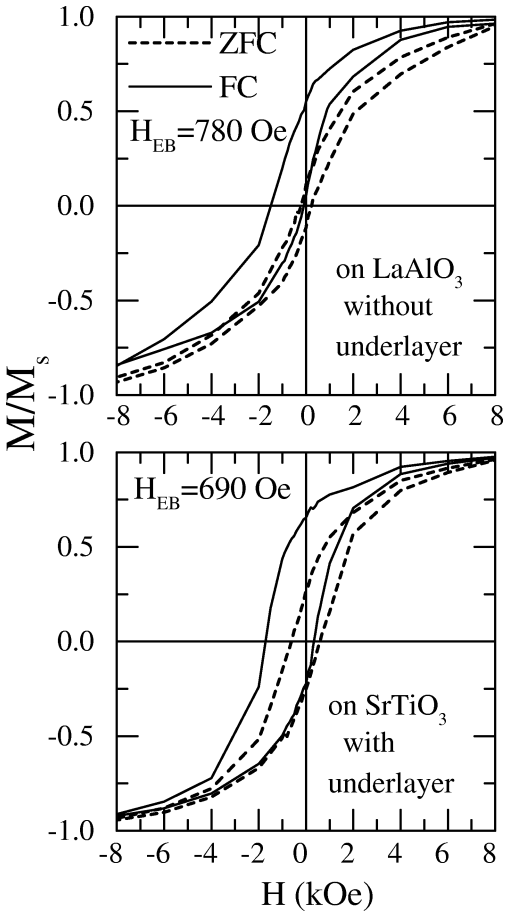

Fig. 56. Magnetic hysteresis loops, measured at 10 K after ZFC from 300 K and FC in 10 kOe, for an $LaAlO_3$/[FM(4 nm)/AF(4 nm)]$_{15}$ multilayer.

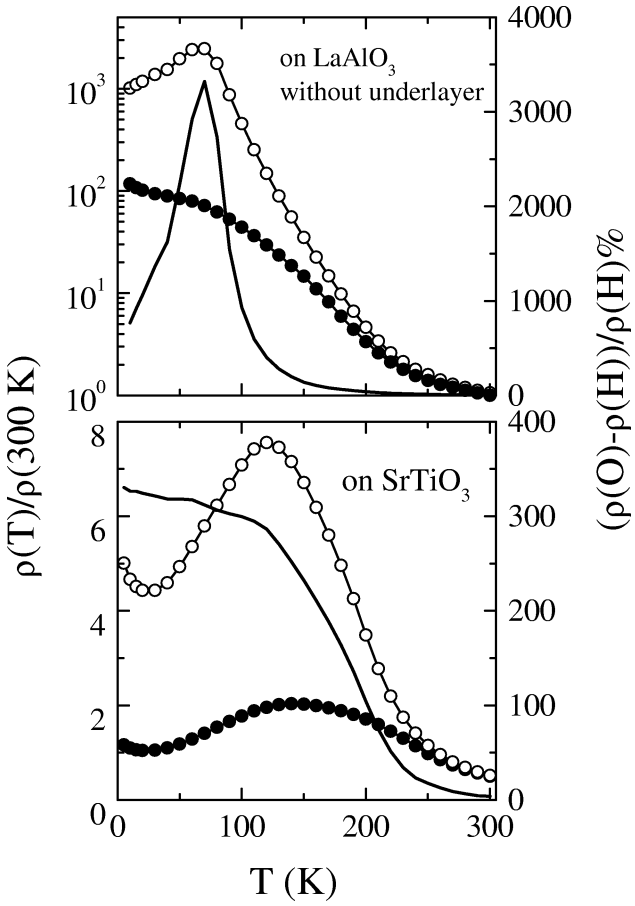

Fig. 57. Resistivity, normalized to the 300-K value, as a function of temperature, measured in 50 kOe (ρ_H) and in zero applied field (ρ_0) for a [FM(4 nm)/AF(4 nm)]$_{15}$ multilayer grown on $LaAlO_3$ and $SrTiO_3$ substrates. The CMR ratio $\Delta\rho/\rho_H = [\rho_0 - \rho_H]/\rho_H$ is plotted as a solid line.

maximum at ∼70 K for the multilayer film grown on LAO and at ∼120 K for that on STO. Thus, in both films the magnetotransport properties exhibit a number of different features relative to pure FM thin films [275, 276]:

(i) The temperature variation of ρ_H, ρ_0 and the resultant CMR curve exhibit their maxima at temperatures well below the ordering temperature (T_c) of the FM layers. The presence of the insulating AF layers of $La_{1/3}Ca_{2/3}MnO_3$ within the multilayered structure may explain the steep increase of resistivity [277] below 150 K that changes the shape of the curves near the maxima. In addition, the observed [275] magnetoresistive curves of 100-nm thick LAO(001)/$La_{2/3}Ca_{1/3}MnO_3$ films, grown under the same deposition conditions, have shown that there are no significant grain boundary and/or low-crystallinity effects [252, 278–280]. Thus, in this case there is no experimental evidence indicating that the increased low-temperature resistivity in Figure 57 originates from grain boundary effects.

(ii) The large differences (Fig. 57) observed in the CMR ratios between films grown on LAO and STO substrates show that the specific deposition conditions favor the enhancement of CMR on LAO. This can be attributed to strain relaxation inside the AF layers, since the AF film exhibits a pseudocubic lattice spacing ($a_p = 0.381$ nm) comparable to that of (100) LAO ($a_p = 0.379$ nm). Thus, the lattice mismatch along the (100) LAO–AF direction is about 0.5% while in the (100)STO–AF interface the lattice mismatch is about 2.2%. Assuming similar surface roughness in both substrates, it is evident that the lower lattice mismatch favors pseudomorphic growth with less strain inside the deposited layers.

The temperature dependence of H_{EB} and H_c values is shown in Figure 58 for $\Lambda = 8$ nm. These values were estimated from isothermal loops measured in constant temperature intervals, after FC the sample from 300 K down to 10 K in 10 kOe and then warming up. It is evident that H_{EB} decreases and disappears around the so-called blocking temperature T_B about 70 K. The H_c values exhibit a similar trend, indicating a connection between the mechanisms that give rise to coercivity and loop displacement. The excess coercivity observed below T_B is induced by random exchange fields at the AF–FM interfaces. This low-temperature anisotropy can be treated as an additional energy barrier in the magnetic free energy, as in the case of superparamagnetic particles [149]. Thus, by applying the same model we derive an equation that describes the temperature

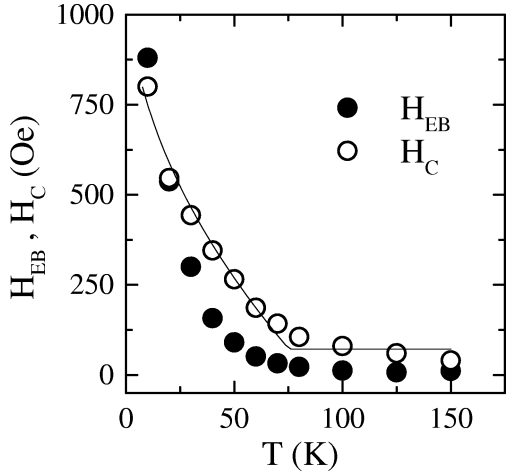

Fig. 58. Temperature dependence of H_{EB} (open circles) and H_c (solid squares) observed in $LaAlO_3$/AF(40 nm)/[FM(4 nm)/AF(4 nm)]$_{15}$ multilayer. The solid line presents a fitting curve according to Eq. (18).

variation of $H_c(T)$ with T,

$$H_c(T) = H_c(0)[1 - (T/T_B)^{1/2}] + H_{\text{back}} \qquad (18)$$

where H_{back} ($\approx$70 Oe) takes into account the observed coercivity above the obtained T_B at 75 K. In Figure 58, a good agreement between the experimental data (open circles) and the fitting curve (solid line) is observed. The existence of an H_{back} term can be explained from the magnetic phase diagram [269], showing that bulk $La_{1/3}Ca_{2/3}MnO_3$ undergoes a *charge-ordering* transition [277] below 260 K, whereas the long-range AF order sets in below 150 K. Thus, above T_B a large H_{back} may arise from magnetic disorder at the AF–FM interfaces due to short-range magnetic interactions inside the $La_{1/3}Ca_{2/3}MnO_3$ layers that persist up to *charge-ordering* transition of the multilayer. Accordingly, below T_B the enhancement of H_c is due to exchange anisotropy related to long-range AF interactions at the interfaces.

In Figure 59, the ZFC and FC measurements of the magnetization, normalized to the total FM volume of the sample, are shown for different Λ as a function of temperature. Both measurements were performed by warming up in 1 kOe after having cooled in zero field and 10 kOe, respectively. The ZFC and FC curves coincide at temperatures higher than 100 K and become zero at about 250 K, where the Curie point T_c of the FM layers is expected. The ZFC curve exhibits a broad peak around the $T_B \sim 70$ K, whereas the FC curve exhibits a steep increase just below T_B. It is reasonable to assume that in the FC measurement an increase of magnetization results from the alignment of interfacial magnetic moments, giving rise to unidirectional anisotropy [254] below T_B. Hence, the observed hump below T_B in the ZFC curve can be attributed to thermally activated magnetic rotation over energy barriers caused by random exchange coupling at the AF–FM interfaces.

Figure 60 shows the variation of the normalized resistivity as a function of temperature, measured in 50 kOe (ρ_H) and in zero applied field (ρ_0). The resistivity increases drastically as

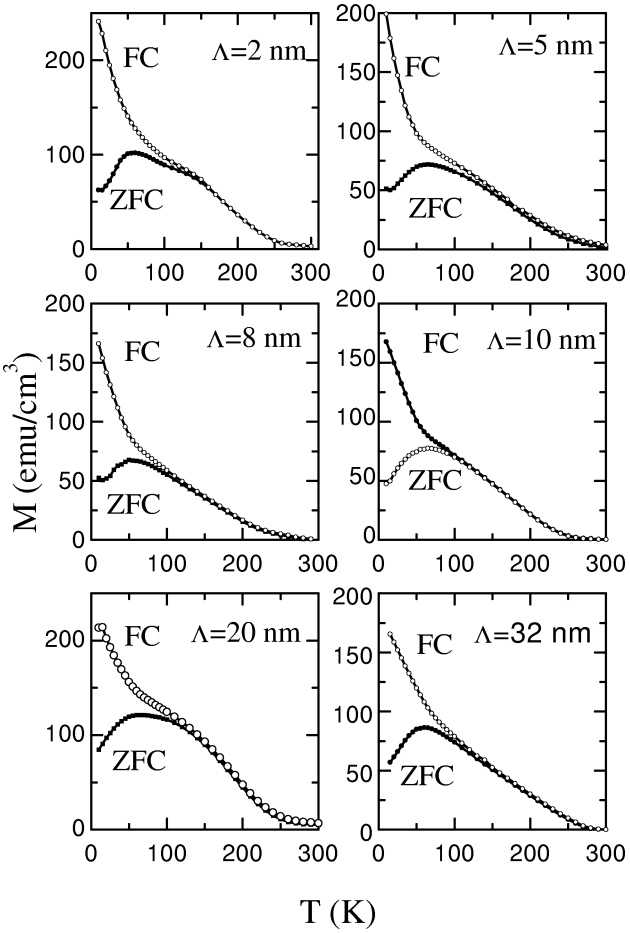

Fig. 59. ZFC and FC measurements of magnetization for a series of $LaAlO_3$/AF(40 nm)/[FM(Λ/2)/ AF(Λ/2)]$_{15}$ multilayers.

we cool down from 300 K, spanning almost 4 orders of magnitude. Additionally, the CMR ratio becomes maximum in the temperature range below T_B ($\approx$70 K). In Figure 60, the steep increase of resistivity at low temperatures is in contrast with the decrease of ρ observed in epitaxial FM films [275, 276]. This provides further experimental evidence that the insulating behavior [277] of the AF layer is dominant at low temperatures.

This extra contribution in ρ is different for every specimen and modifies the shape of the resultant CMR curves (Fig. 60). Clearly, the multilayers with Λ=5 and 8 nm exhibit a peak in the CMR response, indicating a special arrangement of spins at the AF–FM interfaces. As a consequence, the characteristic CMR peak, that is usually reported near the ferromagnetic T_c of $La_{2/3}Ca_{1/3}MnO_3$ films [241], is not observed in the ρ_0 versus temperature curve. This behavior is in agreement with the magnetothermal measurements (Fig. 59) where it is evident that the most drastic change of the average film magnetization does not occur near the T_c of the individual FM layers but at T_B. To answer why T_B remains more or less the same in the examined range of Λ values, it is reasonable to consider that interfacial spin ordering is confined within a few atomic planes near the AF–FM interfaces, defining an *active* film volume V_{int}. Since T_B results from a thermally activated process, following an Ar-

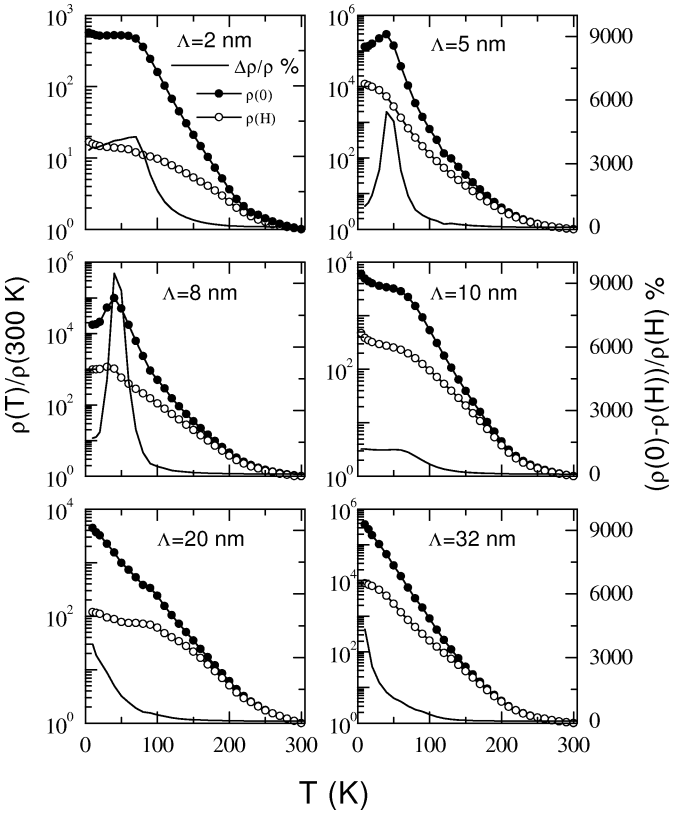

Fig. 60. Resistivity, normalized to the 300-K value, as a function of temperature, measured in 50 kOe (ρ_H) and in zero applied field (ρ_0) for a series of $LaAlO_3$/AF(40 nm)/$[FM(\Lambda/2)/AF(\Lambda/2)]_{15}$ multilayers. The CMR ratio $\Delta\rho/\rho_H = [\rho_0 - \rho_H]/\rho_H$ is plotted as a solid line.

rhenius law [149], its value depends on the active volume at the interfaces ($T_B \propto V_{\text{int}}$) which emerges to be similar in the examined multilayers.

Generally, the enhanced coercivity H_c observed [250–252], in exchange-coupled FM–AF layers relative to the uncoupled FM layer is an unresolved theoretical issue. Figure 58 shows that the observed behavior of H_c and H_{EB} with increasing temperature can be attributed to the complex mechanisms through which charge and spin ordering occurs in the $La_{1/3}Ca_{2/3}MnO_3$ layers [269, 277]. In particular, the temperature dependence of the size of the magnetic domains inside the AF layers should be of key importance in exchange-biased manganites. Another study [274] of $[La_{1/3}Ca_{2/3}MnO_3(t_{\text{AF}})/La_{2/3}Ca_{1/3}MnO_3(t_{\text{FM}})]_{15}$ multilayers grown with variable AF–FM compositions (one series with constant $t_{\text{AF}} = 3$ nm while $t_{\text{FM}} = 1.5$, 3, 4.5, 6 nm and the other with constant $t_{\text{FM}} = 3$ nm while $t_{\text{AF}} = 1.5$, 3, 4.5, 6 nm) reveals that there are two important issues associated with exchange-biased CMR-manganite multilayers. One is the physical origin of the exchange-biasing mechanism itself and the other is the observed independence of T_B on t_{AF} or t_{FM}.

Zero-field-cooling and field-cooling magnetic measurements [274] have revealed that T_B is independent from the FM and the AF layer thickness, indicating that compositional modulation at the $La_{1-x}Ca_xMnO_3$ interfaces are of key importance to the exchange-biasing mechanism in La–Ca–Mn–O-based multilayers. The compositional modulation that occurs at the $La_{1-x}Ca_xMnO_3$ interfaces is important because the type of magnetic interactions is defined by the competition between the double-exchange FM coupling and the AF superexchange interactions [272, 273]. Geometrical (topological) roughness and interdiffusion between adjacent atomic planes with $x = 1/3$ and $2/3$ stoichiometries produces an artificial change of concentration to $x \approx 0.5$ at the interfaces. Thus, the sequence of magnetic phase transitions might be altered at low temperature in regions with $La_{1/2}Ca_{1/2}MnO_3$ stoichiometry. Bulk measurements [241, 269] at $x \approx 0.5$ composition show that the high-temperature FM-conducting phase is followed by a charge-ordering transition, resulting in an AF insulator below 120 K. Furthermore, a theoretical study [281] shows that the charge ordering observed in 50% doped manganites corresponds to an unusual AF-spin ordering, which exhibits a unique electronic structure with a band-insulator behavior. As a result [281], strong anisotropy of short-range double-exchange interactions is formed at the charge-ordering transition. Since both the T_B and the exchange anisotropy fields appear at about 70 K, that is well below the low-temperature magnetic phase transition for bulk $La_{1/2}Ca_{1/2}MnO_3$, it is reasonable to assume that the appearance of exchange biasing depends on the magnetic ordering of interfacial atomic planes inside an interface volume with $x \approx 0.5$ doping. These interface boundaries define a critical volume where thermal-activation energy becomes less than the low-temperature magnetic energy of $La_{1/2}Ca_{1/2}MnO_3$ at a certain T_B value. Consequently, nearly perfect interfaces (small roughness) will always correspond to the same interface volume with $x \approx 0.5$, giving the same T_B. Since the interface volume with $x \approx 0.5$ doping is fixed for all thicknesses of AF ($x = 2/3$) or FM ($x = 1/3$) layers, this model describes the observed independence of T_B on t_{AF} or t_{FM}.

Exchange biasing has been observed either in multilayers with alternating layers [268, 274] of FM $La_{2/3}Ca_{1/3}MnO_3$ and AF $La_{1/3}Ca_{2/3}MnO_3$ compositions or in $La_{0.67}Ca_{0.33}MnO_3$ (FM)/$La_{0.5}Ca_{0.5}MnO_3$(AF) bilayers [282] below a blocking temperature (T_B), which is much less than the magnetic ordering temperatures of the AF (T_N) and the FM (T_c) layers. Generally, the temperature dependence of exchange bias and coercivity at low-T can be modeled by considering two possible factors [284, 285]: (i) the temperature dependence of the magnetic anisotropy coefficient K_A in the AF layer, the exchange stiffness constant A_{AF} in the AF layer, and the energy of a domain wall σ^A_{dw} in the AF (ii) thermally activated switching of AF grains. The former has been attributed [284–286] to magnetization reduction that is basically controlled by long-wavelength spin waves at low-T. The latter causes there to be a blocking temperature T_B that is well below the T_N. Above the T_B the AF order in the grains is not stable, [284] and no unidirectional anisotropy (exchange bias) develops. Below the T_B, the AF order becomes stable and the unidirectional anisotropy at low-T depends [284] on the ratio of the average interfacial coupling energy to the domain wall energy. Furthermore, it was observed [285, 286] that exchange-coupled layers with a

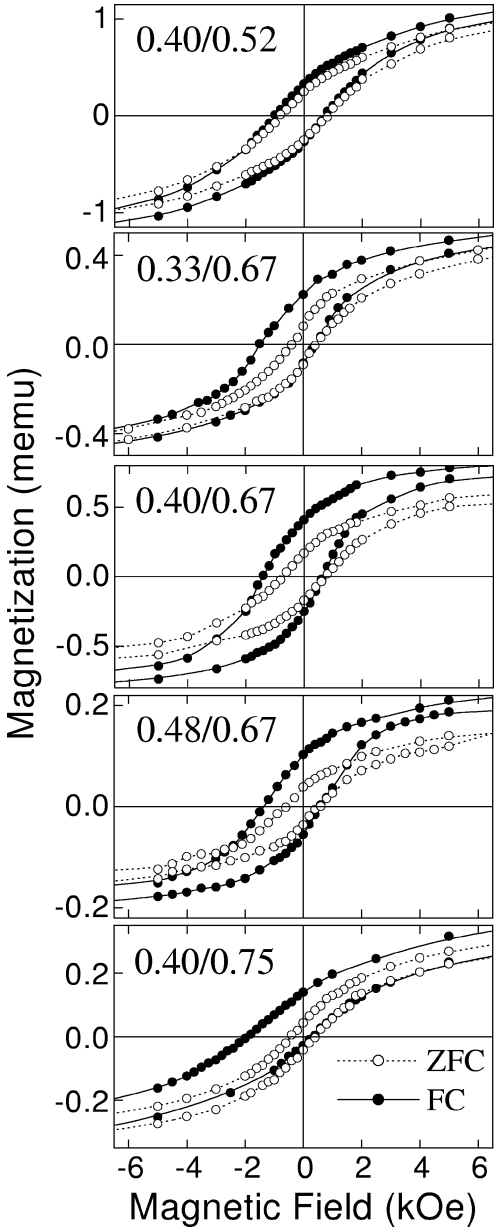

Fig. 61. Magnetic hysteresis loops, measured at 10 K after ZFC from 300 K (dashed line) and FC (solid line) in 50 kOe on $La_{1-x}Ca_xMnO_3$(FM)/ $La_{1-y}Ca_yMnO_3$(AF) multilayers. For brevity, we named the samples by the Ca^{2+} concentration ratio x/y used.

$T_B < T_N$ exhibit assymetric hysteresis loops due to irreversible transitions of the AF order in the AF grains.

Compositionally modulated structures consisting of $La_{1-x}Ca_xMnO_3$ FM layers ($x = 0.33, 0.4, 0.48$) and $La_{1-y}Ca_yMnO_3$ AF layers ($y = 0.52, 0.67, 0.75$) were grown on (001)$LaAlO_3$ to investigate [283] the effect of interfacial composition on the temperature dependence of exchange bias and coercivity at low-T. For brevity, we named the samples by the Ca concentration ratio x/y used. The coercive- and exchange-biasing fields were derived from isothermal loops at low temperatures after zero-field cooling (ZFC) from 300 K and FC in 50 kOe. Typical FC and ZFC loops taken at 10 K are shown in Figure 61. Below 70 K, the ZFC loops are symmetric around zero, whereas the FC loops are shifted toward negative fields, evidencing exchange-biasing mechanisms in all the samples. The H_{EB} is defined as the loop shift and the H_c as the halfwidth of the loop. Thus, if H_1 and H_2 are the fields for which the descending and ascending parts of a hysteresis loop intercept the abscissa, then $H_{EB} = -(H_1 + H_2)/2$ and $H_c = -(H_1 - H_2)/2$.

The magnetothermal ZFC and FC curves in Figure 62 were performed by warming up in 100 Oe after having cooled in zero field and 50 kOe, respectively. In all samples, the bifurcation of the FC and the ZFC magnetizations occurs at temperatures T_{bif}, ranging between 155 K and 215 K, whereas exchange biasing can be detected only below 70 K. Apparently, all the FC curves exhibit a steep decrease of M_{FC} between 5 and 70 K, which defines [263] a blocking temperature T_B. In particular, the magnitude of the M_{FC} at T_B becomes about three times less than the M_{FC} at 5 K, whereas the M_{FC} at 5 K is very close to those expected from the saturation magnetization M_s of the corresponding [287] FM layer. These magnetothermal properties are reminiscent of those observed for an ensemble of fine magnetic grains [288]. Thus, strong thermal fluctuations of magnetic domains are responsible for the observed decrease of magnetic moments in the FM layer. According to literature [284, 285, 289] such an effect comes from the coupling of a FM layer, that exhibits uniform magnetization, to a polycrystalline AF layer with small enough AF grains that they do not break up into domains.

To investigate the dependence of H_{EB} and H_c on the H_{FC}, a sequence of FC loops has been measured by warming up at 5, 10, 20, 30, 40, 50, 60, 70 K in six rounds of FC processes. Each sequence is using one of the six $H_{FC} = 5$, 10, 20, 30, 40, 50 kOe. Each loop in a sequence is performed at a maximum field equal to H_{FC} used. Figure 63 shows the temperature dependence of H_1 and H_2 values, where the average film magnetization becomes zero in a FC loop, on each of the H_{FC} used in the 0.40/0.67 sample. Similar results were observed in samples with $(x + y)/2 \geq 0.5$. Initially, it seems that the dependence of H_{EB} on H_{FC} is due to minor-loop effects. However, in Figure 63 the H_2 is strongly enhanced below ~70 K by increasing the applied H_{FC} from 5 up to 50 kOe, whereas the H_1 is the same, resulting in a constant sum $H_{EB} + H_c^{FC} = H_1$ as a function of H_{FC} at a given temperature. Thus, such assymetric hysteresis loops cannot be attributed to minor-loop effects. In addition, above 70 K ($\approx T_B$) the H_{EB} approaches zero, whereas the H_c^{FC} converges at similar values, indicating that the applied H_{FC} affects in a different way the micromagnetic state only when the exchange-biasing sets in the AF/FM interfaces.

Figure 64 shows the variation of H_{EB} and H_c at low temperatures. Both exhibit an exponential, rather than a power-law [284–286], decrease as a function of temperature. Such an exponential thermal decay of H_c has been observed in some rare-earth pseudobinary compounds [290] and amorphous materials [291], showing that at low temperatures: $H_c(T) = H_c^0 e^{-bT}$ with b a constant and H_c^0 the extrapolation of coercivity at 0 K. It is worth noting that an exponential decay function fits both the H_{EB} and H_c for all the examined cases, whereas

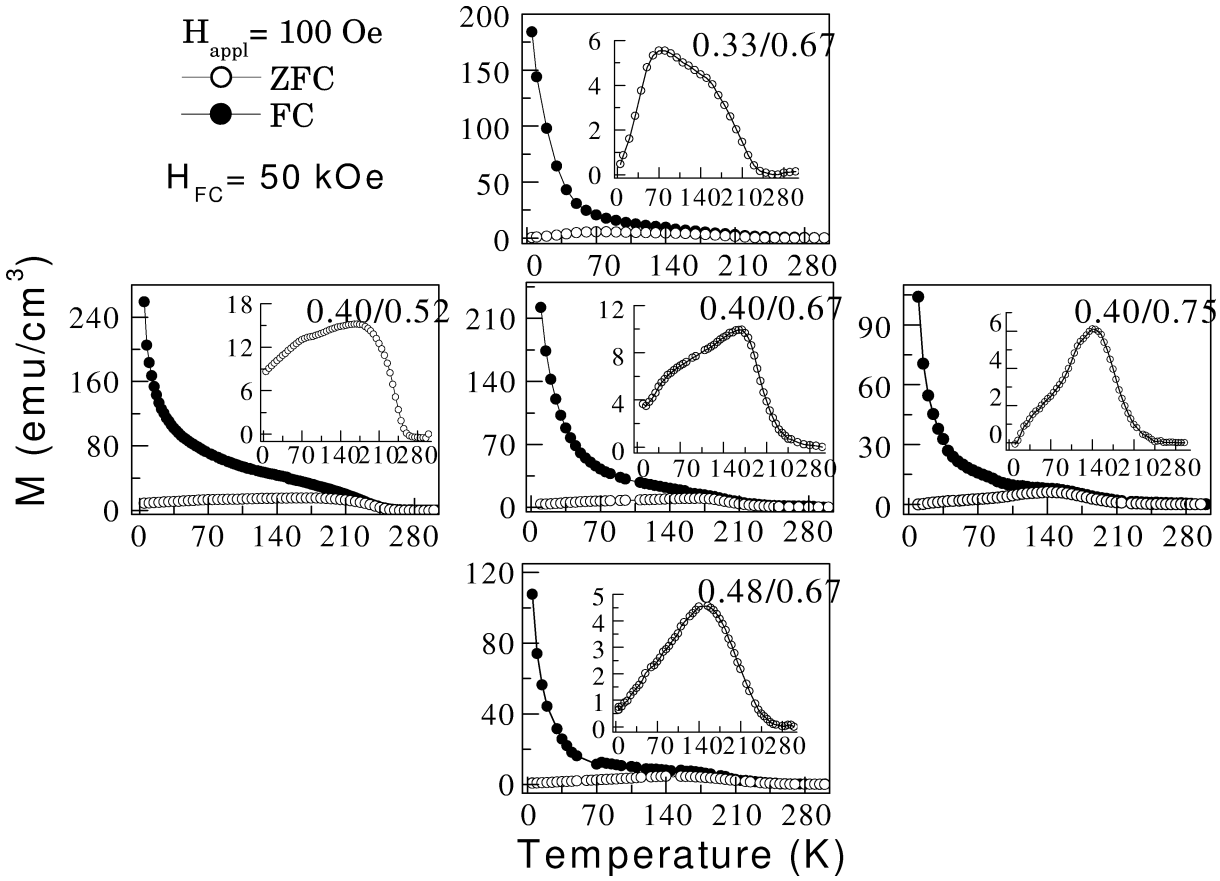

Fig. 62. ZFC and FC magnetothermal measurements performed in a field of 100 Oe on $La_{1-x}Ca_xMnO_3$(FM)/$La_{1-y}Ca_yMnO_3$(AF) multilayers. For brevity, we named the samples by the Ca^{2+} concentration ratio x/y used. The magnetization is normalized to the total FM volume of its sample. The inset shows the ZFC curves.

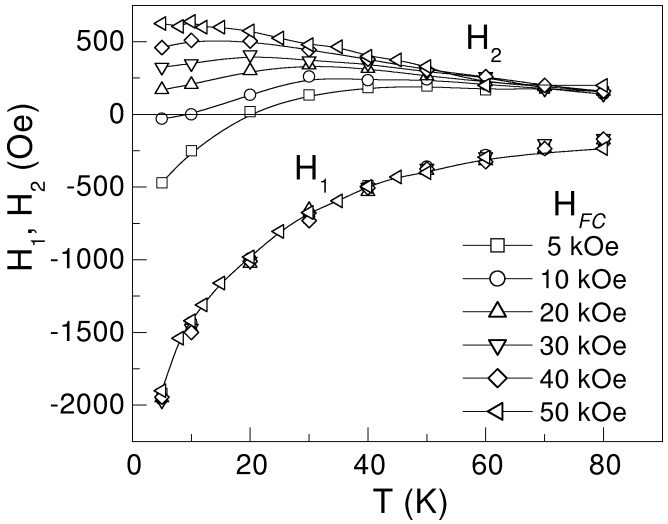

Fig. 63. The temperature dependence of H_1, H_2 at different H_{FC} values applied in exchange coupled $La_{0.6}Ca_{0.4}MnO_3$(FM)/$La_{0.33}Ca_{0.67}MnO_3$(AF) multilayers.

Eq. (18) is limited only in H_c values only for the 0.33/0.67 sample.

Generally, the ground state of the $La_{1-x}Ca_xMnO_3$ system is either FM or AF, depending on Ca doping x that determines the Mn^{3+}:Mn^{4+} ratio, the phase boundary being at $x \approx 0.5$. In the compositionally modulated multilayers considered here, the interfacial Ca concentration x crosses the phase-diagram boundary at $x \approx 0.5$. For $x \approx 0.5$ their properties are very sensitive to the application of magnetic fields [292], affecting both the crystallographic and magnetic phases as a function of temperature. Specifically, the behavior [292] of bulk $La_{1-x}Ca_xMnO_3$, with $x = 0.5$ or $x = 0.53$, shows that below 200 K a FM and an AF phase coexist microscopically, and they transform from one to another as a function of temperature or magnetic field. Furthermore, the AF superexchange (interaction between localized spin moments of Mn^{3+}–Mn^{3+} ions) and the FM double-exchange (transfer of electrons between neighboring Mn^{3+}–Mn^{+4} ions) interactions compete with each other via interface exchange [293]. The existence of frustration due to competing interactions is known to lead to an exponetial decay of H_c, H_{EB} as it has been observed in amorphous/crystalline $NiFe_2O_4$ ferrite [294] and FM/spin-glass Ni/$Ni_{76}Mn_{24}$ bilayers [295]. Thus, it is reasonable to fit the observed H_{EB} and H_c (Fig. 64) with:

$$H_{EB}(T) = H_{EB}^0 \exp(-T/T_1)$$
$$H_c(T) = H_c^0 \exp(-T/T_2) \qquad (19)$$

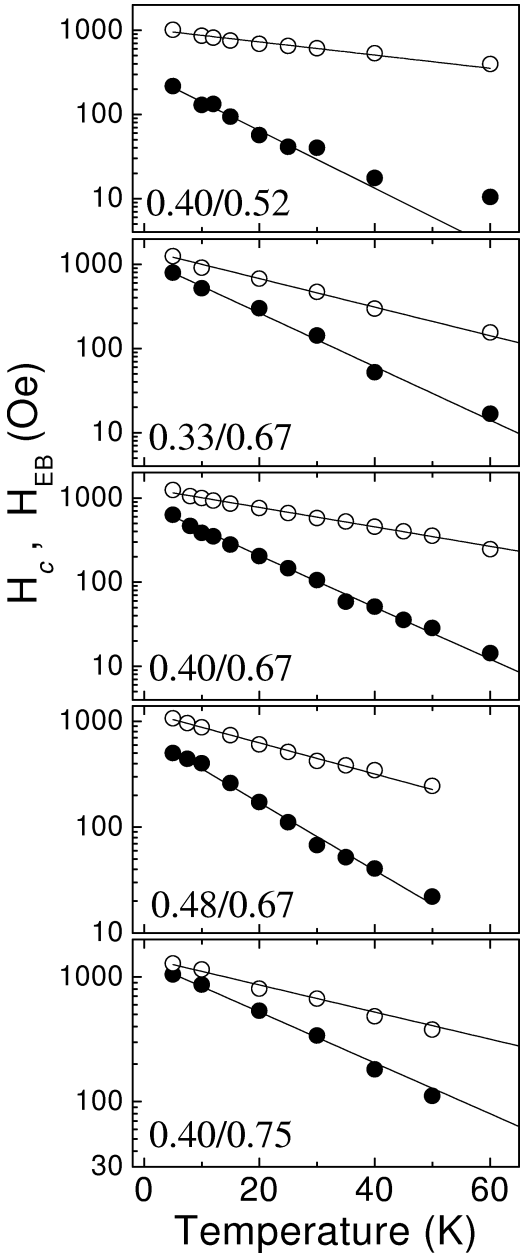

Fig. 64. Temperature dependence of H_{EB} (open circles) and H_c (solid circles) after field cooling in 50 kOe. The solid lines are fits from Eq. (19).

Figure 65 shows the obtained H^0_{EB}, H^0_c, T_1, and T_2 values against the average (interfacial) Ca nominal composition $\xi = (x + y)/2$. These plots reveal a quasilinear increase (decrease) of H^0_{EB} and H^0_c when the Mn^{4+} concentration y increases (is constant) in the AF layers, while the Mn^{4+} concentration x is constant (increases) in the FM layers. However, the variation of T_1 and T_2 parameters does not follow a systematic dependence on ξ, and their values are less than the observed T_B, where $H_{EB} = 0$, in each sample. This result can be associated with a continuous distribution of blocking temperatures due to statistical distribution of superparamagnetic domains. The fact that all the examined samples exhibit $H_{EB} = 0$ above the same temperature (at about 70 K) indicates that there is a similar distribution of superparamagnetic domains. In NiFe/NiO bilayers [296] such a distribution of local T_B's was related with a variety of exchange paths that is caused by inhomogeneous interfaces due to interfacial disorder and fluctuating atomic arrangement. In (La,Ca)MnO_3 multilayers, similar interface effects can be related with the induced change of Ca^{2+} concentration from x to y.

Today, two of the unsolved issues [5, 24, 284, 289] that are associated with the exchange biasing effect concern the shape and the location of the domain wall in the FM or the AF layer. The present study shows that the exchange coupling properties of (La,Ca)MnO_3 FM/AF compositionally modulated structures are related, as expected, with these two issues but exhibit an unexpected exponential thermal decay. The observed exponential thermal decay cannot be reconciled with a model that is usually applied [284, 286, 289] for the temperature dependence of exchange coupling and domain wall σ^A_{dw} energies in the AF layer. This model assumes that the properties of the FM layer and the exchange coupling at the AF/FM interface are temperature independent, whereas the A_{AF}, σ^A_{dw} and K_A parameters exhibit thermal demagnetization by long-wavelength spin waves [284, 286].

A major result is that the thermal variation of H_{EB} and H^{FC}_c cannot be reconciled with models that use [284, 286] spin-waves as collective modes of spatially correlated thermal fluctuations in the AF layer. Thus, the exponential thermal decay indicates that the observed magnetic history depended (ZFC, FC) effects and the associated exchange biasing properties can be described by a thermal fluctuation model where short-range ordering or a spin-glass-like [24, 294] magnetic disorder is established in AF/FM interfaces. Another distinct feature of the examined multilayers is the observed (Fig. 63) asymmetry of H_1 and H_2. Direct experimental observations [289] of the magnetization reversal in exchange coupled NiO/NiFe bilayers has showed that the thin film remagnetization proceeds by domain-wall nucleation and motion. In this system, the observed [289] asymmetry in the activity of domain nucleation centers of NiO/NiFe bilayers has been attributed either to local variations of AF-anisotropy or crystal lattice defects. In parallelism, it can be assumed that such defects [297] can be associated with the asymmetry of H_1 and H_2 observed in (La,Ca)MnO_3 FM/AF multilayers on application (Fig. 63) of different H_{FC}.

5.4. Advantages, Drawbacks, and Prospects of CMR Films in Applications

The observation of a large negative magnetoresistance in thin-film manganites at room temperature has made this class of materials-potential candidate for magnetic sensing applications. The magnitude of magnetoresistance in manganate thin films can be orders of magnitude larger than that of metallic multilayers such as Co/Cu. However, large low-field magnetoresistance has been demonstated only at reduced temperature, whereas the mechanism that governs the large spin-dependent

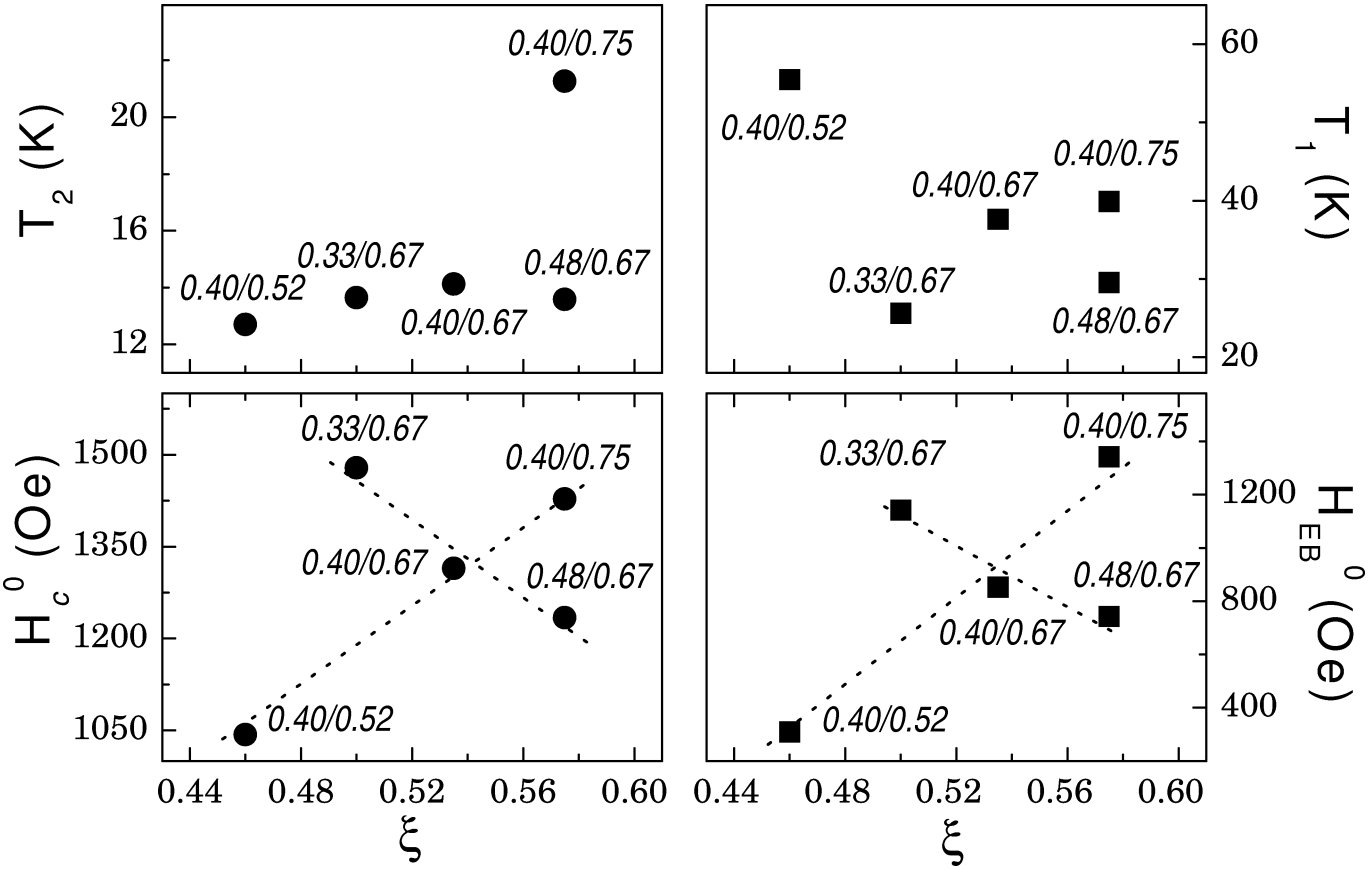

Fig. 65. The obtained values of H_{EB}^0, H_c^0, T_1 and T_2 at $T = 0$, after fitting the observed H_c(T) and H_{EB}(T) with Eq. 19, against $\xi = (x + y)/2$. Dot-lines are guides to the eye.

transport in the doped manganites is not yet fully understood.

Thus far, the most promising property of doped manganate perovskites for applications is the huge magnetoresistance observed by crossing the Curie temperature of the materials used. Some issues that face the major drawbacks for the applicability of this class of materials are listed below.

(i) Low-field magnetoresistance in the manganites has been observed only at reduced temperatures. A possible origin of this effect is that at room temperature a large leakage current across a defect-populated barrier layer acts as a shunt to the magnetoresistance [300].

(ii) Commonly used deposition techniques for perovskite oxide deposition include laser ablation, reactive sputtering, reactive ion-beam sputtering, coevaporation, MBE, and CVD (chemical vapor deposition). Laser ablation is most widely used in a laboratory environment for the deposition of such complex oxides because of the ease of obtaining stoichiometric transfer of material from target to substrate [301]. A major drawback for laser ablation is its limited scalability due to short target-to-substrate distance, demanding a substantial engineering effort for the deposition of films with >2-in diameter. Reactive sputtering excels in the deposition of large-area films. However, deposition of such complex oxides, involving more than one alkaline metal cation, becomes challenging because of the problem of nonstoichiometric transfer due to the resputtering effect. Reactive molecular beam epitaxy using thermal evaporation has been gaining momentum for large-area deposition.

(iii) One striking feature of the manganite films, epitaxial or polycrystalline, is the extreme sensitivity of their properties to postdeposition heat treatment [287]. This is probably related to the strong mutual dependence of the magnetic state and the local lattice configuration, especially that of the Mn−O−Mn bond length and bond angle.

(iv) Since a good lattice matching between the substrate and the manganite film is required for epitaxial growth, most commonly used substrates are single crystals of $SrTiO_3$ and $LaAlO_3$. However, there is progress in the successful growth of high-quality epitaxial thin films on buffered silicon substrates [302], which might be more interesting for technological reasons.

6. OUTLINE

Semiconductors are ubiquitous in device electronics because their charge distributions are easily shaped and controlled to make logic gates. Efforts to improve computational power have led to miniaturization of electronic devices to ever-shrinking

sizes that may soon bring additional complications in the form of quantum mechanical effects. These effects will introduce unpredictable fluctuations in essential design parameters, such as charge distribution, because quantum systems tend to behave statistically. Therefore, quantum statistical fluctuations will affect a chip's performance as device sizes shrink. In the near future, miniaturization may ultimately force the industry to consider alternative schemes for electronics and to embrace nonclassical electronic behavior by controlling the electron spin, rather than its charge—the basis for the new field of *spintronics*.

The use of spin effects in metallic GMR multilayers has led rapidly to commercial applications [301] such as magnetic field sensors, spin-valve read heads for hard-disk drives, GMR gradiometers, magnetic RAM, and GMR isolators. It is perhaps remarkable that in the last few years, magnetic multilayers have evolved from a scientific curiosity to become materials of significant technological importance. This class of magnetic multilayers has revealed a considerable number of scientific insights while the study of their properties has led to significant developments in the preparation of ultrathin (one or two atomic layers thick) magnetic multilayered structures that can now be routinely produced for commercial applications. Currently, there still exist some important subjects for research and development in GMR multilayers or spin-valve structures that may considerably improve the performance of their devices.

In particular, the effect of grain size and crystalline orientation on magnetic switching, magnetoresistance, micromagnetism, and domain-wall scattering is becoming a topic of great current interest in Co-based thin films that exhibits columnar grain morphology or stripe domains. This has been initiated from the relatively large negative magnetoresistance observed [304] at room temperature in epitaxial (0001)-oriented hcp-Co thin films with stripe domains and have been interpreted in terms of a giant domain-wall scattering contribution to the resistivity. In contrast, measurements of the resistivity for currents parallel and perpendicular to domain walls of epitaxial hcp Co indicate that the large negative room-temperature MR is due to the film micromagnetic structure and ferromagnetic resistivity anisotropy whereas the intrinsic effect of domain-wall interface scattering is minor. This result is consistent with the fact that the GMR in layered structures is not an intrinsic quantum mechanical effect of the constituents, but is an interface related effect evidencing macroscopic quantum phenomena. The importance of film morphology and interface roughness has been clearly demonstrated in the case of epitaxial Co/Cu(111) and polycrystalline multilayers. Polycrystalline GMR multilayers based on fcc Co magnetic layers are of particular interest in sensor applications due to the larger GMR ratios at ambient conditions. Thus, understanding the magnetic switching characteristics of patterned film elements is critical to the performance of small size magnetoresistive devices. Not only are the geometric shape and the intrinsic magnetic properties important to magnetic switching, but also are the film microstructures as well. Section 4 shows how the orientation, texture, and size of the crystallites affect the switching (hysteresis and saturation fields) properties. Micromagneting modeling of patterned fcc-Co film elements shows [177] that large grains result in a large switching field for a polycrystalline Co film element. In addition, the switching field is much higher in (001)- and (110)-oriented single-crystal elements than that of (111)-oriented elements.

Currently, two-dimensional phenomena in ultrathin-film magnetism attract a considerable interest and activity now focuses on the complexities of exchange coupling and anisotropy to understand the unusual hysteresis loops that appear in magnetic multilayers. There is steadily accumulating experimental evidence that growth-induced surface roughness can profoundly affect magnetization reversal and coercivity in ultrathin films. Scanning tunneling microscopy graphically demonstrates that roughness at the monolayer scale is the best that can be achieved for any coverage of deposited material [305]. For this reason, even the best as-grown or annealed ultrathin films have some step edges associated either with the perimeter of monolayer-height islands that nucleate during growth or with the steps of an intentionally miscut substrate. This is significant because the magnetic anisotropy at sites of reduced crystallographic symmetry can compete successfully with the intrinsic anisotropy of the flat surface and thereby can control coercivity and magnetization reversal. Such effects can be advantageous in the design of spin-valve sensors. As described in Section 2, growth of few atomic layers of Co on a stepped Cu substrate (miscut by 0.1° with respect to the (100) orientation) defines an easy magnetization parallel to the step edges. This preferred anisotropy axis can replace the external biasing process required to achieve the 90° orientation between the magnetization directions of the pinned and free magnetic layers in spin valves.

A major problem in spin-valve sensors is magnetic stabilization because small-geometry MR sensors exhibit a spontaneous tendency to break up into complicated multidomain states which result in serious (Barkhausen) noise problems during sensor operations. Past studies [306] had shown that, among many factors, the shape demagnetization effect is the primary cause for multidomain formation. This understanding has led to the development of *tail stabilization*, in which the read region of the sensor is stabilized in a single-domain state by preparing longitudinally aligned tail regions on both sides of the read region [307]. These longitudinally aligned tail regions can be created by exchange biasing of a soft magnetic layer with either an antiferromagnet (i.e., NiFe/FeMn) or a hard ferromagnet (NiFe/$Co_{75}Pt_{12}Cr_{13}$) or by using a longitudinally aligned hard magnet (i.e., $Co_{75}Pt_{12}Cr_{13}$) as the only magnetic layer in the tail region. However, exchange-biased bilayers exhibit a number of unusual properties [308], such as positive exchange bias, perpendicular coupling, rotational hysteresis at high fields, magnetic training effects, measurement-dependent loop shifts, memory effects, and asymmetrically shaped hysteresis loops. Furthermore, the remanent magnetization of a hard ferromagnetic $Co_{75}Pt_{12}Cr_{13}$ layer is progressively decreased by repeated switching of a neighboring soft magnetic layer due to domain-wall induced coupling between the ferromagnetic layers [309]. To avoid such exchange-bias problems, a novel [310, 311] ap-

proach uses an alternative design by modifying the shape of the sensing element from rectangular to "end-tapered" spin valves or to "eye-shaped" ferromagnetic layers. This patterning process promotes the coherent rotation of magnetization reversal within the sensing area. In this way the problem of multidomain breaking during the magnetization reversal process can be solved.

Today, the emerging field of magnetoelectronics promises huge enhancements of the speed, reliability, and power consumption of solid-state memory. Ongoing research is focused on developing materials systems consisting of hybrid magnetic tunnel junctions (MTJ) that combine ferromagnetic transition metal (i.e., Co) and manganate perovskite (i.e., $La_{0.7}Sr_{0.3}MnO_3$) electrodes separated by an insulating, ultrathin oxide (i.e., $SrTiO_3$) barrier. Such MTJ exhibit TMR ratios of ∼50% at 5 K which reduce to ∼5% at room temperature [312] due to the low Curie temperature of the strongly spin-polarized $La_{0.7}Sr_{0.3}MnO_3$ electrode. However, other types of oxides of the double-perovskite family combine [313] electronic properties similar to those of manganites with a definitely higher Curie temperature. The challenge to build TMJ structures from double-perovskite materials (i.e., Sr_2FeMoO_6) may open the way for a new generation of tunnel junctions with very high magnetoresistance for room-temperature applications.

In the world of storage, success means enabling users to reliably store and to manage a seemingly endless amount of data as effortlessly as possible, whether it be in a commercial data warehouse, a home computer, or a portable computer on the road. As magnetic disk drives and solid-state magnetic memories become smaller, cheaper and more capacious, new applications will become feasible. Surely, sometime in the twenty-first century, it will become commonplace for people to wear a variety of electronic devices, all communicating with each other and all demanding more storage. The steady improvement in magnetic data storage and retrieval technology raises the question: How long can progress continue? Are there any intractable limits that threaten to prevent future advances? In the future, disk-drive designers are approaching a limit determined by fundamental physics, not engineering ingenuity. As the volume of magnetic material within a single bit (reading head) shrinks to increase areal density (resolution), there comes a point beyond which random jiggling of the electron spins due to temperature is likely to cause the direction of a bit's (head's) magnetization to undergo spontaneous reversals within the expected lifetime of the disk drive. This superparamagnetic limit will eventually limit the progress we can achieve by simply scaling down existing technology. However, it is difficult to estimate when the superparamagnetic limit will be reached, because it depends on many factors, including specific properties of the particular materials being used. A first estimation for the upper limit of magnetic storage devices can be encountered at densities of somewhere between 40 to 100 gigabits per square inch, which is about two to five times greater than those available today. The more promising technologies likely to achieve substantially higher storage densities and product-level performance include those based [314] on holography and molecular-scale devices, as well as other novel techniques, such as scanning interferometric apertureless microscopy.

REFERENCES

1. J. Fraden, "Handbook of Modern Sensors," Am. Inst. of Phys., 2nd ed., Woodbury, NY, 1997.
2. D. Weller and A. Moser, *IEEE Trans. Magn.* 35, 4423 (1999).
3. A. Chiu, I. Croll, D. E. Heim, R. E. Jones Jr., P. Kasiraj, K. B. Klaassen, C. D. Mee, and R. G. Simmons, *IBM J. Res. Develop.* 40, 283 (1996).
4. T. R. McGuire and R. I. Potter, *IEEE Trans. Magn.* MAG-11, 1018 (1975).
5. R. C. O'Handley, "Modern Magnetic Materials," Chap. 15. Wiley, New York, 2000.
6. P. C. Andricacos and N. Robertson, *IBM J. Res. Develop.* 42, 671 (1998).
7. M. N. Baibich, J. M. Broto, A. Fert, F. Nguyen Van Dau, F. Petroff, P. Etienne, G. Greuzet, A. Friederich, and J. Chazelas, *Phys. Rev. Lett.* 61, 2472 (1988).
8. G. Binasch, P. Grünberg, F. Saurenbach, and W. Zinn, *Phys. Rev. B* 39, 4828 (1989).
9. B. Dieny, V. S. Speriosu, S. S. P. Parkin, B. A. Gurney, D. R. Wilhoit, and D. Mauri, *Phys. Rev. B* 43, 1297 (1991).
10. B. Dieny, V. S. Speriosu, S. S. P. Parkin, P. Baumgart, and D. R. Wilhoit, *J. Appl. Phys.* 69, 4774 (1991).
11. B. Dieny, *J. Magn. Magn. Mater.* 136, 335 (1994).
12. C. H. Tsang, R. E. Fontana Jr., T. Lin, D. E. Heim, B. A. Gurney, and M. L. Williams, *IBM J. Res. Develop.* 42, 103 (1998).
13. S. S. P. Parkin and D. Mauri, *Phys. Rev. B* 44, 7131 (1991).
14. M. Johnson, *IEEE Spectr.* 37, 33 (2000).
15. S. Tehrani, E. Chen, M. Durlam, M. DeHerrera, J. M. Slaughter, J. Shi, and G. Kerszykowski, *J. Appl. Phys.* 85, 5822 (1999).
16. S. S. P. Parkin, K. P. Roche, M. G. Samant, P. M. Rice, R. B. Beyers, R. E. Scheuerlein, E. J. O'Sullivan, S. L. Brown, J. Bucchigano, D. W. Abraham, Y. Lu, M. Rooks, P. L. Trouilloud, R. A. Wanner, and W. J. Gallagher, *J. Appl. Phys.* 85, 5828 (1999).
17. M. Johnson, *J. Magn. Magn. Mater.* 156, 321 (1996).
18. B. E. Kane, *Nature* 393, 133 (1998).
19. S. J. C. H. Theeuwen, J. Caro, K. P. Wellock, S. Radelaar, C. H. Marrows, B. J. Hickey, and V. I. Kozub, *Appl. Phys. Lett.* 75, 3677 (1999).
20. S. Nagamachi, M. Ueda, H. Sakakima, M. Satomi, and J. Ishikawa, *J. Appl. Phys.* 80, 4217 (1996).
21. S. Y. Chou, *Proc. IEEE* 85, 652 (1997).
22. T. J. Moran and E. D. Dahlberg, *Appl. Phys. Lett.* 70, 1894 (1997).
23. www.nve.com/technical/GMR/.
24. J. Nogues and I. K. Schuller, *J. Magn. Magn. Mater.* 192, 203 (1999).
25. M. M. Chen, N. Ghersallah, G. Gorman, and J. Latimer, *J. Appl. Phys.* 69, 5631 (1991).
26. H. J. M. Swagten, G. J. Strijkers, P. J. H. Bloemen, M. M. H. Willekens, and W. J. M. de Jonge, *Phys. Rev. B* 53, 9108 (1996).
27. C. Tsang, T. Lin, S. MacDonald, N. Robertson, H. Santini, M. Doerner, T. Reith, L. Vo, T. Diola, and P. Arnett, *IEEE Trans. Magn*. 33, 2866 (1997).
28. C. Tsang, M. Chen, T. Yogi, and K. Ju, *IEEE Trans. Magn.* 26, 1689 (1990).
29. O. Akiyama, H. Konno, D. Inami, and Y. Kuraishi, *IEEE Trans. Magn.* 30, 4617 (1994).
30. Y. Taga, *J. Vac. Sci. Technol. A* 13, 990 (1995).
31. R. E. Fontana Jr., *IEEE Trans. Magn.* 31, 2579 (1995).
32. H. N. Bertram, *IEEE Trans. Magn.* 31, 2573 (1995).
33. J. C. S. Kools, *IEEE Trans. Magn.* 32, 3165 (1996).
34. J. K. Spong, V. S. Speriosu, R. E. Fontana Jr., M. M. Dovek, and T. L. Hylton, *IEEE Trans. Magn.* 32, 366 (1996).
35. K.-M. H. Lenssen, A. E. T. Kuiper, and F. Roozeboom, *J. Appl. Phys.* 85, 5531 (1999).

36. J. Bass and W. P. Pratt, *J. Magn. Magn. Mater.* 200, 274 (1999).
37. T. Valet and A. Fert, *Phys. Rev. B* 48, 7099 (1993).
38. "Ultrathin Magnetic Structures II" (B. Heinrich and J. A. C. Bland, Eds.), Chap. 2. Springer-Verlag, 1994.
39. "Magnetic Multilayers and Giant Magnetoresistance" (U. Hartmann, Ed.), Chaps. 3–6. Springer-Verlag, Berlin/New York, 2000.
40. M. D. Stiles and D. R. Penn, *Phys. Rev. B* 61, 3200 (2000).
41. R. S. Sorbello, *Phys. Rev. B* 39, 4984 (1989); B. Laithtman and S. Luryi, *Phys. Rev. B* 49, 17,177 (1994); R. Landauer, *Phys. Rev. B* 52, 11,225 (1995); C. Kunze, *Phys. Rev. B* 51, 14,085 (1995).
42. K. M. Schep, J. B. A. N. van Hoof, P. J. Kelly, G. E. W. Bauer, and J. E. Inglesfeld, *J. Magn. Magn. Mater.* 177, 1166 (1998).
43. J. A. Katine, A. Palanisami, and R. A. Buhrman, *Appl. Phys. Lett.* 74, 1883 (1999).
44. J. S. Moodera, L. R. Kinder, T. M. Wong, and R. Meservey, *Phys. Rev. Lett.* 74, 3273 (1995).
45. M. Sharma, S. X. Wang, and J. H. Nickel, *Phys. Rev. Lett.* 82, 616 (1999); J. M. de Teresa, A. Barthélémy, A. Fert, J. P. Contour, R. Lyonnet, F. Montaigne, P. Seneor, and A. Vaurès, *Phys. Rev. Lett.* 82, 4288 (1999).
46. J. M. de Teresa, A. Barthelemy, A. Fert, J. P. Contour, F. Montaigne, and P. Seneor, *Science* 286, 507 (1999).
47. J. C. Slonczewski, *Phys. Rev. B* 39, 6995 (1989).
48. M. Julliere, *Phys. Lett. A* 54, 225 (1975).
49. J. Halbritter, *J. Appl. Phys.* 58, 1320 (1985).
50. J. S. Moodera and L. R. Kinder, *J. Appl. Phys.* 79, 4724 (1996).
51. J. S. Moodera, J. Nowak, and R. J. M. van de Veerdonk, *Phys. Rev. Lett.* 80, 2941 (1998).
52. C. H. Shang, J. Nowak, R. Jansen, and J. S. Moodera, *Phys. Rev. B* 58, R2919 (1998).
53. M. Sato, H. Kikuchi, and K. Kobayashi, *J. Appl. Phys.* 83, 6691 (1998).
54. M. Tondra, J. M. Daughton, D. Wang, R. S. Beech, A. Fink, and J. A. Taylor, *J. Appl. Phys.* 83, 6688 (1998).
55. J. M. Daughton, *J. Appl. Phys.* 81, 3758 (1997).
56. H. Boeve, R. J. M. van de Veerdock, B. Dutta, J. de Boeck, J. S. Moodera, and G. Borghs, *J. Appl. Phys.* 83, 6700 (1998).
57. M. Sharma, "Semiconducting Memories: Technology, Testing, and Reliability," IEEE Press, New York, 1997.
58. G. A. Prinz, *Science* 250, 1092 (1990).
59. S. S. P. Parkin, *Phys. Rev. Lett.* 67, 3598 (1991).
60. W. Geerts, Y. Suzuki, T. Katayama, K. Ando, and S. Yoshida, *Phys. Rev. B* 50, 12,581 (1995).
61. R. Mégy, A. Bounouh, Y. Suzuki, P. Beauvillain, P. Bruno, C. Chappert, B. Lecuyer, and P. Veillet, *Phys. Rev. B* 51, 5586 (1995).
62. A. Carl and D. Weller, *Phys. Rev. Lett.* 74, 190 (1995).
63. H. A. Wierenga, W. de Jonge, M. W. J. Prins, Th. Rasing, R. Vollmer, A. Kirilyuk, H. Schwabe, and J. Kirschner, *Phys. Rev. Lett.* 74, 1462 (1995).
64. W. Weber, C. H. Back, A. Bischof, Ch. Wursch, and R. Allenspach, *Phys. Rev. Lett.* 76, 1940 (1996); W. Weber, A. Bischof, R. Allenspach, Ch. Wursch, C. H. Back, and Pescia, *Phys. Rev. Lett.* 76, 3424 (1996).
65. R. Jungblut, M. T. Johnson, J. van de Stegge, A. Reinders, and F. J. A. den Broeder, *J. Appl. Phys.* 75, 6424 (1994).
66. J. Fassbender, C. Mathieu, B. Hillebrands, G. Guntherodt, R. Jungblut, and M. T. Johnson, *J. Magn. Magn. Mater.* 148, 156 (1995).
67. W. Weber, C. H. Back, A. Bischof, D. Pescia, and R. Allenspach, *Nature (London)* 374, 788 (1995).
68. R. K. Kawakami, M. O. Bowen, H. J. Choi, E. J. Escorcia-Aparicio, and Z. Q. Qiu, *Phys. Rev. B* 58, 5924 (1998).
69. P. Krams, F. Lauks, R. L. Stamps, B. Hillbrands, and G. Guntherodt, *Phys. Rev. Lett.* 69, 3674 (1992).
70. R. Allenspach and W. Weber, *IBM J. Res. Develop.* 42, 7 (1998).
71. B. T. Jonker, K.-H. Walker, E. Kisker, G. A. Printz, and C. Carbone, *Phys. Rev. Lett.* 57, 142 (1986); B. Heinrich, K. B. Urquhart, A. S. Arrot, J. F. Cochran, K. Myrtle, and S. T. Purcell, *Phys. Rev. Lett.* 59, 1756 (1987); M. Stampanoni, A. Vaterlaus, M. Aeschlimann, and F. Meier, *Phys. Rev. Lett.* 59, 2483 (1987).
72. P. Schulz and K. Baberschke, *Phys. Rev. B* 50, 13,467 (1994).
73. W. Weber, A. Bischof, R. Allenspach, C. H. Bach, J. Fassbender, U. May, B. Schirmer, R. M. Jungblut, G. Guntherodt, and B. Hillbrands, *Phys. Rev. B* 54, 4075 (1996).
74. R. Allenspach and W. Weber, Magnetoresistive Sensor, PCT Patent Application WO 96/16339, 1996.
75. C.-A. Chang, *Appl. Phys. Lett.* 58, 1745 (1991).
76. G. R. Harp and S. S. P. Parkin, *Appl. Phys. Lett.* 65, 3063 (1994).
77. P. Grunberg, R. Schreider, Y. Pang, M. B. Brodsky, and H. Sowers, *Phys. Rev. Lett.* 57, 2442 (1986).
78. S. S. P. Parkin, N. More, and K. P. Roche, *Phys. Rev. Lett.* 64, 2304 (1990).
79. S. S. P. Parkin, R. Bhadra, and K. P. Roche, *Phys. Rev. Lett.* 66, 2152 (1991).
80. S. S. P. Parkin, Z. G. Li, and D. J. Smith, *Appl. Phys. Lett.* 58, 2710 (1991).
81. R. F. C. Farrow, *IBM J. Res. Develop.* 42, 43 (1998).
82. J. de la Figuera, J. E. Prieto, C. Ocal, and R. Miranda, *Phys. Rev. B* 47, 13,043 (1993); J. Camarero, L. Spendeler, G. Schmint, K. Heintz, J. J. de Miguel, and R. Miranda, *Phys. Rev. Lett.* 73, 2448 (1994).
83. J. F. Bobo, H. Kikuchi, O. Redon, E. Snoeck, M. Piecuch, and R. L. White, *Phys. Rev. B* 60, 4131 (1999).
84. J. Camarero, T. Graf, J. J. de Miguel, R. Miranda, W. Kuch, M. Zharnikov, A. Dittschar, C. M. Schneider, and J. Kirschner, *Phys. Rev. Lett.* 76, 4428 (1996).
85. W. F. Egelhoff Jr., P. J. Chen, C. J. Powell, M. D. Stiles, R. D. McMichael, C.-L. Lin, J. M. Sivertsen, J. H. Judy, K. Takano, and A. E. Berkowitz, *J. Appl. Phys.* 80, 5183 (1966).
86. W. F. Egelhoff Jr., P. J. Chen, C. J. Powell, M. D. Stiles, R. D. McMichael, J. H. Judy, K. Takano, and A. E. Berkowitz, *J. Appl. Phys.* 82, 6142 (1966).
87. M. D. Stiles, *Phys. Rev. B* 48, 7238 (1993).
88. M. Zheng, J. Shen, Ch. Mohan, P. Ohresser, J. Barthel, and J. Kirshner, *Appl. Phys. Lett.* 74, 425 (1999).
89. S. Maat, M. T. Ulmor, D. Orgassa, H. S. Cho, O. Koshkina, H. Fujiwara, and G. J. Mankey, *Phys. Rev. B* 61, 4082 (2000).
90. G. Ehlrich and F. G. Hudda, *J. Chem. Phys.* 44, 1039 (1966); R. L. Schwoebel and E. J. Shipsey, *J. Appl. Phys.* 37, 3682 (1966).
91. J. E. van Nostrand, S. J. Chey, M. A. Hasan, D. G. Cahill, and J. E. Greene, *Phys. Rev. Lett.* 74, 1127 (1995); M. C. Bartelt and J. W. Evans, *Phys. Rev. Lett.* 75, 4250 (1995).
92. G. S. Bales and A. Zangwill, *Phys. Rev. B* 41, 5550 (1990).
93. M. Giesen, G. S. Icking-Konert, and H. Ibach, *Phys. Rev. Lett.* 80, 552 (1998) and references therein.
94. R. Stumph and M. Scheffler, *Phys. Rev. Lett.* 72, 254 (1994).
95. T. J. Minvielle, R. J. Wilson, and R. L. White, *Appl. Phys. Lett.* 68, 2750 (1996).
96. M. Ohring, "The Materials Science of Thin Films." Academic Press, San Diego, 1992, Section 5.7.2 and references therein.
97. A. R. Modak, D. J. Smith, and S. S. P. Parkin, *Phys. Rev. B* 50, 4232 (1994).
98. R. J. M. van de Veerdonk, P. J. L. Belien, K. M. Schep, J. C. S. Kools, M. C. de Nooijer, M. A. M. Gijs, R. Coehoorn, and W. J. M. de Jonge, *J. Appl. Phys.* 82, 6152 (1997).
99. F. N. Hooge, *Phys. Lett.* 29A, 139 (1969).
100. N. Smith, A. M. Zelster, and M. R. Parker, *IEEE Trans. Magn.* 32, 135 (1996).
101. C. Prados, D. Garcia, F. Lesmes, J. J. Freijo, and A. Hernando, *Appl. Phys. Lett.* 67, 718 (1995).
102. J. M. Gallego, D. Lederman, S. Kim, and I. K. Schuller, *Phys. Rev. Lett.* 74, 4515 (1995).
103. N. Song, C. Sellers, and J. B. Ketterson, *Appl. Phys. Lett.* 59, 479 (1991).
104. H. Sato, Y. Kobayashi, Y. Aoki, Y. Saito, and K. Inomata, *Phys. Rev. B* 52, 9823 (1995).
105. D.-H. Han, *Appl. Phys. Lett.* 68, 2153 (1996).
106. J. M. Gallego, D. Lederman, T. J. Moran, and I. K. Schuller, *Appl. Phys. Lett.* 64, 2590 (1994).

107. F. Lesmes, A. Salcedo, J. J. Freijo, D. Garcia, A. Hernado, and C. Prados, *Appl. Phys. Lett.* 69, 2596 (1996).
108. D. C. Look, "Electrical Characterization of GaAs Materials and Devices," pp. 9–21. Willey, New York, 1992.
109. D. G. Stinson, A. C. Palumbo, B. Brandt, and M. Berger, *J. Appl. Phys.* 61, 3816 (1987).
110. D. A. Thomson, L. T. Romankiw, and A. F. Maydas, *IEEE Trans. Magn.* 11, 1039 (1975).
111. C. Christides, S. Stavroyiannis, and D. Niarchos, *J. Phys.: Condens. Matter* 9, 7281 (1997).
112. W. Ke, *Bull. Acad. Sci. USSR, Phys. Ser.* 29, 581 (1965).
113. S. Chikazumi, "Physics of Ferromagnetism," 2nd ed., Chaps. 16–18. Clarendon, Oxford, U.K., 1997.
114. C. Christides, I. Panagiotopoulos, D. Niarchos, T. Tsakalakos, and A. F. Jankowski, *J. Phys.: Condens. Matter* 6, 8187 (1994).
115. G. A. Held, M. G. Samant, J. Stohr, S. S. P. Parkin, B. D. Hermsmeier, M. van Schilfgaarde, and R. Nakajima, *Z. Phys. B* 100, 335 (1996).
116. E. F. Kuritsyna and W. Ke, *Bull. Acad. Sci. USSR, Phys. Ser.* 29, 585 (1965).
117. U. Rudiger, J. Yu, L. Thomas, S. S. P. Parkin, and A. D. Kent, *Phys. Rev. B* 59, 11,914 (1999).
118. Y. Q. Jia, L. Kong, R. C. Shi, and S. Y. Chou, *J. Appl. Phys.* 81, 5475 (1997).
119. D. M. Edwards, J. Mathon, R. B. Muniz, and M. S. Phan, *Phys. Rev. Lett.* 67, 493 (1991).
120. P. Bruno and C. Chappert, *Phys. Rev. Lett.* 67, 1602 (1991); *Phys. Rev. Lett.* 67, 2592 (1991); Phys. Rev. B 46, 261 (1992).
121. J. R. Cullen and K. B. Hathaway, *Phys. Rev. B* 47, 14,998 (1993).
122. Z. Q. Qiu, J. E. Mattson, C. H. Sowers, U. Welp, S. D. Bader, H. Tang, and J. C. Walker, *Phys. Rev.* B 45, 2252 (1994).
123. Z. Zhang, L. Zhou, P. E. Wigen, and K. Quanadjela, *Phys. Rev. B* 50, 6094 (1994).
124. J. N. Chapman, J. Rose, P. A. Aitchison, H. Holloway, and D. J. Kubinski, *J. Appl. Phys.* 86, 1611 (1999).
125. C. Christides, S. Stavroyiannis, G. Kallias, A. G. Nassiopoulou, and D. Niarchos, *Sens. Actuators* 76, 167 (1999).
126. D. J. Kubinski and H. Holloway, *J. Appl. Phys.* 79, 1661 (1996).
127. D. J. Kubinski and H. Holloway, *J. Appl. Phys.* 82, 322 (1997).
128. C. Christides, *J. Appl. Phys.* 88, 3552 (2000).
129. J. F. MacKay, C. Teichert, D. E. Savage, and M. G. Lagally, *Phys. Rev. Lett.* 67, 3925 (1996).
130. J. W. Freeland, K. Bussmann, Y. U. Idzerba, and C.-C. Kao, *Phys. Rev. B* 60, 9923 (1999).
131. C. Christides, S. Stavroyiannis, N. Boukos, A. Travlos, and D. Niarchos, *J. Appl. Phys.* 83, 3724 (1998).
132. F. Bridou, *J. Phys. III France* 4, 1513 (1994).
133. C. Christides, S. Stavroyiannis, D. Niarchos, M. Wojcik, S. Nadolski, and E. Jedryka, *Phys. Rev. B* 59, 8812 (1999).
134. C. Christides, S. Logothetidis, M. Gioti, S. Stergioudis, S. Stavroyiannis, and D. Niarchos, *J. Appl. Phys.* 83, 7757 (1998).
135. T. Gu, A. I. Goldman, and M. Mao, *Phys. Rev. B* 56, 6474 (1997); A. de Bernabé, M. J. Capitán, H. E. Fischer, and C. Prieto, *J. Appl. Phys.* 84, 1881 (1998); Y.-P. Zhao, G.-C. Wang, and T.-M. Lu, *Phys. Rev. B* 55, 13,938 (1997).
136. J. H. Underwood and T. W. Barbee Jr., *Appl. Opt.* 20, 3027 (1981).
137. T. C. Huang, R. Gilles, and G. Will, in "Advances in X-Ray Analysis" (J. V. Gilfrich et al., Eds.), Vol. 37, p. 183. Plenum, New York 1994.
138. D. K. G. de Boer, A. J. G. Leenaers, and W. W. van de Hoogenhof, *J. Phys. III France* 4, 1559 (1994).
139. P. A. Aitchison, J. N. Chapman, D. B. Jardine, and J. E. Evetts, *J. Appl. Phys.* 81, 3775 (1997).
140. N. Persat, H. A. M. van den Berg, and A. Dinia, *J. Magn. Magn. Mater.* 165, 446 (1997).
141. S. C. Ma, C. K. Lo, Y. D. Yao, D. Y. Chiang, T. F. Ying, and D. R. Huang, *J. Magn. Magn. Mater.* 209, 131 (2000).
142. H. Fujiwara, T. Ishikawa, and W. D. Doyle, *J. Appl. Phys.* 75, 6446 (1994).
143. J. Sasaki and F. Matsubara, *J. Appl. Phys.* 87, 3018 (2000).
144. H. Holloway and D. J. Kubinski, *J. Appl. Phys.* 83, 2705 (1998).
145. C. H. Marrows, R. Loloee, and B. J. Hickey, *J. Magn. Magn. Mater.* 184, 137 (1998).
146. C. H. Marrows and B. J. Hickey, *Phys. Rev. B* 59, 463 (1999).
147. N. Persat and A. Dinia, *Phys. Rev. B* 56, 2676 (1997).
148. C. Cowache, B. Dienny, A. Chamberod, D. Benizri, F. Berthet, S. Auffret, L. Giacomoni, and S. Nossov, *Phys. Rev. B* 53, 15,027 (1996).
149. B. D. Cullity, "Introduction to Magnetic Materials," p. 413–418. Addison-Wesley, Reading, MA, 1972.
150. M. S. Cohen, in "The Handbook of Thin Film Technology" (L. I. Maissel and R. Glang, Eds.), Chap. 17. McGraw-Hill, New York, 1983 reissue.
151. M. Kitada, *J. Magn. Magn. Mater.* 208, 244 (2000), and references therein.
152. F. J. A. den Broeder, D. Kuiper, A. P. van de Mosselaer, and W. Hoving, *Phys. Rev. Lett.* 60, 2769 (1988).
153. M. Wojcik, C. Christides, E. Jedryka, S. Nadolski, and I. Panagiotopoulos, *Phys. Rev. B* 63, 012102 (2001).
154. C. G. Lee, S. H. Kim, D. H. Lee, and K. Fukamichi, *IEEE Trans. Magn.* 35, 2856 (1999).
155. J. Bernardi, A. Hutten, and G. Thomas, *J. Magn. Magn. Mater.* 157–158, 153 (1996).
156. S. Stavroyiannis, C. Christides, D. Niarchos, Th. Kehagias, Ph. Komninou, and Th. Karakostas, *J. Appl. Phys.* 84, 6221 (1998), and references therein.
157. Th. Kehagias, Ph. Komninou, C. Christides, G. Nouet, S. Stavroyiannis, and Th. Karakostas, *J. Cryst. Growth* 208, 401 (2000).
158. C. Christides, S. Stavroyiannis, D. Niarchos, M. Gioti, and S. Logothetidis, *Phys. Rev. B* 60, 12,239 (1999).
159. E. A. M. van Alphen and W. J. M. de Jonge, *Phys. Rev. B* 51, 8182 (1995).
160. C. Meny, E. Jedryka, and P. Panissod, *J. Phys.: Condens. Matter* 5, 1547 (1993).
161. E. A. M. van Alphen, S. G. E. te Velthuis, H. A. M. de Gronckel, K. Kopinga, and W. J. M. de Jonge, *Phys. Rev. B* 49, 17,336 (1994).
162. M. Malinowska, M. Wojcik, S. Nadolski, E. Jedryka, P. Panissod, C. Meny, M. Knobel, A. D. C. Viegas, and J. E. Schmidt, *J. Magn. Magn. Mater.* 198–199, 599 (1999).
163. P. Panissod, C. Meny, M. Wojcik, and E. Jedryka, *Mater. Res. Soc. Symp. Proc.* 475, 157 (1997).
164. E. Velu, C. Dupas, D. Renard, J. P. Renard, and J. Seiden, *Phys. Rev. B* 37, 668 (1988).
165. M. Viret, D. Vingoles, D. Cole, J. M. D. Coey, W. Allen, D. S. Daniel, and J. F. Gregg, *Phys. Rev. B* 53, 8464 (1996).
166. A. Fuss, S. Demokritov, P. Grunberg, and W. Zinn, *J. Magn. Magn. Mater.* 103, L221 (1992).
167. C. M. Schneider, A. K. Schmid, P. Schuster, H. P. Oepen, and J. Kirschner, *NATO Adv. Sci. Inst. Ser. B* 309, 453 (1993).
168. M. Nývlt, Ph.D. Thesis, Charles University, Prague, 1996.
169. J. E. Ortega, F. J. Himpsel, G. J. Mankey, and R. F. Willis, *Phys. Rev. B* 43, 1540 (1993).
170. P. Lang, L. Nordstrom, W. Wilderberger, R. Zeller, P. H. Dederichs, and T. Hoshino, *Phys. Rev. B* 53, 9092 (1996).
171. R. K. Kawakami, E. Rotenberg, H. J. Choi, E. J. Escorcia-Aparicio, M. O. Bowen, J. H. Wolfe, E. Arenholz, Z. D. Zhang, N. V. Smith, and Z. Q. Qiu, *Nature* 398, 132 (1999); R. K. Kawakami, E. Rotenberg, E. J. Escorcia-Aparicio, H. J. Choi, T. R. Cummins, J. G. Tobin, N. V. Smith, and Z. Q. Qiu, *Phys. Rev. Lett.* 80, 1754 (1998).
172. M. J. Hall, B. J. Hickey, M. A. Howson, M. J. Walker, J. Xu, D. Creig, and N. Wiser, *Phys. Rev. B* 47, 12785 (1993).
173. V. Grolier, D. Renard, B. Bartelian, P. Beauvillain, C. Chappert, C. Dupas, J. Ferre, M. Galtier, E. Kolb, M. Mulloy, J. P. Renard, and P. Veilet, *Phys. Rev. Lett.* 71, 3023 (1993).
174. C. Christides, R. Lopusnik, J. Mistrik, S. Stavroyiannis, and S. Visnovsky, *J. Magn. Magn. Mater.* 198–199, 36 (1999).
175. M. Cardona, in "Modulation Spectroscopy," Solid State Physics, Suppl. 11 (F. Seitz, D. Turnbull, and H. Ehrenreich, Eds.). Academic, New York, 1969.

176. P. O. Nilsson, "Solid State Physics" (H. Ehrenreich, F. Seitz, and D. Turnbull, Eds.), Vol. 29, p. 139. Academic, New York, 1974.
177. Y. Zheng and J.-G. Zhu, *J. Appl. Phys.* 85, 4776 (1999).
178. Z. J. Yang and M. R. Scheinfein, *Phys. Rev. B* 52, 4263 (1995).
179. R. E. Camley and J. Barnas, *Phys. Rev. Lett.* 63, 664 (1989); J. Barnas, A. Fuss, R. E. Camley, P. Grundberg, and W. Zinn, *Phys. Rev. B* 42, 8110 (1990).
180. J. Barnas, O. Baksalary, and A. Fert, *Phys. Rev. B* 56, 6079 (1997).
181. D. E. Aspnes, E. Kinsborn, and D. D. Bacon, *Phys. Rev. B* 21, 3290 (1980).
182. M. I. Theye, *Phys. Rev. B* 2, 3060 (1970).
183. R. Lasser, N. V. Smith, and R. L. Benbow, *Phys. Rev. B* 24, 1895 (1981).
184. E. Anno, M. Tanimoto, and T. Yamaguchi, *Phys. Rev. B* 38, 3521 (1988).
185. C. Viguier, A. Cros, A. Humbert, C. Ferrieu, O. Thomas, R. Madar, and J. P. Senateur, *Solid State Commun.* 60, 923 (1986).
186. J. H. Weaver, E. Colavita, D. W. Lynch, and R. Rosei, *Phys. Rev. B* 19, 3850 (1979).
187. Y.-C. Yu, T. M. Donovan, and W. E. Spicer, *Phys. Rev.* 167, 670 (1968).
188. P. Heimann, H. Miosga, and H. Neddermeyer, *Phys. Rev. Lett.* 42, 801 (1979).
189. R. Atkinson, W. R. Hendren, I. W. Salter, and M. J. Walker, *J. Magn. Magn. Mater.* 130, 442 (1994).
190. S. Visnovsky, M. Nyvlt, V. Prosser, J. Ferre, G. Penissard, D. Renard, and G. Sczigel, *J. Magn. Magn. Mater.* 128, 179 (1993).
191. S. Uba, L. Uba, A. Ya Perlov, A. N. Yaresko, V. N. Antonov, and R. Gontarz, *J. Phys.: Condens. Matter* 9, 447 (1997).
192. S. Logothetidis, J. Petalas, N. K. Flevaris, and R. L. Johnson, *Thin Solid Films* 234, 538 (1993).
193. S. Logothetidis and N. K. Flevaris, *J. Appl. Phys.* 75, 7978 (1994).
194. L. Vina, S. Logothetidis, and M. Cardona, *Phys. Rev. B* 30, 1979 (1984).
195. P. T. Coleridge and I. M. Templeton, *Phys. Rev. B* 25, 7818 (1982).
196. B. Voigtlander, G. Meyer, and N. M. Amer, *Phys. Rev. B* 44, 10,354 (1991).
197. J. V. Barth, H. Brune, G. Ertl, and R. J. Behm, *Phys. Rev. B* 42, 9307 (1990).
198. P. D. Johnson, K. Garrison, Q. Dong, N. V. Smith, D. Li, J. E. Mattson, J. Pearson, and S. D. Bader, *Phys. Rev. B* 50, 8954 (1994); C. Carbone, E. Vescovo, R. Klasges, W. Eberhardt, O. Rader, and W. Gubat, *J. Appl. Phys.* 76, 6966 (1994); N. B. Brookes, Y. Chang, and P. D. Johnson, *Phys. Rev. B* 50, 15330 (1994); P. D. Johnson, *Rep. Prog. Phys.* 60, 1217 (1997).
199. J. Mathon, A. Umerski, M. Villeret, and R. B. Muniz, *Phys. Rev. B* 59, 6344 (1999).
200. J. Barnas and A. Fert, *Phys. Rev. B* 49, 12,835 (1994).
201. S. S. P. Parkin and T. Rabedeau, *Appl. Phys. Lett.* 68, 1162 (1996).
202. C. Meny, P. Panissod, and R. Loloee, *Phys. Rev B* 45, 12,269 (1992).
203. E. Jedryka, M. Wojcik, S. Nadolski, D. J. Kubinski, and H. Holloway, *J. Magn. Magn. Mater.* 165, 292 (1997).
204. P. Panissod, J. Ph. Jay, C. Meny, M. Wojcik, and E. Jedryka, *Hyperfine Interact.* 97–98, 75 (1996); N. Persat, A. Dinia, J. P. Jay, C. Meny, and P. Panissod, *J. Magn. Magn. Mater.* 164, 37 (1996).
205. P. Panissod, A. Qachaou, J. Durand, and H. Hasegawa, *Nucl. Instrum. Methods Phys. Res.* 199, 231 (1982); A. Qachaou, Ph.D. Thesis (3e cycle), Strasbourg, 1981.
206. T. Kingetsu and K. Sarai, *Phys. Rev. B* 48, 4140 (1993); *J. Appl. Phys.* 74, 6308 (1993); *J. Appl. Phys.* 73, 7622 (1993); T. Kingetsu, *Jpn J. Appl. Phys.* 36, 1658 (1997).
207. H. A. M. de Gronckel, P. J. H. Bloemen, E. A. M. van Alphen, and W. J. M. de Jonge, *Phys. Rev. B* 49, 11,327 (1994).
208. Ch. Rath, J. E. Prieto, S. Muller, R. Miranda, and K. Heinz, *Phys. Rev. B* 55, 1079 (1997).
209. M. A. Parker, T. L. Hylton, K. R. Coffey, and J. K. Howard, *J. Appl. Phys.* 75, 6382 (1994).
210. J. R. Childress and C. L. Chien, *Phys. Rev. B* 43, 8089 (1991).
211. C. Gente, M. Oehring, and R. Bormann, *Phys. Rev. B* 48, 13,244 (1993).
212. G. L. Zhou, M. H. Yang, and C. P. Flynn, *Phys. Rev. Lett.* 77, 4580 (1996).
213. H. Lefakis, M. Benaissa, P. Humbert, V. S. Speriosou, J. Werckmann, and B. A. Gurney, *J. Magn. Magn. Mater.* 154, 17 (1996).
214. M. Speckmann, H. P. Oepen, and H. Ibach, *Phys. Rev. Lett.* 75, 2035 (1995).
215. M. Dreyer, M. Kleiber, A. Wadas, and R. Wiesendanger, *Phys. Rev. B* 59, 4273 (1999).
216. N. Marsot, R. Belkhou, H. Magnan, P. Le Fevre, C. Guillot, and D. Chandersis, *Phys. Rev. B* 59, 3135 (1999).
217. I. Meunier, G. Treglia, J.-M. Gay, B. Aufray, and B. Legrand, *Phys. Rev. B* 59, 10,910 (1999).
218. D. Renard and G. Nihoul, *Phil. Mag. B* 55, 75 (1987).
219. R. Clark, S. Elagoz, W. Vavra, E. Schuler, and C. Uher, *J. Appl. Phys.* 70, 5775 (1991).
220. N. Mliki, K. Abdelmoula, G. Nihoul, C. Marliere, and D. Renard, *Thin Solid Films* 224, 14 (1993).
221. F. Hakkens, A. De Veirman, W. Coene, and F. J. A. den Broeder, *J. Mater. Res.* 8, 1019 (1993).
222. H. Ardhuin, E. Snoeck, and M.-J. Casanove, *J. Cryst. Growth* 182, 394 (1997).
223. T. L. H. Hylton, K. R. Coffey, M. A. Parker, and J. K. Howard, *Science* 261, 1021 (1993).
224. Y. K. Kim and S. C. Sanders, *Appl. Phys. Lett.* 66, 1009 (1995).
225. S. S. P. Parkin, *Appl. Phys. Lett.* 60, 512 (1992).
226. W. Folkerts, *J. Magn. Magn. Mater.* 94, 302 (1991); W. Folkerts and S. T. Purcell, *J. Magn. Magn. Mater.* 111, 306 (1992).
227. C. Christides, S. Stavroyiannis, and D. Niarchos, *J. Appl. Phys.* 80, 4512 (1996).
228. E. E. Fullerton, I. K. Schuller, H. Vanderstraeten, and Y. Bruynseraede, *Phys. Rev. B* 45, 9292 (1992).
229. D. W. Pashley, "Processing of Metals and Alloys: Materials Science and Technology" (R. W. Cahn, P. Haasen, and E. J. Kramer, Eds.), Vol. 15, Chap. 7, pp. 290–328. VCH, Weinheim, 1991.
230. O. S. Song, C. K. Kim, and R. C. O'Handley, *J. Appl. Phys.* 79, 3141 (1996); O. S. Song, C. A. Ballentine, and R. C. O'Handley, *Appl. Phys. Lett.* 64, 2593 (1994).
231. I. J. Garshelis, *J. Appl. Phys.* 73, 5629 (1993).
232. L. Callegaro and E. Puppin, *Appl. Phys. Lett.* 68, 1279 (1996); E. Puppin and L. Callegaro, *IEEE Trans. Magn.* 32, 281 (1996).
233. S. S. P. Parkin, *Appl. Phys. Lett.* 61, 1358 (1992).
234. B. Dieny, V. S. Speriosou, J. P. Nozieres, B. A. Gurney, A. Vadyayev, and N. Ryzhanova, "Magnetism and Structure in Systems of Reduced Dimension" (R. F. C. Farrow, B. Dienny, M. Donath, A. Fert, and B. D. Hermsmeier, Eds.), Vol. 309, p. 279. Plenum, New York, 1993.
235. G. H. Jonker and J. H. van Santan, *Physica* 16, 337 (1950); *Physica* 19, 120 (1953); G. H. Jonker, *Physica* 22, 707 (1956).
236. C. Zener, *Phys. Rev.* 82, 403 (1951); P. W. Anderson and H. Hasegawa, *Phys. Rev.* 100, 675 (1955).
237. P. G. de Gennes, *Phys. Rev.* 118, 141 (1960).
238. R. von Helmolt, J. Wecker, B. Holzapfel, L. Schultz, and K. Samwer, *Phys. Rev. Lett.* 71, 2331 (1995).
239. S. Jin, T. H. Tiefel, M. McCormack, R. A. Fastnacht, R. Ramesh, and L. H. Chen, *Science* 264, 413 (1994).
240. E. O. Wollan and W. C. Koehler, *Phys. Rev.* 100, 545 (1955).
241. P. Schiffer, A. P. Ramirez, W. Bao, and S.-W. Cheong, *Phys. Rev. Lett.* 75, 3336 (1995).
242. G. Xiao, G. Q. Gong, C. L. Canedy, E. J. McNiff Jr., and A. Gupta, *J. Appl. Phys.* 81, 5324 (1997).
243. H. Kuwahara, Y. Tomioka, A. Asamitsu, Y. Moritomo, and Y. Tokura, *Science* 270, 961 (1995).
244. M. Tokunaga, N. Miura, Y. Tomioka, and Y. Tokura, *Phys. Rev. B* 57, 5259 (1998).
245. J. Z. Sun, W. J. Gallanger, P. R. Duncombe, L. Krusin-Elbaum, R. A. Altman, A. Gupta, Y. Lu, G. Q. Gong, and G. Xiao, *Appl. Phys. Lett.* 69, 3266 (1996).
246. A. Gupta, G. Q. Gong, G. Xiao, P. R. Duncombe, P. Lecoeuer, P. Trouilloud, Y. Y. Wang, V. P. Dravid, and J. Z. Sun, *Phys. Rev. B* 54, 15,629 (1996).
247. T. Kimura, Y. Tomioka, H. Kuwahara, A. Asamitsu, M. Tamura, and Y. Tokura, *Science* 274, 1698 (1996).

248. S.-W. Cheong, H. Y. Hwang, and B. Batlogg, *Bull. Amer. Phys. Soc.* 41, 634 (1996).
249. I. Bozovic and J. N. Eckstein, *Appl. Surf. Sci.* 113–114, 189 (1997).
250. W. H. Meiklejohn and C. P. Bean, *Phys. Rev.* 105, 904 (1957); *Phys. Rev.* 102, 1413 (1956).
251. C. Tsang, N. Heiman, and K. Lee, *J. Appl.Phys.* 52, 2471 (1981); *J. Appl. Phys.* 53, 2605 (1982).
252. R. Jungblut, R. Coehoorn, M. T. Johnson, J. van de Stegge, and A. Reinders, *J. Appl. Phys.* 75, 6659 (1994).
253. P. J. van der Zaag, A. R. Ball, L. F. Feiner, R. M. Wolf, and P. A. A. van er Heijden, *J. Appl. Phys.* 79, 5103 (1996).
254. K. Takano, R. H. Kodama, A. E. Berkowitz, W. Cao, and G. Thomas, *Phys. Rev. Lett.* 79, 1130 (1997).
255. T. Ambrose, R. L. Sommer, and C. L. Chien, *Phys. Rev. B* 56, 83 (1997).
256. Y. Ijiri, J. A. Bochers, R. W. Erwin, S. H. Lee, P. J. Van der Zaag, and R. M. Wolf, *Phys. Rev. Lett.* 80, 608 (1998).
257. J. Nogues, D. Lederman, T. J. Moran, I. Shuller, and K. V. Rao, *Appl. Phys. Lett.* 68, 3186 (1998).
258. Yu Lu, X. W. Li, G. Q. Gong, G. Xiao, A. Gupta, P. Lecoeur, J. Z. Sun, Y. Y. Wang, and V. P. Dravid, *Phys. Rev. BR* 54, 8357 (1996).
259. V. A. Vasko, V. A. Larkin, P. A. Kraus, K. R. Nikolaev, D. E. Grupp, C. A. Nordman, and A. M. Goldman, *Phys. Rev. Let.* 78, 1134 (1997).
260. G. Q. Gong, A. Gupta, G. Xiao, P. Lecoeur, and T. R. McGuire, *Phys. Rev. B* 54, R3742 (1996).
261. M. Sahana, M. S. Hedge, V. Prasad, and S. V. Subamanyam, *J. Appl. Phys.* 85, 1058 (1999).
262. M. Izumi, Y. Murakami, Y. Konishi, T. Manako, M. Kawasaki, and Y. Tokura, *Phys. Rev. B* 60, 1211 (1999).
263. K. R. Nikolaev, A. Bhattachrya, P. A. Kraus, V. A. Vas'ko, W. K. Cooley, and A. M. Goldman, *Appl. Phys. Lett.* 75, 118 (1999).
264. B. Wiedenhorst, C. Höfener, Y. Lu, J. Klein, L. Alff, R. Gross, B. H. Freitag, and W. Mader, *Appl. Phys. Lett.* 74, 3636 (1999).
265. C. Kwon, K.-C. Kim, M. C. Robson, J. Y. Gu, M. Rajeswari, T. Venkatesan, and R. Ramesh, *J. Appl. Phys.* 81, 4950 (1997).
266. K. Ghosh, S. B. Ogale, S. P. Pai, M. Robson, E. Li, I. Jin, Z. Dong, R. L. Greene, R. Ramesh, T. Venkatesan, and M. Johnson, *Appl. Phys. Lett.* 73, 689 (1998).
267. R. Cheng, K. Li, S. Wang, Z. Chen, C. Xiong, X. Xu, and Y. Zhang, *Appl. Phys. Lett.* 72, 2475 (1998).
268. I. Panagiotopoulos, C. Christides, M. Pissas, and D. Niarchos, *Phys. Rev. B* 60, 485 (1999).
269. A. J. Mlllis, *Nature* 392, 147 (1998).
270. W. Prellier, M. Rajeswari, T. Venkatesan, and R. L. Greene, *Appl. Phys. Lett.* 75, 1446 (1999).
271. T. C. Schulthess and W. H. Butler, *Phys. Rev. Lett.* 81, 4516 (1998); *J. Appl. Phys.* 85, 5510 (1999).
272. M. Hennion, F. Moussa, J. Rodriguez-Carvajal, L. Pinsard, and A. Revcolevschi, *Phys. Rev. B* 56, R497 (1997).
273. J. B. Goodenough, *J. Appl. Phys.* 81, 5330 (1997).
274. I. Panagiotopoulos, C. Christides, D. Niarchos, and M. Pissas, *J. Appl. Phys.* 87, 3926 (2000).
275. I. Panagiotopoulos, G. Kallias, M. Pissas, V. Psycharis, and D. Niarchos, *Mat. Science Engin. B* 53, 272 (1998).
276. S. V. Pietambaram, D. Kumar, R. K. Singh, and C. B. Lee, *Phys. Rev. B* 58, 8182 (1998).
277. M. T. Fernandez-Diaz, J. L. Martinez, J. M. Alonso, and E. Herrero, *Phys. Rev. B* 59, 1277 (1999).
278. E. S. Gillman, M. Li, and K.-H. Dahmen, *J. Appl. Phys.* 84, 6217 (1998).
279. C.-C. Chen and A. de Lozanne, *Appl. Phys. Lett.* 73, 3950 (1998).
280. C. Srinitiwarawong and M. Ziese, *Appl. Phys. Lett.* 73, 1140 (1998).
281. I. V. Solovyev and K. Terakura, *Phys. Rev. Lett.* 83, 2825 (1999).
282. H. B. Peng, X. X. Zhang, Z. Xie, H. J. Tao, B. Xu, H. Liu, and B. R. Zhao, *Phys. Rev. B* 61, 8955 (2000).
283. N. Moutis, C. Christides, I. Panagiotopoulos, and D. Niarchos, *Phys. Rev. B* 64, (2001), in press.
284. M. D. Stiles and R. D. McMichael, *Phys. Rev. B* 60, 12,950 (1999); *Phys. Rev. B* 60, 3722 (1999).
285. A. F. Khapikov, J. W. Harrel, H. Fujiwara, and C. Hou, *J. Appl. Phys.* 87, 4954 (2000).
286. J. Wang, W. N. Wang, X. Chen, H. W. Zhao, J. G. Zhao, and W. Sh. Zhan, *Appl. Phys. Lett.* 77, 2731 (2000).
287. D. Cao, F. Bridges, D. C. Worledge, C. H. Booth, and T. Geballe, *Phys. Rev. B* 61, 11,373 (2000).
288. L. Néel, *Ann. Goephysique* 5, 99 (1949).
289. V. I. Nikitenko, V. S. Gornakov, L. M. Dedukh, Yu. P. Kabanov, A. F. Khapikov, A. J. Shapiro, R. D. Shull, A. Chaiken, and R. P. Michel, *Phys. Rev. B* 57, R8111 (1998).
290. F. T. Parker and H. Oesterreicher, *Phys. Status Solidi* a75, 273 (1983).
291. K. Moorjani and J. M. D. Coey, "Magnetic Glasses." Elsevier, Amsterdam, 1984.
292. Q. Huang, J. W. Lynn, R. W. Erwin, A. Santoro, D. C. Dender, V. N. Smolyaninova, K. Ghosh, and R. L. Greene, *Phys. Rev. B* 61, 8895 (2000).
293. H. Tanaka and T. Kawai, *J. Appl. Phys.* 88, 1559 (2000).
294. V. Korenivski, R. B. van Dover, Y. Suzuki, E. M. Gyorgy, J. M. Phillips, and R. J. Felder, *J. Appl. Phys.* 79, 5926 (1996).
295. B. Aktas, Y. Oner, and H. Z. Durusoy, *J. Magn. Magn. Mater.* 119, 339 (1993).
296. S. Soeya, T. Imagawa, K. Mitsuoka, and S. Narishige, *J. Appl. Phys.* 76, 5356 (1994).
297. G. H. Yu, C. L. Chai, F. W. Zhu, J. M. Xiao, and W. Y. Lai, *Appl. Phys. Lett.* 78, 1706 (2001).
298. Q. Huang, J. W. Lynn, R. W. Erwin, A. Santoro, D. C. Derder, V. N. Smolyaninova, K. Ghosh, and R. L. Green, *Phys. Rev. B* 61, 8895 (2000).
299. A. E. Berkowitz and K. Takano, *J. Magn. Magn. Mater.* 200, 552 (1999).
300. J. Z. Sun, L. Krusin-Elbaum, P. R. Duncombe, A. Gupta, and R. B. Laibowitz, *Appl. Phys. Lett.* 70, 1769 (1997).
301. P. R. Willmott and J. R. Huber, *Rev. Mod. Phys.* 72, 315 (2000).
302. P.-J. Kung, D. B. Fenner, D. M. Potrepka, and J. I. Budnick, *Appl. Phys. Lett.* 69, 427 (1996); Z. Trajanovic, C. Kwon, M. C. Robson, M.-C. Kim, M. Rajeswari, R. Ramesh, T. Venkatesan, S. E. Lofland, S. M. Bhagat, and D. Fork, *Appl. Phys. Lett.* 69, 1005 (1996).
303. J. Daughton and J. Granley, *The Industrial Physicist* 5, 22 (1999).
304. J. F. Gregg, W. Allen, K. Ounadjech, M. Viret, M. Hehn, S. M. Thomson, and J. M. D. Coey, *Phys. Rev. Lett.* 77, 1580 (1996).
305. D. T. Pierce, J. A. Stroscio, J. Urgunis, and R. J. Cellota, *Phys. Rev. B* 49, 14564 (1994); H. J. Elmers, J. Hauschild, H. Fritzsche, G. Liu, U. Grandman, and U. Kohler, *Phys. Rev. Lett.* 75, 2031 (1995).
306. C. Tsang, *J. Appl. Phys.* 55, 2226 (1981).
307. T. Lin, C. Tsang, R. Fontana, and J. Howard, *IEEE Trans. Magn.* 31, 2585 (1995); T. Lin, G. Gorman, and C. Tsang, *IEEE Trans. Magn.* 32, 3443 (1996).
308. M. R. Fitzsimmons, P. Yashar, C. Leighton, I. K. Schuller, J. Nogués, C. F. Majkrzak, and J. A. Dura, *Phys. Rev. Lett.* 84, 3986 (2000), and references therein.
309. L. Thomas, M. G. Samant, and S. S. P. Parkin, *Phys. Rev. Lett.* 84, 1816 (2000).
310. J. Zhou, "Dynamic Micromagnetic Modeling for Magnetic Films and Devices," invited Lecture in the Summer School Proceedings on "Mesomagnetism, Spin-Dynamics and Spin-Electronics," September 11–17, Rhodes Greece 1999; www-ipcms.u-strasbg.frDynaspin.
311. K. J. Kirk, J. N. Chapman, S. McVitie, P. R. Aitchison, and C. D. W. Wilkinson, *J. Appl. Phys.* 87, 5105 (2000).
312. J. M. De Teresa, A. Barthélémy, A. Fert, J. P. Contour, R. Lyonnet, F. Montaigne, P. Seneor, and A. Vaurés, *Phys. Rev. Lett.* 82, 4288 (1999).
313. K. I. Kobayashi, T. Kimura, H. Sawada, K. Terakura, and Y. Tokura, *Nature* (London) 395, 677 (1998).
314. *IBM J. Res. Develop.* 44, pp. 309–452 (2000).